Shear-Flexible RC Fibre Frame Elements with Bond-Slip for Seismic Analysis

A thesis sumitted

in partial fulfillment of the requirements

for the award of the degree of

Doctor of Philosophy

by

Saroj Kumar Sahu

to the

Department of Civil Engineering

Indian Institute of Technology Guwahati

Guwahati - 781039, Assam, India

January 2024

Declaration

I hereby declare that the work contained in this thesis is the outcome of research conducted by me at the Indian Institute of Technology Guwahati, India. No part of this work has been submitted for the award of any degree, diploma, associateship, fellowship, or its equivalent to any University or Institution. The sources referred in the citation of this work have been appropriately acknowledged by explicit references and footnotes. Other assistance received has been acknowledged. I have not knowingly copied or used the words or ideas of others without acknowledgement.

Date:

Place: Guwahati

.....

Saroj Kumar Sahu
Roll No. 166104006
Department of Civil Engineering
Indian Institute of Technology Guwahati
Guwahati, Assam-781039, India

Certificate

This is to certify that **Saroj Kumar Sahu** (166104006) has been working under my supervision since July 2016 as a Ph.D. student. His thesis entitled "**Shear-Flexible RC Fibre Frame Elements with Bond-Slip for Seismic Analysis**" is an authentic record of the results obtained from the research work carried out under my supervision in the Department of Civil Engineering, Indian Institute of Technology Guwahati, Assam, India. The thesis, in my opinion, is worthy of consideration for the award of the degree of Doctor of Philosophy in accordance with the regulations of the institute. To the best of my knowledge, it has not been submitted elsewhere for the award of the degree.

Date:

Place: Guwahati

.....

Dr. Arbind Kumar Singh

Professor

Department of Civil Engineering

Indian Institute of Technology Guwahati

Guwahati, Assam-781039, India

Acknowledgements

I want to express my deep gratitude to the wonderful individuals who played a crucial role in my academic journey and offered unwavering support.

Foremost, I extend heartfelt thanks to Prof. Arbind Kumar Singh. His advice, patience, and support have been invaluable throughout my thesis. I feel fortunate to have a supervisor who not only allowed me the freedom to explore but also remained encouraging and tolerant during challenging times. His faith in me has been a driving force, keeping me motivated in my PhD work. The valuable advice he provided will undoubtedly shape my future career.

I am also grateful to my Doctoral Committee members, Prof. Konjengbam Darunkumar Singh, Prof. Uday Shanker Dixit, and Dr. Abhishek Kumar. Their suggestions and constructive criticism have significantly improved my research work.

A warm appreciation goes out to my colleagues, Maharshi, Kankan, Meera, Wanraplang, and Rantu for their constant encouragement and support in various aspects of my PhD work. Special thanks to my lab mates, Subhadip, Pallab, Monjusha, Arpita, Tori, Lavish, Pranjal, Kasturi, and Bonisha, whose presence made my time in the lab lively and engaging. I also extend my gratitude to my hostel friends, Anant, Rajeev, Rahul, Prasanta, Chandan, Arnab, Argha, Subhra, Siddharth, and Suman, whose support and friendship made the journey truly memorable.

Above all, my deepest gratitude goes to my parents, my sister and brother-in-law, my niece and nephew for their continuous support. Their belief in my abilities, as well as their encouragement, have been a constant source of motivation for me. Finally, I want to thank Priyanka, my life partner whom I met during this journey. Her faith and support have been invaluable, making this academic journey truly special.

This thesis is dedicated to
my parents

Abstract

Seismic assessment of reinforced concrete structures requires a reliable numerical model to predict the behaviour of structural members to aid in the design and retrofitting process. The existing experimental studies have identified the deformation in an RC member, mainly, consisting of bending (flexure), shearing and sliding of an anchored bar in the anchorage regions. Consideration of each of these deformations is essential for a reliable prediction of structural behaviour and failure. Although finite element models are capable of simulating the response accurately, these are not practical for the analysis of building structures. Alternatively, frame element models can provide a reliable prediction of inelastic behaviour exhibited by the structural members in a simple and effective manner.

Among the different modelling options, fibre frame elements are popular for studying the flexural behaviour of reinforced concrete frames due to their accuracy with respect to their computational demand. However, the modelling of shear and bond-slip deformation is important for a realistic prediction. In this thesis, fibre-based elements are developed to effectively consider the axial, flexure, and shear deformation in reinforced concrete members and rebar bond-slip in the anchorage region.

The first element developed in this thesis is a force-based fibre beam element with full axial-flexure-shear interaction at the element and section level, to consider the shear deformation. In this element, a multiaxial constitutive model is used for the concrete material based on a rotating smeared crack approach. Modified Compression Field Theory together with Mander confining model is implemented. The suitability of the available regularization methods is also examined to eliminate the localization issue to the softening of the section.

The use of a multiaxial constitutive model increases the computational demand of

the element. To further reduce the computational demand another force-based fibre beam element with simple flexure-shear interaction is developed. The element uses a shear force-shear strain relationship at the section level. A methodology is proposed to account for the flexure-shear interaction effect by reducing the shear force-shear strain relationship as a function of the amount of bending moment on the section.

To consider the anchorage-slip, a fibre hinge element is developed. The element consists of a single fibre section whose properties are expressed using stress-displacement relationships. The anchorage-slip element is added in series with the fibre beam element at the joint-member interface to consider the anchorage-slip deformation in an effective way.

The performance of the developed elements in simulating the seismic response analysis of reinforced concrete is verified by simulating the response of two reinforced concrete columns in shake-table experiments from the literature. The advantage of the proposed modelling approaches to incorporate the shear and anchorage-slip deformations is established by comparing the results with that of the traditional fibre element model.

Table of Contents

List of Figures

List of Tables

Nomenclature

All abbreviations and symbols used in the present research work are enlisted here along with their definitions.

List of Abbreviations

1D	One dimension
2D	Two dimension
3D	Three dimension
DB	Displacement-based
FB	Force-based
FE	Finite element
FS	Flexure-shear
MCFT	Modified Compression Field Thoery
RC	Reinforced concrete

List of Greek Symbols

α	Orientation of the element local coordinate with respect to global coordinate
$\boldsymbol{\sigma}$	2D State of stress ($\{\sigma_x, \sigma_y, \tau_{xy}\}^T$)
$\boldsymbol{\sigma}'_c$	Concrete stresses in principal direction
$\boldsymbol{\varepsilon}$	2D State of strain ($\{\varepsilon_x, \varepsilon_y, \gamma_{xy}\}^T$)
$\boldsymbol{\varepsilon}'$	Strain in principal direction
$\Delta()$	Incremental quantity

γ	Shear strain at the centroid of the section
μ_e	Average bond stress along the elastic development length
μ_y	Average bond stress along the plastic development length
ω	Natural frequency
ϕ	Section curvature
ψ	Function defining the shape of the shear strain distribution over the rectangular section
ρ_{sx}, ρ_{sy}	Ratio of smeared steel in longitudinal and transverse direction
σ_x, σ_y, τ_{xy}	Stress in longitudinal direction, stress in transverse direction and shear stress
θ	Direction of principal strain and principal stress
θ	Rotation of the section
θ_i	Rotation at element end 'i'
ε	Axial strain at the centroid of the section
ε_c^p	Concrete plastic strain
ε_1, ε_2	Strain in two principal directions
ε_c	Concrete uniaxial strain
ε_s	Steel uniaxial strain
ε_x, ε_y, γ_{xy}	Strain in longitudinal direction, strain in transverse direction and shear strain
ε_{c0}, ε_p	Concrete strain corresponding to f_{c0} and f_p
ξ	Damping ratio

List of Roman Symbols

$\mathbf{a}_s$	Section compatibility matrix
$\mathbf{b}$	Force interpolation matrix
$\mathbf{C}$	Structural damping matrix
$\mathbf{d}$	Section generalized displacement ($\{\phi, \gamma, \varepsilon\}^T$)
$\mathbf{D}$	2D Composite material matrix relating $\boldsymbol{\sigma}$ and $\boldsymbol{\varepsilon}$ as per MCFT
$\mathbf{D}_c'$	2D material matrix for plane concrete in principal direction

$\mathbf{D}_c$	2D material matrix for plane concrete
$\mathbf{D}_{ss}$	2D material matrix for smeared steel
$\mathbf{e}$	Fibre strains: for flexure-shear case $\mathbf{e} = \{\epsilon_x, \gamma_{xy}\}^T$; for flexure case $\mathbf{e} = \epsilon_x$
$\mathbf{F}$	Internal resisting force vector
$\mathbf{F}_{ele}$	Element flexibility matrix in basic system
$\mathbf{F}_s$	Section flexibility matrix
$\mathbf{I}$	Mass influence vector
$\mathbf{k}$	Fibre tangent stiffness
$\mathbf{K}_{st}$	Structural tangent stiffness matrix
$\widetilde{\mathbf{K}}_{st}$	Effective stiffness matrix
$\mathbf{K}_{ele}$	Element stiffness matrix in basic system
$\mathbf{K}_s$	Section Stiffness matrix
$\mathbf{M}$	Structural mass matrix
$\ddot{\mathbf{p}}$	Structural acceleration vector
$\dot{\mathbf{p}}$	Structural velocity vector
$\mathbf{p}$	Structural displacement vector
$\mathbf{P_0}$	Gravity load vector
$\mathbf{P}$	External load vector
$\overline{\mathbf{P}}$	Element nodal forces in the global reference system
$\mathbf{Q}$	Element nodal forces in the basic reference system ($\{M_I, M_J, N_J\}^T$)
$\mathbf{q}$	Element nodal displacements in the basic reference system ($\{\theta_I, \theta_J, u_J\}^T$)
$\overline{\mathbf{Q}}$	Element nodal forces in the local reference system
$\overline{\mathbf{q}}$	Element nodal displacements in the local reference system
$\mathbf{r}$	Residual section deformation
$\widetilde{\mathbf{R}}$	Effective force vector
$\mathbf{s}$	Fibre stresses: for flexure-shear case $\mathbf{s} = \{\sigma_x, \tau_{xy}\}^T$; for flexure case $\mathbf{s} = \sigma_x$
$\mathbf{S}$, $\hat{\mathbf{S}}$	Section generalized force and force resultant ($\{M_z, V, N\}^T$)
$\mathbf{T}_1$	Transformation matrix for transforming global coordinate to local coordinate
$\mathbf{T}_2$	Transformation matrix for transforming local force/displacement to basic

	force/displacement under the linear transformation assumption
$\mathbf{T}_{\varepsilon}$	Transformation matrix for transforming strain in Cartesian direction $\boldsymbol{\varepsilon}$ to strain principal direction $\boldsymbol{\varepsilon}'$
$\overline{\mathbf{u}}$	Element nodal displacements in the global reference system
$\mathbf{v}$	Residual element deformation
a_0, a_1	Rayleigh damping coefficient for mass and stiffness
a_g	Ground acceleration
d_b	Diameter of rebar
D_{ij}	Element of matrix $\mathbf{D}$
E	Tangent modulus of material
E_{c1}, E_{c2}	Tangent modulus of concrete in principal directions
E_{sx}, E_{sy}	Tangent modulus of smeared steel in x and y direction
f'_c	Cylindrical compressive strength
f_c	Concrete uniaxial stress
f_s	Steel uniaxial stress
f_{c0}, f_p, f_t	Concrete unconfined compressive strength, concrete peak compressive strength, concrete tensile strength
f_{c1}, f_{c2}	Concrete stress in two principal directions
f_{cx}, f_{cy}, v_{cxy}	Concrete stress in the longitudinal direction, the stress in the transverse direction and shear stress
f_{sx}, f_{sy}	Stress in smeared steel in longitudinal and transverse direction
G_c	Assumed shear modulus in the orthotropic model of concrete
H	Depth of the section
L	Length of the element
L^s	Straight length of the hooked bar
L_d	Development length
L_{drq}	Required development length of rebar
L_{ed}	Full elastic development length
L_{embd}	Embedment length of rebar
M	Moment
N	Axial force

S	Slip at the loaded end of the rebar
S_0	Slip at free end of rebar
t	Time period
u	Extension
u_0	Axial displacement at the centroid of the section
u_x	Axial displacement in fibre of anchorage slip element
V	Shear force
y	Height measured from the centroid

Chapter 1

Introduction

1.1 Background

The seismic events pose a major problem to the building structures. During an earthquake, the ground motion can induce lateral forces on a building, causing it to sway horizontally. These lateral forces can result in the deformation of structural components, potentially leading to structural damage or failure if not adequately accounted for in the building's design. The deformation of structural components primarily encompasses axial deformation, flexural deformation, and shear deformation. In addition to the above deformations, the joint behaviour between the beams-columns and column-footing also affects the member deformation.

The development of accurate and computationally efficient numerical models that can account for the deformation components within structural members has been a major research interest for many decades. Yet, the nonlinear response analysis of reinforced concrete buildings till collapse remains a complex task. Figure 1.1 shows some of the commonly used models for the framed type structures (Deierlein et al., 2010). These can be broadly classified into two groups, (i) discrete finite elements as shown in Figure 1.1 (a)-(d) and (ii) 2D/3D finite elements shown in Figure 1.1 (e). In discrete finite elements, each beam-column member of the structure is modelled as a 1D element whereas the members are modelled using a large number of finite elements in the 2D or 3D continuum finite element model. Although the latter approach produces

the most accurate results but is not practical to use due to their large computational demand. The discrete elements if properly designed can give insight into the response of structural members as well as the entire structure with significantly less computation and are commonly used nowadays to model large structures.

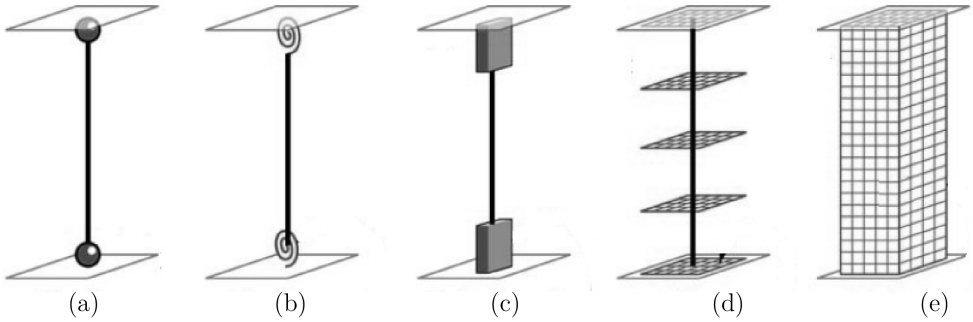

Figure 1.1: Different modelling approaches for framed structures (Deierlein et al., 2010): (a) nonlinear spring hinge model; (b) generalized plastic hinge model; (c) finite length hinge model; (d) fibre frame element model; (e) finite element model

The discrete finite elements, also referred to as frame elements or beam-column elements. These can be further categorized into two types based on the assumption of the spread of the nonlinearity along the element, namely (i) Lumped plasticity element (Figure 1.1 (a),(b)) and (ii) Distributed plasticity element (Figure 1.1 (c),(d)). In the Lumped plasticity element, nonlinear behaviour is concentrated at the ends of the element. The concentrated nonlinearity is represented with lumped springs in which the moment–rotation relationship is calibrated based on a sectional analysis or experimental results. These are simple but require a priori knowledge of the location of hinge and speard of inelastic behaviour. Alternatively, the distributed plasticity model allows modelling the spread of nonlinearity throughout the member. This model requires fine discretization, either in terms of mesh refinement or the number of integration points, to better reflect the realistic structural response.

The distributed plasticity element shown in Figure 1.1 (d) uses the section response at finite number of sections along the element. The section responses are used in integral over the length of the beam element to give the overall member response. The section behaviour of a reinforced concrete member is described by stress resultant plasticity-based model in some of the frame models (Takizawa and Aoyama, 1976; Chen and

Powell, 1982; El-Tawil and Deierlein, 1998) and by fibre models in other (Mari and Scordelis, 1984; Lai et al., 1984; Zeris and Mahin, 1988; Spacone et al., 1996). In the fibre model, each section response is obtained by integrating fibre responses at a finite number of material points on the section. The distributed plasticity element with fibre section referred to as the fibre frame element offers many merits compared with the other element models. In such an element, the nonlinearity can occur over any section, thus, it represents the spreading of nonlinearity along the member and produces a realistic representation of the structural response with the geometric and material data without any calibration requirement. The axial-bending interaction effect is naturally accounted for in the element.

Frame elements based on lumped- and distributed-plasticity approaches have been proposed in many earlier studies. Most of these models focus on modelling the ductile response of reinforced concrete members governed by flexural yielding. It is important to recognise that reinforced concrete member displays a range of behaviours based on the relative contribution of the different deformation components. Considering each of these deformation components and their interaction with each other is essential for correctly capturing the behaviour of members in order to assure the construction of reliable structures against seismic events. This thesis attempts to consider the shear deformation along the element and strain penetration in the anchorage region in the fibre frame element.

1.2 Shear Behaviour in RC Members

Reinforced concrete members exhibit a diverse range of behaviour starting from a ductile flexural failure to brittle shear failure depending on the relative contribution of flexural deformation and shear deformation. It has been observed that RC members with inadequate detailing are prone to experience a significant shear deformation and fail in brittle shear mode or ductile shear mode in plastic hinge zone under the combined effect of axial, flexure and shear. A shear mode failure typically undergoes severe degradation and exhibits significant pinching behaviour. It has also been shown that RC columns may become shear critical as more damage accumulates even when its

initial shear strength is higher than the flexural capacity (Sezen and Moehle, 2004). This phenomenon occurs due to the flexure-shear interaction effect, where the shear capacity of the member reduces with loading. The correct representation of the flexure-shear interaction effect is important for a reliable simulation of RC structure.

1.3 Anchorage Bond-Slip Behaviour in RC Members

The bond behaviour between the rebar and concrete in the anchorage region affects the response of the RC member. The slippage of rebar due to penetration of rebar strain in the anchorage region results in localized deformation in the form of fixed-end rotation at the member-joint interface. The joint deformation can become significant based on the anchorage condition. It has been found that this type of deformation can contribute up to 40% of the total displacement (Saatcioglu et al., 1992).

1.4 Objectives and Scope of the Present Work

Experimental findings suggest that the behaviour of reinforced concrete members is affected by the shear deformation and anchorage slip effect. A frame element used for the numerical modelling should be able to account for axial-flexure-shear interaction closer to experimental results for understanding the seismic behaviour of framed structures. The available fibre frame elements based on the Euler-Bernoulli plane section hypothesis, are only suitable to model the flexure-dominated response of the member. The exact modelling of shear deformation and the anchorage bond-slip in fibre elements are computationally demanding. There is a need for the development of a simple and efficient fibre frame element considering the shear interaction effect and anchorage-bond slip for the reinforced concrete members.

This thesis aims to develop fibre-based elements capable of considering shear and joint rotation due to anchorage bond slip and to perform seismic analysis (nonlinear static and transient dynamic analysis) considering axial, flexure, shear, and anchorage

bond-slip deformations. Based on the literature review and research gap identified in Chapter 2, the following objectives are formulated for the present research work.

1. To develop fibre element with axial-flexure-shear interaction
   (a) Force-based fibre frame element with coupled axial-flexure-shear interaction using Modified Compression Field Theory as concrete consecutive relation
   (b) Force-based fibre frame element with semi-uncoupled flexure-shear interaction using a simplified cyclic shear force-shear strain relation
2. To develop a fibre link element to consider the end rotation due to slippage of rebar in the anchorage region
3. To study the seismic behaviour of RC structural members using the developed elements

This study is limited to the development of force-based fibre-based element for 2D plane frame. Only material nonlinearity is considered. The axial, flexure and shear deformations are considered along the element. The bond-slip in the anchorage region has been considered. Although the slip along the element also affects the element deformation, it is out of the scope of the work. Strength degradation is only considered for concrete material. The complexity of the adopted material models was kept to a minimum.

1.5 Organization of the Thesis

The thesis has been arranged into seven chapters in addition to appendices and references. The contents of each of the chapters are briefly summarized below.

- In the second chapter, review of existing literature on incorporating shear deformation and anchorage bond-slip in the fibre frame element model is carried out. Some of the gaps in the current literature were identified.
- In the third chapter, a coupled axial-flexure-shear force-based fibre element based on parabolic shear strain distribution has been developed for the plane frame.

The concrete constitutive model is based on smeared rotating-crack model based on Modified Compression Field Theory to account the axial-flexure-shear interaction. The performance of the element has been studied and the effect of a number of integration points on the softening behaviour of the element has also been studied.

- In the fourth chapter, a force-based fibre element with semi-uncoupled flexure-shear interaction is proposed. The element uses a variable shear force-shear strain relation which is obtained from the coupled sectional analysis. Simplified shear force-shear strain hysteresis rules are proposed for the cyclic loading. The performance of the element has been studied by simulating the experimental results from the literature.

- In the fifth chapter, a fibre-based anchorage-slip element is implemented to enhance the capability of the developed shear elements. A parametric study is conducted to study the effect of fibre stress-displacement properties of the response of the anchorage-slip element.

- In the sixth chapter, the performance of the developed elements in earlier chapters in the seismic analysis is studied.

- Finally, the seventh chapter concludes the thesis and discusses the future directions in this domain.

Chapter 2

Literature Review

2.1 Introduction

The fibre element is an effective means to model the inelastic behaviour of RC structural members. An element should be able to account for axial-flexure-shear interaction closer to experimental results for understanding seismic behaviour of framed structures. Anchorage slip plays an important role in the behaviour of these structures. The consideration of each of the deformation contributions as well as their interaction is essential for a reliable prediction of the overall behaviour and failure of the structure. This chapter first discusses different fibre element and their effectiveness in modelling the response of reinforced concrete members. It is followed by a detailed literature review of various methods for modelling inelastic shear response, shear-flexure interaction, and anchorage slip in fibre beam-column elements for nonlinear response analysis of reinforced concrete structures. The research gaps in these areas were identified that led to the formulation of objectives presented in Section 1.4.

2.2 Fibre Frame Element Models

Numerical modelling of frame structure is generally performed using discrete element model or finite element model as shown in Figure 1.1. The discrete element models are particularly suitable for the analysis of large structures as each beam-column member of the structure is modelled as a 1D element. These elements can be further categorized

into two types based on the assumption of the spread of the nonlinearity along the element, namely

(i) lumped plasticity element, and

(ii) distributed plasticity element

In the lumped plasticity element, nonlinear behaviour is concentrated at the ends of the element. These are simple but require a priori knowledge of the location of hinge and speard of inelastic behaviour. Alternatively, the distributed plasticity model allows modelling the spread of nonlinearity throughout the member. In this type of element, the nonlinearity is evaluated at selected monitoring sections along the element. The section response is integrated over the length of the beam element to give the overall member response. In this study distributed plasticity element is used.

Fibre frame element shown in Figure 1.1 (d) is a type of distributed plasticity element in which each monitoring section is further divided into concrete and steel fibres. The strains in these fibres were calculated from the centroidal strain and section curvature by assuming that plane sections remain plane. From the assumed uniaxial stress-strain relationships, tangent stiffness moduli were calculated for the various fibres. From these fibre stiffness moduli, the section stiffness can be arrived by proper summation. These stiffness are integrated by using interpolation functions depending on the formulation to obtain the element stiffness. This type of model has the advantage that the axial load-bending interaction is automatically accounted for (Spacone et al., 1996). Fibre element is an effective means to model the structural members as it can reproduce the local and global behaviour using the geometry of member and section and material stress-strain relationship without the need for any significant calibration. Based on formulation, the fibre frame elements can be classified as:

(a) displacement-based element

(b) force-based element, and

(c) mixed method elements.

The displacement-based formulation assumes the element displacements as the primary unknowns and uses displacement interpolation functions to derive the element deformations. The force-based and mixed formulation uses force interpolation functions to derive the element force field. In this study force-based element has been used.

This study concern developed of force based element considering axial-flexure-shear interaction and anchorage-bond slip. Literature review is presented on the following topics:

(i) force-based fibre frame element,

(ii) approaches to account the shear deformation in the fibre element, and

(iii) approaches to account bond-slip effect in the fibre element.

2.3 Force-Based Fibre Frame Element

The element formulated following the force-based and mixed methods provides many advantages compared to the displacement-based method. Unlike the displacement-based approach, force interpolation functions used in force-based elements satisfy equilibrium in a strict sense. The force-based formulation does not restrain the expected development of inelastic curvatures along the element. Consequently, only one element per structural member is required when no internal element loads are present. A discretization error, as generally encountered in stiffness-based formulations, does not occur. Thus, when material nonlinearities are considered, it provides more accurate results with fewer elements per member (Calabrese et al., 2010). Very recently, some displacement-based model has been proposed that can consider a single element per member (Tarquini et al., 2017; Pantò et al., 2019).

Another advantage of using force-based elements is there is no issue of shear locking (Zienkiewicz and Taylor, 2005). The shear locking problem that is always present when displacement-based, shear-deformable beam elements are adopted requires special treatment in order to be avoided. Various methods can be found in the literature for circumventing such situations on displacement-based beams (Oñate, 2013).

2.3.1 State determination of force-based fibre element

The main difficulty with the flexibility formulation arises in the element state determination phase. In the context of a standard finite element analysis program, this phase involves the determination of the stiffness matrix and the element resisting forces for given end displacements. The state determination is not straightforward as there are

non-deformation interpolation functions to relate the deformations along the element to the end displacements. The initial methods for force-based elements rely on ad hoc solution methods (Kaba and Mahin, 1984; Zeris and Mahin, 1988). Later, the element formulation based on a mixed method gave a consistent way of determining element resisting forces from the given displacement (Ciampi and Carlesimo, 1986; Spacone et al., 1996; Neuenhofer and Filippou, 1997).

2.3.2 Localization issue in fibre element

Fibre elements have a numerical problem in the presence of a deformation-softening response. Both displacement-based and force-based elements produce objective (mesh convergent) responses at the global and local levels for hardening (i.e., pre-peak) constitutive relations. Whereas the results are nonobjective in the case of a softening constitutive law. This numerical issue is commonly known as strain localization or simply localization, as the computed damage is localized into a limited zone. This numerical issue was first discussed by Zeris and Mahin (1988) for displacement-based elements and by Coleman and Spacone (2001) for force-based elements. A proper definition of localization is given in Calabrese et al. (2010) from the physical and numerical viewpoints. It is found that the post-peak response using displacement- and force-based elements are highly sensitive to the number of element discretization and to the number of integration points considered along the member, respectively. For force-based elements, several mesh regularization techniques have been proposed. Different approaches can be grouped into following:

(a) nonlocal approach

(b) constant fracture energy approach, and

(c) scaling of integration weight approach.

They are reviewed in the next sections.

(a) Nonlocal approach

In the presence of softening material, the highly strained section of a beam-column element continues to load into the softening region while the neighbouring section unloads.

This local behaviour of the traditional element results in a discontinuity in the strain. Nonlocal approaches address this problem by considering the influence of neighbouring regions on the behaviour of the softening section. Nonlocal methods can be categorized into integral nonlocal models Valipour and Foster (2007) and gradient-based nonlocal models Sideris and Salehi (2016); Feng et al. (2016). Both approaches define nonlocal strain and incorporate them either in the constitutive model or strain-displacement relation to avoid the formation of strain localization and provide a smoother strain distribution. It's important to note that computational costs may increase due to the additional effort required to evaluate nonlocal strains. Therefore, careful implementation of nonlocal approaches is essential to ensure computational efficiency.

(b) Constant fracture energy approach

The softening behaviour of an element is found to have a strong correlation with the softening of concrete under compression. Coleman and Spacone (2001) used the concept of constant fracture energy Bažant and Oh (1983) to the stress-strain relation of concrete in compression to regularize the element response. They introduced an additional parameter known as the fracture energy in compression. They used this prescribed parameter to modify the post-peak branch of the concrete stress-strain relation at different locations of the element. Note that this is equivalent to assuming a constant stress-displacement relation rather than a constant stress-strain law. This approach effectively ensured objectivity in the global response. However, the local response is not regularized. To obtain an objective local section response, additional geometric scaling is required (Coleman and Spacone, 2001).

(c) Scaling of integration weight approach

For force-based beam-column FEs, the strain concentration usually occurs at the end cross-section. This approach takes advantage of this fact and tries to manipulate the numerical integration of the section strains along the element length. The techniques basically calibrate the weighting lengths associated to the end quadrature points (where localization occurs) so that the resulting solution does not depend on the total number of the element quadrature points. Different regularization techniques based on scaling

of integration weight have been proposed by Addessi and Ciampi (2007); Scott and Fenves (2006); Scott and Hamutçuoğlu (2008) among others.

Addessi and Ciampi (2007) and Scott and Fenves (2006) divided an element into three sub-regions, one plastic hinge region at each end and one interior region, each with a different number and location of the integration points. Addessi and Ciampi (2007) used Gauss-Lobatto integration over each region. Scott and Fenves (2006) applied a mixture of Gauss-Radau and Gauss-Legendre quadrature, with Gauss-Radau quadrature over the plastic hinge region and Gauss-Legendre quadrature over the interior region. Both methods scaled the integration weights at the element ends equal to the specified characteristic lengths to regularize the element response. Scott and Hamutçuoğlu (2008) used interpolation quadrature to regularize softening response in force-based elements. In interpolatory quadrature, the integration weights at the element ends are made equal to characteristic values and then solved by the system of equations for the remaining unknown integration weights.

Another limitation with the approaches based on the modification of integration weights ensures objectivity for strain-softening behaviour, but it shows a lack of convergence for a strain-hardening response. Scott and Hamutçuoğlu (2008) proposed further modification to interpolatory quadrature with two additional integration points at small distances from the element ends to regularize force-based element response while maintaining numerical accuracy for strain-hardening behaviour. Some of the other researchers have proposed methods based on a similar idea and accounting for the evolution of hinge length Almeida et al. (2012); Feng and Ren (2017).

2.3.3 Discussion on force-based fibre element

Based on the literature review conducted in the preceding sections, force-based fibre beam element are an effective means to model the material nonlinearity in reinforced concrete structural members. However, the force-based element has the issue of strain localization in the presence of a softening section response. Where the element result becomes dependent on the number of sections considered along the element. Several techniques have been developed to address the issue. But, these developments are

limited to the fibre elements based on the Euler-Bernoulli beam theory. The evaluation of these techniques for the force-based frame elements that consider shear deformation were not explored. In last three decades, several researchers have incorporated the shear in the fibre model. A review of the methods is presented in the following sections.

2.4 Modelling of Inelastic Shear Deformation

Many different approaches have been proposed to include shear deformation in one-dimensional frame elements. These can be categorized into two groups based on the scale of the adopted shear constitutive relation:

(i) member level model, and

(ii) section level model.

The first group of models takes shear into account at the member level. These models typically concentrate the inelastic shear response at a point hinge (lumped plasticity models) or along a finite length of the member. The shear response of the hinge is expressed by an empirical hysteretic shear force-deformation relation derived from experimental or analytical studies. The emphasis of these models is to capture the global behaviour of the member without being overly concerned with local response. On the contrary, the second group of models account for shear at the local (section or material) level and allows for shear strain variation along the element. These belong to the distributed plasticity model and can capture both the local and global behaviour of the member. The following section discusses some of the representative models from each group. As this work is focused on modeling the shear deformation along the element the member level models are only briefly reviewed here.

2.4.1 Member level model

In general, a member-level model isolates and models each contributing component of the inelastic displacement. Therefore, these are also referred to as component models. The most basic approach for modelling the inelastic shear behaviour is to use a shear spring in series with a flexural element (concentrated plasticity or distributed plasticity). The spring material properties are defined using an envelope curve for monotonic

lateral force-shear displacement ($V - \Delta_s$) behaviour, as well as rules for cyclic excursion between the envelope curves. Several models have been proposed in the literature to predict the shear envelope under monotonic loading. These include empirical expressions (Ang et al., 1989; Watanabe and Ichinose, 1991; Priestley et al., 1994) and theoretical models such as Compression Field Theory (CFT) by Collins (1978); Modified Compression Field Theory (MCFT) by Vecchio and Collins (1986); Disturbed Stress Field Theory (DSFT) by Vecchio (2000); Rotating-Angle Softened Truss Model (RA-STM) by Belarbi and Hsu (1995); Pang and Hsu (1995); Fixed-Angle Softened Truss Model (FA-STM) by Pang and Hsu (1996); Softened Membrane Model (SMM) by Hsu and Zhu (2002); Cyclic Softened Membrane Model (CSMM) by Mansour and Hsu (2005). Some examples of member-level models that include shear effects are given briefly below. It begins with a single component spring-in-series element and is followed by a generalized hinge element and finite size inelastic zones element model.

(a) Spring in series model

The earliest models in this category are the models proposed by D'Ambrisi and Filippou (1999); Pincheira et al. (1999). D'Ambrisi and Filippou (1999) proposed a subelement model where a separate subelement is used to describe the basic mechanisms that control the hysteretic behaviour. The shear subelement consists of two shear springs connected by a rigid bar. The properties of the monotonic shear force-deformation relation of the shear subelement were established with the MCFT. The reduction of flexural and shear strength due to cyclic damage was not included in the model. Pincheira et al. (1999) developed a column element with rotational springs at the end and a shear spring in the middle. The moment-rotation relation for the rotational springs included strength degradation with increasing rotations. The backbone curve of the shear spring was derived with the MCFT and accounted for strength degradation under cyclic loading conditions. Shirai et al. (2001) similarly decomposed the beam deformation into flexural and shear components. The flexural model uses the fibre section discretization and is in series with the shear model.

These models do not account for shear strength degradation with inelastic flexural deformations. They may not accurately predict the point of shear failure for columns

experiencing flexural yielding prior to shear failure (Elwood and Moehle, 2003). Several models have been developed to represent the degradation of shear strength with increasing deformation (Ichinose, 1992; Ascheim and Moehle, 1992; Priestley et al., 1994; Sezen and Moehle, 2004; Biskinis et al., 2004). However, Elwood pointed out that shear-strength models are not appropriate for predicting the drift at shear failure. To overcome this limitation, several drift capacity models have been proposed by Elwood (2004); Pujol et al. (1999); Sasani (2007); Mostafaei et al. (2009); Ghannoum and Moehle (2012).

Elwood (2004) proposed an empirical drift capacity model for shear and axial load failure of RC columns with flexural yielding prior to shear failure. According to the model when the column drift ratio exceeds the pre-defined drift capacity, shear resistance begins degradation. The degrading slope after shear failure is represented by a shear-friction model. Later, Ghannoum and Moehle (2012) proposed a deformation capacity model with a rotation limit instead of a drift limit considering rotations across the plastic hinge region are a better measure of column demand in multistory frame structure. Take note that the limiting drift capacity proposed by Elwood was developed based on calibration with limited test results of columns expected to experience flexural yielding prior to shear failure. Recently Zimos et al. (2018) developed a deformation criterion based on local shear deformation from a large number of column test results.

Sezen and Chowdhury (2009) proposed a spring in series model with separate springs for flexure, reinforcement slip and shear response. The shear response was calculated from the MCFT model by considering the displacements at the onset of shear strength degradation and axial failure following the model proposed by Elwood. The authors modified the cyclic rules proposed by Ozcebe and Saatcioglu (1989) to eliminate the details. The combined flexure, shear and slip response are calculated based on the dominant failure mode as proposed by Setzler and Sezen (2008).

The influence of the axial force-moment interaction on the post-peak behaviour of reinforced concrete members is not considered in most single-component hinge models, resulting in significant limitations because the effects of variable axial load on the flexural and shear capacity have been shown to have a significant impact on stiffness and

strength degradations. Some later developments took into account the full interaction of axial, flexure, and shear effects. Some examples include the models proposed by Lee and Elnashai (2002), Mostafaei and Kabeyasawa (2007), Xu and Zhang (2011, 2012).

Lee and Elnashai (2002) developed the hysteretic shear model for axial force variation to simulate flexure-shear-axial interaction in shear-dominated reinforced concrete columns. They did not account for the degradation of shear strength due to inelastic flexural deformation, so their model may not accurately predict the shear capacity for columns experiencing flexural yielding before shear failure.

Mostafaei and Kabeyasawa (2007) proposed ASFI, a displacement-based analysis method that accounts for axial-shear-flexure interaction in the column response. This macro-model-based approach consists of two models that simultaneously evaluate axial-flexural and axial-shear responses to obtain the total response of elements subjected to axial, flexure and shear loads. In this method, axial-flexure behaviour is simulated using conventional section analysis or fibre model whereas axial-shear response is determined using MCFT and one integration point in the in-plane stress conditions. The axial-flexural and axial-shear mechanisms are coupled in an average stress-strain field considering axial deformation interaction and softening of concrete compression strength while satisfying compatibility and equilibrium conditions. One limitation of this method in comparison to other spring in series models is that its state determination requires high computational demand and does not capture the hysteretic response of the RC element.

Later Mostafaei and Vecchio (2008) proposed UFSM to reduce some of the complexity of the method. This concept was also used by Lodhi and Sezen (2012) and Shoraka and Elwood (2013) to improve the previous models of Sezen and Elwood. Shoraka and Elwood (2013) proposed deformation limits for two types of shear failure (diagonal tension and compression failure) based on MCFT and used the shear deformation in the plastic hinge region of the column to detect the onset of shear failure.

Xu and Zhang (2011, 2012) presented a modelling approach for axial-shear-flexural interaction, first considering a model with shear-flexure interaction for a constant axial load and a second more complex model able to consider more properly the behaviour with a variation of axial load level, which becomes a controlling factor for the interaction

between shear and flexure failure mode and strength level in RC members.

(b) Other member level model

Yield-surface and evolution models approaches have been employed by some of the studies to account for the force interaction in the case of multiaxial loading to overcome some of the limitations in the spring in series models,(Ricles et al., 1998; Aboutaha et al., 1999; Galal and Ghobarah, 2003; Kaul, 2004; Reshotkina, 2015).

Ricles et al. (1998) used a macro-element with an elastic beam and nonlinear springs at the end. Three flexural springs and one shear spring were used in series at each end. A yield surface is defined for each flexural spring. The yield surfaces of each flexural spring were independent of the axial and shear force, while the flexural response did not account for strength deterioration. A shear failure surface was used on each shear spring. When a shear spring reached the failure surface, its capacity deteriorated with increasing shear deformation. The contraction of the original to the final failure surface took place in proportion to increasing shear deformation. The shear failure surface also contracted with increasing flexural ductility. Reshotkina (2015) proposed a similar generalized hinge element model based on a damage-based lumped plasticity formulation to account for different degradation effects and considering a 3D interaction between shear, flexure and axial load.

The lumped representation, in the above models, exhibits efficiency and ease of modelling. However, the approach has the limitation that the spread of inelasticity is not accounted for. Roufaiel and Meyer (1987) proposed a nonlinear beam model with finite-size inelastic zones. The inelastic zone at the beam ends spreads into the element as a function of the moment distribution, while the rest of the beam remains elastic. Shear deformations are not included in the model, but the Shear effects are accounted for through empirical modification of the hysteretic behaviour of the inelastic zone. The hysteretic model accounts for the strength degradation of the flexural response, but only includes the effect of shear in the stiffness deterioration and "pinching" of the hysteresis loops. Mergos and Kappos (2012) proposed a gradual spread plasticity model with shear deformation. Later Zimos et al. (2018) improved the model for simulating the post-peak response by developing a deformation criterion based on local shear

deformation from a large number of column test results.

2.4.2 Section level model

The previous section discussed member-level models that deal with concentrated plasticity and finite hinge length element models. This section belongs to the distributed plasticity class of elements where the nonlinearity is distributed along the element using a fibre cross-section or section resultant plasticity approach. In the fibre cross section, the resultant forces are obtained by integrating the stresses at the fibre locations that correspond to the strains according to section kinematic assumption. The stress and strains are related by the constitutive stress-strain model. The distributed plasticity element with fibre section has the ability to reproduce axial and flexural response and is increasingly being used for the modelling of RC elements. However, it should be noted that the overly simplified assumption of the conventional fibre element is not suitable to simulate the shear mode of failure. The enhancement of the method requires improved section kinematic relation and multi-axial material stress-strain relationship. The available section level models or local models with shear deformation can be classified into two groups:

(a) uncoupled section model, and

(b) coupled section model.

The list of literature reviewed is shown in Table 2.1. These models are presented under the following subsections.

(a) Uncoupled section model

The first group of models is based on the traditional Euler-Bernoulli beam theory but considers the shear effects by a separate model. As a result, only in partially coupling with axial forces and bending moments is achieved. (Guedes and Pinto, 1997; Martinelli, 2000; Ranzo and Petrangeli, 1998; Marini and Spacone, 2006; Sae-Long and Limkatanyu, 2018). The hysteretic shear model is defined at the section level in terms of shear force vs shear distortion $V-\gamma$ relationship, which consists of a backbone curve and the hysteresis rules for the response under cyclic loading. Both Guedes et al. 1994,

Table 2.1: Review of section models to account shear deformation in fibre elements

		References
Uncoupled/Semi-uncoupled		Martino et al. (2000); Ranzo and Petrangeli (1998); Marini and Spacone (2006); Sae-Long et al. (2019, 2020)
Fully coupled	Predefined shear strain\stress distribution	Rericha (1991); Petrangeli et al. (1999); Filippou and Saritas (2006); Ceresa et al. (2009); Mullapudi and Ayoub (2010); Guner and Vecchio (2011); Navarro-Gregori et al. (2013); Feng et al. (2017, 2019)
	Satisfying inner fibre equilibrium	Bentz (2000); Bairan and Mari (2007); Mohr et al. (2010); Kagermanov and Ceresa (2017); Di Re et al. (2018); Rajapakse et al. (2019)

and Martinelli 1998 introduced shear effects with an equivalent truss model. The $V-\gamma$ backbone curve was defined disregarding interaction with flexure. It should be noted that considering the $V-\gamma$ relation without degradation is equivalent to the spring in the series model. Thus, these earlier models do not account for the variation of the shear along the element.

Later models, based on a similar framework, include some degradation of the shear response in the section shear model. Ranzo and Petrangeli (1998) developed a force-based beam finite element model with bending moment, shear force and axial force interaction. The nonlinearity was distributed along the element length and over each section. The axial-flexural behaviour was obtained by a fibre discretization, and the shear response was described by a uniaxial force-deformation relation. The coupling of the shear response with flexure was accomplished with a damage parameter based on flexural ductility. Marini and Spacone (2006) construct the element formulation based on Timoshenko beam theory and used a separate constitutive law for shear response at the section level. Similarly, Sae-Long and Limkatanyu (2018) proposed a model based on an empirical shear force-deformation relationship.

This type of model has all the advantages of fibre beam elements in terms of robustness and simplicity of the material laws. In this element, the flexure and shear forces interact at the element level and maintain equilibrium due to the use force interpolation

in the formulation. That is, when a section becomes critical in shear the moment get reduced accordingly to maintain equilibrium at the element level. However, it has a similar limitation with shear spring as the constitutive law is based on empirical shear forces-deformation relations.

(b) Coupled section model

The second group of models utilizes multi-axial material laws instead of uniaxial material laws to account for the interaction of axial force, bending moment and shear force at the section and element levels. The element is based on Timoshenko or higher-order theory. The application of multiaxial constitutive stress-strain relation enables the coupling of longitudinal normal stress and shear stress at a material point, which naturally takes care of the interaction between the forces. Different models differ in terms of the underlying kinematic assumption and constitutive relationship. A detailed review of the models is presented in the following based on the kinematic assumptions. The models were classified as:

(i) kinematic incompatible models, and

(ii) kinematic compatible models.

Various constitutive models based on elasticity theory, plasticity theory, damage mechanics and fracture mechanics were used by researchers, which are not discussed here.

i. Kinematic incompatible model

The kinematics in this group of models is based on an assumed fixed distribution of shear on the section, such as those with constant or parabolic patterns. It should be noted that the consideration of a fixed distribution of shear is an approximation as the actual shear distribution is (highly dependent on the loading conditions through and section details) state-dependent and varies as the applied load varies. However, consideration of fixed distribution reduces the complexity of the problem substantially (Vecchio and Collins, 1988). In this type of model, the longitudinal axial strains are evaluated using the plane section assumption, while transverse strains are determined from equilibrium in the vertical direction using classical beam assumptions. The multi-

axial model is used to describe axial-shear interaction at the fibre level (Rericha, 1991; Petrangeli et al., 1999; Ceresa et al., 2009; Guner and Vecchio, 2011; Navarro-Gregori et al., 2013; Rajapakse et al., 2019; Mullapudi and Ayoub, 2010; Mazars et al., 2006; Feng et al., 2017, 2019).

Rericha (1991) proposed a displacement-based beam finite element within the framework of the Timoshenko beam theory. The study includes transverse strains by satisfying the transverse equilibrium equations for concrete and transverse reinforcement. Transverse strains were previously studied by Bazant and Bhat (1977) in the context of an RC section response but without implementation in a beam finite element model. In addition to the normal and shear strains of the section, transverse normal strains were included as parameters in order to account for the confinement effect of the transverse reinforcement. The section was subdivided into several layers in order to account for the combined effect of axial deformation, curvature and shear deformation by integration of the multiaxial material response. The endochronic theory was used to derive the multiaxial concrete stress-strain relation.

Petrangeli et al. (1999) proposed a force-based beam element within the framework of the Timoshenko beam theory. They considered the interaction between axial force, shear force and bending moment through fibre discretization of the section. The normal stress and shear stress were coupled at a material point using the multiaxial microplane concrete material model. The transverse strains were included by satisfying the transverse equilibrium equations of concrete and transverse reinforcing steel.

Filippou and Saritas (2006) proposed a beam element based on mixed formulation. The section kinematic is based on a parabolic distribution and the concrete biaxial relation is based on an orthotropic model based on the MCFT.

Based on a similar basic idea Ceresa et al. (2009) proposed displacement-based beam element within the framework of the Timoshenko beam theory. The concrete biaxial relation is based on an orthotropic model based on the MCFT. Guner and Vecchio (2011) proposed displacement-based beam element within the framework of the Timoshenko beam theory. concrete biaxial relation is based on an orthotropic model based on the DSFM. Navarro-Gregori et al. (2013) proposed displacement-based beam element within the framework of the Timoshenko beam theory. Mullapudi and Ayoub

(2010) proposed displacement-based beam element within the framework of the Timoshenko beam theory. Mazars et al. (2006) proposed displacement-based beam element within the framework of the Timoshenko beam theory. Feng et al. (2017) proposed displacement-based beam element within the framework of the Timoshenko beam theory. Feng et al. (2019) proposed force-based beam element within the framework of the Timoshenko beam theory.

ii. Kinematic compatible model

As previously stated, the assumption of a predefined fixed shear pattern in kinematic incompatible models is a limitation because the shear pattern on the section is state-dependent. Several researchers have proposed elements based on Timoshenko or higher-order theory that do not require any prior knowledge of shear stress or strain distribution (Vecchio and Collins, 1988; Bentz, 2000; Bairan and Mari, 2007; Mohr et al., 2010; Kagermanov and Ceresa, 2017). These models satisfy inter-fibre equilibrium conditions.

Vecchio and Collins (1988) developed a dual-section analysis for the case of 2D frame elements. The coupling between longitudinal and transverse stresses is obtained by explicitly considering the equilibrium between fibres, which involves the analysis of two adjacent cross-sections to approximate the longitudinal stress gradient. The dual-section model is a non-local model, as it needs information from adjacent points, so an ad hoc element formulation is needed. To overcome this problem, Bentz (2000) introduced the Longitudinal Stiffness Method, where the longitudinal stress gradient was calculated locally considering equilibrium equations at the beam level. This method is a local sectional model, but only for 2D elements. Tortolini et al. (2012) included dual-section analysis in beam-column element. Rajapakse et al. (2019) developed a force-based element with the section analysis of Benz, the element able to analyse monotonic increasing loading.

Kagermanov and Ceresa (2017) proposed a section model for the evaluation of an exact shear strain profile. The exact shear strain profile is obtained from an averaged form of inter-fibre equilibrium over the section, using linear interpolation functions. The formulation was implemented into a force-based, fibre-based frame element with

a smeared-crack, fixed-crack cyclic constitutive model.

In the models presented in the previous section, the element kinematics still relies on the Timoshenko beam theory, i.e. plane section assumption and no section distortion or warping, resulting in kinematic incompatibility between fibre deformations and element displacements. More recently, several higher-order theories were proposed dealing with the latter shortcomings (Bairan and Mari 2007, Mohr et al. 2010, Almeida 2009, Le Corvec 2012, Papachristidis et al 2010). Their application to nonlinear analysis of RC member is still in development. Moreover, their practical implementation for inelastic dynamic analysis is still in development. Moreover, their practical implementation for inelastic dynamic analysis needs further research due to the complexities associated with their formulation and high computational demands.

Bairan and Mari (2007) presented a detailed 3D sectional model called TINSA (Total Interacting Nonlinear Sectional Analysis). It is based on the enhancement of the kinematic field of Navier-Bernoulli theory by means of a warping-distortion displacement field which is obtained by solving the inter-fibre equilibrium in the section domain with a 2D FE model. The warping-distortion field considered is independent of the x-coordinate neglecting its variation along the beam length, this leads to a sectional model that is completely independent of the frame formulation. Thus there is no need for an additional degree of freedom at the beam level. A consequence of this assumption is that the effect of non-uniform warping and shear lag effects are neglected, but this is relevant in this-walled sections rather than in compact cross-sections as is the case of most reinforced concrete beams and columns. This formulation proved to capture the interaction between the six possible internal forces in sections of any shape and takes into account both longitudinal and transverse reinforcement explicitly. Its main drawback is the higher computation demand compared with traditional beam models.

Mohr et al. (2010) presented a modification of the TINSA model for the case of 2D frames. The complementary displacement field is calculated as a weighted sum of Taylor's polynomials defined in the section height. This method avoids the FE solution, reducing the computation cost of the original model. The sectional model was implemented on a flexibility-based frame element and tested in beams with bending moment and shear. As it was developed for 2D frames, no torsion or bidirectional shear

flow can be analysed with this model.

Le Corvec (2012) and Di Re et al. (2018) presented 3D frame element based also on the displacement decomposition. As an additional hypothesis to the original formulation, they presented a complementary displacement field, which only produces warping neglecting the distortion of the cross-section. The out of plane displacement is obtained by interpolation over the section domain but also on the beam length, this allows the model to capture the non-uniform warping and shear lag effect. As an interpolation function over the cross-section domain, Le Corvec (2012) used Lagrange's polynomials, while Di Re et al. (2018) included Hermite's polynomials. Both models were implemented in 3D force-based elements based on the Hu-Washizu variational principle. These models can capture the interaction of the internal forces in a tri-dimensional element, but the hypothesis of considering a complementary field with only warping has the drawback that distortion of the section is not captured, so transverse reinforcement is not considered explicitly. Besides, as the complementary field is interpolated on the beam length, a special frame formulation is developed with more degree of freedom at the beam level that has to be considered or properly condensed.

2.4.3 Discussion on modelling of inelastic shear deformation

From the literature review on modelling of shear deformation, it is inferred that many approaches have been proposed till date to include the shear deformation in one-dimensional beam-column elements. The member level spring-in-series model exhibits efficiency and ease of modelling. However, the approach has limitations in that the spring behaviours are based on empirical force-displacement relation. These are suitable to capture the global load-displacement behaviour only. On the other hand, the available local model based on the coupled section method based on different kinematic relations provides the axial-flexure-shear interaction effect but requires complex multi-axial constitutive relationships. Further development is required to ensure stable performance of this type of element and reduce the computational demand. The uncoupled section model is an attractive approach. It provides ease of implementation due to the incorporation of shear force-shear strain relation and also considers the vari-

ation of shear deformation along the element. The development of this type of model is comparatively limited.

2.5 Modelling of Bond Slip

Based on the complexity, the available models to account bond-slip effect in beam-column elements can be categorized into two groups:

(i) model based on assumed bond stress distribution, and

(ii) model based on bond stress-slip relation

In general, macro models deal with the average slip behaviour and often assume a uniform or stepped bond stress over the development length of the reinforcing bar (Sezen and Satzler, 2008). The macro models take the bond slip effect into consideration through zero-length springs or by reducing the stiffness of the steel stress-strain relation. The detailed model takes into account the local bond stress-slip relationship between the steel bar and the concrete interface. In these models, finite element method is usually required in the solution process and requires multiple iterations. The list of literature reviewed from each category is shown in Table 2.2. Sections 2.5.1 and 2.5.2 provide an overview of the reference models that account for strain penetration and bond-slip effects.

Table 2.2: Review of bond-slip model in fibre elements

Approach	References
Modification of rebar stress-strain relation	Kwak and Kim (2006); Braga et al. (2012); Pan et al. (2017, 2018); Feng and Xu (2018)
Use of link elements	Berry (2006); Zhao and Sritharan (2007); Ghannoum (2007); Sousa et al. (2017)
Detailed model	Monti and Spacone (2000); Limkatanyu and Spacone (2002); Ayoub (2006); Lee and Filippou (2010); Lobo and Almeida (2015)

Besides these methods, many alternate simplified methods were also proposed to increase the element flexibility by some means. One such method is to extend the member by an estimated strain penetration length (Fardis, 2009; Priestley et al., 2007). The underlying idea of this approach relies on the assumption that these deformations

spread along the strain penetration length, contributing to the overall member deformation. It is relevant to note that this simple procedure is able to predict the response of structures that are expected to respond in the nonlinear range (Goodnight et al., 2014). However, the application of this modelling option becomes increasingly difficult number of bays and stories increases. Another such simplified approach considers an elastic rotational spring at the base of the member, thus keeping the element dimensions unchanged. The elastic stiffness of the spring can be determined such that the stiffness of the system with the spring is the same as the stiffness-at-yield of a similar element, fixed at the base, but elongated by the strain penetration length (Correia, 2011). These methods will not be discussed further here.

2.5.1 Model based on assumed bond stress distribution

Two common macro models to account for bond slip are

(a) modification of the rebar stress-strain relationship, and

(b) introduction of a link element

The first method reduces the Young's modulus of the reinforcing steel to simulate the increase in member flexibility due to the strain penetration effects. The link element model are based on the assumption that SP deformation can be lumped into a single element located at the members end(s), usually in the form of a zero-length element. These are discussed below.

(a) Modified rebar stress-strain relation

One of the simplest approaches to simulate the increase in member flexibility due to strain penetration effects involves modification of stress-strain relation for the bars. The reinforcement slip effect is considered in the stress-strain relationship of the steel bar by adding the slip to the rebar strain.

Belarbi and Hsu (1994) proposed a modified stress-strain relation for longitudinal bars embedded in concrete. The yielding point of the bars with concrete is assumed to be lower than that of the bare bar (Figure 2.1), and used in numerical calculations.

Similarly, Kwak and Kim (2006) performed analysis using a layered section method.

The bond-slip effect along the reinforcing bar is quantified with the force equilibrium and compatibility condition at the post-cracking stage and its contribution is indirectly implemented into the stress–strain relation of reinforcing steel. This analytical procedure has the advantage that it takes the bond-slip effect into account while using the conventional fibre method. Comparisons between experimental data and analytical results verify that the proposed analytical procedure can effectively simulate the cracking behaviour of RC beams, columns, and frames that accompany the stiffness degradation caused by bond-slip.

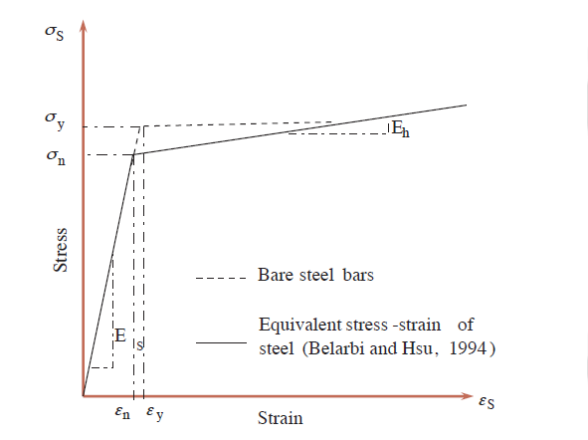

Figure 2.1: Modified stress-strain relation of steel bars, with permission from Belarbi and Hsu (1994), copyright ACI

Pan et al. (2017) proposed a simple and computationally efficient fibre beam–column element model to consider reinforcement anchorage slip in the footing. The reinforcement anchorage slip in the footing is formulated using a macro model for calculating anchorage slip. The macro model assumed stepped bond stress to deal with the bond–slip relationship, and the slip is derived by integrating the strain over the development length. Then, the derived anchorage slip is introduced into the framework of the conventional fibre element model. By considering the rebar fibre strain in the footing fibre element as the sum of the rebar deformation and the anchorage slip, the stress–strain skeleton curve and the hysteretic law of rebar are modified. Feng and Xu (2018) used a similar method.

The above macro model with a simplified bond stress distribution may not be able to accurately predict the elastic range anchorage slip (Pan et al., 2018).

Braga et al. (2012) proposed a modified steel bar model incorporating bond slip through the adoption of simple equilibrium, compatibility and constitutive equations. The model is developed by assuming a linear bond-slip field along the bar anchorage length and provides a simplified stress-strain relation to assign to the longitudinal reinforcement. The model also considers inadequate anchorage length. The model was based on the oversimplified assumption of elasto-plastic constitutive law for steel bars. Later Braga et al. (2015) improved the model by including the hardening slip model.

Pan et al. (2018) developed a modified macromodel with a refined bond-stress distribution obtained by solving a validated micromodel.

(b) Link element model

The link element model are based on the assumption that SP deformations can be lumped into a single element located at the member ends, usually in the form of a zero-length element. Their properties are generally based on empirical data and can be assigned at the cross-sectional level with suitable moment-slip rotation relations (Sezen and Setzler, 2008) or at the material level (reinforcement and concrete) with suitable stress-deformation relation(Zhao and Sritharan, 2007).

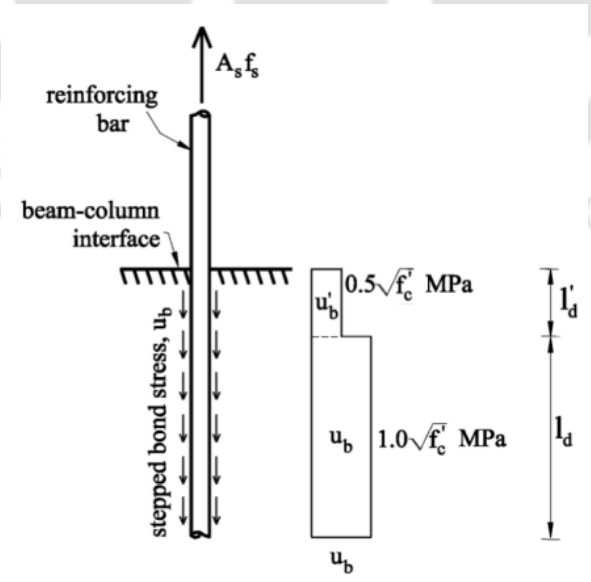

Figure 2.2: Constant bond stress model, with permission from Sezen and Setzler (2008), copyright ACI

Nonlinear rotational spring models have been proposed by Otani (1973); Alsiwat

and Saatcioglu (1992); Sezen and Setzler (2008); Sezen and Chowdhury (2009). The spring properties were established by formulating the moment-slip rotation skeleton curve and assuming the hysteretic law. These models are based on the assumption that the bond stress variation along the embedment region can be represented as a stepped constant average bond stress (Figure 2.2).

The rotational spring method uses constant flexural stiffness properties that are user-calibrated as constant axial loads. To avoid this deficiency, many zero-length fibre element-based models have been proposed that can consider the coupling effect by Berry (2006); Zhao and Sritharan (2007); Ghannoum (2007); Sousa et al. (2017) among others. The material properties of the fibre section are defined by stress-deformation rather than a stress-strain relation. This approach by virtue of its formulation produces bar slip rotations about the flexural neutral axis of the section and has the advantage of adopting varying levels of axial loads.

Berry (2006) implemented bar slip rotation effect through a zero-length fibre-section placed in series with the member. The bar slip steel fibres are defined as a bilinear material calibrated to the stress-slip model developed by Lehman and Moehle (2000). The concrete stress-deformation properties in the bar slip element were defined integrating the concrete material properties over an effective depth in the anchorage zone. The optimum depth was determined empirically to be half the depth of the compression zone in the section.

Zhao and Sritharan (2007) proposed rebar stress-slip hysteretic model, shown in Figure 2.3. This relation was empirically derived using experimental results and used as a constitutive relation for steel fibres in a zero-length fibre-section element. The material properties of the concrete fibres are the same as those in the adjacent column element except the residual stress at large strains is taken as $0.8f'_c$. This effectively creates a uniform concrete compression stress block in the bar slip section at the strain levels expected in the formulation.

Both approaches by Berry (2006) and Zhao and Sritharan (2007) have drawbacks. These methods alter the stiffness ratio between the steel and concrete fibres in the bar slip fibre-section from the ratio present in the adjacent frame-element fibre-section. This results in discontinuities in steel stresses and neutral axis locations at the bar

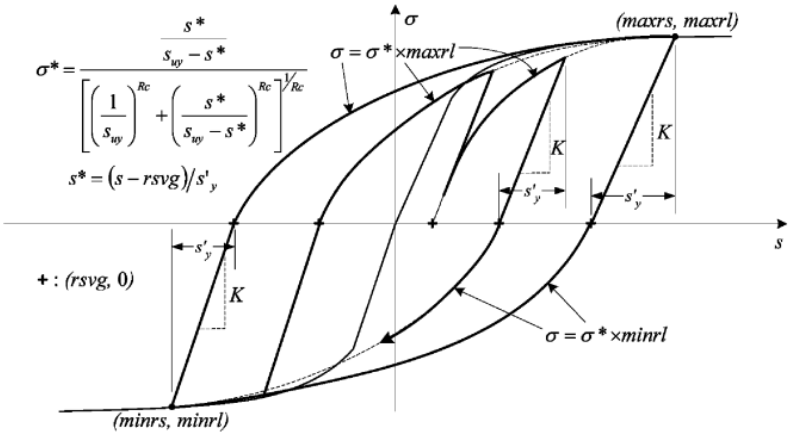

Figure 2.3: Reinforcing bar stress-slip model, with permission from Zhao and Sritharan (2007), copyright ACI

slip interface between adjacent fibre-sections. Ghannoum (2007) implement the model maintaining strain compatibility in the zero-length fibre-section such that the bar-slip induced rigid body rotations are centred at the flexural neutral axis of the adjacent frame element. The material stress-deformation is defined by scaling the steel and concrete stress-strain relations by the ratio $r_y = S_y/\epsilon_y$, where S_y and ϵ_y are the bar slip and bar strain at yield respectively.

Sousa et al. (2017) proposed a zero-length element using a bond-slip constitutive model that computes the localized member-end deformation accounting response at each reinforcing bar of a given RC section. The concrete stress-deformation property is determined by using an influence length. They specify the influence length of size between one and twice the depth of the anchorage region providing a good estimation for most typical conditions.

2.5.2 Model based on bond stress-slip relation

The macro models discussed in the previous section have low computational cost and therefore are suitable for simulation of full-scale structures; conversely, they do not study explicitly the bond behaviour but merely reflect the additional flexibility provided by bond-slip.

Monti and Spacone (2000) proposed a fibre beam element with anchorage slip by combining the force-based fibre beam model by Spacone et al. (1996) with the anchored bar formulation by Monti et al. (Monti et al., 1997). The rebar fibre strain in the fibre element is computed as the sum of two contributions, the rebar deformation and the reinforcement slip. The reinforcement slip is assumed to be uniformly distributed in the rebar fibre of the element and modelled through a series of additional FB elements representing the embedment length of the rebars. The definition of several elements with different IPs along the embedment length is a very interesting strategy, bypassing the limitation of simpler models as the one described before. Although effective, this model requires a high computational effort for the complex state determination process of the rebar fibre.

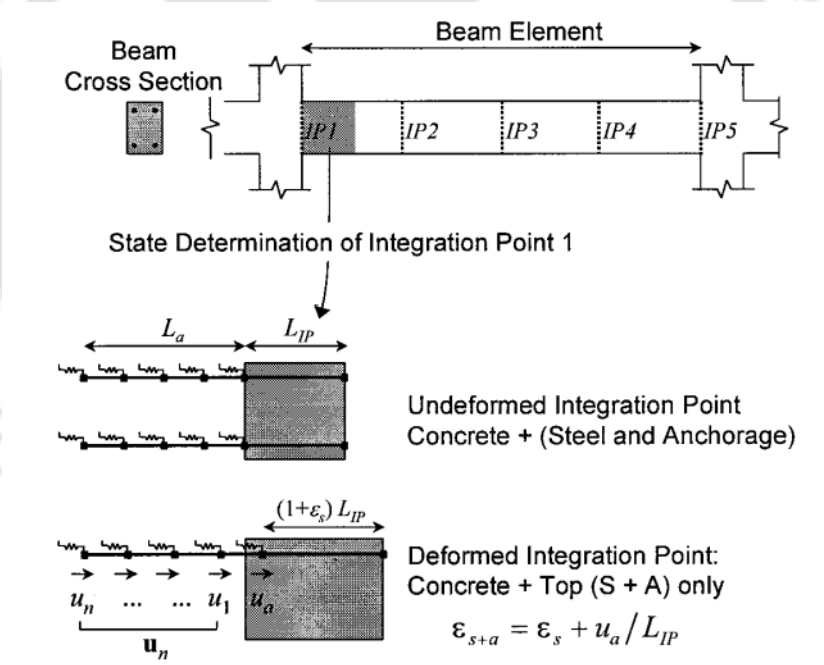

Figure 2.4: Beam element with rebar slip, , with permission from Monti and Spacone (2000), copyright ASCE

Limkatanyu and Spacone (2002) proposed an RC frame element with bond slip, considering the general idea that, each element is a combination of a concrete component and finite number of steel bar components. Separate degrees of freedom are used for the concrete and bar components, to allow different displacements in the reinforcing bars and the surrounding concrete. The bond-slip between the steel bar and the

surrounding concrete is computed directly as the difference in the steel and concrete displacements at the bar level. They proposed general theoretical framework of the displacement-based, force-based, and two-field mixed formulations of RC frame elements with bond slip in the steel bars. The model considered only monotonic loading and did not account for reversed cyclic loading.

Ayoub (2006) pointed out that the models by Monti and Spacone (2000) and Limkatanyu and Spacone (2002) did not model pullout cracks accurately. He proposed a model for nonlinear analysis of RC beam-column with bond-slip. Both bond-slip and pull-out effects are represented in the model. The model is derived from a two-field mixed formulation with an independent approximation of forces and displacements. Their correlation study showed the model can represent global and local parameters.

Hashemi and Vaghefi (2011) used a similar approach in their study. They have also included joint elements in modelling reinforced concrete frames to consider the joint effect. They used a spring-type joint model with the model proposed by Limkatanyu and Spacone (2002). (Lobo and Almeida, 2015) proposed a fibre force-based FE with continuous anchored bars. This model makes it possible to consider bond slip in interior joint regions and, being fiber-section-based, accounts for the effect of the variation of the axial force due to the overturning effects on the hysteretic behaviour of the element.

Most formulations to date interpolate the displacement or the force field, or both for each component in the element. The bond-slip field is derived from the difference of the component displacement fields. Lee and Filippou (2010) pointed out some drawbacks of these approaches: (1) since the nodal axial displacements of each component are global degrees of freedom, the transformation from the local to the global reference frame requires a special constraint matrix for the transverse displacements and rotations. While such a transformation is inconvenient but feasible under linear geometry, it is impossible under nonlinear geometry conditions for large node translations and rotations. (2) Since the section force fields of each component are interpolated separately in existing force and mixed formulations, the exact interpolation of the total section forces for the composite beam is not guaranteed. Without this exact interpolation, the force and mixed formulations may loss the benefit of accuracy and computational efficiency over the displacement formulation.

Lee and Filippou (2010) proposed a composite beam formulation based on the Hu-Washizu variational principle with exact interpolation of the total section forces of the member. Instead of treating each component of the composite element separately for the interpolation of force and displacement fields, as previous formulations propose. They treat the composite member as a single element with the introduction of a new type of section that monitors the bond-slip response at the interface. In the formulation, they considered interface slip among components as one of the independent variables. The interface slip was considered an additional degree of freedom. The formulation relaxes the slip continuity but ensures force continuity at element nodes upon convergence. The interpolation function for bond-slip is a piecewise polynomial. Lee and Filippou (2015) included the nonlinear geometry effects in the formulation through the corotational formulation.

2.5.3 Discussion on modelling of bond-slip

From the review of modeling of bond-slip in fibre elements, it is inferred that among different approaches the fibre link element is efficient for modelling of member end rotation due to slippage of rebar in the anchorage region. The models based on the local bond slip relation are accurate but experimental results indicate that the slip along the element is small and can be neglected (Alsiwat and Saatcioglu, 1992). The performance of the fibre link element depends on the stress-displacement properties of the fibres. A comparative study of different fibre properties on the response of the fibre link element is limited.

2.6 Research Gaps

The research gaps identified from the above literature review are summarized below to establish the need for the present study.

1. Most of the studies on shear behaviour in fibre beam-column elements using multi-axial stress-strain relation are computationally demanding. Further research is required to increase the efficiency and stability of these models for cyclic and

general loading conditions.

2. The uncoupled approach uses empirical equations, which may lead to misleading predictions. Further improvement of the uncoupled approach is possible.

3. Studies on the softening behaviour of shear flexible frame elements are limited

4. The anchorage bond-slip is usually accounted for by a link element. The selection of properties of the link element needs careful judgement.

5. Limited work has considered fibre elements with both shear and bond-slip effects in seismic analysis.

2.7 Conclusion

In this chapter literature review is presented on: (a) force-based fibre frame element, (b) approaches to account the shear deformation in the fibre element, and (c) approaches to account bond-slip effect in the fibre element. Some of the research gaps in the current literature are identified. Based on the research gaps, the objectives for the study are formulated, which were presented in Section 1.4. The next four chapters present the work carried out to fulfil the objectives of this study.

Chapter 3

Axial-Flexure-Shear Coupled Force-Based Fibre Frame Element

3.1 Introduction

The development of an element considering axial-flexure-shear interaction is vital for understanding seismic behaviour of framed structures. This chapter presents a force-based fibre beam-column element that effectively accounts for the axial, bending, and shear deformations as well as the interaction between them. The element uses a multi-axial constitutive relation based on a smeared crack model to define the concrete constitutive relation that establishes a direct coupling between normal stress and shear stress at a material point and allows the axial-flexure-shear interaction effect. The developed element uses a sectional analysis model similar to those used by Petrangeli et al. (1995); Guner and Vecchio (2011) and others. However, it is based on the tangent stiffness approach and employs different equivalent uniaxial relations for the concrete under compression to account for the strength enhancement effect due to the confinement of stirrup. It uses Modified Compression Field Theory approach to model the axial-flexure-shear interaction. The performance of the element in simulating the cyclic response of RC members is examined and the localization issue in the developed element is investigated.

The chapter starts with a description of the general formulation of the force-based

fibre beam-column element in Section 3.2. The subsequent sections (Sections 3.3 to 3.5) present the detailed description of the coupled fibre model along with the concrete and steel constitutive stress-strain relations. Section 3.6 describes the implementation of the developed element in the general-purpose program. The implementation is carried out in a computer program written in Matlab R2019a. The localization issue in the developed element and the numerical examples are presented in Section 3.8.

3.2 Force-Based Fibre Element Framework

The developed element is based on the force-based framework of Spacone et al. (1996). The formulation is given for a two-noded plane beam-column element under small strain, and small displacement assumption. The element is based on a shear beam theory with parabolic shear strain distribution over the cross-section to consider the shear-deformation. The finite element is schematically represented in the global reference system in Figure 3.1. The element formulation is given in a simply supported basic reference system. The relation between the different reference systems is defined at the onset. It is followed by the general element formulation.

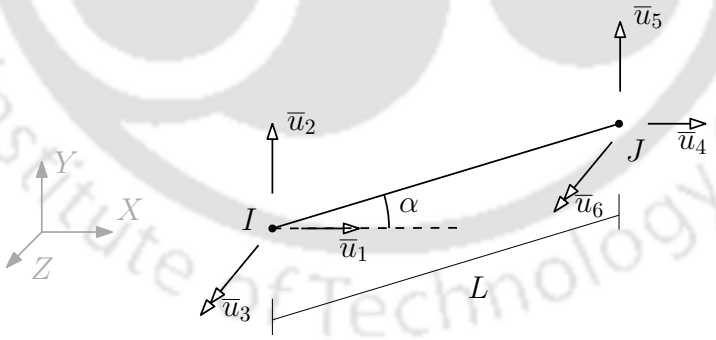

Figure 3.1: Element nodal displacements in global reference system

3.2.1 Element reference systems

Figures 3.1 and 3.2 shows three reference systems to describe the nodal forces and displacements of the element: (i) global reference system represented by X-Y, (ii) local reference system represented by x-y, and (iii) simply supported basic reference system (which is local reference system without rigid body modes). The element forces

and displacements in the global reference system are denoted by $\overline{P}_i$, i=1 to 6 and $\overline{u}_i$, i=1 to 6. The force vector and displacement vector are represented by vector $\overline{\mathbf{P}}$ and $\overline{\mathbf{u}}$ respectively. The components of element force and displacement in the local reference system are denoted by $\overline{Q}_i$, i=1 to 6 and $\overline{q}_i$, i=1 to 6. These are represented by vector $\overline{\mathbf{Q}}$ and $\overline{\mathbf{q}}$ respectively. In the basic reference system, there are three generalized nodal displacements, as shown in Figure 3.2. The generalized nodal displacements are represented by vector $\mathbf{q}$

$$\mathbf{q} = \{\theta_I \ \theta_J \ u_J\}^T \tag{3.1}$$

where θ_I, θ_J are end rotations, u_J is the axial extension of the element. The corresponding element forces are represented by vector $\mathbf{Q}$ denoting the end bending moments (M_I, M_J) and the axial force N_J.

$$\mathbf{Q} = \{M_I \ M_J \ N_J\}^T \tag{3.2}$$

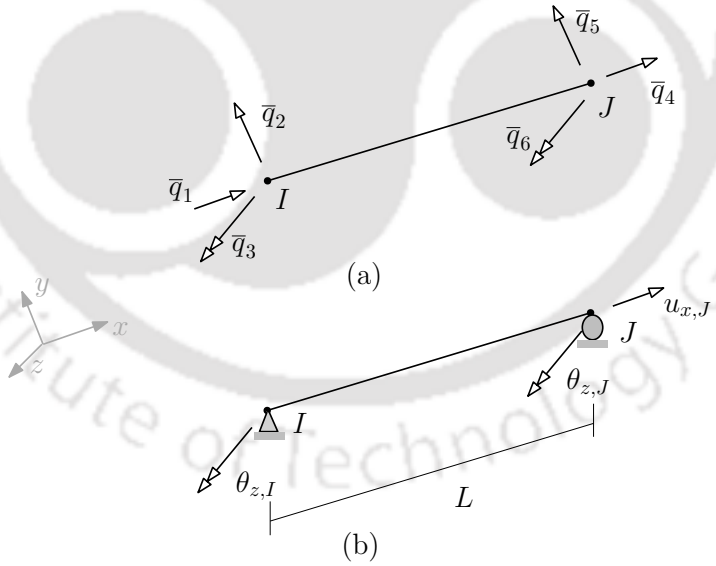

Figure 3.2: Element nodal displacements in (a) local reference system; and (b) local reference system without rigid modes

The transformation between the three reference systems can be performed with the help of a standard transformation matrix. The relationship between the global

displacements $\overline{u}_i, i = 1to6$ and local displacements $\overline{q}_i, i = 1to6$ is given by

$$\begin{Bmatrix} \overline{q}_1 \\ \overline{q}_2 \\ \overline{q}_3 \\ \overline{q}_4 \\ \overline{q}_5 \\ \overline{q}_6 \end{Bmatrix} = \begin{bmatrix} \cos\alpha & \sin\alpha & 0 & 0 & 0 & 0 \\ -\sin\alpha & \cos\alpha & 0 & 0 & 0 & 0 \\ 0 & 0 & 1 & 0 & 0 & 0 \\ 0 & 0 & 0 & 0 & \cos\alpha & \sin\alpha \\ 0 & 0 & 0 & 0 & -\sin\alpha & \cos\alpha \\ 0 & 0 & 0 & 0 & 0 & 1 \end{bmatrix} \begin{Bmatrix} \overline{u}_1 \\ \overline{u}_2 \\ \overline{u}_3 \\ \overline{u}_4 \\ \overline{u}_5 \\ \overline{u}_6 \end{Bmatrix} \tag{3.3}$$

or

$$\overline{\mathbf{q}} = \mathbf{T}_1 \overline{\mathbf{u}} \tag{3.4}$$

where $\mathbf{T}_1$ is the rotational transformation matrix, α is the angle to the element axis from the global X axis Figure 3.1. Similarly, the transformation between global forces and local forces is given as

$$\overline{\mathbf{Q}} = \mathbf{T}_1 \overline{\mathbf{P}} \tag{3.5}$$

The relationship between the local force $\overline{\mathbf{Q}}$ and basic force $\mathbf{Q}$ is given by

$$\begin{Bmatrix} \overline{Q}_1 \\ \overline{Q}_2 \\ \overline{Q}_3 \\ \overline{Q}_4 \\ \overline{Q}_5 \\ \overline{Q}_6 \end{Bmatrix} = \begin{bmatrix} 0 & 0 & -1 \\ \frac{1}{L} & \frac{1}{L} & 0 \\ 1 & 0 & 0 \\ 0 & 0 & 1 \\ -\frac{1}{L} & \frac{1}{L} & 0 \\ 0 & 1 & 0 \end{bmatrix} \begin{Bmatrix} M_I \\ M_J \\ N_J \end{Bmatrix} \tag{3.6}$$

or

$$\overline{\mathbf{Q}} = \mathbf{T}_2^T \mathbf{Q} \tag{3.7}$$

where $\mathbf{T}_2$ is the transformation matrix obtained from the equilibrium of element forces in the basic reference system

The relation between the displacements in the local reference system and displacement in the basic reference system is obtained from the virtual force principle or linear approximation displacement-deformation relation for small displacement assumption

as (Filippou and Fenves, 2004)

$$\mathbf{q} = \mathbf{T}_2\overline{\mathbf{q}} \tag{3.8}$$

3.2.2 Element formulation

The formulation is described in the element basic reference system. Unlike the displacement-based method, in the force-based method, the internal force field is interpolated along the element. The element stiffness is estimated by integrating the section stiffness.

Representing the section forces and deformations by vectors $\mathbf{S}$ and $\mathbf{d}$ as

$$\mathbf{S}(x) = \begin{Bmatrix} M_z(x) \\ V(x) \\ N(x) \end{Bmatrix}; \qquad \mathbf{d}(x) = \begin{Bmatrix} \phi(x) \\ \gamma(x) \\ \varepsilon(x) \end{Bmatrix} \tag{3.9}$$

where, $M_z(x)$ is the bending moment, $V(x)$ is the shear force, $N(x)$ is the axial force, $\phi(x)$ is the curvature, $\gamma(x)$ is the shear deformation, $\varepsilon(x)$ is the axial strain.

The section forces $\mathbf{S}(x)$ at a location x are related to the element end forces $\mathbf{Q}$ by equilibrium condition as

$$\mathbf{S}(x) = \mathbf{b}(x)\mathbf{Q} \tag{3.10}$$

where $\mathbf{b}(x)$ represents the force interpolation function along the element length L. In the absence of element load, it consists of linear bending moment distribution and constant axial and shear force distribution.

$$\mathbf{b}(x) = \begin{bmatrix} x/L - 1 & x/L & 0 \\ -1/L & -1/L & 0 \\ 0 & 0 & 1 \end{bmatrix} \tag{3.11}$$

The section constitutive relation between the section forces $\mathbf{S}(x)$ and section deformations $\mathbf{d}(x)$ is assumed to be known and its expression in linearised form is

$$\mathrm{d}\mathbf{S}(x) = \mathbf{K}_s(x)\mathrm{d}\mathbf{d}(x) \tag{3.12}$$

where $\mathbf{K}_s(x)$ represents the section tangent stiffness matrix. The element formulation is independent of the choice of the section constitutive formulation. Any suitable section formulation can be used. A section model with axial-flexure-shear interaction is presented in the Section 3.3. Another section model with simple flexure-shear interaction is presented in the next Chapter.

The compatibility condition between section deformation and element deformation is obtained by the application of the principle of virtual force as

$$\delta\mathbf{Q}^T\mathbf{q} = \int_L \delta\mathbf{S}^T(x)\mathbf{d}(x)\mathrm{d}x \tag{3.13}$$

Substituting Equation (3.10) in Equation (3.13) and using $\delta\mathbf{Q}$ as an arbitrary, we obtain

$$\mathbf{q} = \int_L \mathbf{b}^T(x)\mathbf{d}(x)\mathrm{d}x \tag{3.14}$$

Subsequently, the element flexibility $\mathbf{F}_{ele}$ can be obtained by taking the derivative of Equation (3.14), with respect to the element force vector $\mathbf{Q}$ as

$$\mathbf{F}_{ele} = \frac{\mathrm{d}\mathbf{q}}{\mathrm{d}\mathbf{Q}} = \int_L \mathbf{b}^T(x)\mathbf{F}_s(x)\mathbf{b}(x)\mathrm{d}x \tag{3.15}$$

where $\mathbf{F}_s$ denotes the section flexibility, which is the inverse of the section stiffness $\mathbf{K}_s$ obtained from Equation (3.12).

The element stiffness $\mathbf{K}_{ele}$ is obtained by

$$\mathbf{K}_{ele} = \mathbf{F}_{ele}^{-1} \tag{3.16}$$

Equations (3.10), (3.14) and (3.15) constitute the general governing equations of the force-based formulation. The element equilibrium is satisfied exactly irrespective of the level of nonlinearity when no element load is present. This is a major advantage of the force-based formulation over the displacement-based formulation. In force-based formulation, element compatibility is satisfied in a weighted sense. The integrals in Equations (3.14) and (3.15) are calculated by numerical integration. The common choice for the integration is the Gauss-Lobatto quadrature, as it includes two

integration points at the ends of the element.

The implementation of force-based elements is not straightforward. The element state determination procedure proposed by Spacone et al. (1996) is used in this work. In this procedure, for a given element displacement, the element state is determined iteratively by correcting the element forces. The detailed implementation steps for the element state determination are provided in the Section 3.6.1 for completeness.

3.3 Axial-Flexure-Shear Coupled Fibre Section

The element formulation presented in the last section is independent of the section analysis method. A fibre section model is adopted to perform section analysis as it has the ability to account for the force interaction effect. The fibre section model is based on a multi-axial constitutive relation to establish coupling between normal stress and shear stress at a material point and allow the axial force-moment-shear force (stress resultants) interaction at the section level. This model is referred to as the axial-flexure-shear coupled fibre section model or coupled fibre section model in the rest of the thesis. For given the section generalized deformation vector, $\mathbf{d}$, the model estimates the section force resultant $\mathbf{S}$ and section stiffness matrix $\mathbf{K}_s$ using the section kinematic assumptions and material stress-strain information.

The coupled fibre section is shown in Figure 3.3. The section is considered as an assembly of concrete and reinforcing steel layers (fibres). The section resultant is calculated by integrating the fibre stresses. The concrete fibres are assumed to be in a state of biaxial stress, (Figure 3.3-d). The state of the fibres is determined using a linear flexure strain distribution and a supplementary shear strain distribution with the fixed parabolic pattern. Note that the adoption of the fixed parabolic shear strain pattern is an approximation as in actuality the shear strain profile does not follow a fixed profile and is state-dependent. A comparison of the different shear strain assumptions is given in Appendix A. It is found that the use of the fixed parabolic pattern leads to significant ease of implementation and provides reasonable results. A similar observation is also made by Vecchio and Collins (1988) where they compared the response of section with fixed parabolic pattern with that of the more rigorous 'Dual section' method.

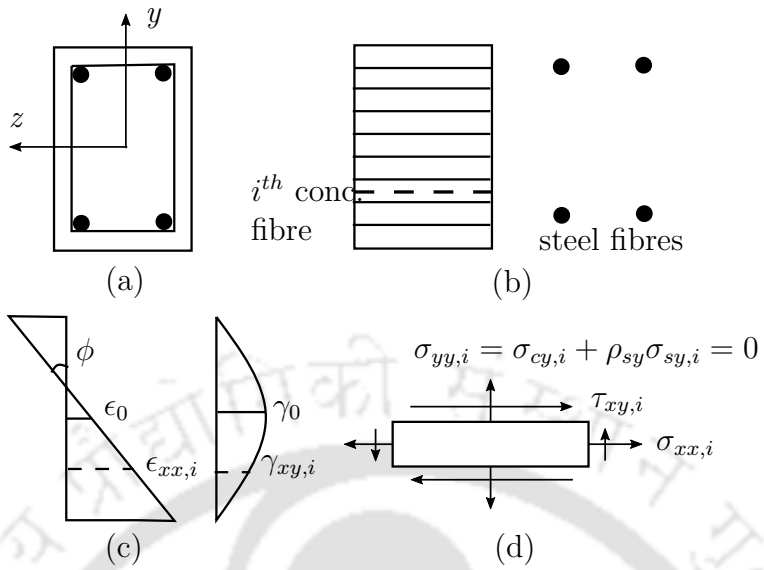

Figure 3.3: Axial-flexure-shear coupled fibre section: (a) typical RC cross-section, (b) concrete fibres and reinforcing steel fibres, (c) axial strain and shear strain distribution, (d) stresses in a concrete fibre

Following the standard displacement-based approach, the section deformations, $\mathbf{d}(x)$, are known at the beginning. Consequently, the axial strain ε_{xx} and shear strain γ_{xy} at a fibre height y from the centroid of the section, denoted by vector $\mathbf{e}(x,y) = \{\varepsilon_{xx}, \gamma_{xy}\}^T$, are determined as

$$\mathbf{e}(x,y) = \mathbf{a}_s(y)\mathbf{d}(x) \tag{3.17}$$

where $\mathbf{a}_s(y)$ is the section compatibility matrix that depends on the assumed section kinematic relation. For the kinematic relation assumed in the current study

$$\mathbf{a}_s(y) = \begin{bmatrix} -y & 0 & 1 \\ 0 & \psi & 0 \end{bmatrix} \tag{3.18}$$

The variable ψ in Equation (3.18) depends on the assumed shear strain distribution. For parabolic shear strain distribution on rectangular section, the variable $\psi = \frac{5}{4}\left(1 - 4\frac{y^2}{H^2}\right)$. As the reinforcement fibres are assumed to resist only axial stress, the variable $\psi = 0$ for these fibres.

The stresses and strains of the concrete fibre are related according to a multi-axial stress-strain model, which introduces the normal-shear coupling. The reinforcement

fibres are assumed to resist only axial stresses and the stress-strain relationship is expressed using uniaxial stress-strain relationship. This is a reasonable assumption because the reinforcement steel is usually thin and long in RC beams and columns. Thus, the predominant effect is uniaxial. The stresses and stiffness matrix are denoted as

$$\mathbf{s}(\mathbf{e}(x,y)) = \{\sigma_{xx}, \tau_{xy}\}^T, \qquad \mathbf{k} = \frac{\mathrm{d}\mathbf{s}}{\mathrm{d}\mathbf{e}} \tag{3.19}$$

Once all the fibre stress is calculated, the section resisting forces are derived based on the principle of virtual displacement

$$\delta\mathbf{d}^T(x)\hat{\mathbf{S}}(x) = \int_A \delta\mathbf{e}^T(x,y)\mathbf{s}(\mathbf{e}(x,y))\mathrm{d}A \tag{3.20}$$

Applying Equation (3.17) and implying arbitrary nature of $\delta\mathbf{d}$, we obtain

$$\hat{\mathbf{S}}(x) = \int_A \mathbf{a}_s^T(y)\mathbf{s}(\mathbf{e}(x,y))\mathrm{d}A \tag{3.21}$$

The tangent section stiffness matrix is obtained by taking derivative of the section force with the section deformation as

$$\frac{\mathrm{d}\hat{\mathbf{S}}(x)}{\mathrm{d}\mathbf{d}(x)} = \int_A \mathbf{a}_s^T(y)\frac{\mathrm{d}\mathbf{s}(\mathbf{e}(x,y))}{\mathrm{d}\mathbf{e}(x,y)}\mathbf{a}_s(y)\mathrm{d}A \tag{3.22}$$

The integrals in Equations (3.21) and (3.22) are calculated by the midpoint integration rule over the fibres

$$\hat{\mathbf{S}}(x) = \sum_i^n \mathbf{a}_s^T(y_i)\mathbf{s}(\mathbf{e}(x,y_i))A_i \tag{3.23}$$

$$\mathbf{K}_{sec}(x) = \sum_i^n \mathbf{a}_s^T(y_i)\mathbf{k}(\mathbf{e}(x,y_i))\mathbf{a}_s(y_i)A_i \tag{3.24}$$

where n is the total number of fibres in the section.

3.4 Constitutive Model for Concrete

A multiaxial material model is required to account for the interaction of axial force, shear and bending moment. Many multiaxial material models are available for concrete. These can be categorized based on their underlying constitutive theory, e.g., elasticity theory, plasticity theory, damage mechanics, and fracture mechanics (CEB, 1996; Park et al., 2022). The simplest among these models is the smeared crack model. These belong to the class of models derived from the theory of elasticity. In this model the concrete is described as an orthotropic material and equivalent stress-strain relations are set up separately for each axis of orthotropy. The stress-strain relations in orthotopic direction of these models are empirically derived from concrete experiments under multi-axial stress states. The smeared crack models are attractive because these are simple, and are also capable of accurately predicting the shear strength of RC panel members. Several such models are present in the literature (Collins, 1978; Vecchio and Collins, 1986; Belarbi and Hsu, 1995; Pang and Hsu, 1996; Kaufmann and Marti, 1998; Zhu, 2000; Vecchio, 2000).

The smeared crack model or orthotropic model for concrete can be broadly classified as a rotating and fixed smeared crack model, based on the orientation of the crack (i.e., axes of orthotropy) during the loading process. A rotating smeared crack model fixes the axes of orthotropy to the crack and assumes it co-rotates with the axes of principal strain. This assumption simplifies the computation since it results in no shear stress along the cracks. Some references for the rotating crack model are MCFT (Vecchio and Collins, 1986) and RA-STM (Belarbi and Hsu, 1995; Pang and Hsu, 1995). On the other hand, a fixed crack model fixes the axes of orthotropy for the entire computational process. In other words, it assumes the local crack axes to remain unaltered. This model allows a deviation between principal strain and crack direction and thus allows concrete shear stress to develop parallel to a crack. Different fixed crack models are available. Some references for the fixed crack model are Pang and Hsu (1996); Pimanmas and Maekawa (2001); So (2008); Kagermanov and Ceresa (2016); Orakcal et al. (2019).

In the present work, the concrete constitutive relation is based on the Modified

Compression Field Theory developed by Vecchio and Collins (1986).

3.4.1 Modified Compression Field Theory

MCFT theory was developed by Vecchio and Collins (1986) provides good correlation with the experimental results (Vecchio and Collins, 1986, 1988; Bhide and Collins, 1989; Vecchio and Emara, 1992). The description of the MCFT is given for ready reference.

The MCFT is a rotating smeared crack model. It assumes the cracked concrete as an orthotropic material. The method calculates the principal direction on the basis of total strain components and the direction of the principal strain is assumed same as the direction of the principal stresses. In this theory, the response of a reinforced concrete membrane element is determined by employing compatibility, equilibrium and average stress-average strain relationships. Based on the assumption that there is no slip between reinforcement and concrete, compatibility requires that any change in reinforcement corresponds to an equal change in concrete strain. Therefore for reinforcement oriented parallel to the Cartesian axes

$$\varepsilon_x = \varepsilon_{sx} = \varepsilon_{cx}; \quad \varepsilon_y = \varepsilon_{sy} = \varepsilon_{cy} \tag{3.25}$$

where ε_{sx} and ε_{cx} = average strain in longitudinal reinforcement and concrete respectively in x direction, and ε_{sy} and ε_{cy} = average strain in transverse reinforcement and concrete respectively in y direction. The angle of inclination of principal strains θ with respect to x axis (Figure 3.4) is given as follows:

$$\theta = \frac{1}{2}\tan^{-1}\left(\frac{\gamma_{xy}}{\varepsilon_x - \varepsilon_y}\right) \tag{3.26}$$

The total average principal tensile and compressive strain can be calculated as

$$\varepsilon_1 = \frac{\varepsilon_x + \varepsilon_y}{2} + \frac{1}{2}\sqrt{(\varepsilon_x + \varepsilon_y)^2 + \gamma_{xy}^2} \tag{3.27}$$

$$\varepsilon_1 = \frac{\varepsilon_x + \varepsilon_y}{2} - \frac{1}{2}\sqrt{(\varepsilon_x + \varepsilon_y)^2 + \gamma_{xy}^2} \tag{3.28}$$

Neglecting the small reduction in the concrete cross-sectional area due to reinforce-

ments, the equilibrium conditions are as follows:

$$\sigma_x = f_{cx} + \rho_{sx} f_{sx} \tag{3.29}$$

$$\sigma_y = f_{cy} + \rho_{sy} f_{sy} \tag{3.30}$$

$$f_{cx} = f_{c1} - v_{cxy} / \tan(90 - \theta) \tag{3.31}$$

$$f_{cy} = f_{c1} - v_{cxy} \tan(90 - \theta) \tag{3.32}$$

where σ_x = total longitudinal stress, f_{cx} = longitudinal stress in a concrete layer, f_{sx} = stress of a longitudinal reinforcement element, ρ_{sx} = longitudinal reinforcement ratio, f_{c1} = principal tensile stress, v_{cxy} = shear stress sustained by the concrete, θ = angle of inclination of principal stresses in the concrete (taken same as the angle of inclination of principal strains), and subscript y in Equations (3.30) and (3.32) denotes the parameters in the transverse direction. Figures 3.4 and 3.5 show the graphical representation of strains and stresses, respectively.

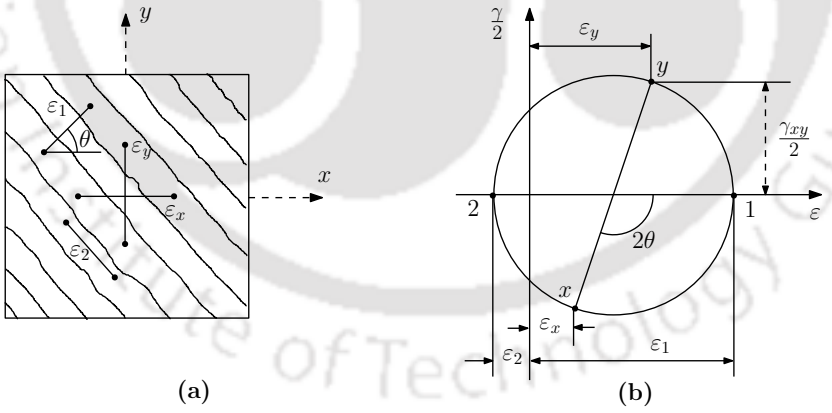

Figure 3.4: Strain state representation in MCFT: (a) average strains in cracked element, (b) Mohr's circle of average strain

Vecchio (1989) presented the MCFT in matrix form to facilitate the implementation of the model into the finite element analysis program. They presented the formulation for secant formulation. A tangent formulation of the 2D stress-strain relationship of an RC element can be written as

$$\mathrm{d}\boldsymbol{\sigma} = \mathbf{D}\mathrm{d}\boldsymbol{\varepsilon} \tag{3.33}$$

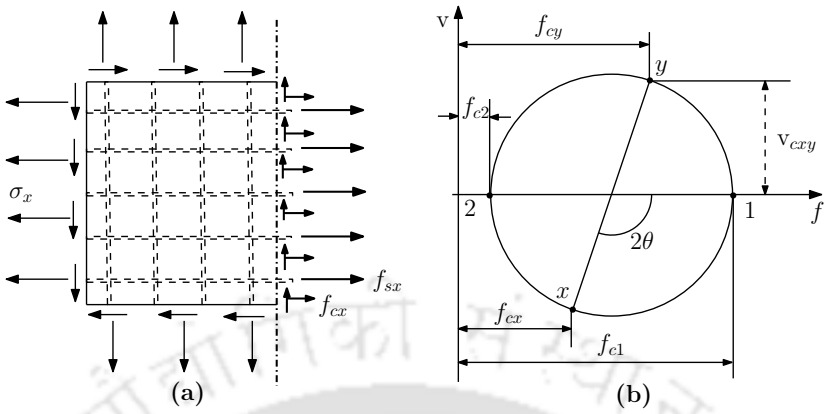

Figure 3.5: Stress state representation in MCFT: (a) free body diagram of reinforced concrete element, (b) Mohr's circle of average stress of reinforced concrete

$$\begin{Bmatrix} d\sigma_x \\ d\sigma_y \\ d\tau_{xy} \end{Bmatrix} \begin{bmatrix} D_{11} & D_{12} & D_{13} \\ D_{21} & D_{22} & D_{23} \\ D_{31} & D_{32} & D_{33} \end{bmatrix} \begin{Bmatrix} d\epsilon_x \\ d\epsilon_y \\ d\gamma_{xy} \end{Bmatrix} \tag{3.34}$$

where, $\mathbf{D}$ is the tangent stiffness matrix. This is derived by adding the components of concrete and smeared transverse steel.

$$\mathbf{D} = \mathbf{D}_c + \mathbf{D}_{ss} \tag{3.35}$$

where, $\mathbf{D}_c$ is the concrete tangent stiffness matrix, $\mathbf{D}_{ss}$ is the smeared reinforcement tangent stiffness matrix in y- direction.

$$\mathbf{D}_c = \mathbf{T}^T \mathbf{D}_c' \mathbf{T} \tag{3.36}$$

where $\mathbf{T}_\varepsilon$ denotes the strain transformation matrix relating $\boldsymbol{\varepsilon}' = \mathbf{T}_\varepsilon \boldsymbol{\varepsilon}$ with

$$\mathbf{T}_\varepsilon(\theta) = \begin{bmatrix} \cos^2\theta & \sin^2\theta & \sin\theta\cos\theta \\ \sin^2\theta & \cos^2\theta & -\sin\theta\cos\theta \\ -2\sin\theta\cos\theta & 2\sin\theta\cos\theta & \cos^2\theta - \sin^2\theta \end{bmatrix} \tag{3.37}$$

$\mathbf{D}'_c$ is the orthotropic stiffness matrix in the principal plane

$$\mathbf{D}'_c = \begin{bmatrix} E_{c1} & 0 & 0 \\ 0 & E_{c2} & 0 \\ 0 & 0 & G_c \end{bmatrix} \tag{3.38}$$

where, E_{c1}, E_{c2} are the tangent modulus along two principal directions obtained from the equivalent uniaxial stress-strain relation and G_c is shear modulus in the principal plane. These are further discussed in Section 3.4.2.

$\mathbf{D}_{ss}$ is the stiffness component due to the smeared stirrup. For reinforcement oriented in Cartesian axes, it is given as

$$\mathbf{D}_{ss} = \begin{bmatrix} 0 & 0 & 0 \\ 0 & \rho E_{ss} & 0 \\ 0 & 0 & 0 \end{bmatrix} \tag{3.39}$$

where ρ is the reinforcement ratio, E_{ss} is the tangent modulus of smeared transverse steel.

Total stress is similarly computed as the sum of the concrete stresses in the principal plane and stress in smeared transverse steel as

$$\boldsymbol{\sigma} = \mathbf{T}_{\varepsilon}^{T} \boldsymbol{\sigma}'_c + \boldsymbol{\sigma}_{ss} \tag{3.40}$$

where

$$\boldsymbol{\sigma}'_c = \begin{Bmatrix} \sigma_{c1} \\ \sigma_{c2} \\ 0 \end{Bmatrix}, \quad \boldsymbol{\sigma}_{ss} = \begin{Bmatrix} 0 \\ \rho_s \sigma_s \\ 0 \end{Bmatrix} \tag{3.41}$$

3.4.2 Equivalent uniaxial stress-strain relation and shear modulus

(a) Concrete stress-strain relation in compression

For concrete response in uniaxial compression, the expression given by Popovics (1973) is adopted with strength enhancement due to the confinement of the stirrup according to Mander et al. (1988). The stress-strain relation at any instant is expressed as

$$f_c = f_p \left(\frac{\varepsilon}{\varepsilon_p}\right) \frac{r}{r - 1 + \left(\frac{\varepsilon}{\varepsilon_p}\right)^r} \tag{3.42}$$

$$r = \frac{E_c}{E_c - E_{sec}} \tag{3.43}$$

$$E_c = 5000\sqrt{f_{co}} \tag{3.44}$$

$$E_{sec} = \frac{f_p}{\varepsilon_p} \tag{3.45}$$

where $f_p = \beta_2 \beta_1 f_{co}$ and $\varepsilon_p = \varepsilon_{co}\,(1 + 5\beta_1 - 1)$ are the peak compressive stress and its corresponding strain considering strength enhancement due to lateral confinement of stirrup. β_1 is the strength enhancement factor due to confinement. β_2 is the compression softening factor, it is added to the peak compressive stress to account for the softening effect due to transverse tensile stress.

Strength enhancement factor β_1

The factor β_1 denotes the ratio of compression strength of confined concrete to that of unconfined concrete and is related to the effective confining stress, f_l, developed at the yield of the transverse reinforcement. The detailed expression of β_1 is given by Mander et al. (1988) is as follows

$$\beta_1 = -1.254 + 2.254\sqrt{1 + \frac{7.94 f_l}{f_{co}}} - \frac{2 f_l}{f_{co}} \tag{3.46}$$

For rectangular sections, the confining stresses are given by $f_{lx} = K_e \rho_x f_{yh}$ and

$f_{ly} = K_e \rho_y f_{yh}$ where $\rho_x = A_{sh,x}/sh_c$ and $\rho_y = A_{sh,y}/sb_c$, s is the spacing of the transverse hoops, $A_{sh,x}$ and $A_{sh,y}$ are the area of the transverse steel running parallel to the x and y directions, and h_c and b_c are the concrete core dimensions (measured from the centreline of perimeter hoops) in the y and x directions, respectively. f_{yh} is the yield strength of the transverse reinforcement. K_e is a confinement effectiveness coefficient that relates the area of the effectively confined core to the nominal core area, given by Mander et al. (1988) as follows

$$K_e = \frac{\left(1 - \dfrac{\sum_{i=1}^{n} w_i^2}{6 b_c h_c}\right)\left(1 - \dfrac{s}{2b_c}\right)\left(1 - \dfrac{s}{2h_c}\right)}{1 - \rho_{cc}} \tag{3.47}$$

where ρ_{cc} is the ratio of longitudinal steel area to core section area, w_i is the ith clear transverse spacing between adjacent longitudinal bars, n is the number of longitudinal bars.

Compression softening factor β_2

In the biaxial model case, the stress-strain relation of concrete is determined from equivalent uniaxial stress-strain relations. The term equivalent denotes these are uniaxial relations with some modification to represent the biaxial concrete behaviour. It is observed experimentally that the presence of transverse tension reduces the compressive strength and stiffness in concrete. This effect is known as compression softening. The compression softening is considered in the model by multiplying a softening factor β_2 by the peak stress in compression. The expression of reduction factor β_2 is given in Equation 3.48 (Vecchio and Collins, 1986).

$$\beta_2 = \frac{1}{0.8 - 0.34(\varepsilon_{c1}/\epsilon_p)} \leq 1, \qquad \text{for } \varepsilon_{c1} > 0 \tag{3.48}$$

where ε_{c1} is the tensile strain in transverse direction. Other relations are taken similar to the uniaxial law without modification.

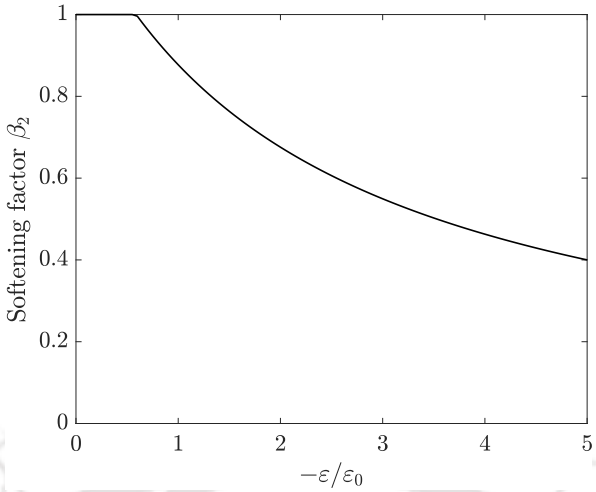

Figure 3.6: Concrete compressive strength reduction factor

(b) Concrete stress-strain relation in tension

For concrete in tension, two separate expressions are used to represent the uncracked and cracked response. The uncracked response is represented by a linear-elastic relation. After cracking the concrete still carries some tension due to bond action between the cracks. This phenomenon is known as tension stiffening. An expression of average stress for this post-cracking behaviour is given by Vecchio and Collins (1986)

$$f_c = \frac{f_t}{1 + \sqrt{200\varepsilon}}, \qquad \text{for } \varepsilon > \varepsilon_{cr} \tag{3.49}$$

where f_{cr} and ε_{cr} are the cracking strength and corresponding strain in concrete.

(c) Shear modulus

Different authors have used different shear modulus in the formulations. Most of the shear modulus were empirical in nature. In this study, the shear modulus used by Zhu et al. (2001) among others is chosen because it has been derived assuming the direction of the principal stress of concrete coincides with the principal strain. The expression for shear modulus G_c employed in this study is

$$G_c = \frac{(\sigma_1 - \sigma_2)}{2(\epsilon_1 - \epsilon_2)} \tag{3.50}$$

It shows that the shear modulus of smeared crack concrete should be the same in any coordinate system as long as the coincidence of the direction of principal stresses and principal strains is assumed.

3.4.3 Stress-strain relations in cyclic case

The hysteretic relations of concrete are defined based on a plastic offset strain parameter $\varepsilon_c^{p'}$ (Vecchio, 1999). In the compression domain, at any given compressive strain ϵ_c the parameter is computed as:

$$\begin{aligned} \varepsilon_c^{p'} &= \epsilon_c - \epsilon_p \left[0.87 \left(\frac{\epsilon_c}{\epsilon_p} \right) - 0.29 \left(\frac{\epsilon_c}{\epsilon_p} \right)^2 \right] && ; 1.5\epsilon_p < \epsilon_c \\ \varepsilon_c^{p'} &= \epsilon_c - 0.001305 \left(\frac{\epsilon_p}{0.002} \right) && ; \epsilon_c < 1.5\epsilon_p \end{aligned} \tag{3.51}$$

where ϵ_p is the strain corresponding to the peak stress on the compression base curve.

If concrete is damaged during the compression at the initial loading, tensile cracking would occur at the compressive strain due to the residual plastic strain developed by the initial compressive loading. This is modelled by shifting the tensile base curve to the plastic strain calculated in the compression domain. No positive offset is considered in the tension domain. The hysteresis loop is described using linear unloading reloading relations to and from the plastic offset strain as shown in Figure 3.7. The loading and unloading steps are modelled as follows.

1. Unloading from the compression envelope follows the line joining the unloading point and the plastic strain.

2. After crossing the zero stress axis the reloading to the tension envelope follows the line joining plastic strain to the maximum stress in tension side in the previous cycles. If it is the first loading on the tension side or the maximum strain on the tension side is exceeded, the line follows the tension envelope curve.

3. The unloading from the tension envelope follows the straight line to the plastic strain.

4. The reloading to the compression envelope follows the line joining plastic strain

to the maximum stress in compression side in the previous cycles. On exceeding the maximum stress on the compression side the curve follows the compression envelope.

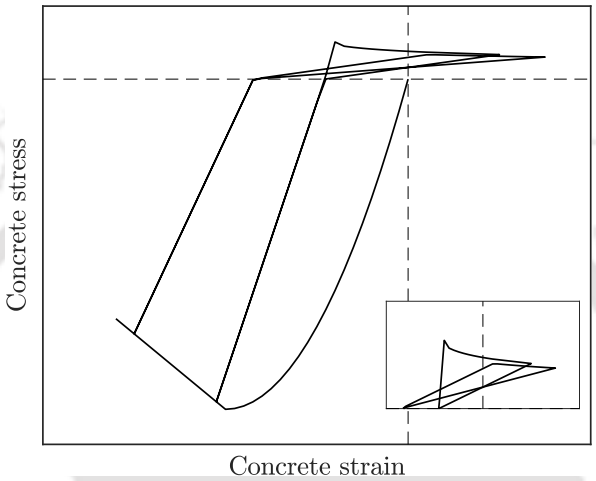

Figure 3.7: Concrete hysteretic stress-strain relation

The history parameters in crack coordinates are required to define the hysteretic relations of concrete equivalent uniaxial relations. For the fixed-crack approach, as the crack orientation is fixed, the history parameters can be easily stored and used in the uniaxial stress-strain relations. However, in the rotating crack approach, the crack orientation is free to rotate. It presents difficulty to track and store history variables for the 2D stress-strain relationship of concrete. To solve this problem, Vecchio (1999) used an incremental formulation to approximate the strain histories corresponding to an arbitrary direction. In this method, the concrete history variables are stored in the Cartesian (x,y) axes. The incremental changes in any history variables are calculated in the current crack axes, these are then transferred to the Cartesian axes and updated by addition to the stored values in the Cartesian axes.

The procedure is explained for concrete plastic strain. The concrete plastic strain is stored in component form as ε^p_{cx},ε^p_{cy},γ^p_{cxy}. If in a load step, the inclination of the crack is θ, then the plastic strain components in $x-y$ axes are transformed to the crack axes

ε^p_{c1}, ε^p_{c2} using transformation matrix $\mathbf{T}_\varepsilon$ (Equation (3.37)) as

$$\varepsilon^p_{c1} = \varepsilon^p_{cx}\cos^2\theta + \varepsilon^p_{cy}\sin^2\theta + \gamma^p_{cxy}\sin\theta\cos\theta \tag{3.52}$$

$$\varepsilon^p_{c2} = \varepsilon^p_{cx}\sin^2\theta + \varepsilon^p_{cy}\cos^2\theta - \gamma^p_{cxy}\sin\theta\cos\theta \tag{3.53}$$

These denote the plastic offset reached in the principal direction till the previous cycle. The plastic offset values are checked with the new plastic strains in the principal direction. If the new plastic offset strain exceed the previous plastic offset strains, the incremental plastic strains $\Delta\varepsilon^p_{c1}$ and $\Delta\varepsilon^p_{c2}$ in the principal directions are estimated. These are then transformed back to the Cartesian axis using transformation matrix $\mathbf{T}_\varepsilon(-\theta)$ (Equation (3.37)) and updated by adding them to the previous stored values.

$$\begin{aligned}
\varepsilon^p_{cx} &= \varepsilon^p_{cx} + \Delta\varepsilon^p_{c1}\cos^2\theta + \Delta\varepsilon^p_{c2}\sin^2\theta \\
\varepsilon^p_{cy} &= \varepsilon^p_{cy} + \Delta\varepsilon^p_{c1}\sin^2\theta + \Delta\varepsilon^p_{c2}\cos^2\theta \\
\gamma^p_{cxy} &= \gamma^p_{cxy} + \Delta\varepsilon^p_{c1}\sin 2\theta - \Delta\varepsilon^p_{c2}\sin 2\theta
\end{aligned} \tag{3.54}$$

where

$$\Delta\varepsilon^p_{c1} = \epsilon_1 - \varepsilon^p_{c1} \tag{3.55}$$

$$\Delta\varepsilon^p_{c2} = \epsilon_2 - \varepsilon^p_{c2} \tag{3.56}$$

A similar procedure is followed for the other strain history parameters, maximum compressive strains and maximum tensile strain of concrete fibre.

3.5 Constitutive Model for Reinforcing Steel

The stress-strain relation of steel is expressed using a bilinear linear elastic-strain hardening model in this work. The unloading and reloading behaviour is expressed using Pinto et al. model (Giuffre, 1970; Menegotto and Pinto, 1973). The model is based on a single equation for the curved transition from a straight-line asymptote with slope E_0 to another asymptote with slope $E_1 = bE_0$, where parameter b is the strain hardening ratio. The model provides a good representation of the Bauschinger effect, which

describes the phenomenon of lower yield stress in the reverse direction upon loading past the yield point in the forward direction. The equation is defined as

$$\sigma^* = b\varepsilon^* + \frac{(1-b)\varepsilon^*}{(1+\varepsilon^{*R})^{1/R}} \tag{3.57}$$

where $\sigma^* = (\sigma - \sigma_r)/(\sigma_o - \sigma_r)$, $\varepsilon^* = (\varepsilon - \epsilon_r)/(\epsilon_o - \epsilon_r)$, σ_o and ϵ_o are the stress and strain at the point where the two asymptotes of the branch under consideration meet (point A in Figure 3.8); similarly, σ_r and ϵ_r are the stress and strain at the point where the last strain reversal with stress of equal sign took place (point B in Figure 3.8). R is a parameter that affects the curvature of the transition curve, to represent the Bauschinger effect.

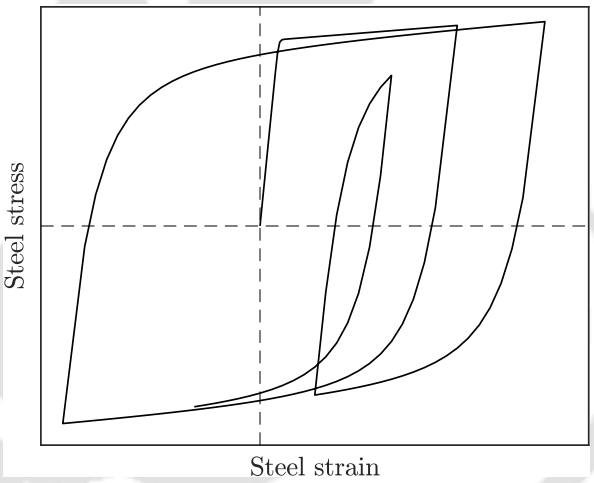

Figure 3.8: Reinforcing steel hysteretic stress-strain relation

3.6 Implementation Procedure

The implementation for static monotonic and cyclic load scenarios is explained here. Given an external load, the analysis is carried out using an incremental, iterative method. Where the total load is applied in incremental steps and the structure's state is determined iteratively. Some of the common solution algorithms are provided in Appendix C. The element state determination procedure is straightforward for displacement-based element. Given nodal displacements (from any standard non-linear solution procedure, such as load-control method, displacement-control method

etc), section deformation is directly obtained by the interpolation functions and section analysis is performed. However, the solution procedure for force-based elements is little involved. Many variants of force-based element algorithms are available in the literature. The iterative state determination procedure proposed by Spacone et al. (1996) is implemented in the developed program. The implementation steps are briefly summarized as follows.

3.6.1 Element state determination of force-based element

The solution procedure gives the incremental nodal displacements for the structure in global coordinates. To continue the solution procedure the internal force vector $\mathbf{R}$ and tangent stiffness $\mathbf{K}_{st}$ are required. These are estimated by the assembly of the respective quantities from the element state determination. The element state determination procedure adopted from Spacone et al. (1996) is explained here for one element where for an element nodal displacement the element end forces and element stiffness are estimated. A flowchart of the procedure is given in Figure 3.9.

1. For structural iteration number 'i', the nodal deformations $\mathbf{q}$ of an element, is obtained from the element displacement increments $\Delta\overline{\mathbf{u}}$ in the global coordinates using Equations (3.4) and (3.8). and

$$\mathbf{q}^i = \mathbf{q}^{i-1} + \Delta\mathbf{q}^i$$

2. The internal iteration counter '$j = 1$' is Initialized and the state of the system at 'i' is used as initial guess for the solution.

3. The increment of basic element forces is determined as

$$\Delta\mathbf{Q}^j = \left[\mathbf{K}_{eb}^{j-1}\right] \Delta\mathbf{q}^j$$

   Update the current value of basic element forces $\mathbf{Q}^j = \mathbf{Q}^{j-1} + \Delta\mathbf{Q}^j$

4. The section deformation increments at each monitoring section of element is

estimated as

$$\Delta \mathbf{d}^j = \left[\mathbf{K}_{sec}^{j-1}\right]^{-1} \left(\mathbf{S}^j - \hat{\mathbf{S}}^{j-1}\right) \quad \text{where} \quad \mathbf{S}^j = \mathbf{b}\mathbf{Q}^j$$

5. The section deformations is updated as

$$\mathbf{d}^j = \mathbf{d}^{j-1} + \Delta \mathbf{d}^j$$

The section analysis is performed to determine the state of the section state, i.e., section stiffness matrix $\mathbf{K}_{sec}^j$ and the section resisting force vector $\hat{\mathbf{S}}^j$ corresponding to the updated section deformation.

In the present study, the section resisting forces, and stiffness are obtained by integrating respectively the fibre stresses and the fibre stiffness, over the entire section, Equations (3.23) and (3.24).

6. The residual deformations at each monitoring section is evaluated form the unbalance section forces as

$$\mathbf{r}^j = \left[\mathbf{K}_{sec}^j\right]^{-1} \mathbf{S}_U^j \quad \text{where} \quad \mathbf{S}_U^j = \mathbf{S}^j - \hat{\mathbf{S}}^j$$

7. The flexibility matrix of the element is determined by integration the section flexibilities as

$$\mathbf{F}_{ele}^j = \sum \mathbf{b}^T \left[\mathbf{K}_{sec}^j\right]^{-1} \mathbf{b} \quad \text{corresponding stiffness} \, \mathbf{K}_{ele}^j = \left[\mathbf{F}_{ele}^j\right]^{-1}$$

8. The residual element deformation is estimated from the residual section deformations of the sections along the element as

$$\mathbf{v}^j = \sum \mathbf{b}^T \mathbf{r}^j$$

The norm of the residual element deformation compared with the specified tolerance. If the condition is satisfied, The state determination procedure for the

element is over. The procedure is performed for another element. If the condition is not satisfied, the element iteration counter is incremented $j = j + 1$ and Step 6 onward is repeated, with $\Delta\mathbf{q}^{j+1}$ set equal to $-\mathbf{v}^j$ to satisfy the element compatibility.

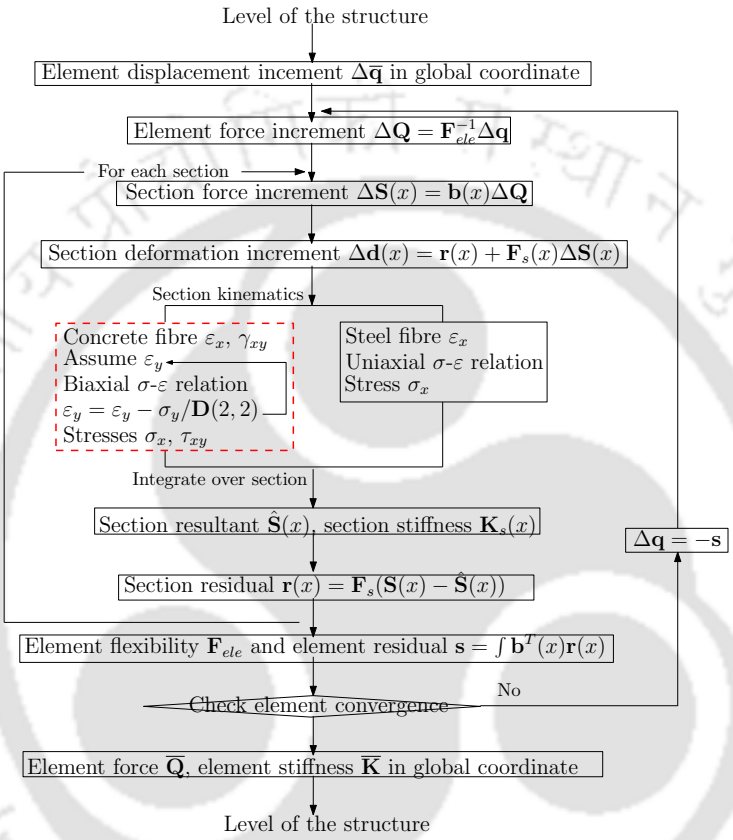

Figure 3.9: Flowchart showing the implementation of the coupled flexure-shear fibre element

3.6.2 Implementation of concrete constitutive relation

In Step 5 of the element state determination procedure, the section resisting force and stiffness are obtained from the concrete and steel fibre stress and stiffness. This section explain the procedure to obtain concrete fibre stress and stiffness. The concrete fibre stresses and stiffness are calculated assuming the shear beam kinematics with parabolic shear strain distribution and using the bi-dimensional constitutive relation based on the MCFT. The application of MCFT requires a complete strain tensor but only the axial and shear strain components are known from the assumed kinematic relations and the transverse strain is unknown. An iterative procedure is used to

determine the state of each concrete fibre till the transverse equilibrium is satisfied in each concrete fibre (Rericha, 1991; Petrangeli et al., 1999). An initial guess is used to start the calculation and it is subsequently corrected following a Newton-Raphson type method. In the implementation, the Newton-Raphson method is combined with the Bisection method to increase the convergence characteristic of the algorithm. Once the equilibrium in the transversal direction is achieved within a specified tolerance error, the static condensation of the tangent material stiffness matrix is performed to obtain the required reduced stiffness matrix of the concrete fibre.

1. For given axial strain ε_x and shear strain γ_{xy}, a transverse strain ε_y is assumed

2. The principal angle θ and principle strains ε_1, ε_2 are estimated for the strain state $\boldsymbol{\varepsilon} = [\varepsilon_x \ \varepsilon_y \ \gamma_{xy}]^T$ as

$$\theta = 0.5 \tan^{-1}\left(\frac{\gamma_{xy}}{\varepsilon_x - \varepsilon_y}\right)$$

$$\begin{Bmatrix} \varepsilon_1 \\ \varepsilon_2 \\ \gamma_{12} \end{Bmatrix} = \mathbf{T}_\varepsilon(\theta) \begin{Bmatrix} \varepsilon_x \\ \varepsilon_y \\ \gamma_{xy} \end{Bmatrix}$$

3. The concrete stresses in principal strain directions σ_{c1}, σ_{c2} is estimated from equivalent uniaxial stress-strain relationships.

4. The concrete stresses in principal directions are transformed to the Cartesian x-y direction. These stresses are added with the smeared steel stresses to obtain combined stress in the Cartesian x-y direction, as given in Equation (3.40) .

5. Similarly the concrete stiffness in the principal direction is transformed to the Cartesian direction and added with the smeared steel stiffness to obtain the combined stiffness matrix, as in Equation (3.40).

6. The combined stress in the transverse direction is checked for $\sigma_{yy} = 0$. If the condition is not satisfied a improved estimate of transverse strain is calculated as

$$\epsilon_y = \epsilon_y - \frac{\sigma_y}{D_{22}} \tag{3.58}$$

and the procedure is repeated form the Step 2 onwards.

7. If the condition is satisfied the strain and stress state of the concrete fibre has been determined, static reduction is performed to obtain the required form of concrete stress vector **s** and concrete tangent matrix **k** to use in section stiffness and section resultant calculation in Equations (3.23) and (3.24) respectively.

   the required reduced form of the stress vector is obtained from Equation (3.40) by omitting the transverse stress σ_y.

$$\mathbf{s} = \begin{Bmatrix} \sigma_x \\ \tau_{xy} \end{Bmatrix} \tag{3.59}$$

   Similarly, the required reduced form stiffness matrix is determined by static reduction of the row and column into the transverse direction in Equation (3.35), which leads to

$$\mathbf{k} = \begin{bmatrix} D_{11} & D_{13} \\ D_{31} & D_{33} \end{bmatrix} - \frac{1}{D_{22}} \begin{Bmatrix} D_{12} \\ D_{32} \end{Bmatrix} \begin{bmatrix} D_{21} & D_{23} \end{bmatrix} \tag{3.60}$$

3.6.3 Implementation of steel constitutive relation

The reinforcement fibre stresses and stiffness are calculated using a uniaxial stress-strain relation.

It is assumed that the longitudinal steel bars provide negligible shear resistance and carry only axial strain. Thus the section compatibility matrix of Equation (3.18) is modified as

$$\mathbf{a}_s(y) = \begin{bmatrix} -y & 0 & 1 \\ 0 & 0 & 0 \end{bmatrix} \tag{3.61}$$

The axial stress and tangent stiffness can be calculated from the steel material models. For consistency, these are stored in the following vector and matrix form, analogous to

the corresponding quantities of the concrete fibre.

$$\mathbf{s} = \begin{Bmatrix} \sigma_x(\varepsilon_x) \\ 0 \end{Bmatrix} \tag{3.62}$$

$$\mathbf{k} = \begin{bmatrix} E & 0 \\ 0 & 0 \end{bmatrix} \tag{3.63}$$

where E is the calculated tangent stiffness of the steel fibre.

3.6.4 Consideration for circular section

In the case of a rectangular cross-section, the determination of stress in transverse reinforcement is straightforward. For a circular section, the determination of transverse stress and stiffness in a circular hoop needs some modification due to the non-alignment of the stirrup with the Cartesian axes. To facilitate calculation, the circular cross-sections are discretized into a number of sectors along the circumferential direction. It is difficult to find the transverse strain, and stress in the Cartesian coordinates directly, therefore they are determined along the $x' - y'$ coordinate and then transformed to the Cartesian coordinate. The strain in the Cartesian coordinate system $\boldsymbol{\varepsilon}_{x-y}$ is converted to the $x' - y'$ coordinate system as

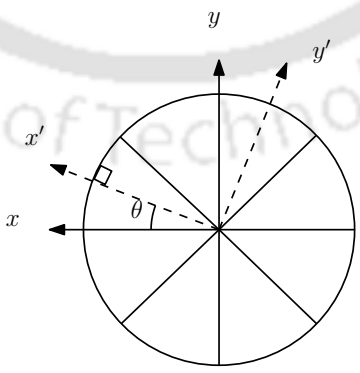

Figure 3.10: $x' - y'$ Coordinate system for circular cross-section

$$\boldsymbol{\varepsilon}_{x'-y'} = \mathbf{T}_{\varepsilon}\boldsymbol{\varepsilon}_{x-y}$$

where

$$\mathbf{T}_{\varepsilon} = \begin{bmatrix} c^2 & s^2 & sc \\ s^2 & c^2 & -sc \\ -2sc & 2sc & c^2 - s^2 \end{bmatrix}$$

where T_{ε} is transformation matrix. Then the stress and stiffness in the circular hoop are determined in the tangential direction of the stirrup and transformed back to the Cartesian coordinate system as

$$\boldsymbol{\sigma}_{ss} = \mathbf{T}_{\varepsilon}^{T} \boldsymbol{\sigma}_{x'-y'}$$

$$\mathbf{D}_{ss} = \mathbf{T}_{\varepsilon}^{T} \mathbf{D}_{x'-y'} \mathbf{T}_{\varepsilon}$$

All components of the above strain tensor are not considered. Only the components corresponding to tangential y' direction after transformation are retained. The expression of strain in tangential direction $\varepsilon_{y'}$ is calculated as

$$\varepsilon_{y'} = \varepsilon_{xx} \sin^2\theta + \varepsilon_{yy} \cos^2\theta - \gamma_{xy} \sin\theta \cos\theta$$

Having obtained the uni-axial stress and stiffness values in the $x' - y'$ coordinate system, these values are converted to the Cartesian coordinate system to satisfy equilibrium. The transverse steel reinforcement stress in the y-direction becomes $\sigma_y = \sigma_{y'} \cos^2\theta$, and the shear stress contribution of the steel is neglected. With similar transformations, the transverse steel reinforcement stiffness in the y-direction becomes $E_{y'} \cos^4\theta$, the other stiffness contribution of the steel is neglected. Thus, the stress and stiffness expression in Equations (3.39) and (3.41) for circular section becomes respectively

$$\boldsymbol{\sigma}_{ss} = \begin{Bmatrix} 0 \\ \rho_s \sigma_{y'} \cos^2\theta \\ 0 \end{Bmatrix} \tag{3.64}$$

and

$$\mathbf{D}_{ss} = \begin{bmatrix} 0 & 0 & 0 \\ 0 & \rho E_{y'} \cos^4\theta & 0 \\ 0 & 0 & 0 \end{bmatrix} \tag{3.65}$$

3.7 Localization Problem

Fibre elements are known to have numerical problems when modelling softening behaviour. In the presence of softening material, the strain/damage localises into a limited zone (Calabrese et al., 2010). The highly strained section of a frame element continues to load into the softening region while the neighbouring section unloads. This leads to a loss of objectivity and nonuniqueness of the post-peak response with mesh refinement (for the force-based element it is the number of integration points along the element).

The localization issue in the conventional Euler-Bernoulli element is well-studied in the literature. However, the localization issue in the flexure-shear element is very limited. The present study investigates the localisation issue in the developed force-based shear-flexible frame element and suitability of the available regularization techniques for this case.

3.7.1 Regularization techniques

This section provides an overview of two regularisation strategies for force-based elements that use the scaling of integration weight approach. To regularise the element response, both approaches scaled the integration weights at the element ends to the given characteristic lengths L_p.

(a) Method 1

The first method divides the element into three subregions, each with a different number and location of the integration points Addessi and Ciampi (2007); Scott and Fenves (2006). The idea used in Scott and Fenves is adopted in this study. The end regions are integrated with two points Gauss-Radau quadrature, while the interior region is

integrated with two points Gauss-Lagendre quadrature rule. This arrangement results in the fewest number of integration points along the element, with integration points at both ends, and the sequence of integration is exact for a linear curvature distribution over each subregion. The Gauss-Radau quadrature places one integration point at one end of the interval. The two-point Gauss-Radau Integration for the interval $[0, L_{end}]$ places the integration points at $\{0, 2L_{end}/3\}$, with an integration weight of $\{1/4L_{end}, 3/4L_{end}\}$. Therefore considering the $L_{end} = 4L_p$, the weight of the end section will be L_p. Thus, the final expression for the integration points and the corresponding integration weight for the element integration are obtained as

$$x_i = \begin{bmatrix} 0, & 8L_p/3, & 4L_p + L_{int}(1 - 1/\sqrt{3})/2, & 4L_p + L_{int}(1 + 1/\sqrt{3})/2, & L - 8L_p/3, & L \end{bmatrix} \tag{3.66}$$

$$w_i = \begin{bmatrix} L_p, & 3L_p, & L_{int}/2, & L_{int}/2, & 3L_p, & L_p \end{bmatrix} \tag{3.67}$$

where $L_{int} = L - 4L_p - 4L_p$

(a) Method 2

The second method uses interpolation quadrature to regularize softening response in force-based elements Scott and Hamutçuoğlu (2008). The integration weights at the element ends are set equal to characteristic values in interpolatory quadrature and then solved using the system of equations for the remaining unknown integration weights. As a result, there are 2N-4 unknowns (the coordinates and weights of the N-2 integration points). The solution can be simplified by fixing the locations of the integration points without significant loss of accuracy, for example, the Gauss-Lobatto scheme can be used as an underlying scheme for fixing the location of integration points. Subsequently, the remaining N-2 weights can be calculated as

$$\begin{bmatrix} 1 & 1 & \cdots & 1 \\ x_2 & x_3 & \cdots & x_{N-1} \\ \vdots & \vdots & & \vdots \\ x_2^{N-3} & x_3^{N-3} & \cdots & x_{N-1}^{N-3} \end{bmatrix} \begin{bmatrix} w_2 \\ w_3 \\ \vdots \\ w_{N-1} \end{bmatrix} = \begin{bmatrix} L - L_p - L_p \\ L^2/2 - LL_p \\ \vdots \\ L^{N-2}/(N-2) - L^{N-3}L_p \end{bmatrix} \tag{3.68}$$

where x_i denotes the integration point locations in the domain $[0, L]$, L_p is the length associated with the endpoints, and w_i denotes the unknown integration weights.

The modification of the integration rule generally lowers the order of accuracy; however, adopting a sufficient number of integration points (4 to 7) yields acceptable results. The suitability of these methods to get the objective response for the shear-flexible frame element is accessed in the following section.

3.8 Numerical Study

In this section, the performance of the developed element is accessed by simulating the monotonic and cyclic behaviour of experimental results from literature. In Sections 3.8.1 and 3.8.2 a shear critical column specimen is simulated to check the monotonic load-displacement behaviour of the element and the localization issue in the developed element. In Section 3.8.3 the cyclic load-displacement behaviour of different column specimens failured in different failure modes are simulated. In Section 3.8.4 a shear critical frame specimen is simulated.

3.8.1 Comparison with available software

A typical shear critical column specimen under transverse loading experimentally tested by Imai and Yamamoto (1986) is considered to check the implementation of the element with respect to VecTor5 software. VecTor5 is a nonlinear modelling software developed by VecTor Analysis Group at the University of Toronto. The trial software is used in present study. The VecTor5 is also based on the Modified Compression Field Theory. It uses displacement-based elements and is based on secant stiffness formulation.

The column was modelled by using one force-based coupled flexure-shear element. In VecTor5 the column is modelled using three displacement-based elements. Default options in the software were used in the model. However, the input material model and parameters were kept similar as far as possible. The dimension and material properties are obtained from the PEER's SPD database (Berry et al., 2004).

Figure 3.11 shows the comparison of load-displacement response obtained from the developed element with that of VecTor5 software. The monotonic results for both

flexure element and flexure-shear element are almost similar in both models indicating the validity of the implementation.

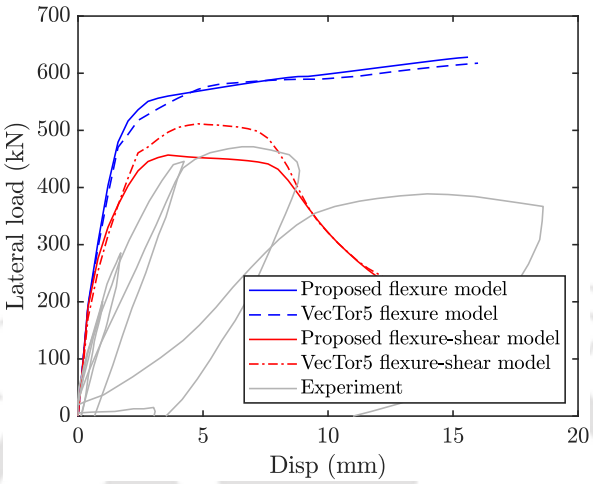

Figure 3.11: Comparison with VecTor5 software: monotonic load-displacement response)

3.8.2 Typical element response and mess regularization

The shear critical column specimen considered in Section 3.8.1 is again considered to check the localization issue in the developed element and the suitability of the available regularisation technique based on scaling of integration weight for shear-flexible frame element. The column was modelled by using one force-based shear-flexible element. First, the column was analysed with varying numbers of integration points as per the standard Gauss-Lobatto integration scheme to illustrate the strain localization issue. The column was reanalysed with the regularization methods based on the Gauss-Radau quadrature (method 1) and interpolatory quadrature method (method 2) presented in the Section 3.7 to check their effectiveness in the regularization of the softening response of the shear-flexible frame element.

The effect of the number of standard Gauss-Lobatto integration points on the global load-displacement response of the element is shown in Figure 3.12. Two typical columns with hardening type response and softening type response are selected for the study. Each column is analysed with one force-based element with three, four, five and six integration points as per the Gauss-Lobatto integration scheme. For hardening response, the increase in integration points using the standard Gauss-Lobatto integration scheme

leads to a convergent element response. However, for the softening type of response, the global response is found to be objective initially till the peak point. Then the response diverges, showing a stiffer degradation with the increase in the number of integration points.

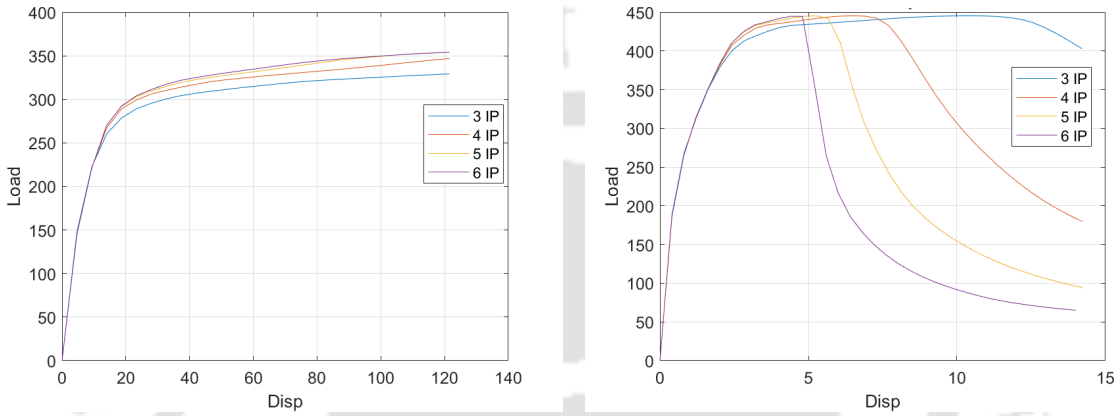

Figure 3.12: Effect of number of Gauss-lobatto integration points along the element on: (a) hardening response; and (b) softening response

Figure 3.13 further analyses the softening behaviour of the column. It illustrates the moment-curvature and shear force-strain response at the first integration point corresponding to the base of the column. It indicates that the section reached its shear capacity earlier in all cases. It is evident that the shear response is degrading while the moment response is unloading. Adopting the different number of integration points leads to the nonuniqueness of the result (Figure 3.13). With the increase of the integration points, the shear strain on the first integration point increases (shown by markers in the figure), it corresponds to the stiffer degradation of the global load-displacement response. Figure 3.13(b) shows the curvature and shear strain distribution along the column. It is observed that the end-section deformations have a significant effect on the element response. The contribution of the other sections along the element is comparatively less. This behaviour is similar to that in the conventional Euler-Bernoulli element (Calabrese et al., 2010; Coleman and Spacone, 2001).

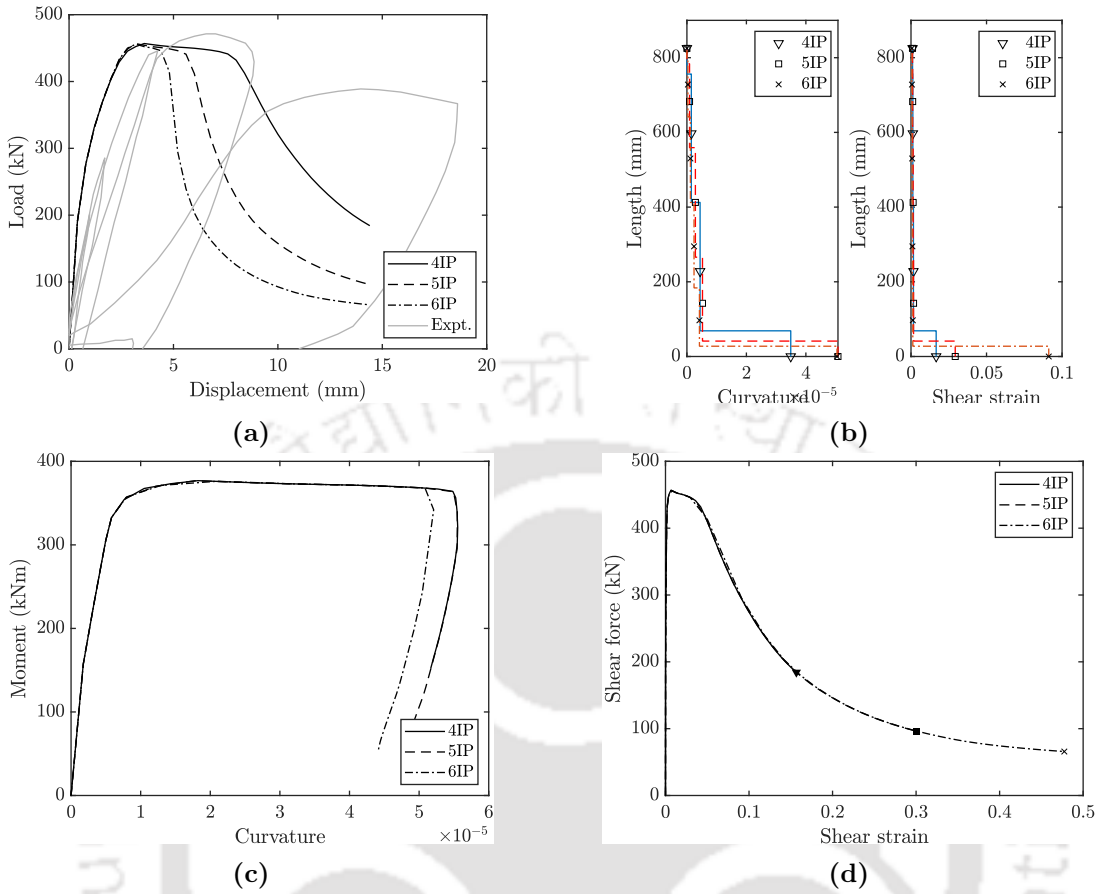

Figure 3.13: Results for standard Gauss-Lobatto integration: (a) global load-displacement response, (b) distribution of the curvature and shear strain along the height of the column corresponding to 5 mm displacement, (c) moment-curvature response at the end-section, (d) shear force-shear strain response at the end-section

The effectiveness of the regularization method-2 based on the Interpolatory quadrature (Scott and Hamutçuoğlu, 2008) is evaluated in Figure 3.14. The location of the integration point is chosen similarly to the Gauss-Lobatto scheme, with the weights of the end sections taken as $0.1L$, where L is the height of the column. The weight of the remaining interior points is determined by solving Equation (3.68). Figure 3.14 illustrates the global and end-section responses for different integration points. It implies that the method can provide an objective global and local response.

The distribution of curvature and shear strain along the length of the column for the regularisation scheme considered is presented in Figure 3.14(b). The figure is compared with the distribution of the curvature and the shear strain corresponding to the post-peak displacement of 5 mm using Gauss-Lobatto quadrature in Figure 3.13(b). By adopting standard Gauss-Lobatto quadrature, the integration weight associated with

the end section decreases while the shear strain increases with the increase of the integration point (see Figure 3.13(b)). By fixing the end integration weight using method-2, the curvature and the shear strain distribution over the end section remain similar irrespective of the number of integration points (Figure 3.14(b)).

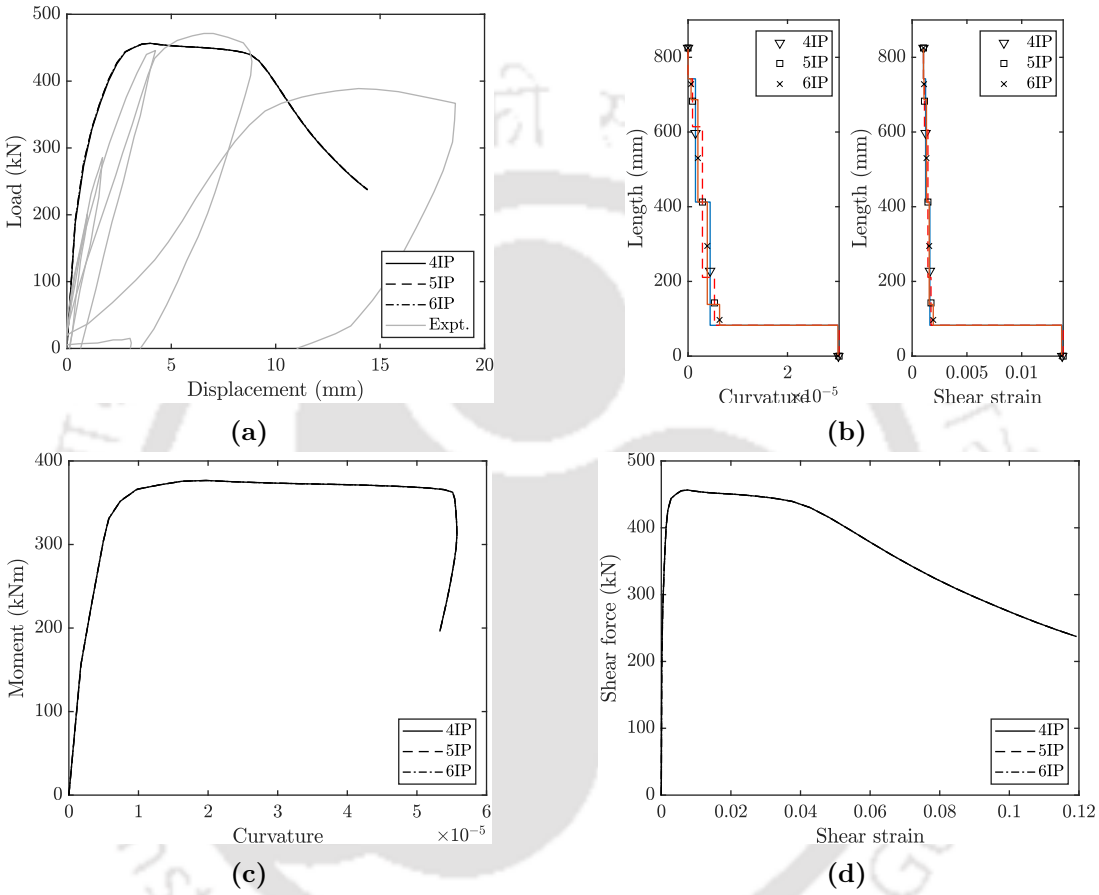

Figure 3.14: Results for Interpolatory integration: (a) global load-displacement response, (b) distribution of the curvature and shear strain along the height of the column corresponding to 5 mm displacement, (c) moment-curvature response at the end-section, (d) shear force-shear strain response at the end-section

The effectiveness of regularisation method-1 is shown in Figure 3.15. It uses modified Gauss-Radau integration in the end regions and Gauss-Lagendre quadrature in the interior region (Scott and Fenves, 2006). The location and weight of the integration points are taken according to Equations (3.66) and (3.67). This method again regularises the element response. It is observed that the global load-displacement response as well as the curvature and shear strain distribution along the column length, are similar to that obtained using method-2 (Figure 3.14(a) and 3.15 for $L_p = 0.1L$). Thus,

it can be said that both regularisation methods based on the scaling of integration weight provide similar responses with the same prescribed length. The effect of the length of the integration weight L_p is studied in Figure 3.15. Two different lengths were considered $L_p = 0.1L$ and $L_p = 0.12L$. The element integrals were performed using method-1. The results indicate that considering a larger prescribed integration weight $L_p = 0.12L$ leads to lesser shear and curvature demand on the end section. This results in a more ductile response and the strength degradation is delayed. Thus, while the responses are objective due to the scaling of the integration weights technique, they are reliant on the length of the integration weight assumed at the outset.

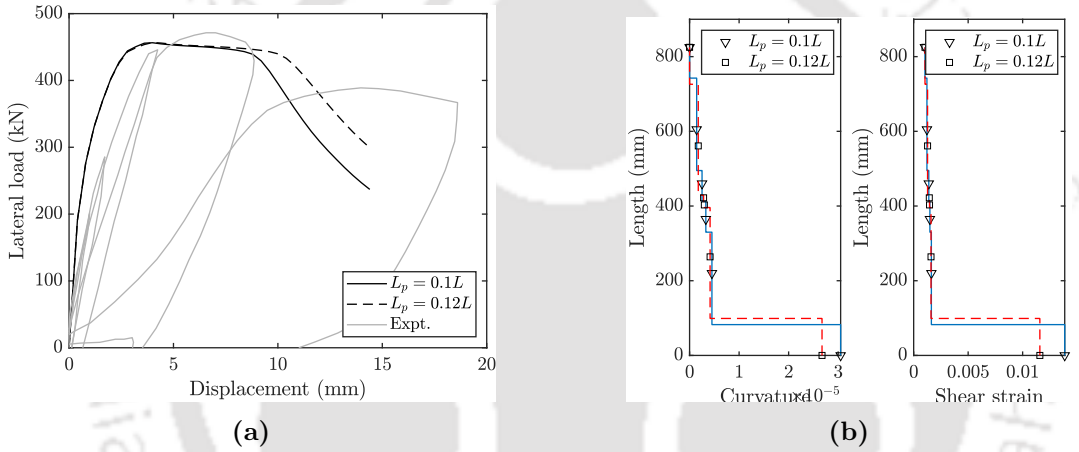

Figure 3.15: Effect of different length parameter (a) global load-displacement response (b) curvature and shear strain distribution corresponding to 5 mm displacement

3.8.3 Analysis of RC columns

To study the performance of t RC columns with different failure modes are analysed. A total of six RC column specimens tested by other researchers from the literature are selected, two flexure-critical columns, two shear-critical columns and two flexure-shear critical columns. The geometric and material details of the columns and their experimental response are obtained from the PEER Structural Performance Database (PEER SPD) and the reference literature. It is noted that the PEER SPD database provides column test data for a large number of column specimens. Some of the specimens were originally tested in a double cantilever configuration. The geometry and column response were modified for an equivalent cantilever configuration and provided

in the PEER SPD database.

The columns were modelled as axially loaded cantilever under reverse cyclic lateral loading with one FB element with 4 integration points. The numerical integration is performed using Gauss-Lobatto integration scheme. The cross-section is discretized into 20 concrete layers and a reinforcing steel layer. The concrete in compression is modelled using the Mander stress-strain relation, the concrete in tension is modelled using the tension stiffening relation of Vecchio and Collins (1986), and the reinforcement is modelled using the bilinear stress-strain relation. The global and local results are discussed in the following sections.

(a) Flexure critical columns

The specimens selected are Specimen A1 (Wehbe et al., 1999), and specimen BG-8 (Saatcioglu and Grira, 1999) both failed in flexure mode. The geometric and material data are given in Table 3.1.

Table 3.1: Column geometric and material data for flexure critical columns

Specimen:	FC-1	FC-2
Reference:	A1, Wehbe et al. 1998	BG-8, Saatcioglu and Grira 1999
Test config.	Cantilever	Cantilever
Section dimension $b \times h$ (mm^2)	380×610	350×350
Shear span a (mm)	2335	1645
Axial load P (kN)	615	961
Long. reinf. (mm)	18-ϕ19.1	12-ϕ19.5
Cover (mm)	28	29
Tran. reinf. (mm)	ϕ6	ϕ6.6
Shear leg	4	4
Stirrup spacing (mm)	110	76
Concrete strength f'_c (MPa)	27.2	34
Tran. reinf. yield stress f_{yt} (MPa)	428	580
Long. reinf. yield stress f_{yl} (MPa)	448	455.6

The load-displacement response of the specimen was shown in Figure 3.16 and Figure 3.17 for conventional element and flexure-shear element respectively. Comparing

the responses, it can be seen that both element yields similar responses comparable to the experimental result. The flexure-shear element produces only a slightly less peak strength and initial stiffness compared to that of the conventional element. Because the effect of shear is negligible in this type of element with aspect ratio near to 4. For such member, the conventional element is sufficient to capture the load-displacement response where the failure mode is due to flexure. The higher stiffness in the predicted response is due to neglecting the localized deformation due to the slip of the reinforcement bar in the anchorage region.

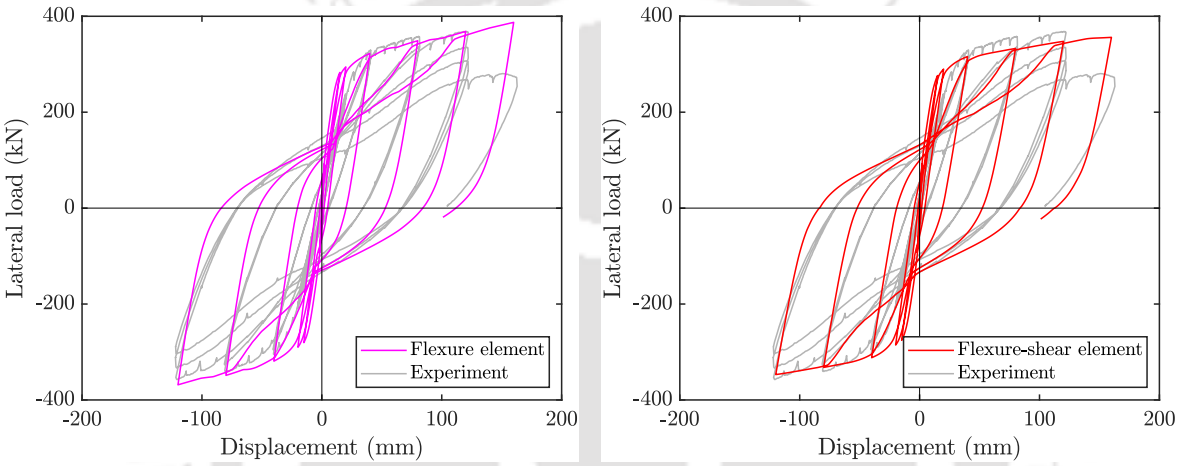

Figure 3.16: Comparison of load-displacement response for column FC-1: (a) flexure element, (b) coupled flexure-shear element

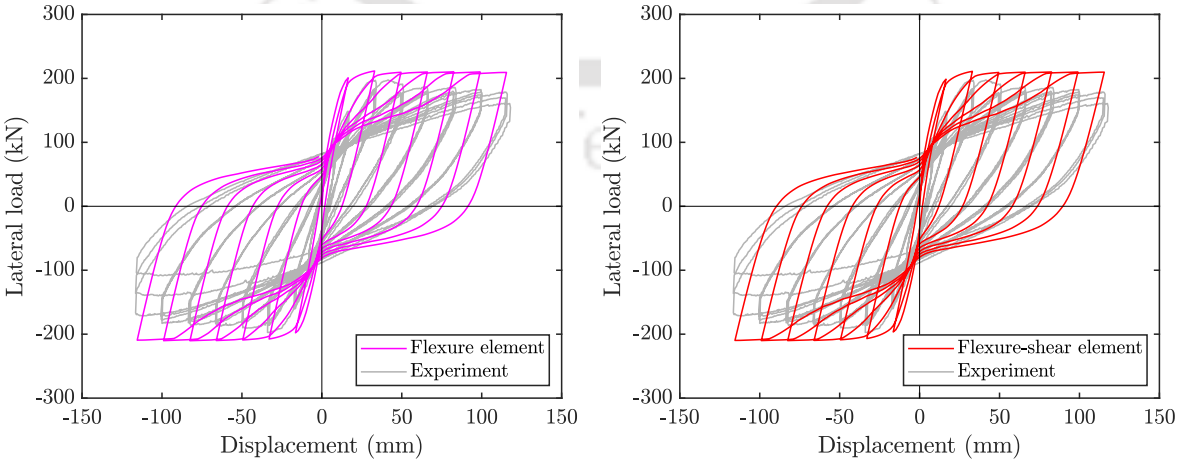

Figure 3.17: Comparison of load-displacement response for column FC-2: (a) flexure element, (b) coupled flexure-shear element

(b) Shear critical columns

The specimens selected are specimen No. 1 (Imai and Yamamoto, 1986), and specimen SC3 (Aboutaha et al., 1999). The columns were designed to have a shear capacity of less than the moment capacity. The experimental response of both the columns has shown significant shear deformation and failed in shear mode. The geometric and material data is given in Table 3.2.

Table 3.2: Column geometric and material data for shear critical columns

Specimen:	SC-1	SC-2
Reference:	1, Imai and Yamamoto 1986	SC3, Aboutaha et al. 1999
Test config.	Double cantilever	Cantilever
Section dimension $b \times h$ (mm^2)	400×500	914.4×457.2
Shear span a (mm)	825	1219.2
Axial load P (kN)	392	0
Long. reinf. (mm)	14-ϕ22	16-ϕ25
Cover (mm)	37	38
Tran. reinf. (mm)	ϕ9	ϕ9.53
Shear leg	2	5 (along b) 2 (along h)
Stirrup spacing (mm)	100	406.4
Concrete strength f'_c (MPa)	27.1	21.9
Tran. reinf. yield stress f_{yt} (MPa)	336	400
Long. reinf. yield stress f_{yl} (MPa)	318	434

The load-displacement responses of the specimen were shown in Figure 3.18 and Figure 3.19 for conventional element and flexure-shear element respectively. It can be seen that the prediction of the conventional element is unreliable when the contribution of shear deformation is significant. In these cases, the conventional element model overestimates the strength, energy dissipation capacity and ductility.

The prediction of the flexure-shear element in Figures 3.18 and 3.19 shows that for the shear critical columns, the overall response is predicted reasonably well compared

to that of the conventional element. For column SC-1 (Figure 3.18), the strength and initiation of strength degradation point is correctly predicted. The pinching of the hysteresis loop are also predicted by the developed flexure-shear element. The post-peak degradation is predicted greater than that reported in the experiment.

For column SC-2 (Figure 3.19) the peak strength is reasonably predicted. The initial stiffness and energy dissipation are less than that in the experiment. This might be due to the effect of post-peak localization and due to neglecting the effect of the anchorage-slip effect.

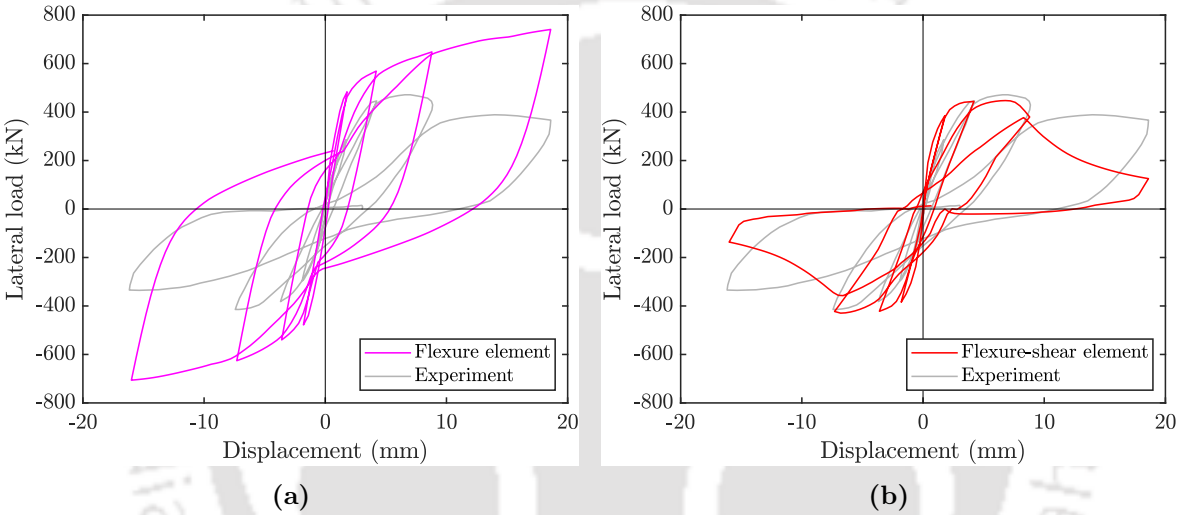

Figure 3.18: Comparison of load-displacement response for column SC-1: (a) flexure element, (b) coupled flexure-shear element

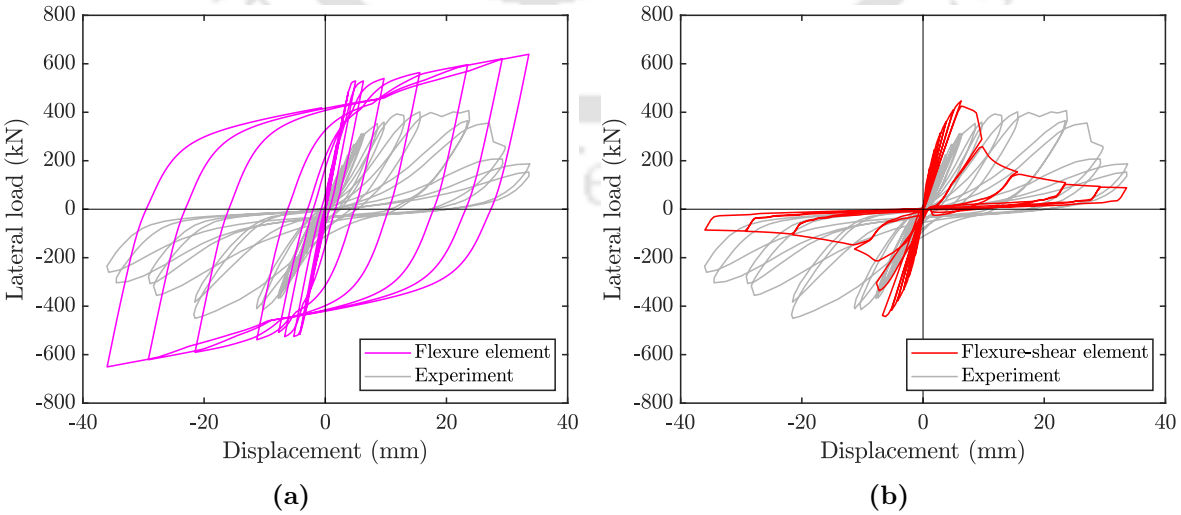

Figure 3.19: Comparison of load-displacement response for column SC-2: (a) flexure element, (b) coupled flexure-shear element

(c) Flexure-shear columns

The specimens selected are specimen 4D13RS (Ohue et al., 1985), and specimen No. 17 (Ang et al., 1989) both failed in flexure-shear mode. These are referred to as FS-1 and FS-2 respectively. Both the columns first yielded in flexure but ultimate failure is in shear mode of failure. The geometric and material data is given in Table 4.3.

Table 3.3: Column geometric and material data for flexure-shear columns

Specimen:	FS-1	FS-2
Reference:	4D13RS, Ohue et al. 1985	17, Ang et al. (1989)
Test config.	Double cantilever	Cantilever
Section dimension $b \times h$ (mm^2)	200×200	400
Shear span a (mm)	400	1000
Axial load P (kN)	183	431
Long. reinf. (mm)	8-ϕ13	20-ϕ16
Cover (mm)	12.5	15
Tran. reinf. (mm)	ϕ5.5	ϕ6
Shear leg	2	spiral
Stirrup spacing (mm)	50	60
Concrete strength f'_c (MPa)	29.9	34.3
Tran. reinf. yield stress f_{yt} (MPa)	316	326
Long. reinf. yield stress f_{yl} (MPa)	370	436

The load-displacement responses of Specimen FS-1 and Specimen FS-2 are shown in Figure 3.20 and Figure 3.21, respectively, using conventional element and flexure-shear element. It can be seen that the initial response till peak strength is similar for both of the elements. However, the later degrading behaviour denoting the presence of significant shear deformation is not captured by the conventional element. The conventional element overestimates the strength, energy dissipation capacity and ductility. Whereas the flexure-shear element captures the degrading behaviour.

Figure 3.20 shows the response of column FS-1. The overall column response is

predicted reasonably well by the flexure-shear element. The strength and initiation of the strength degradation point are correctly predicted. The hysteresis curve of the element shows some discrepancies near the zero load axis. This might be due to some issue in the hysteresis parameter handling in the concrete constitutive model. A similar result is obtained for the column FS-2 (Figure 3.20). The degradation point denoting shear failure is correctly predicted. It should be noted that both columns were reported to have a localized slip deformation. As it is not considered in this study, the initial stiffness is not correctly captured in the simulation with the flexure-shear element.

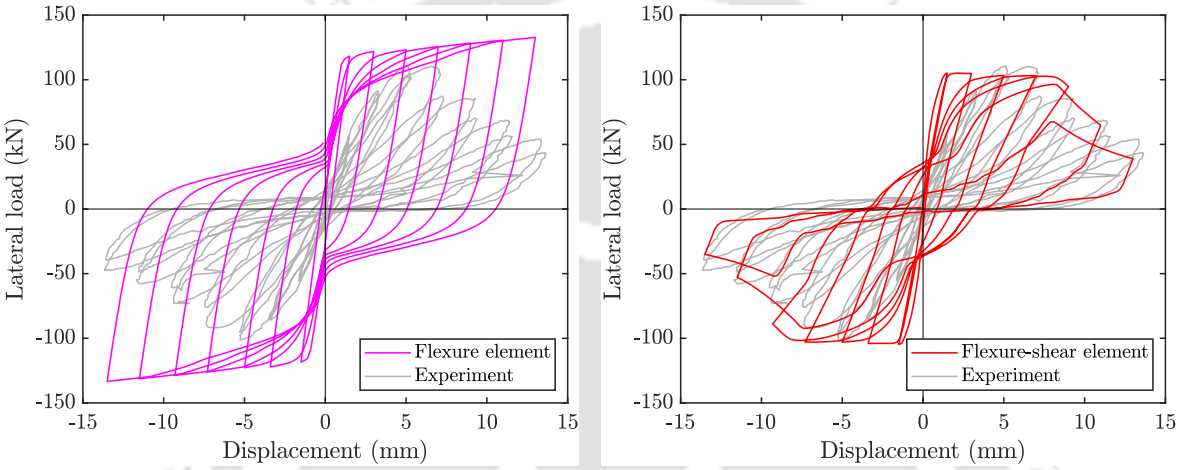

Figure 3.20: Comparison of load-displacement response for column FS-1: (a) flexure element, (b) coupled flexure-shear element

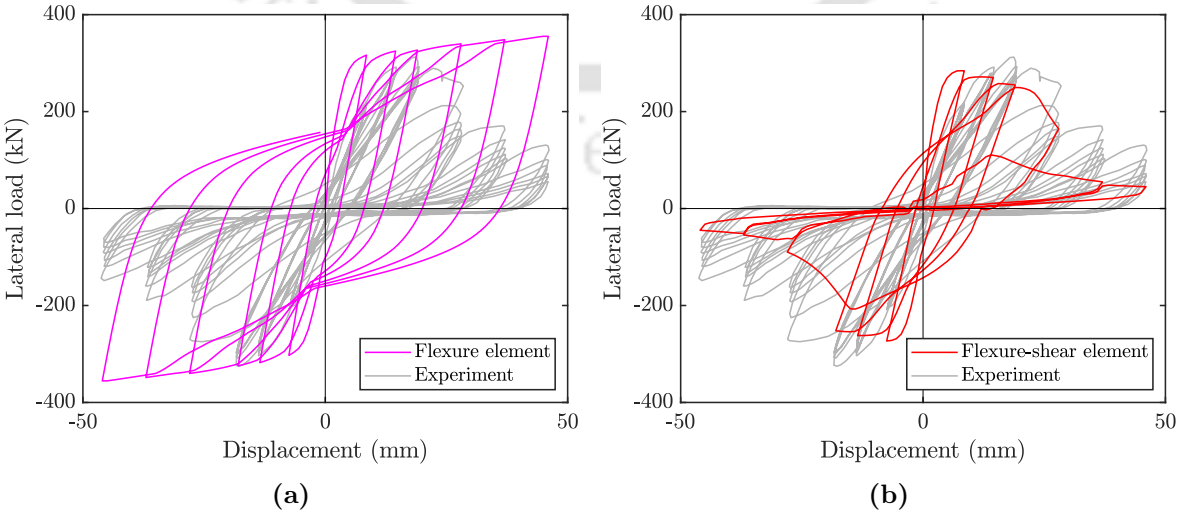

Figure 3.21: Comparison of load-displacement response for column FS-2: (a) flexure element, (b) coupled flexure-shear element

(d) Local responses

Figures 3.22 to 3.24 presents the detailed analysis of the results. One column from each category of failure mode is analysed for (i) the contribution of flexure and shear deformation to the total displacement and (ii) critical section moment-curvature response and shear force-shear strain response. It is noted that the implemented force-based element the global response is dominated by the response of the critical section. Hence, only the response of the critical section is analysed.

Figure 3.22 shows the analysis of specimen BG-8 (Saatcioglu and Grira, 1999) which is reported to fail in a flexure critical mode. It can be seen from the response of the critical section that although shear response goes to the nonlinear range, it is relatively small and till the end of the analysis, it did not degrade. The global response is dominated by the flexural contribution. For this type of member, the simplifying assumption of the conventional element leads to reasonable results.

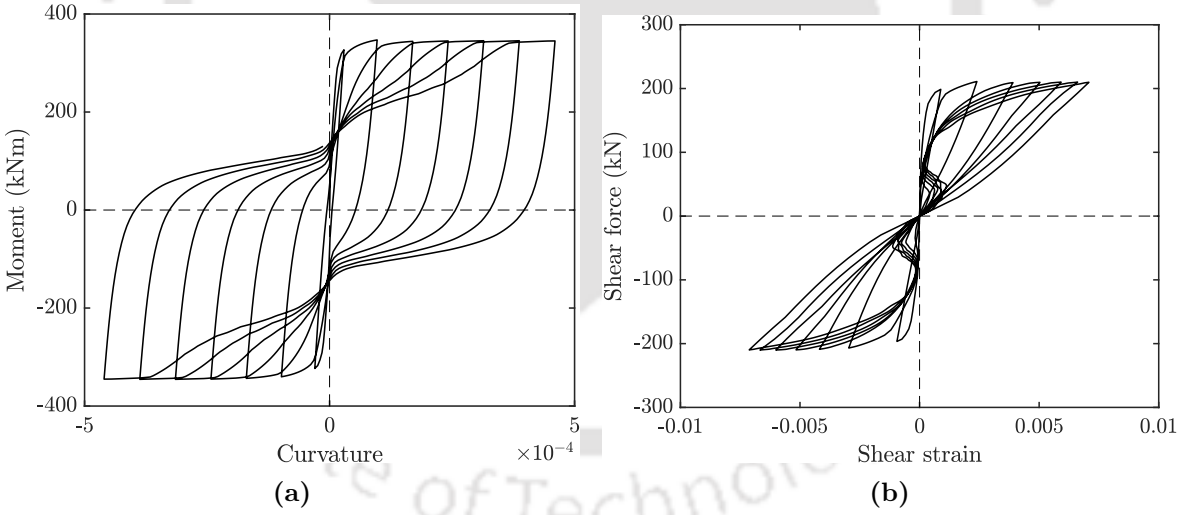

Figure 3.22: Local response of Column FC-2 obtained with coupled flexure-shear element: (a) moment-curvature response of end section, (b) shear force-shear strain response of end section

Figure 3.23 shows the analysis of specimen No. 1 (Imai and Yamamoto, 1986) which is reported to fail in a shear critical mode. It can be seen from the response of the critical section that in this case the shear deformation is large and the shear response starts degrading before the moment response. The global response is dominated by the shear contribution. For this type of member, the neglecting shear can lead to large

errors in the response prediction.

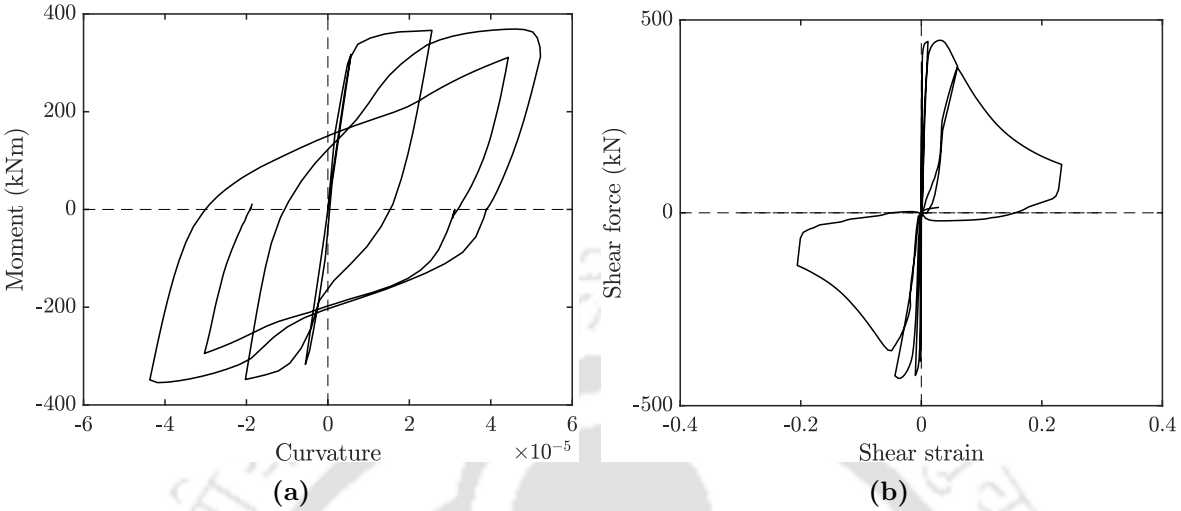

Figure 3.23: Local response of Column SC-1 obtained with coupled flexure-shear element: (a) moment-curvature response of end section, (b) shear force-shear strain response of end section

Figure 3.24 shows the analysis of specimen No. 17 (Ang et al., 1989) which is reported to fail in a flexure-shear mode. It can be seen from the response of the critical section that yielding occurs before the degradation of the shear response. On further loading, the shear deformation becomes large. The peak global response occurs at the yielding of the section but the later post-peak response is dominated by the shear contribution. For this type of member, the neglecting shear can lead to large errors in the response prediction. The cyclic response of the element is not in agreement with the experimental results

3.8.4 Analysis of shear critical RC frame

An RC frame with shear-critical beams is simulated and compared. The frame was a one-bay, two-story frame tested by Duong et al. (2007). It was subjected to a vertical load of 420 kN at the top of each of the columns and tested in lateral reverse cyclic loading in two phases. In phase one the frame was subjected to a lateral reverse cyclic loading at the second story until substantial diagonal cracking of beams occurred. The frame was then repaired with CFRP and retested (phase two). Herein the phase one response is simulated and examined.

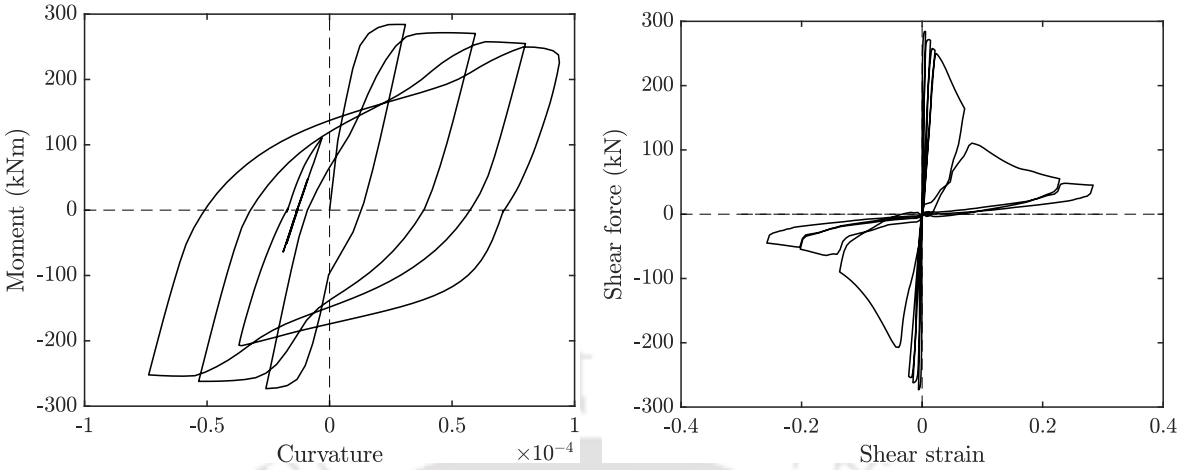

Figure 3.24: Local response of Column FS-2 with coupled flexure-shear element: (a) moment-curvature response of end section, (b) shear force-shear strain response of end section

The centreline dimension of the frame is used to model the frame specimen. The member length and the cross-section dimensions are shown in Figure 3.25. Each column is modelled using two force-based elements per story to consider the increase in longitudinal reinforcement at the ends of the columns. Each beam is modelled using one force-based element. Five integration points are considered per element in the analysis. The cross-section is discretized into 20 concrete layers and reinforcing steel layers. The concrete in compression is modelled using the Mander stress-strain relation, the concrete in tension is modelled using the tension stiffening relation of Vecchio and Collins (1986), and the reinforcement is modelled using the bilinear stress-strain relation. The compressive strength of the concrete is reported as 42.9 MPa and the corresponding peak strain is 0.0023. The material properties of different steel used in the frame are summarized in Table 3.4.

Table 3.4: Material properties for steel (Duong et al., 2007)

Bar size	Diameter (mm)	Area (mm^2)	f_y (MPa)	f_u (MPa)	E_s (MPa)	ϵ_u (%)
No. 20	19.5	300	447	603	198400	130.8
No. 10	11.3	100	455	583	192400	129.9
US #3	9.5	71	506	615	210000	134.6

The analytical and experimental lateral load-displacement response for the second-

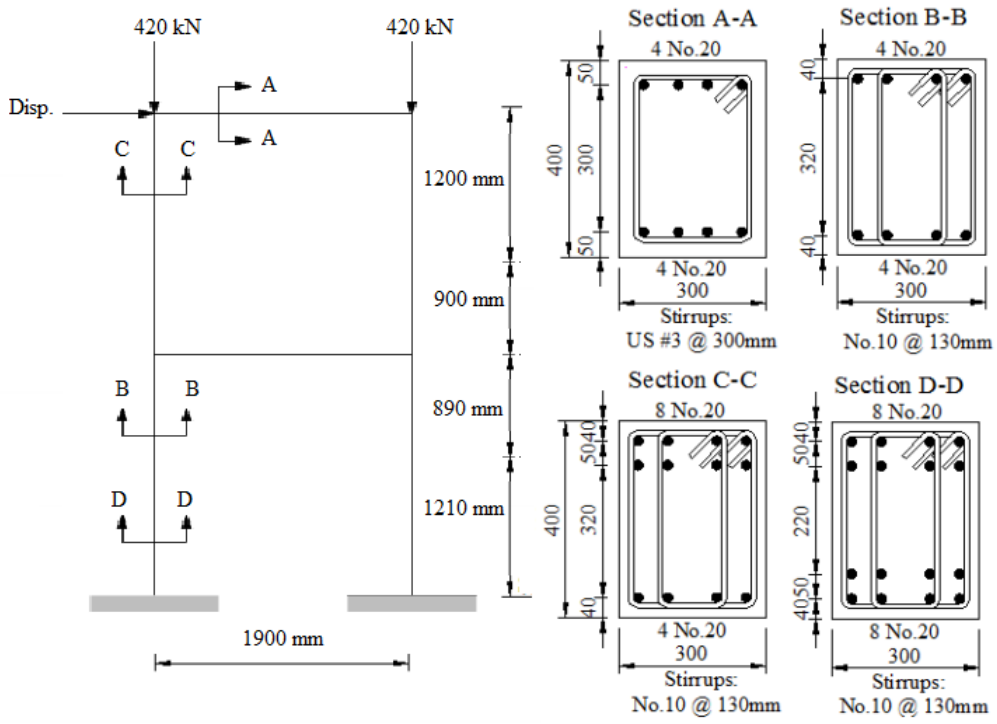

Figure 3.25: Dimensions of shear critical frame (Duong et al., 2007)

storey beam are compared in Figure 3.26. As seen in Figure 3.26, the overall response of the frame under cyclic loading was predicted with good accuracy. The predicted strength of the frame in the forward and reverse half cycle are estimated as 355 kN and -311 kN; which are close to 327 kN and -304 kN found in the experiment. The residual displacement at the top storey is calculated at 13.6 mm which is approximately 9% overestimation compared to the experimental value. The total energy dissipated by the frame was predicted with excellent accuracy, in the analytical model the value is found to be 12.57 kNm while the experimental value is 12.5 kNm.

The axial deformation of both columns, as determined experimentally and analytically at the top of the columns (second storey level), are compared in Figure 3.27. The first and second-storey beam axial deformation responses are presented in Figure 3.28. As seen from the graphs above, the predicted column and beam axial deformation response showed reasonably good agreement with the experimental responses.

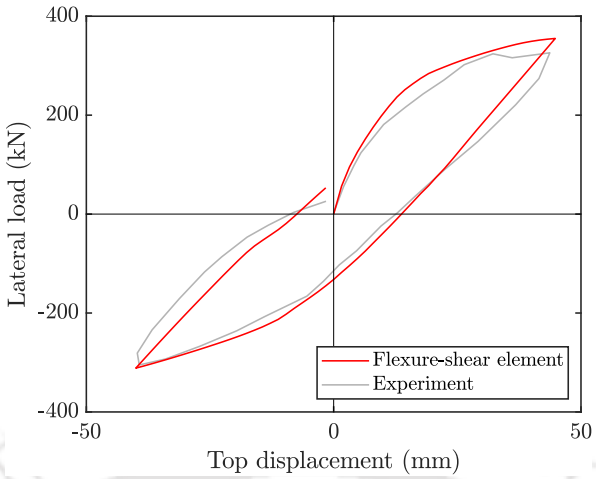

Figure 3.26: Lateral load- top displacement response of shear critical frame

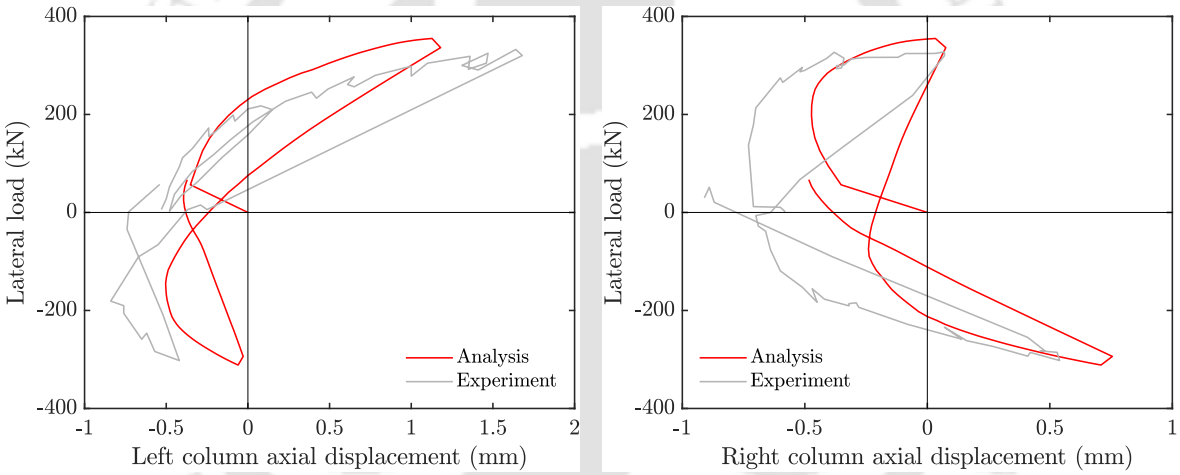

Figure 3.27: Column axial deformation response for the shear critical frame

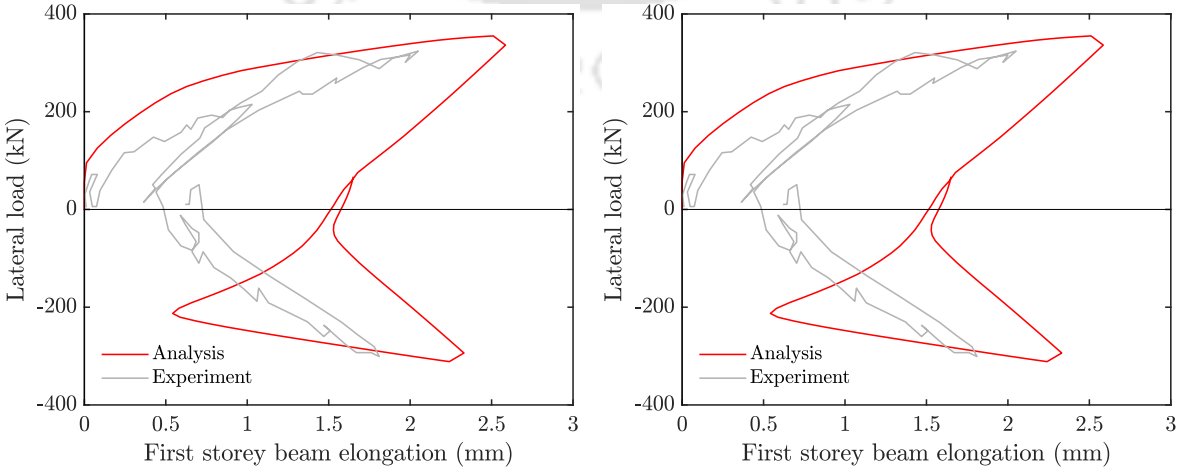

Figure 3.28: Beam elongation response of shear critical frame

3.9 Conclusion

In this chapter, the general formulation of a force-based fibre element is first introduced and followed by the development of an axial-flexure-shear coupled fibre element by incorporating a multiaxial constitutive relation for concrete material. The 2D constitutive material of the concrete is based on a rotating smeared-crack model based on Modified Compression Field Theory (Vecchio and Collins, 1986). However, the concrete compression stress-strain relation is considered following the Mander model (Mander et al., 1988) to consider the confining effect of stirrup and the shear modulus is obtained by Zhu et al. (2001) to enforcing the coaxiality of the principal stress and principal stress direction. The numerical model is validated by the test results of different column specimens that failed in flexure mode, shear mode and flexure shear mode. The localization issue in the developed element is studied. It is found that the available regularizing techniques based on scaling of integration weight is equally suitable for the developed element.

Chapter 4

Force-Based Fibre Frame Element with Semi-Uncoupled Flexure-Shear Interaction

4.1 Introduction

The axial-flexure-shear coupled force-based fibre element presented in Chapter 3 provides necessary enhancement over the conventional fibre element based on Euler-Bernoulli beam theory. However, it requires a complex concrete multi-axial constitutive model and additional iterative calculation for each concrete fibre to determine the strain and stress state. This chapter introduces a semi-uncoupled fibre section that accounts for axial-shear-moment interaction with reduced complexity by partially removing the shear coupling with axial-moment terms in section stiffness expression. The shear response of the section is obtained from a variable shear relation that accounts for the effect of flexure on the shear strength. The semi-uncoupled fibre section is incorporated in a force-based element framework similar to that given in the previous chapter and the element performance is evaluated. Also a simplified cyclic shear force-shear strain hystertic curve is proposed and implemented in the present study.

The next section, Section 4.2 describe the general formulation of the semi-uncoupled fibre section. It is followed by a detailed description of the proposed section shear force-

shear strain relation in Sections 4.3 and 4.4. Its implementation procedure is presented in Section 4.5. The performance of the force-based element with the semi-uncoupled fibre section is assessed by comparing the model result with that of the developed axial-flexure-shear coupled force-based element and conventional fibre element in Section 4.6.

4.2 Semi-Uncoupled Fibre Section

The semi-uncoupled fibre section formulation is similar to the conventional fibre section based on Euler-Bernoulli theory given in Appendix B with the difference in the shear force calculation. The fibre section is based on Timoshenko beam kinematics and assumes the shear response is uncoupled from the axial and bending response. The section axial and bending response is derived from the plane section hypothesis and uniaxial stress-strain relation as in the conventional fibre beam-column element, while the shear response is considered according to an explicit nonlinear shear relation (Ranzo and Petrangeli, 1998; Martino et al., 2000; Marini and Spacone, 2006; Sae-Long et al., 2019, 2020). A schematic representation of the section model is shown in Figure 4.1. It should be noted that although the axial-flexure and the shear responses are uncoupled at the section level because of the force-based formulation, the axial-flexure and shear responses get coupled at the element level. A detailed methodology to obtain the shear relation with flexure-shear interaction proposed is presented in the next section.

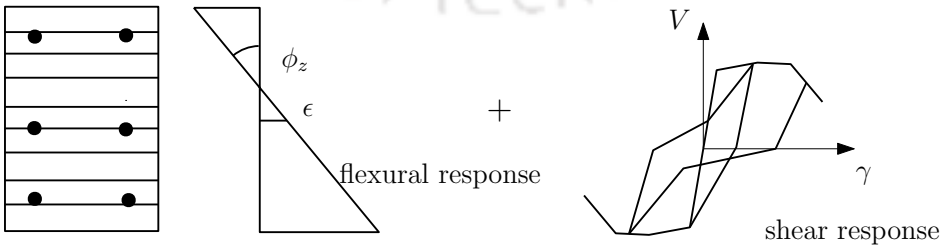

Figure 4.1: Semi-uncoupled fibre section

A section deformation denoted by $\mathbf{d} = \{\phi(x), \gamma(x), \varepsilon(x)\}^T$. The expression of the

section force resultant $\hat{\mathbf{S}}$ and the tangent stiffness matrix $\mathbf{K}_s$ are obtained as

$$\hat{\mathbf{S}} = \begin{Bmatrix} M(x) \\ V(x) \\ N(x) \end{Bmatrix} = \begin{Bmatrix} -\sum_i \sigma_i A_i y_i \\ V(\gamma) \\ \sum_i \sigma_i A_i \end{Bmatrix} \tag{4.1}$$

$$\mathbf{K}_s = \begin{bmatrix} \sum_i E_i A_i y_i^2 & 0 & -\sum_i E_i A_i y_i \\ 0 & \mathrm{d}V/\mathrm{d}\gamma & 0 \\ -\sum_i E_i A_i y_i & 0 & \sum_i E_i A_i \end{bmatrix}. \tag{4.2}$$

where $V(\gamma)$ represent the section shear force obtained from the shear relation, $dV/d\gamma$ is the shear tangent modulus, A_i, y_i represent the area and location of the fibre, σ_i, E_i represent the stress and tangent modulus of the fibre obtained from uniaxial stress-stress relation of fibre.

4.3 Shear Relation: Envelope Curve

Shear envelope curves available in the literature are obtained by fitting a multilinear curve to the analytical results or empirical relations. However, the consideration of the effect of axial flexure on the shear envelope is important to realistically account for the shear deformation along the member. In the literature, the flexure-shear interaction effect is considered approximately by modifying the shear relation. The present study differs from that of previous studies (Ranzo and Petrangeli, 1998; Marini and Spacone, 2006; Sae-Long et al., 2019, 2020) in terms of the definition of the sectional shear relation. The shear relation is derived from a detailed sectional analysis using a fibre section model with a multiaxial stress-strain relation. The shear relation is described as multi-linear curve with two components: (a) variable envelope curve with flexure-shear interaction, and (b) hysteresis rules. The process for obtaining the shear force-shear strain response of an RC section and calibrating the envelope curve is described in the next section. The rules for hysteresis shear force-shear strain are described in the subsequent section (Section 4.4).

4.3.1 Typical section response

The shear relation used in this chapter is obtained from the result of the axial-flexure-shear coupled fibre section model, presented in Section 3.3. The fibre section model is shown in Figure 3.3. The model is based on a fixed shear-strain approach (Vecchio and Collins, 1988), where a supplementary shear-strain of the predefined pattern is imposed over the section. In present work, parabolic shear strain distribution is considered. The concrete behaviour is modelled using a rotating smeared-crack model and reinforcing steel is modelled using uniaxial stress-strain relation.

Figure 4.2 shows the flow chart for the calculation of the shear force-shear strain response of a section for a given constant axial load N and bending moment M. Similar procedure can be used to obtain moment-curvature response of a section for a given axial load and shear force. Note that in the current implementation, the axial load variation is not considered.

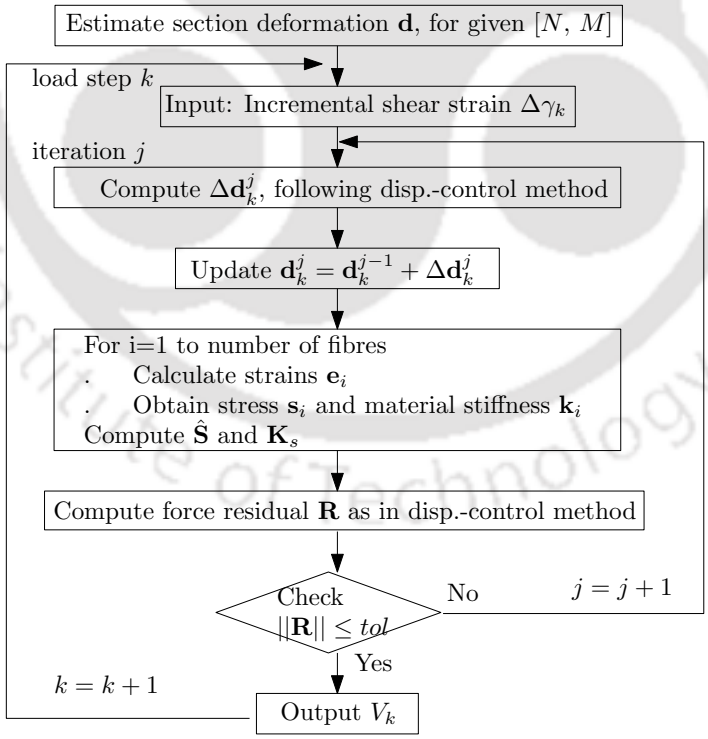

Figure 4.2: Flowchart for calculation of shear force-shear strain response

Figures 4.3 and 4.4 shows the influence of shear force on the moment-curvature response and the effect of moment on the shear force-shear strain response for a typical

reinforced concrete section. The cross-section studied belongs the shear-critical short column (specimen 1-1) tested by Bett et al. (1985) in double curvature. The dimensions of the column are given here for ready reference. The detailed description can be found in Bett et al. (1985). The length of the column is 914 mm (3'). The column is subjected to a constant axial load of 288 kN (64.8 kip). The cross-section dimensions are 305 mm $\times$ 305 mm (12" $\times$ 12"). The concrete strength is 29.9 MPa (4333 psi). Longitudinal reinforcement are eight bars of 19 mm (0.75") diameter and yield stress of 462 MPa (67 ksi). Stirrups are of 6 mm diameter spaced at 203 mm (8") and 414 MPa (60 ksi) yield stress.

The moment-curvature diagram of the section for different constant shear forces is shown in Figure 4.3(a). It is observed that the shape of the moment-curvature diagrams is severely influenced by the presence of a large shear force. The presence of shear force reduces the initial stiffness and moment-carrying capacity of the section. The variation of moment capacity in plotted in Figure 4.3(b). It is observed that the reduction in moment capacity is negligible for small values of shear force, but is significant in the presence of higher-level shear force. These observations are similar to Bairan and Mari (2004).

The effect of the constant moment on the shear force vs shear strain diagram is shown in Figure 4.4. It is seen that the shear strength of the section decreases with increasing moment. The initial stiffness also decreases with the increase in moment level. Similar observations have been made by Bairan and Mari (2004). Therefore, in order to obtain the correct behaviour of the reinforced member, the flexure-shear interaction should be taken into account in the model.

For the particular section under consideration, on comparing the lateral load levels corresponding to maximum moment and shear capacity, it is found that the section has a maximum moment capacity of 164 kNm (Figure 4.3) corresponding to a lateral load of 359 kN ($V = 2M/L$). The maximum shear capacity of the section is 244 kN (Figure 4.4). This indicates that the section is critical in shear. Further, for the experimental peak load of 220 kN (49 kip measured by Bett et al. (1985)), the moment at the column end section is estimated to be 100.5 kNm. The shear capacity corresponding to this moment predicted from Figure 4.4(b) is found to be around

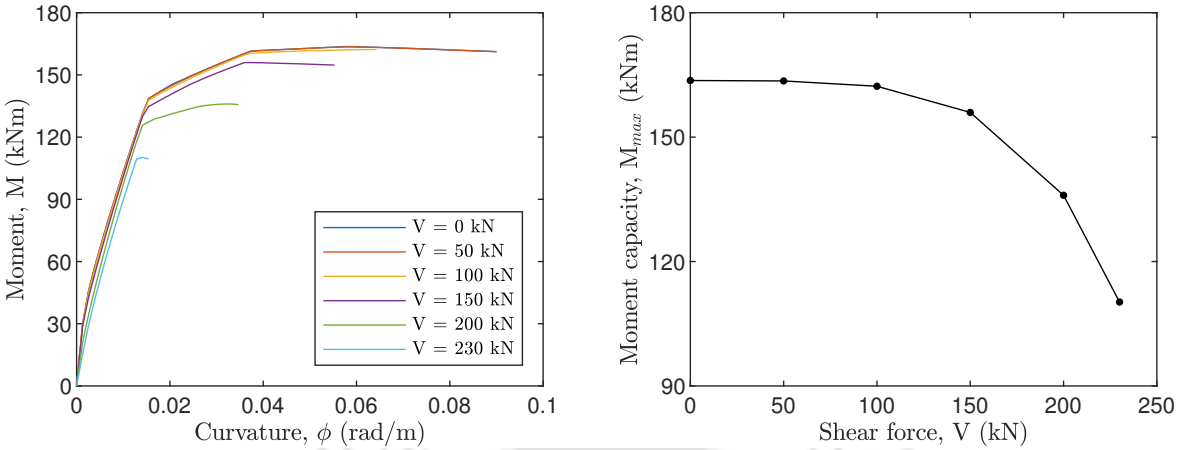

Figure 4.3: (a) Moment-curvature diagrams for different shear force, (b) variation of moment capacity with shear force

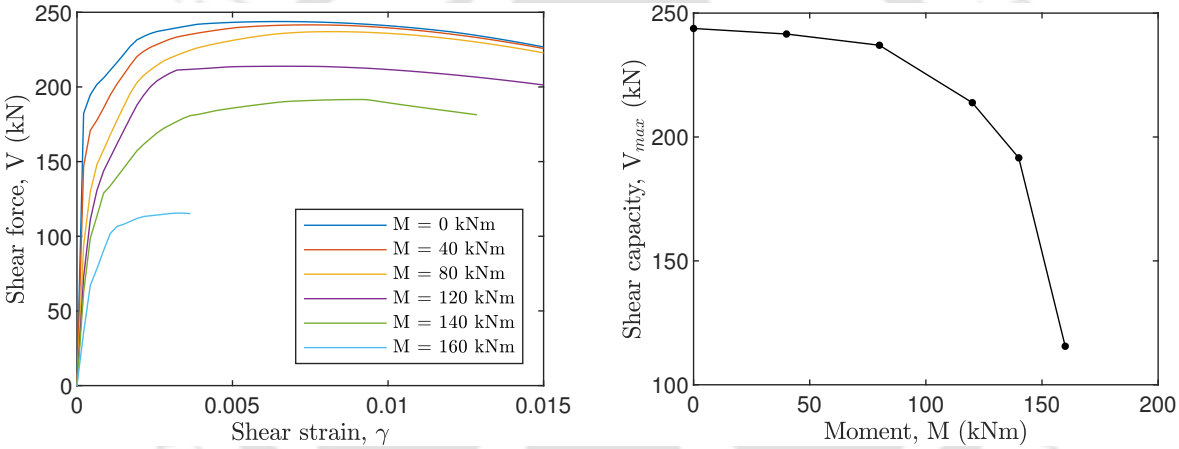

Figure 4.4: (a) Shear force-shear strain diagram for different moments, (b) variation of shear capacity with bending moment

230 kN. The value is close to the reported value in the experiment. This shows the shear interaction model developed in the present study is able to capture the typical behaviour of the RC section and also is in good agreement with the experimental result.

4.3.2 Idealized envelope curve

A multi-linear envelope curve is used to fit the shear response derived from the coupled sectional analysis. The envelope curve is shown in Figure 4.5. It has a trilinear ascending branch till ultimate point (V_u,γ_{u1}), a plateau region with constant shear strength V_u (between γ_{u1} and γ_{u2}) and a bilinear descending branch beyond the strength degradation point (V_u,γ_{u2}). The trilinear ascending branch is selected to facilitate the hys-

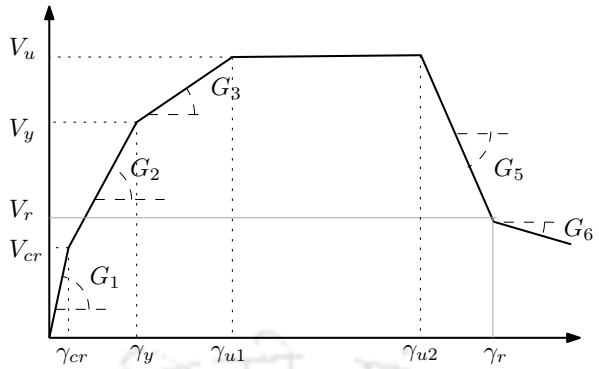

Figure 4.5: Multi-linear envelope curve for the shear force-shear strain relation

teresis relations (presented in Section 4.4) that requires the definition of a cracking point (V_{cr},γ_{cr}) and yielding point (V_y,γ_y). Selecting appropriate parameters a variety of shear responses can be represented by this envelope curve.

In the proposed model, the shear force-shear strain curve corresponding to zero moment level is considered as primary curve and used to fit the muliti-liner envelope. The complete definition of this curve requires a total of ten parameters (G_1, V_{cr}, V_y, γ_y, V_u, γ_{u1}, γ_{u2}, V_r, γ_r, G_6). However, in the current implementation, only six parameters, namely: initial shear modulus G_1, max shear strength V_u, two shear strains, γ_{u1} and γ_{u2}, denoting the range of plateau region, residual shear strength V_r and its corresponding shear strain γ_r are used to define the envelope curve. The remaining parameters are assumed as, $V_{cr} = 0.25V_u$, $V_y = 0.75V_u$, $\gamma_y = 0.375\gamma_{u1}$, $G_6 = bG_5$ with $0.2 < b < 0.5$. The parameter G_6 represents degradation slope after residual point (Figure 4.5).

In the proposed model, the shear force-shear strain curve corresponding to zero moment level is considered as primary curve and used to fit the muliti-liner envelope. Some form of flexure and shear forces interaction is required at the section level to improve the prediction of the element (Ranzo and Petrangeli, 1998; Marini and Spacone, 2006; Sae-Long et al., 2019, 2020). In present study, the effect of fleuxre-shear interaction is approximately accounted in the model by modifying the shear relation as a function of the axial force and bending moment. The implementation of this method requires a preprocessing step where a detailed sectional analysis is carried out for different possible combinations of axial force and bending moment. Then the responses are used as a reference value to obtain maximum shear strength for any given axial

force and bending moment.

The reduced shear envelope curve is obtained by adjusting two parameters V_u and γ_{u2} of the shear envelope curve as a function of the given a moment level while keeping the other parameters constant. The max shear strength parameter V_u corresponding to a moment level is obtained by interpolation of moment versus shear strength data. The shear strain γ_{u2} is updated to represent a point on the degrading branch of the primary shear curve. Note that the uniform slope of the descending branch (shown in solid line in Figure 4.6-b) is taken for the ease of implementation and avoid numerical problems. Figure 4.6 shows the shear curves for an RC section with varying bending moment and constant axial force evaluated using coupled sectional analysis and the proposed multi-linear shear curve with flexure-shear interaction. The shear envelopes are able to capture the flexure-shear interaction effect effectively. The proposed model has the advantage that it's simple to implement and it does not requires empirical equations. Instead, it is obtained for a specific RC section using a coupled section model.

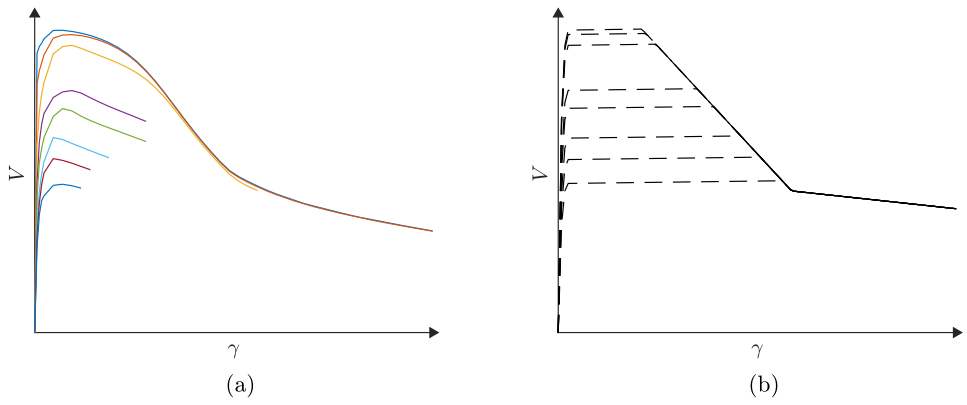

Figure 4.6: (a) Typical shear force-shear strain $V-\gamma$ response for different moment levels, (b) proposed shear force-shear strain relation

4.4 Shear Relation: Hysteresis rules

This section describes the hysteresis rules for the unloading and reloading paths of the shear relation when applied to reversed cyclic loading. These are based on rules proposed by Ozcebe and Saatcioglu (1989) with some modifications for ease of imple-

mentation.Ozcebe and Saatcioglu (1989) proposed a set of rules for the flexure-shear column specimen based on experimental observations. The major limitation of the model is that it doesn't account for the strength decay. A simplified rule is added here to define the hysteresis rules on the softening branch. Further, some of the original rules are simplified for ease of implementation. The unloading and reloading rules are described in the following paragraph and are illustrated in Figure 4.7.

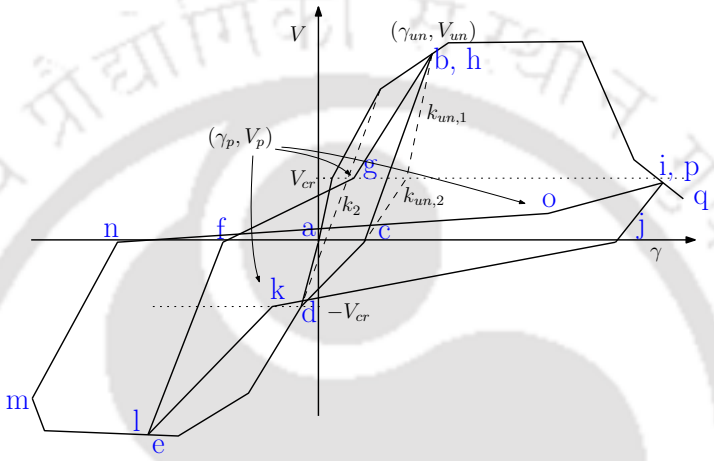

Figure 4.7: Hysteresis rules for shear force-shear strain relation

The point where unloading initiates is denoted as (γ_{un}, V_{un}). The slope of the unloading branch is determined by the location of the unloading point. The rule for the unloading branch is stated as follows:

1. If the cracking point is not exceeded in either direction [$V_{un} < V_{cr}$ and $\gamma_{un} < \gamma_{cr}$], unloading stiffness follows the primary curve

$$k_{un} = G_1$$

2. If the unloading point is between the cracking and yield point, i.e., $V_{cr} < V_{un} < V_y$ and $\gamma_{un} < \gamma_y$, the unloading stiffness is obtained by interpolating k_1 and k_2 where $k_1 = G_1$ and k_2 is the slope of line joining (γ_y, V_y) in one direction and (γ_{cr}, V_{cr}) in other direction, as shown in Figure 4.7.

$$k_{un} = k_1 - \frac{k_1 - k_2}{\gamma_y - \gamma_{cr}} (\gamma_{un} - \gamma_{cr})$$

3. Beyond the yield point, i.e., $V_{un} > V_y$ and $\gamma_{un} > \gamma_y$, the unloading slope is determined using a single unloading slope instead of two slopes defined by Ozcebe and Saatcioglu (1989) (e.g., bc, ef, mn). A similar rule is also adopted by Mergos and Kappos (2008) for ease of implementation.

$$k_{un} = \frac{k_{un1}k_{un2}V_{un}}{(k_{un1} - k_{un2})\,V_{cr} + k_{un2}V_{un}}$$

where k_{un1}, k_{un2} represent slope above and below cracking load defined as in Figure 4.7. These are calculated as per the revised equation proposed in Xu and Zhang (2011).

$$k_{un1} = k_5 \left(1.4exp\left(-0.35\left(\frac{\gamma_{un}}{\gamma_y}\right)^{0.01}\right)\right)\left(1 - 0.02\frac{\gamma_{un}}{\gamma_y}\right)^{3.5}$$

$$k_{un2} = 0.6k_5 \left(1.3exp\left(-0.35\left(\frac{\gamma_{un}}{\gamma_y}\right)^{0.01}\right)\right)\left(1 - 0.02\frac{\gamma_{un}}{\gamma_y}\right)^{5.5}$$

4. If the unloading point on the degrading branch and below the cracking load, i.e., $V_{un} < V_{cr}$ and $\gamma_{un} < \gamma_{u2}$ the unloading slope is defined as (e.g., line joining ij)

$$k_{un} = k_{un2}$$

The reloading branch initiates from the zero force axis and it is given by two slopes to represent the pinching behaviour. The coordinates of pinching point (γ_p, V_p) are defined as fractions of the maximum unloading point in that direction. The rules for the reloading branch are stated as follows:

1. If the cracking load V_{cr} is not exceeded, the initial reloading path aims at the cracking point (e.g., line joining cd).

2. If the cracking load V_{cr} is exceeded, it follows a bilinear curve. The curve passes through the pinching reference point (γ_p, V_p) and then aims at the previous maximum point. The pinching reference point implemented is according to Ding et al. (2016) (e.g., lines fgh, jkl, nop)

$$\gamma_p = \beta_x \gamma_{un}$$

$$V_p = min\left(\beta_y V_{un}, V_{cr}\right)$$

where $\beta_x = 0.4$ and $\beta_y = 0.25$

3. On reaching the previous maximum point the branch follows the envelope curve.

The implementation of section shear relation with hysteresis rules requires tracking the maximum sectional moment achieved in the previous loading. This parameter is used to update the envelope curves in the positive and negative directions and the hysteresis rules are defined between these reduced envelope curves. The proposed shear relation is applied in the section constitutive relation defined in Section 4.2. The implementation of the proposed semi-uncoupled model is presented in the next section.

4.5 Implementation

The implementation follows a similar procedure as provided in Section 3.6. The only difference is in the section analysis steps described in Step 4 of the element state determination procedure. In the section analysis of semi-uncoupled model, the coupling between the normal and shear stresses is neglected. The coupled axial-flexure response is obtained from axial strain and uniaxial stress-strain relationship. These steps are similar to that in the conventional fibre section. The shear force is obtained from a nonlinear shear relation. The detailed procedure to obtain the section resisting force and stiffness of the section is described in the following. A flowchart for the implementation of the semi-uncoupled flexure-shear element is shown in Figure 4.9.

1. The axial strain at a fibre location 'y' is obtained from the section deformation vector as $\epsilon_x = -y\phi + \epsilon_0$.

2. The corresponding axial stress and tangent modulus are estimated from the uniaxial material stress-strain relationship. The concrete compression stress-strain

response is modelled using Mander model (Mander et al., 1988), the concrete tension stress-strain response is modelled using the tension stiffening model of Vecchio and Collins (1986) and the reinforcement steel stress-strain response is modelled using GMP model (Menegotto and Pinto, 1973).

3. The fibre axial stresses are integrated to obtain the axial force and bending moment of the section (see Equation (4.1)).

4. The tangent moduli of the fibres are integrated to obtain the coupled axial-flexure stiffness matrix of the section (see Equation (4.2)).

5. The generalized section shear strain is directly obtained from the section deformation vector.

6. The section moment is used to estimate the reduced shear envelope curve. The shear force corresponding to the shear strain is obtained from the reduced shear envelope curve. A sample input file used for the shear envelope curve is given in Figure 4.8.

7. The shear stiffness obtained from the reduced shear relation is superimposed over the coupled axial-moment stiffness matrix to obtain the required section stiffness matrix of the semi-uncoupled fibre model (Equation (4.2)).

```
Approximate shear primary curve:
G1 (N),       γu1,    γu2,   γr,          Vr (N),  G6/G5
1.08866e+09, 0.007, 0.02, 0.0345859, 396000, 0.25

Variation of Vmax with M (N is considered constant):
N (N),     M (Nmm), Vmax (N)
-9.61e+05,         0, 8.33e+05
-9.61e+05, 8.78e+07,  8.3e+05
-9.61e+05, 1.76e+08, 7.87e+05
-9.61e+05, 2.63e+08, 6.65e+05
-9.61e+05, 2.85e+08, 6.18e+05
-9.61e+05, 3.07e+08, 5.57e+05
-9.61e+05, 3.18e+08,  5.2e+05
-9.61e+05, 3.29e+08, 4.72e+05
-9.61e+05,  3.4e+08, 4.04e+05
```

Figure 4.8: Sample input file for the proposed shear force-shear strain relation

.

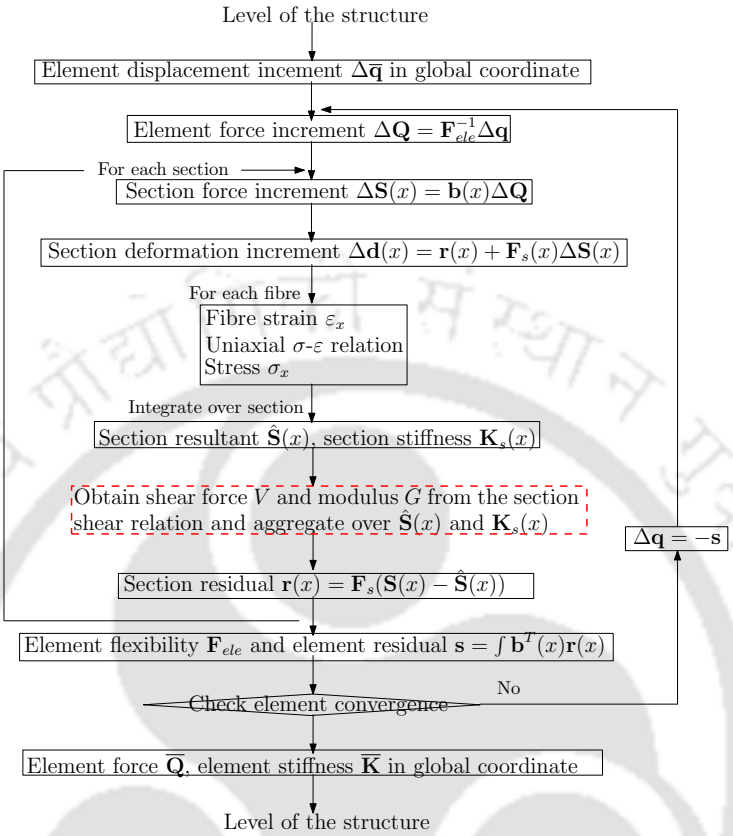

Figure 4.9: Flowchart showing the implementation of the semi-uncoupled flexure-shear fibre element

4.6 Numerical Study

Six experimental studies on the hysteretic response of reinforced concrete column specimens with ultimate failure mode in flexure, shear and flexure-shear modelled and compared to verify the performance of the developed simplified semi-uncoupled flexure-shear element. These columns were tested by other researchers. The geometric and material details of the columns and their experimental response are obtained from the PEER Structural Performance Database (PEER SPD). The element performance was further assessed by comparing the model results with that of the conventional flexure element model and the previously developed coupled flexure-shear fibre element model.

In all simulations, the column cross-section is discretized into 20 concrete layers and a reinforcing steel layer. The uniaxial stress-strain response for concrete in compression

is modelled using the Mander stress-strain relation (Mander et al., 1988). The stress-strain response for the concrete is tension is modelled using the tension stiffening relation of Vecchio and Collins (1986). The cyclic stress-strain behaviour is taken as given in Section 3.4. The uniaxial stress-strain response of the reinforcement is modelled using a bilinear stress-strain relation (Menegotto and Pinto, 1973). The section shear force-shear strain response is modelled using the derived shear relation. The model results are discussed in the following sections.

4.6.1 Flexure critical columns

The two flexure critical column tests selected are specimen A1 (Wehbe et al., 1999), and specimen BG-8 (Saatcioglu and Grira, 1999). These are referred as FC-1 and FC-2 respectively in present work. The columns were modelled axially loaded cantilever under reversed cyclic lateral load with one force-based element with 4 integration points. The geometric and material data of the columns are given in Table 4.1.

Table 4.1: Column geometric and material data for flexure critical columns

Specimen:	FC-1	FC-2
Reference:	A1, Wehbe et al. 1998	BG-8, Saatcioglu and Grira 1999
Test config.	Cantilever	Cantilever
Section dimension $b \times h$ (mm^2)	380×610	350×350
Shear span a (mm)	2335	1645
Axial load P (kN)	615	961
Long. reinf. (mm)	18-ϕ19.1	12-ϕ19.5
Cover (mm)	28	29
Tran. reinf. (mm)	ϕ6	ϕ6.6
Shear leg	4	4
Stirrup spacing (mm)	110	76
Concrete strength f'_c (MPa)	27.2	34
Tran. reinf. yield stress f_{yt} (MPa)	428	580
Long. reinf. yield stress f_{yl} (MPa)	448	455.6

The lateral load-total displacement response of the column FC-1 and FC-2 obtained from the conventional flexural fibre element based Euler-Bernoulli theory and the proposed numerical model along with the experimental result is shown in Figures 4.10

and 4.11, respectively. The columns showed no shear distress during the experiment and the response showed a stable energy dissipation. Both the conventional flexure element and the proposed simplified flexure-shear element response are able to identically capture the experimentally observed behaviour. for FC-2 (Figure 4.11), both the models predicted a little higher peak strength however the overall response is in close agreement with the experimental result. It should be noted that anchorage-slip and buckling of reinforcing bars were observed in the experimental column (Saatcioglu and Grira 1999), whereas in the proposed model no such behaviour was considered. This results in a stiffer initial response for the numerical model than the experimental result.

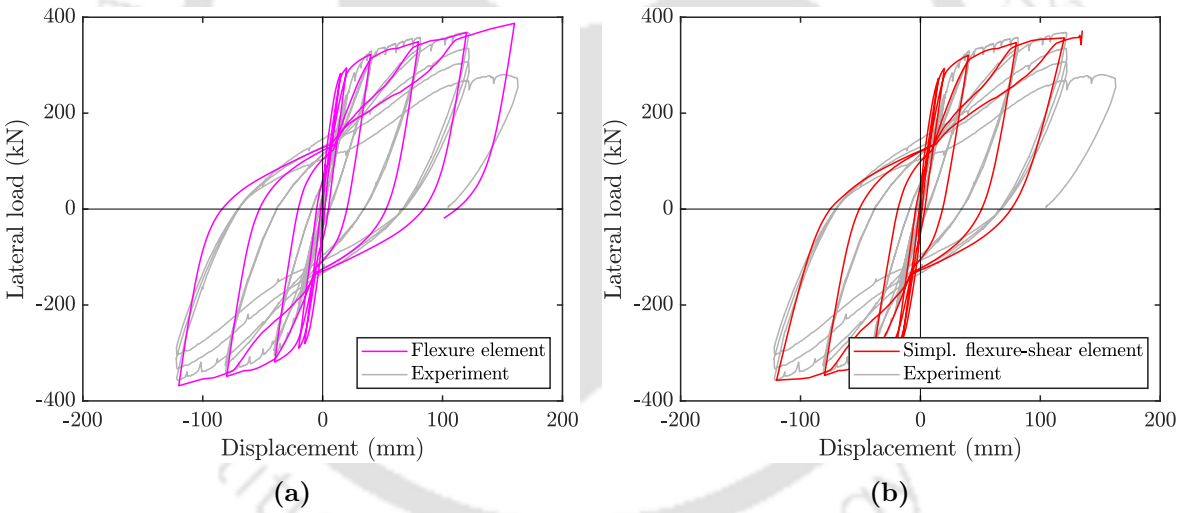

Figure 4.10: Comparison of load-displacement response for Column FC-1: (a) flexure element, (b) semi-uncoupled flexure-shear element

Figure 4.12 compares the lateral force-displacement response obtained from the proposed uncoupled flexure-shear model and coupled flexure-shear model. Both responses are close to each other. For Column FC-1, the unloading stiffness at the later cycles is close to the experimentally observed response for the proposed semi-uncoupled element model (Figure 4.12(a)).

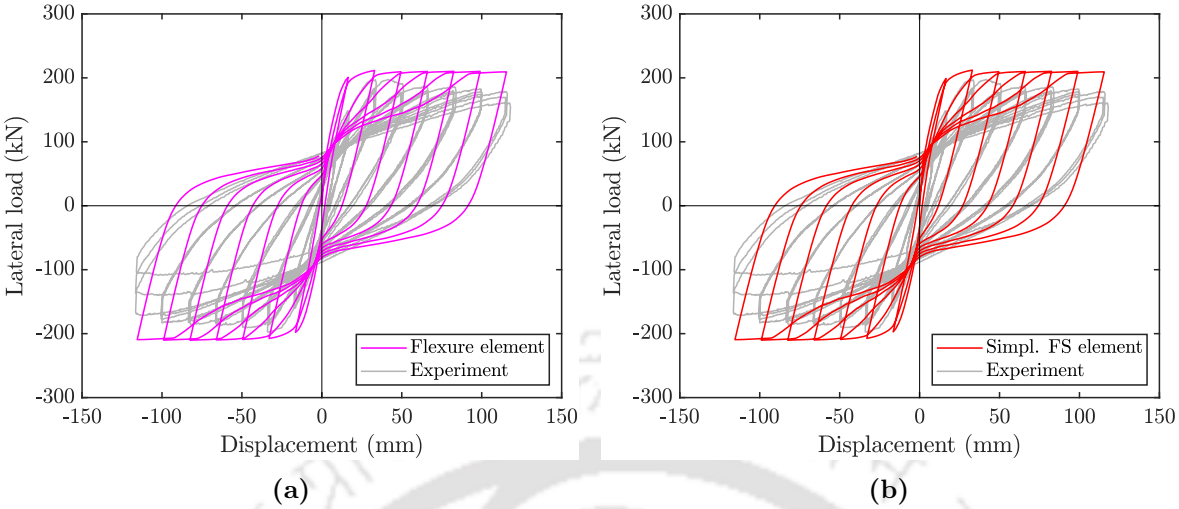

Figure 4.11: Comparison of load-displacement response for Column FC-2: (a) flexure element, (b) semi-uncoupled flexure-shear element

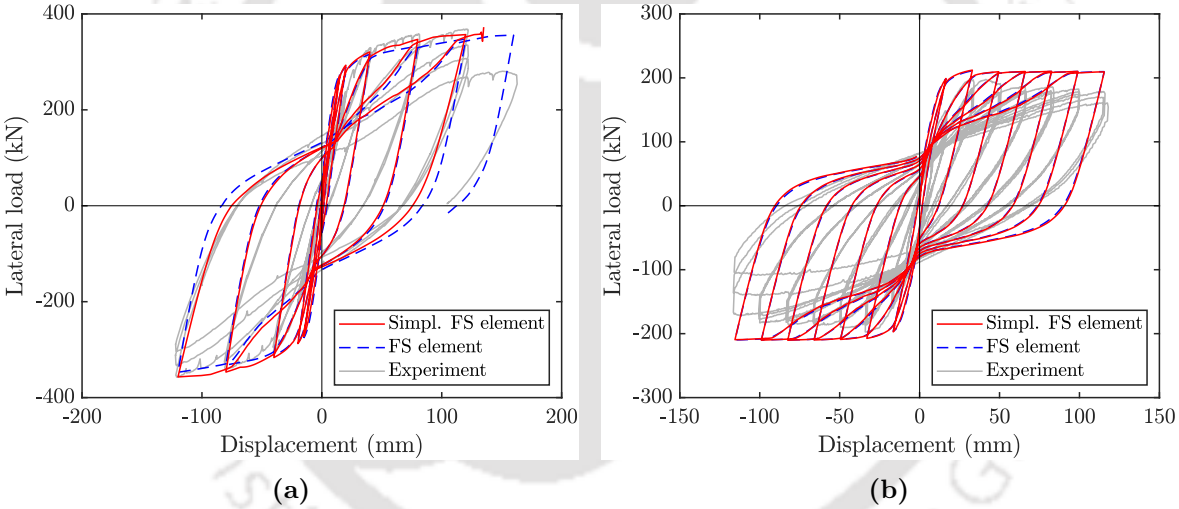

Figure 4.12: Comparison of load-displacement response obtained from coupled element and semi-uncoupled element for flexure critical columns: (a) Column FC-1, (b) Column FC-2

4.6.2 Shear critical columns

The two shear critical specimens selected are specimen No. 1 (Imai and Yamamoto, 1986), and specimen SC3 (Aboutaha et al., 1999). These are referred to as column SC-1 and column SC-2 in the present study. The columns were designed to have an initial shear capacity of less than the moment capacity. The experimental response of both the columns has shown significant shear deformation and failed in shear mode. The column SC-1 was tested in a double cantilever configuration and SC-2 was tested

in a cantilever configuration. However, both the columns were modelled as axially loaded cantilevers under reversed cyclic lateral load with one force-based element with 4 integration points. For SC-1 only half of the column length was modelled as a cantilever here and the numerical response is compared with the equivalent cantilever response obtained from the PEER database. The geometric and material data is given in Table 4.2.

Table 4.2: Column geometric and material data for shear critical columns

Specimen:	SC-1	SC-2
Reference:	1, Imai and Yamamoto 1986	SC3, Aboutaha et al. 1999
Test config.	Double cantilever	Cantilever
Section dimension $b \times h$ (mm^2)	400×500	914.4×457.2
Shear span a (mm)	825	1219.2
Axial load P (kN)	392	0
Long. reinf. (mm)	14-ϕ22	16-ϕ25
Cover (mm)	37	38
Tran. reinf. (mm)	ϕ9	ϕ9.53
Shear leg	2	5 (along b),2 (along h)
Stirrup spacing (mm)	100	406.4
Concrete strength f'_c (MPa)	27.1	21.9
Tran. reinf. yield stress f_{yt} (MPa)	336	400
Long. reinf. yield stress f_{yl} (MPa)	318	434

Figures 4.13 and 4.14 shows the lateral load-total displacement response of the column observed in the experiment and that obtained using the conventional flexure model and proposed simplified flexure-shear element model for SC-1 and SC-2 respectively. It can be seen that the conventional flexure model overestimates the strength, ductility and energy dissipation capacity of both the column whereas the proposed model can predict the peak load and strength degradation point close to the actual response. It shows clearly that the conventional flexure model response is unreliable for such reinforced concrete members. Figure 4.15 compares the lateral force-displacement response obtained from the proposed uncoupled flexure-shear model and coupled flexure-shear model for SC-1 and SC-2. Responses from both developed models are close to each other. The proposed semi-uncoupled element is able to model the shear degradation

and flexure-shear interaction effect.

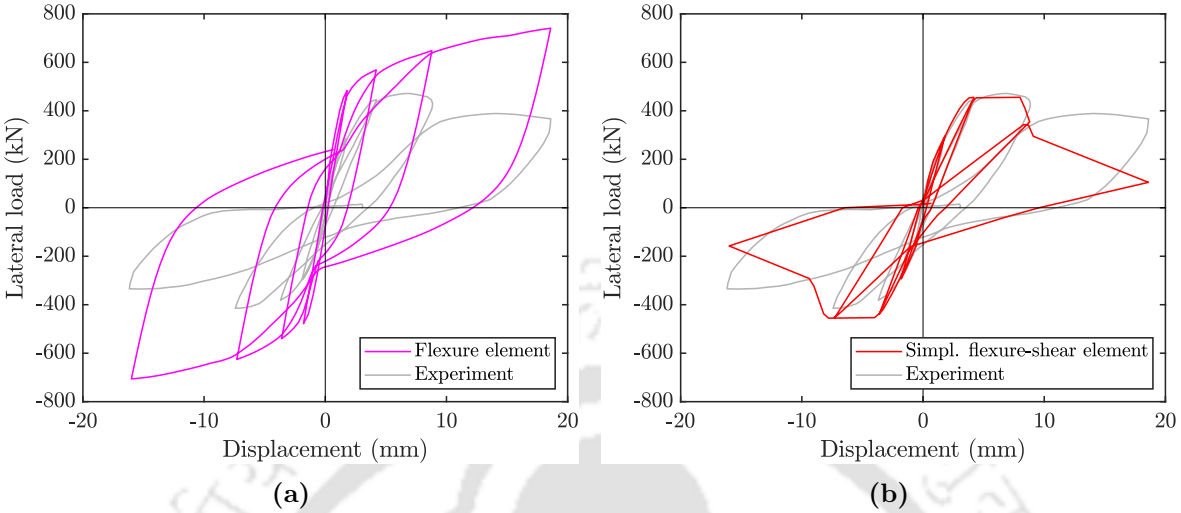

Figure 4.13: Comparison of load-displacement response for Column SC-1: (a) flexure element, (b) semi-uncoupled flexure-shear element

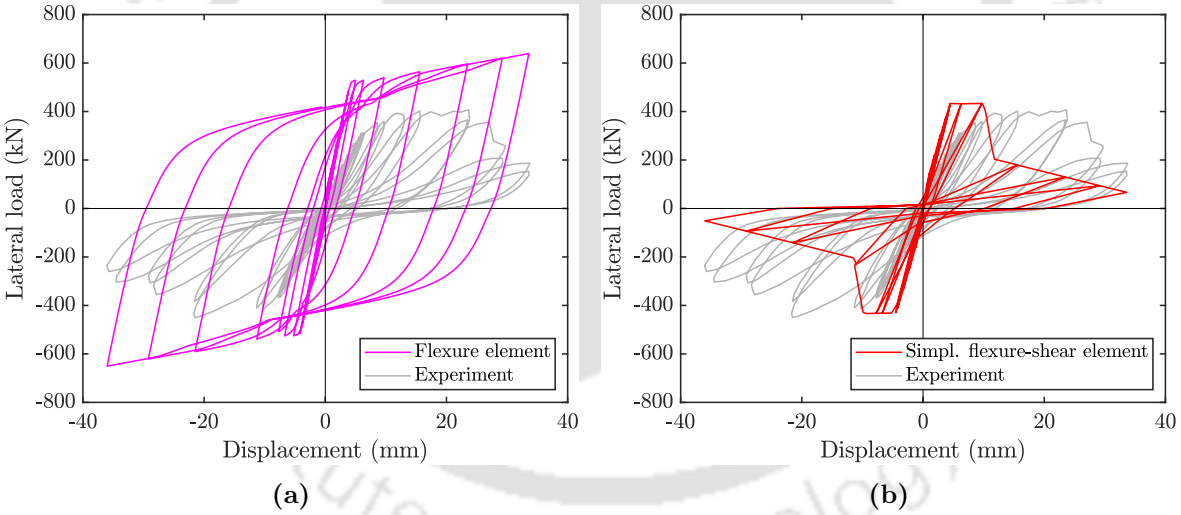

Figure 4.14: Comparison of load-displacement response for Column SC-2: (a) flexure element, (b) semi-uncoupled flexure-shear element

4.6.3 Flexure-shear columns

To further check the performance of the proposed element, two flexure-shear specimens are selected. These are Specimen 4D13RS tested by Ohue et al. (1985), and Specimen No. 17 tested by Ang et al. (1989). These are referred to as FS-1 and FS-2 respectively in present study. Both columns have an initial moment capacity greater than the shear

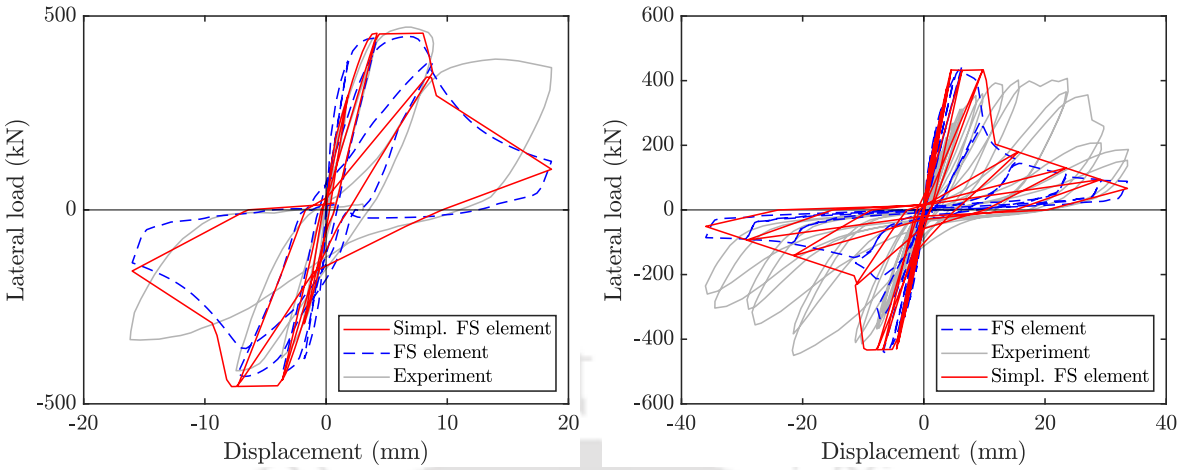

Figure 4.15: Comparison of load-displacement response obtained from coupled element and semi-uncoupled element for shear critical columns: (a) Column SC-1, (b) Column SC-2

capacity however the ultimate failure mode is in shear mode of failure. The columns were tested experimentally in a double curvature configuration and under constant axial load and cyclic lateral loading. The columns are modelled as a cantilever here with a length equal to half the length of the test specimen. The geometric and material data is given in Table 4.3.

Table 4.3: Column geometric and material data for flexure-shear columns

Specimen:	FS-1	FS-2
Reference:	4D13RS, Ohue et al. 1985	17, Ang et al. (1989)
Test config.	Double cantilever	Cantilever
Section dimension $b \times h$ (mm^2)	200×200	400
Shear span a (mm)	400	1000
Axial load P (kN)	183	431
Long. reinf. (mm)	8-ϕ13	20-ϕ16
Cover (mm)	12.5	15
Tran. reinf. (mm)	ϕ5.5	ϕ6
Shear leg	2	spiral
Stirrup spacing (mm)	50	60
Concrete strength f'_c (MPa)	29.9	34.3
Tran. reinf. yield stress f_{yt} (MPa)	316	326
Long. reinf. yield stress f_{yl} (MPa)	370	436

Figures 4.16 and 4.17 shows the lateral load-total displacement plot of the shear

column FS-1 and FS-2 and that obtained using the conventional and the proposed simplified flexure-shear model. The conventional flexure model demonstrates comparable performance to the experimentally observed response in terms of the yield load. However, it fails to capture degradation and predicts a hardening response. It significantly overestimates the strength, initial stiffness, ductility, and energy dissipation capacity of the column. In contrast, the proposed simplified element response closely matches the experimental result effectively capturing the pinching hysteresis loop. The peak load and the strength degradation point are predicted close to the actual response. The proposed model has a flexible initial stiffness, however it is slightly stiffer than the experimentally observed response. This difference might be because the model neglects the anchorage bond slip deformation.

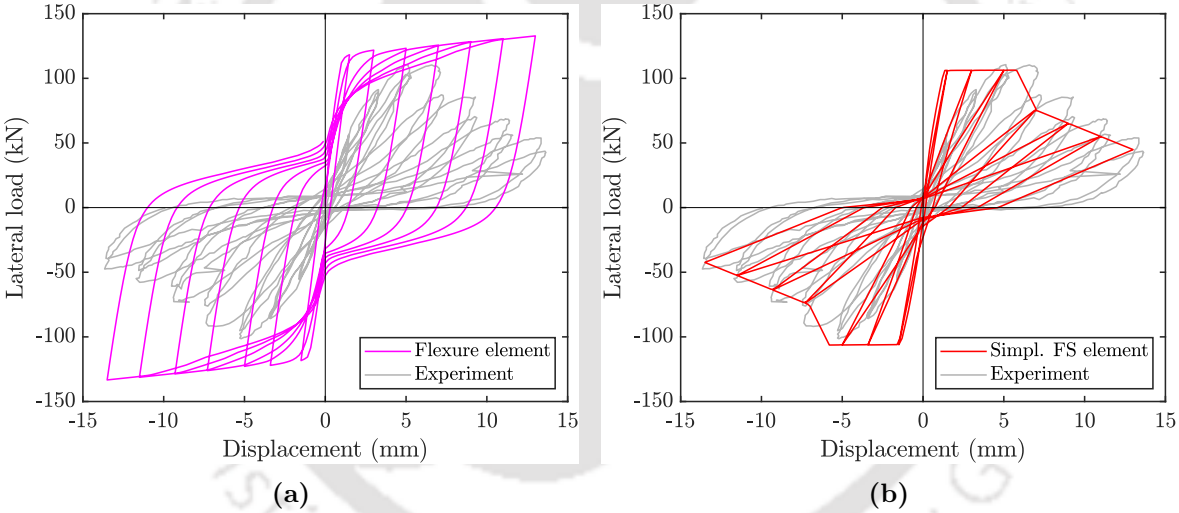

Figure 4.16: Comparison of load-displacement response for Column FS-1: (a) flexure element, (b) semi-uncoupled flexure-shear element

Figure 4.18 shows the comparison of the load-displacement response obtained from both the developed coupled flexure-shear element and the simplified semi-uncoupled flexure-shear element for columns FS-1 and FS-2. It can be seen that in both cases the response of the proposed semi-uncoupled model matches the response of the coupled flexure-shear element. The peak strength and the strength degradation are in agreement with each other. The reloading issue in the coupled flexure-shear element is not present in the proposed semi-uncoupled element. The simplified hysteresis rules of the shear force-shear strain response results in a stiffer unloading branch than the

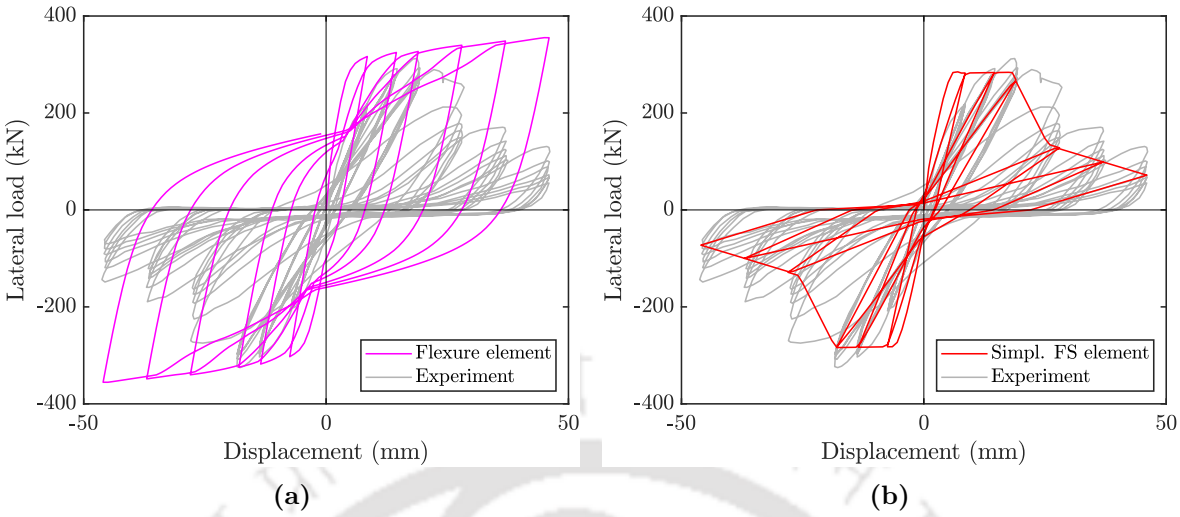

Figure 4.17: Comparison of load-displacement response for Column FS-2: (a) flexure element, (b) semi-uncoupled flexure-shear element

experiment.

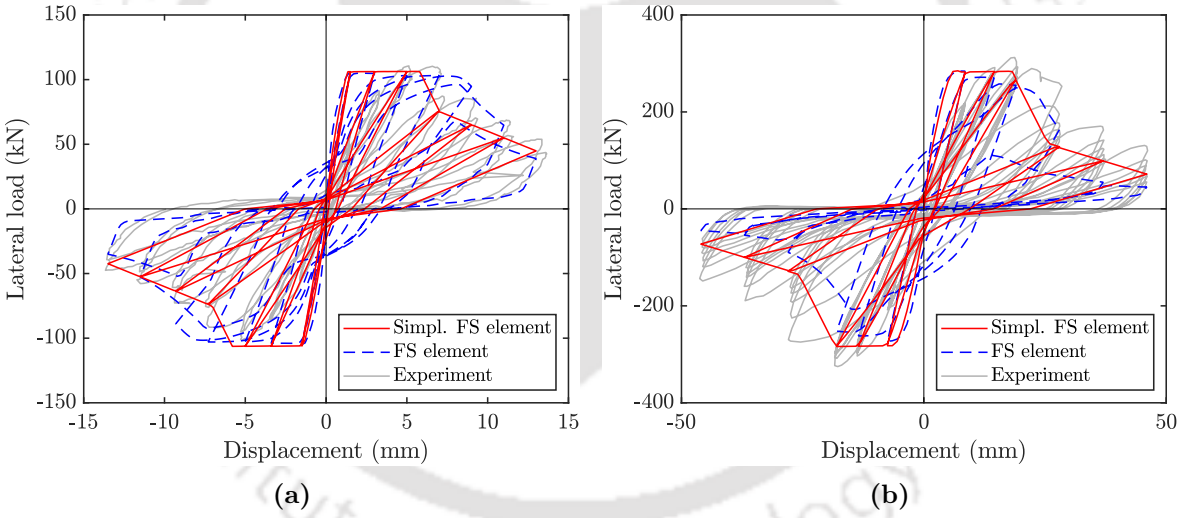

Figure 4.18: Comparison of load-displacement response obtained from coupled element and semi-uncoupled element for flexure-shear columns: (a) Column FS1, (b) Column FS2

The above numerical study indicates the response of the semi-uncoupled element closely resembles that of the coupled element. The efficiency of the developed semi-uncoupled element is evident from the data presented in Table 4.4. The table compares the computation time required by the analysis using the developed axial-flexure-shear coupled element and the developer semi-uncoupled flexure-shear element with that of the conventional flexure element. Note that the developed program can be further optimized to reduce the computation time. It can be observed that the required run

time of the developed semi-uncoupled element is comparable to that of the conventional flexure element.

Table 4.4: Computation efficiency of the developed semi-uncoupled element

	Column	Load steps	Run time (s)		
			Conventional Flexure element	Developed coupled FS element	Developed semi-uncoupled FS element
Flexure critical column	FC-1	1329	284	651	300
	FC-2	1121	222	467	230
Shear critical column	SC-1	316	51	170	59
	SC-2	1310	172	700	191
Flexure-shear column	FS-1	1016	38	309	66
	FS-2	608	103	556	120

* System: Intel i3 processor, CPU max speed 1.70 GHz, RAM 4 GB, Windows 8.1 64-bit OS

4.6.4 Local responses

Figures 4.19 to 4.21 presents some detailed analysis of the results. One column from each category of failure mode is analysed for the moment-curvature response and shear force-shear strain response at the base of the column.

Figure 4.19 shows the analysis of column FC-2. It can be seen from the response of the critical section that the although shear response goes to the nonlinear range it is relatively small and till the end of the analysis, it did not degrade. The global response is dominated by the flexural contribution. Figure 4.20 shows the analysis of Column SC-1, which is reported to fail in a shear critical mode (Imai and Yamamoto, 1986). It can be seen from the response of the critical section that in this case the shear deformation is large and the shear response starts degrading before the moment response. The global response, as shown in Figure 4.13(b), is dominated by the shear contribution. For this type of member, the neglecting shear can lead to large. Similar observation is seen in case of flexure-shear column FS-2 (Figure 4.21). For this case, although the critical section yields before the degradation of the shear response. With further loading, the shear deformation becomes large. The peak global response occurs at the yielding of the section but the later post-peak response is dominated by the shear contribution.

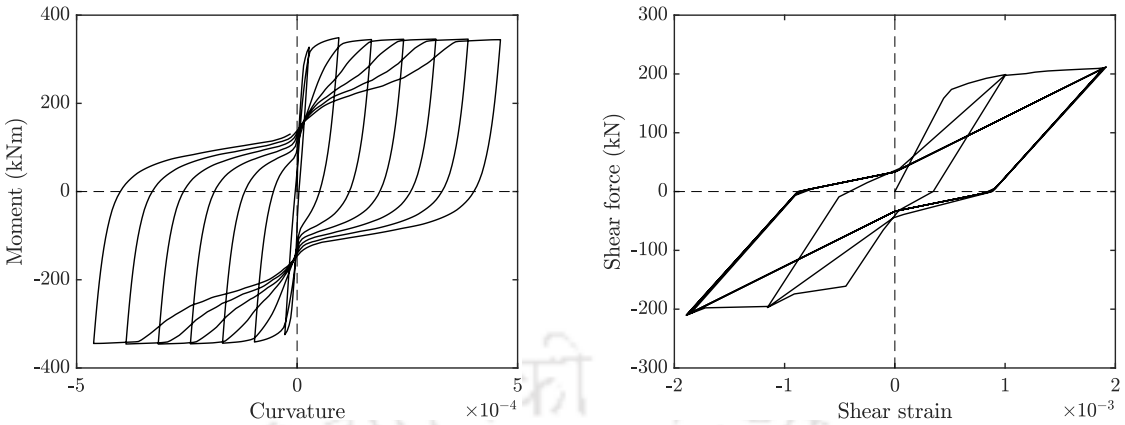

Figure 4.19: Local response of Specimen FC-2: (a) moment-curvature response of end section, (b) shear force-shear strain resposne of end section

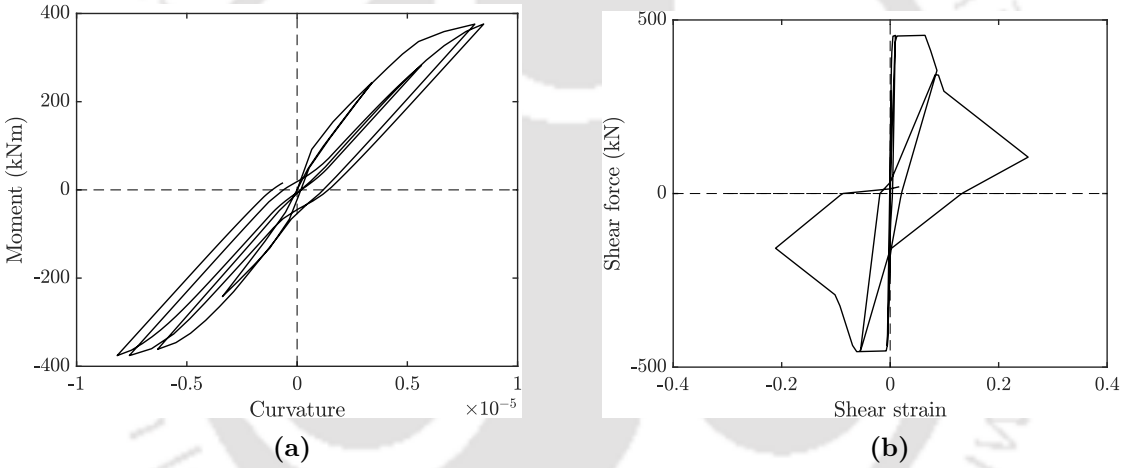

Figure 4.20: Local response of Column SC-1: (a) moment-curvature response of end section, (b) shear force-shear strain response of end section

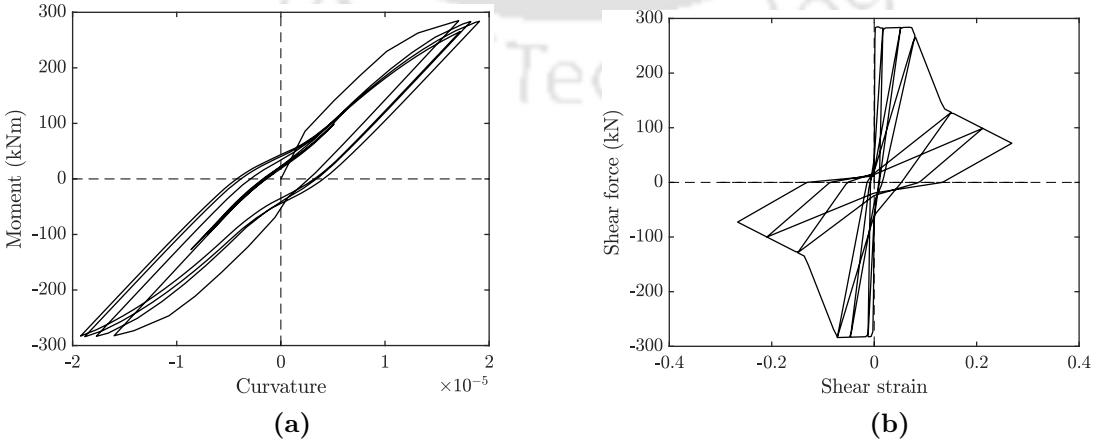

Figure 4.21: Local response of Column FS-2: (a) moment-curvature response of end section, (b) shear force-shear strain response of end section

4.7 Conclusion

In this chapter, a simplified fibre element is proposed which uses an semi-uncoupled approach to incorporate the shear deformation. The shear relation is obtained by fitting a multiaxial relation to the response obtained from the coupled section analysis. A simplified cyclic shear force-shear strain hystertic curve is proposed and implemented in the present study. The performance of the simplified semi-uncoupled flexure-shear element is compared with the previously developed coupled flexure-shear element and conventional element based on the Euler-Bernoulli theory. It is observed that the performance of the proposed semi-uncoupled element is similar to the fully coupled flexure-shear element with comparatively less computation. The proposed element is able to predict the peak strength and shear degradation similar to that of the coupled flexure-shear element.

Chapter 5

Anchorage Slip Element

5.1 Introduction

Anchorage zone in beam-column joints, column-footing and shear wall-beam connection is an area of complex behaviour due to bond slip of rebar together with axial-flexure-shear interaction. The behaviour of reinforced concrete beam or column element is influenced by the interaction of axial, flexural, shear forces, and the slip rotation resulting from bond-slip in the anchorage zone. The element developed in Chapters 3 and 4 effectively accounts for the shear deformation and the flexure-shear interaction effect. However, some of the simulated responses are stiffer compared to the experimental response. It is because of neglecting the joint flexibility and the perfect bond assumption between the concrete and reinforcing steel. In this chapter, the joint flexibility is modelled using a separate link element that can be used in series with the developed elements to account for the anchorage slip of the embedded reinforcement in the anchorage region. The slip element is based on the fibre concept with the fibre properties defined as a stress-deformation rather than a stress-strain relation. Thus, the usual section analysis gives rotation directly instead of curvature.

In the next section, the anchorage slip element is discussed along with the stress-displacement properties of the concrete and steel fibres. It is followed by the examples to study the performance of the proposed element. Finally, the validation examples presented in Chapter 3 and Chapter 4 are reanalysed considering anchorage bond slip

to check the improvement in the prediction.

5.2 Anchorage Slip Element

The rebar slippage in the anchorage region results in rotation at the member-joint interface. In the present study, the slip rotation is modelled with a separate zero-length fibre element. It consists of a single fibre section which gives the moment-rotation behaviour of the anchorage. The element is shown in Figure 5.1 in between Nodes i and j at the end of a beam-column element. The distance between nodes is zero. The translational degree-of-freedom of the nodes is constrained to each other to prevent sliding of the beam-column element under lateral loads.

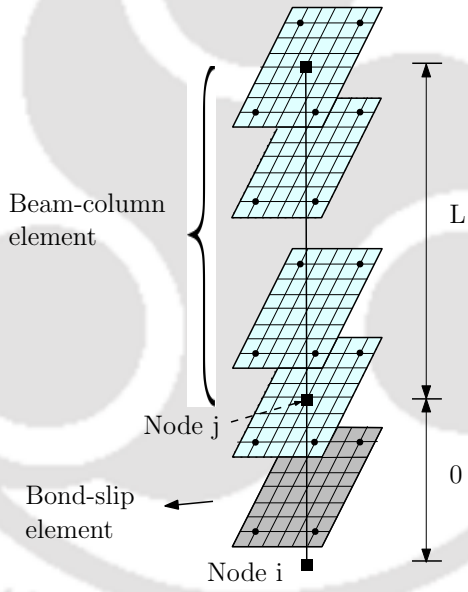

Figure 5.1: Zero-length section element in series with beam-column element

The single fibre section of the zero-length element is assumed to have a unit length such that the element deformations (i.e., elongation and rotation) are equal to the section deformations (i.e., axial strain and curvature). The fibre properties of the zero-length section element are defined as a stress-deformation rather than a stress-strain relation. Thus, the section analysis of the zero-length section element gives the moment-rotation behaviour due to bond slip in the anchorage region. In other words, the rotation of zero-length elements is calculated by performing a standard sectional analysis. However, in the section analysis, the strain terms are replaced with

their corresponding displacement terms and fibre properties defined in terms of stress-displacement relation.

The shear deformation is neglected in the section. The axial displacement in a fibre u_x is obtained from plane section assumption as

$$u_x = -y\theta + u_0 \tag{5.1}$$

where θ is the rotation of the section, u_0 is the axial displacement at the centroid of the section.

With the stress and modulus of the fibres known, the section resisting forces $\hat{\mathbf{S}}$ and the tangent section stiffness matrix $\mathbf{K}_s$ of the section are evaluated by summation of the stress and modulus of fibre over the section by midpoint integration rule as

$$\hat{\mathbf{S}}(x) = \begin{Bmatrix} -\sum_i \sigma_i A_i y_i \\ \sum_i \sigma_i A_i \end{Bmatrix} \tag{5.2}$$

$$\mathbf{K}_s(x) = \begin{bmatrix} \sum_i E_i A_i y_i^2 & -\sum_i E_i A_i y_i \\ -\sum_i E_i A_i y_i & \sum_i E_i A_i \end{bmatrix}. \tag{5.3}$$

where σ_i is the stress and E_i is the material modulus of a fibre 'i' determined from the uniaxial stress-displacement relationship of the fibre material. A_i is the area of the fibre, y_i is the distance of the fibre from the centroid axis. In the present study, the steel fibre properties can be calibrated to the analytically derived stress-slip model. The concrete fibre property is obtained using an 'influence factor' to convert concrete stress strain relation to stress-deformation relation. These are further explained in the subsequent sections.

5.3 Steel Fibre Stress-Displacement Relation

The anchorage bar in concrete under a tensile force for bar slip study involves four field variables namely bond stress μ, bar stress f, bar strain ε and slip S. The basic equations that describe force transfer form a bar to the surrounding concrete through

bond are

1. Equilibrium

$$\frac{\mathrm{d}f}{\mathrm{d}x} = \frac{4\mu}{d_b} \tag{5.4}$$

where d_b is the bar diameter

2. Compatibility

$$\frac{\mathrm{d}S}{\mathrm{d}x} = \varepsilon - \varepsilon_c = \varepsilon \tag{5.5}$$

where ε_c is the strain in concrete. For normal concrete, the magnitude of ε_c is negligible compared to steel strain, as its value is limited by cracking strain. Thus the slip is defined as the relative movement of the reinforcing bar with respect to the face of the beam-column joint.

3. Interface constitutive relation

$$\mu = \mu(S) \tag{5.6}$$

4. Material constitutive relation

$$f = f(\varepsilon) \tag{5.7}$$

The general solution of the above governing equations is obtained by numerical methods such as FEM. However, for the particular assumption of the bond stress distribution compatible with experimental results, the solution of the above equations gets simplified. In the present study, a stepped bond stress distribution is assumed and the rest of the fields are obtained analytically. Given a bond stress distribution, the development length is obtained from the equilibrium Equation (5.4). Then the bar slip is obtained by integrating the bar stain along the development length from Equation (5.5).

5.3.1 Analytical model

The bar stress-slip relation is quantified using an analytical method using a step bond distribution and bilinear stress-strain model of steel. The adopted bond stress distri-

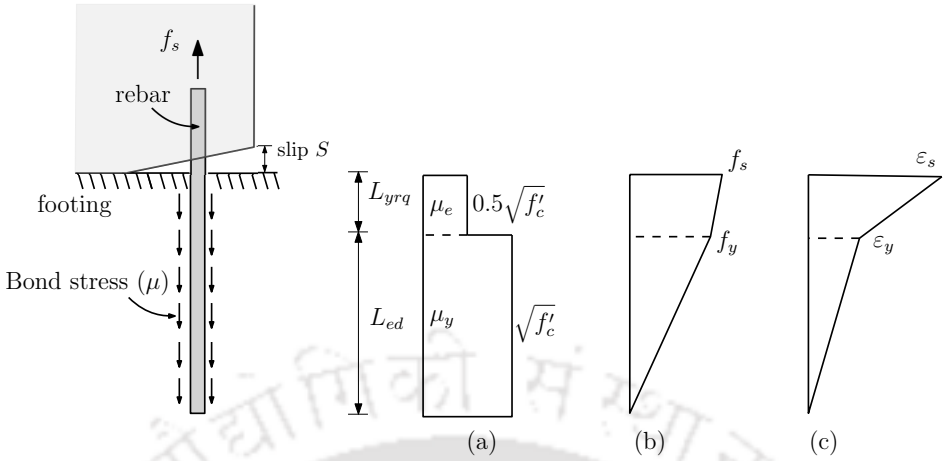

Figure 5.2: Analytical model for rebar slip: (a) assumed bond stress distribution, (b) rebar stress distribution, (c) rebar strain distribution

bution is shown in Figure 5.2(a). It consists of a constant average bond stress (μ_e) along the elastic development length and frictional bond stress (μ_y) over the plastic development length. The value of μ_e and μ_y has been calibrated by Sezen and Setzler (2008) as

$$\mu_e = \sqrt{f'_c}$$

$$\mu_y = 0.5\sqrt{f'_c}$$

where f'_c is the cylindrical compressive strength of concrete. The length of elastic and plastic development regions varies based on the imposed level of stress on the rebar. Assuming embedment length is sufficient ($L_{embd} > L_{drq}$), the required development length L_{drq} can be calculated from equilibrium condition Equation (5.4) as

$$L_{drq} = \begin{cases} L_{erq} = \dfrac{f_s d_b}{4\mu_e}, & \text{for } f_s < f_y \\ L_{ed} = \dfrac{f_y d_b}{4\mu_e}, & \text{for } f_s = f_y \\ L_{ed} + L_{yrq} = \dfrac{f_y d_b}{4\mu_e} + \dfrac{(f_s - f_y)\, d_b}{4\mu_y}, & \text{for } f_s > f_y \end{cases} \tag{5.8}$$

where f_s is the applied stress, f_y is the yield stress of the rebar, L_{erq} is the required elastic development length, L_{ed} is the elastic development length corresponding to stress level of f_y ($L_{erq} <= L_{ed}$) and L_{yrq} is the required plastic development length for

$f_s > f_y$.

Once the required development length is estimated, the slip at the loaded end is computed by integrating the strain distribution over the development length.

$$S = \int_0^{L_d} \varepsilon_s(x)dx \qquad \text{if } L_{embd} > L_{drq} \tag{5.9}$$

Note the above equation is valid when the embedment length is sufficiently long. In the case where the embedment length is insufficient ($L_{embd} < L_{drq}$), the bond stress is developed over the entire embedment length of the bar. The bar gets stressed up to the endpoint and rebar slip occurs at the free end. The total slip at the loaded end is computed as an extension due to strain over the bar plus the free end slip. The expression for the slip in this case is computed as (Alsiwat and Saatcioglu, 1992)

$$S = S_0 + \int_0^{L_d} \varepsilon_s(x)dx \qquad \text{if } L_{embd} < L_{drq} \tag{5.10}$$

where S_0 is the free end slip which is given by Alsiwat and Saatcioglu (1992)

$$S_0 = \left(\frac{30}{f'_c}\right)^{1.75} \left(\frac{f_s d_b}{4L_e(20 - d_b/4)}\right)^{2.5} \tag{5.11}$$

In the study, a linear elastic and linear strain hardening model is used for the steel stress-strain relation to obtain the strain distribution over the embedded bar. The resulting distribution of the steel stress and steel strain over the embedded rebar is schematically shown in Figure 5.2(b,c). The expression of slip for a given stress is given in the following.

Figure 5.3 shows four possible cases of bar strain distribution due to tension at one end of the embedded bar. The slip in each case can be obtained according to the relation between the embedded length L_{embd} and required development length L_{drq}. In this study, the embedment length is defined according to the anchorage condition. The embedment length is considered the actual one for a straight anchored bar, while for a hooked bar the embedded length is considered an equivalent length as $L_{embd} = L^s + 5d_b$ (Filippou et al., 1983; Sezen and Setzler, 2008) where L^s is the straight length of the hooked bar. The explicit expression of slip for four different lengths of embedment

length is given below.

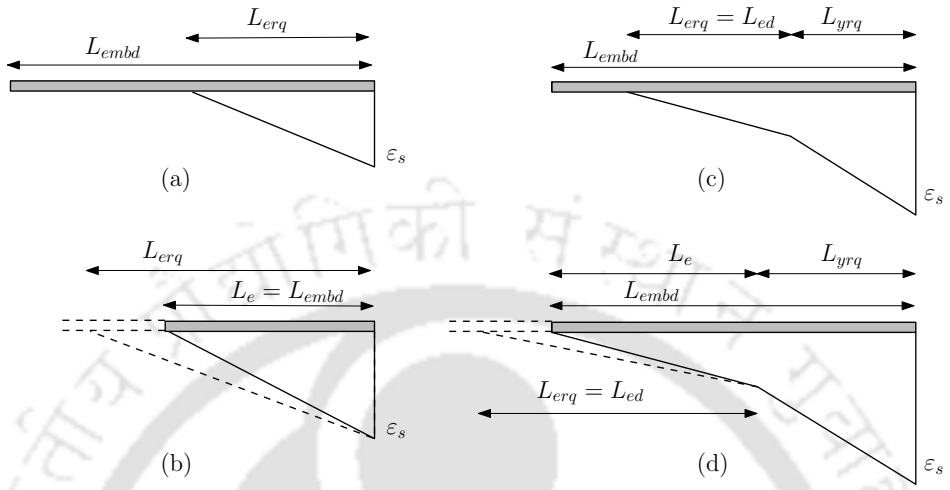

Figure 5.3: Rebar strain distribution for different embedment length: (a) $L_{erq} < L_{embd}$, (b) $L_{erq} > L_{embd}$, (c) $L_{ed} + L_{yrq} < L_{embd}$, (d) $L_{ed} + L_{yrq} > L_{embd}$

Case 1: $f_s < f_y$ and $L_{embd} > L_{erq}$

$$L_d = L_{erq} \tag{5.12}$$

$$S = \frac{\varepsilon_s}{2} L_{erq} \tag{5.13}$$

Case 2: $f_s < f_y$ and $L_{embd} < L_{erq}$

$$L_d = L_{embd} \tag{5.14}$$

$$S = S_0 + \frac{\varepsilon_s}{2} L_e \tag{5.15}$$

where $L_e = L_{embd}$

Case 3: $f_s > f_y$ and $L_{embd} > L_{ed} + L_{yrq}$

$$L_d = L_{ed} + L_{yrq} \tag{5.16}$$

$$S = \frac{\varepsilon_y}{2} L_{ed} + \frac{(\varepsilon_y + \varepsilon_s)}{2} L_{yrq} \tag{5.17}$$

Case 4: $f_s < f_y$ and $L_{embd} < L_{ed} + L_{yrq}$

$$L_d = L_{embd} \tag{5.18}$$

$$S = S_0 + \frac{\varepsilon_y}{2} L_e + \frac{(\varepsilon_y + \varepsilon_s)}{2} L_{ydb} \tag{5.19}$$

where $$L_e = L_{embd} - L_{ydb}$$

To verify the analytical stress-slip model, some of the pull-out tests of reinforcement bars tested by Ueda et al. (1986) are modelled. The required data are obtained from Ueda et al. (1986). Figure 5.4 shows the comparison of the analytically derived stress-slip model with the reported experimental data. The overall agreement of the analytical model implies the reliability of the model.

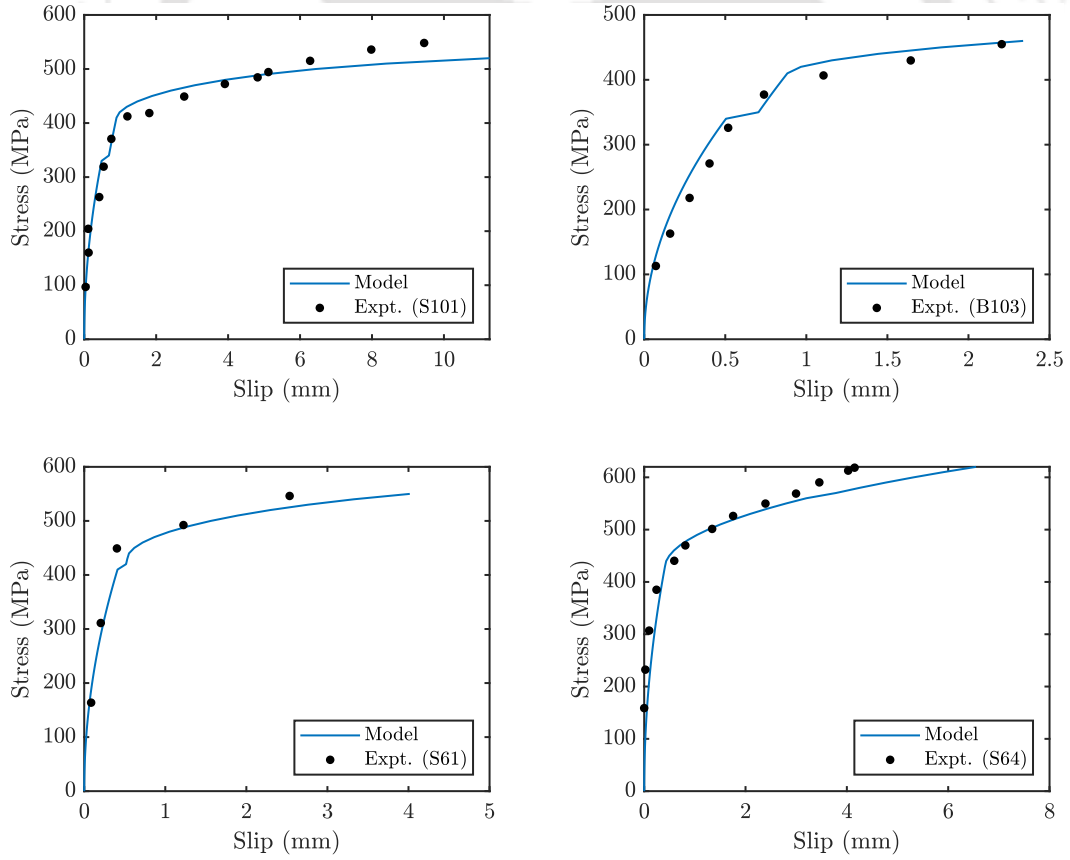

Figure 5.4: Comparison of the analytical stress–slip model with experimental tests by Ueda et al. (1986)

5.3.2 Idealised Steel Stress-Slip Model

Figure 5.5 shows three models to idealise stress-slip response. These are (i) linear elastic-exponential hardening, (ii) bilinear and (iii) trilinear. The analytical stress-slip response is obtained by varying the steel stress to the ultimate steel stress. The initial elastic branch of the three idealise curve are taken as the line joining the yield point of the steel. The hardening part is modeled as a single line joint yield point to the ultimate point in the bilinear model. For trilinear model it is modelled by a bilinear line. and for the exponential model it is modelled using the empirical relation proposed by Zhao and Sritharan (2007). It is observed that the exponential and trilinear forms fit better the typical stress-slip response of a rebar, whereas the use of the bilinear form tends to provide an increased slip in the hardening range. In the present study, a modified bilinear model is proposed as shown in Figure 5.5. This is obtained from the trilinear model by extrapolating the elastic and the strain hardening branch. This leads to slightly higher yield stress. The proposed modified bilinear model is able to provide a reasonable slip in the hardening range.

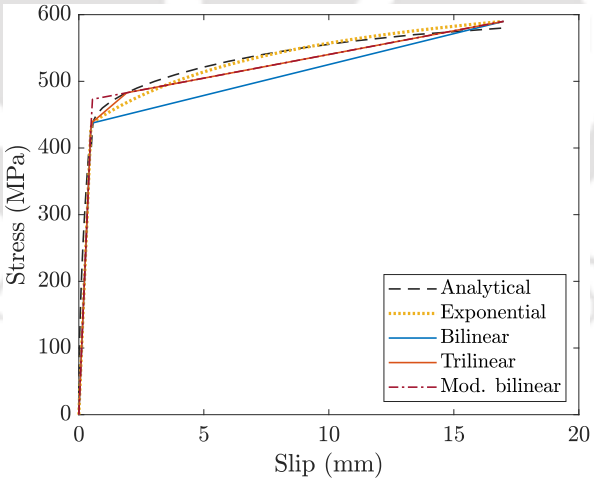

Figure 5.5: Calibrated steel stress-slip models

5.4 Concrete Fibre Stress-Displacement Relation

In literature, different researchers have used different methods to obtain the stress-displacement properties of the concrete fibre of the slip element. Ghannoum (2007)

used a common factor to convert the stress-strain relation to the stress-displacement relation of concrete and steel fibre by multiplying the strain axis with the factor. Sightly different approaches were given by Berry (2006) and Zhao and Sritharan (2007). Zhao and Sritharan (2007) kept the material properties of concrete fibres the same as those in the adjacent element except the residual stress at large strains is taken as $0.8f'_c$. Berry (2006) modified the concrete stress-strain relation to a stress-displacement relation by integrating the material properties over an 'effective' depth in the anchorage zone. The optimal depth was determined empirically to be half of the depth of the compression zone in the section.

In the present study, the material properties of concrete fibres are determined according to Berry (2006). The concrete stress-displacement relationship of the concrete was calculated from the stress-strain relationship by assuming an effective depth over which the compressive strains act (d_{comp}), and multiplying the strains by this assumed depth to obtain a displacement. The response of zero-length elements is affected by the choice of fibre properties. A parametric study on the effect of influence length on the response of the zero-length element is given in Figure 5.6. Three different influence lengths with lengths equal to $0.5H$, H and $1.5H$ are considered, where H is the height of the section. It is observed that an increase in influence length leads to a softer moment-rotation response.

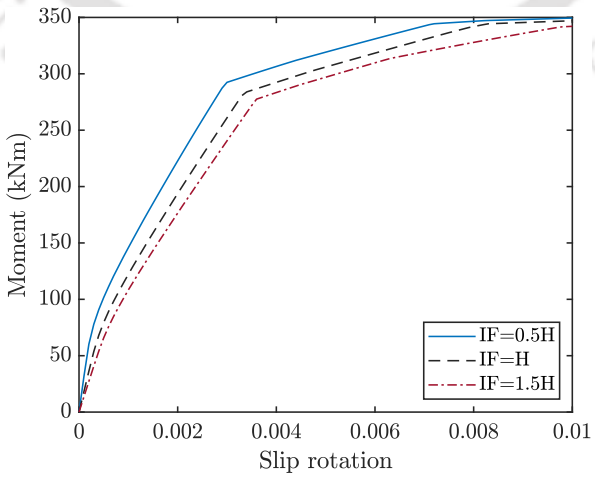

Figure 5.6: Effect of influence length for the concrete on moment-rotation response

5.5 Implementation

A zero-length section element is implemented together with a fibre beam element to model the anchorage bond-slip. A duplicate node is added to incorporate a zero-length section element in the beam-column model (see Figure 5.1, the distance between Node i and j is zero). The translational degree-of-freedom of the nodes are constrained to each other to prevent sliding of the beam-column element at Node j in Figure 5.1 under lateral loads because the shear resistance is not included in the zero-length section (Zhao and Sritharan 2007). The standard solution algorithm for nonlinear structural analysis yields nodal displacements for the zero-length anchorage slip element. For a given structural nodal displacement increment, the element state determination procedure is described in the following steps. A flowchart showing the implementation of the zero-length element is given in Figure 5.7.

1. With the nodal displacement known from the structural analysis, usual transformation is applied to obtain the nodal displacement in the local coordinates. The orientation of the element is taken similar to that of the adjacent beam-column element.

2. The required section displacements (axial displacement u_0 and rotation θ) are obtained from the nodal displacements in local coordinates using transformation matrix. Note shear resistance is not included in the element.

$$\begin{Bmatrix} u_0 \\ \theta \end{Bmatrix} = \begin{bmatrix} -1 & 0 & 0 & 1 & 0 & 0 \\ 0 & 0 & -1 & 0 & 0 & 1 \end{bmatrix} \begin{Bmatrix} \overline{q}_1 \\ \vdots \\ \overline{q}_6 \end{Bmatrix} \tag{5.20}$$

3. The axial displacement of a fibre is obtained using plane section assumption as in Equation (5.1).

4. The fibre stress and tangent modulus are obtained from the stress-displacement relation of the fibre material. For reinforcement fibre, the idealized stress-displacement

relation as described in Section 5.2 is used. The model gives the stress and modulus directly.

For concrete fibre, the stress-strain model similar to that of the adjacent beam-column element is used. An influence factor of $L_i = 0.5H$ is used to convert the fibre axial displacement to strain.

$$\varepsilon_x = \frac{u_x}{L_i}$$

The material modulus is similarly obtained as

$$E = \frac{E}{L_i}$$

5. section resisting forces and the tangent section stiffness matrix of the section is evaluated by summation of the stress and modulus of fibre over the section as given in Equation (5.2) and (5.3)

6. Once the section force and section stiffness are evaluated. The inverse transformation is performed to obtain the element resisting force and the element stiffness matrix.

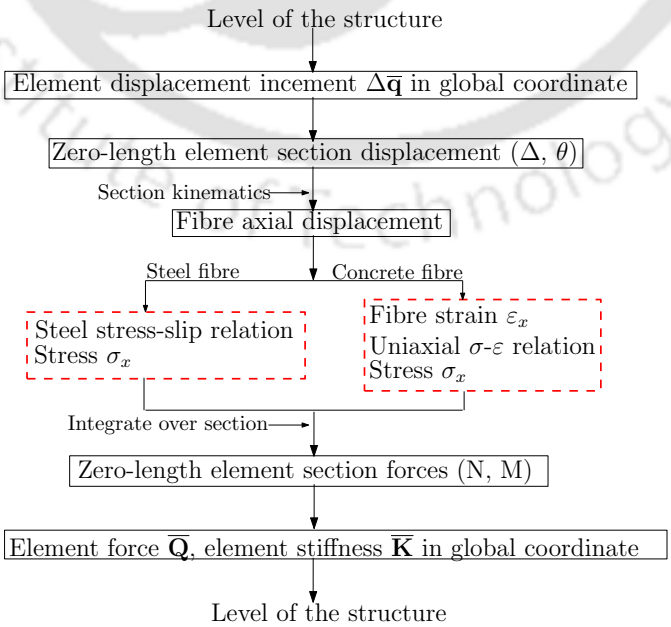

Figure 5.7: Flowchart showing the implementation of the zero-length slip element

5.6 Numerical Study

The combined modelling framework using a shear-flexible element and zero-length slip element is verified here. Two RC columns tested under constant axial load and lateral cyclic loading from literature and an RC column experiment on a shake table are simulated. To further demonstrate the advantage of the combined modelling framework the columns are also analysed with alternate modelling approaches using (i) only shear-flexible element without slip element and (ii) conventional element based on Euler-Bernoulli beam theory that neglect both shear and bond-slip deformation. The necessary column details were obtained from the DEEDs datacenter hub. ref

The columns are modelled using a single force-based fibre beam element. Fibre section along the element length is defined according to the 4-point Gauss-Lobatto integration. For cases where The slip rotation due to anchorage bar slip is considered, a zero-length fibre element is used at the column-footing interface. All fibre sections are uniformly discretized into 20 concrete layers and 'n' reinforcing fibres which are located as per the section detailing. The concrete and steel fibre material properties are selected according to the type of the element. For the shear-flexible element, the concrete material behaviour is obtained from a rotating smeared crack model, with equivalent uniaxial stress-strain relation in the principal directions (Section 3.4). The concrete compression stress-strain relation is calculated according to the Mander model (Mander et al., 1988). The concrete tensile strength is assumed as 10% of the concrete peak compressive strength. The concrete tensile stress-strain relation is calculated using the tensile stiffening relation given in reference (Vecchio and Collins, 1986). The steel material behaviour is obtained using a uniaxial bilinear stress-strain model. For zero-length fibre elements, the Mander stress-strain model along with an influence length of $0.5H$ is used to obtain the concrete material stress-displacement relation. The steel material stress-slip relations are obtained from the modified bilinear model envelope calibrated to the analytically derived rebar stress-slip response. For conventional beam elements based on the Euler-Bernoulli beam theory, the concrete and steel material behaviour is obtained from the Mander model and the bilinear stress-strain model, respectively.

5.6.1 Saatcioglu column

The first example considered is the column specimen U6, tested under lateral cyclic load by Saatcioglu et al. (1992). The column was 1000 mm long and subjected to a constant axial load of 600 kN. The column section had a dimension of 350 mm × 350 mm. It was reinforced with 8 longitudinal 25 mm diameter bars with a yield stress of 437 MPa. The column reinforcement was extended 450 mm into the footing with a 90-degree bent. The transverse reinforcement is composed of 6.4 mm diameter double-layer steel stirrups with ties. The stirrups were spaced 65 mm from centre to centre. The transverse steel had a yield stress of 425 MPa. The specified concrete compressive strength was 37.3 MPa.

Table 5.1: Column geometric and material data for Saatcioglu et al. (1992) column

Specimen:	U6, Saatcioglu et al. (1992)
Test config.	Cantilever
Section dimension $b \times h$ (mm^2)	350×350
Shear span a (mm)	1000
Axial load P (kN)	600
Long. reinf. (mm)	8-ϕ25
Cover (mm)	26
Anchorage type	90 degree hook
Straight embedment length (mm)	450
Tran. reinf. (mm)	ϕ6.4
Shear leg	6
Stirrup spacing (mm)	65
Concrete strength f'_c (MPa)	37.3
Tran. reinf. yield stress f_{yt} (MPa)	425
Long. reinf. yield stress f_{yl} (MPa)	437

The column is analysed using a load-controlled incremental-iterative procedure to analyse the constant axial load, followed by a displacement-controlled incremental-iterative procedure to analyse the cyclic lateral load. The analysis results are shown

in Figures 5.8 and 5.9.

The importance of modelling bond-slip deformation is established in Figure 5.8. The considered modelling approach is able to predict the global deformation response close to the experimental response. The initial stiffness and the unloading are in better agreement. The reloading slope is slightly more pinching effect predicted by the model than what is reported in the experiment. Nonetheless, the prediction of the combined approach is comparatively better than the other modelling options. The other modelling option using the conventional flexure element and shear-flexure element without slip is found to provide a stiffer response and overpredict the initial stiffness and strength of the column.

Figure 5.9 shows the ratio of the different displacement components to the total displacement from the combined modelling approach and the experiment (Saatcioglu et al., 1992). It can be observed that the column shear displacement is comparatively less compared to the flexure and slip displacement. This is reliably captured by the combined modelling method with a shear-flexible element and zero-length slip element.

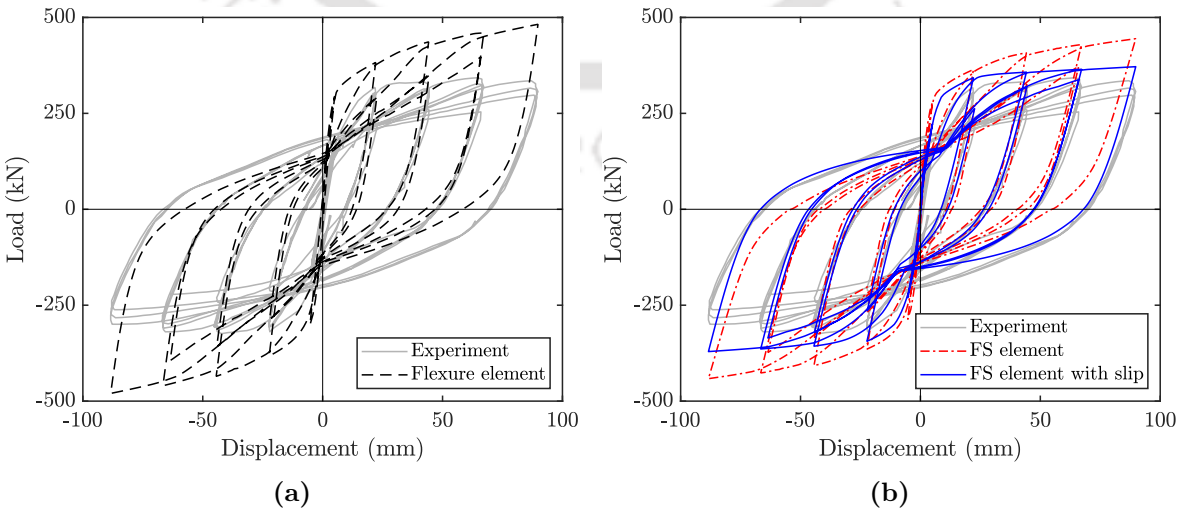

Figure 5.8: Comparison of load-displacement response for Saatcioglu et al. (1992) column: (a) Flexure element, (b) Coupled flexure-shear element with slip element

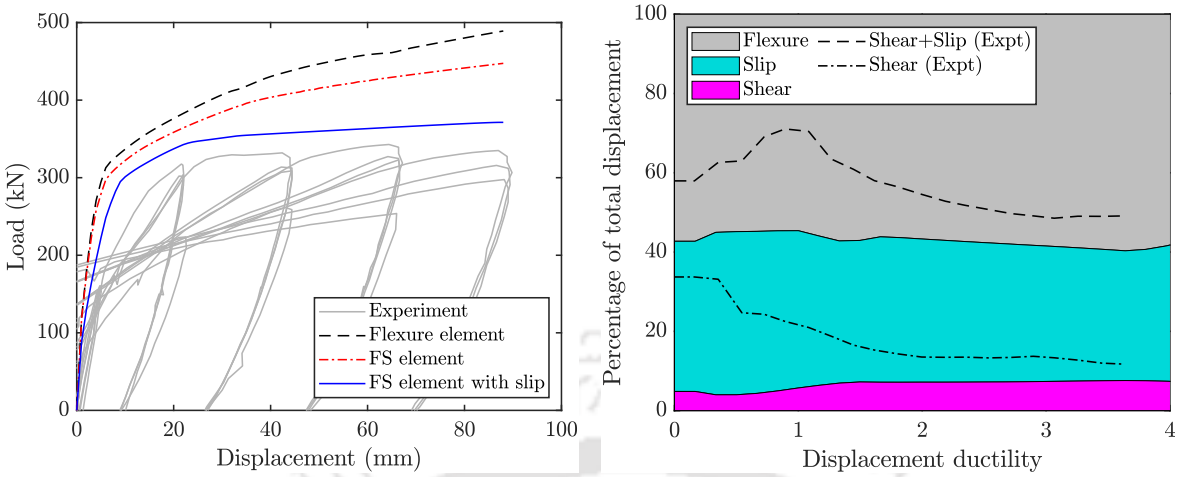

Figure 5.9: (a) Comparison of monotonic envelope curves, (b) Comparison of predicted displacement contribution with the reported data (Saatcioglu et al., 1992)

Figure 5.10 compares the effect of incorporating the anchorage slip element on the moment-curvature behaviour of the beam-column element. It shows that anchorage slip significantly affects the local response of the element. When anchorage slip is considered in the analysis, the curvature demand at the end section of the beam-column element is reduced compared to an analysis that neglects it. This observation is similar to Zhao and Sritharan (2007), which indicates that excluding anchorage slip leads to an overestimation of the local response in the plastic hinge zone.

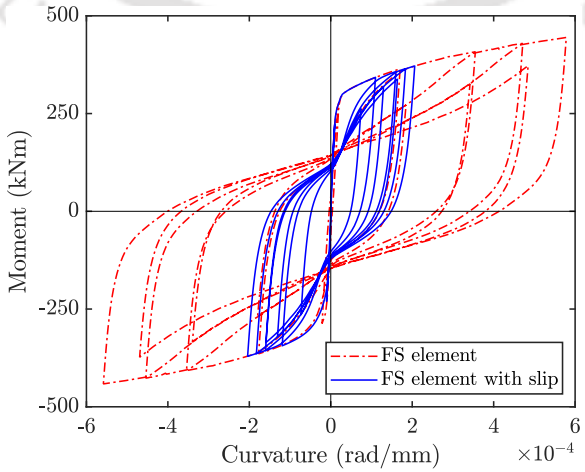

Figure 5.10: Effect of anchorage slip on the moment-curvature behaviour for Saatcioglu column

5.6.2 Lehman column

The second example considered is column specimen 415, tested under constant axial load and lateral cyclic load by Lehman and Moehle (2000). The column was 2438 mm long and subjected to a constant axial load of 653.86 kN. The column section had a diameter of 609.6 mm. It was reinforced with 22 longitudinal bars of 15.9 mm diameter with a yield stress of 462 MPa. The column reinforcement was extended 546 mm into the footing with a 90-degree bent. The transverse reinforcement is composed of a 6.4 mm diameter spiral with a spacing of 31.8 mm. The transverse steel had a yield stress of 606.8 MPa. The specified concrete compressive strength was 31 MPa.

Table 5.2: Column geometric and material data for Lehman and Moehle (2000) column

Specimen:	415, Lehman et al., 1997
Test config.	Cantilever
Section diameter (mm)	609.6
Shear span a (mm)	2438.4
Axial load P (kN)	653.86
Long. reinf. (mm)	22-ϕ15.9
Cover (mm)	19
Anchorage type	90 degree hook
Straight embedment length (mm)	546
Tran. reinf. (mm)	ϕ6.4 spiral
Stirrup spacing (mm)	31.8
Concrete strength f'_c (MPa)	31
Tran. reinf. yield stress f_{yt} (MPa)	606.8
Long. reinf. yield stress f_{yl} (MPa)	462

The column is analysed using a load-controlled incremental-iterative procedure to analyse the constant axial load, followed by a displacement-controlled incremental-iterative procedure to analyse the cyclic lateral load. The analysis results are shown in Figures 5.11 and 5.12. In this case also, the considered modelling approach is able

to capture the predict the global deformation response close to the experimental response. The initial stiffness is in better agreement although the strength is slightly underpredicted. The other modelling option using a conventional Euler-Bernoulli element or shear-flexible element without slip gives a stiffer response and overpredicts the strength of the column (Figure 5.11). From the comparison of the ratio of the different displacement components to the total displacement (Figure 5.12), it is found that the column shear displacement is comparatively less compared to the other components. This is correctly captured by the model.

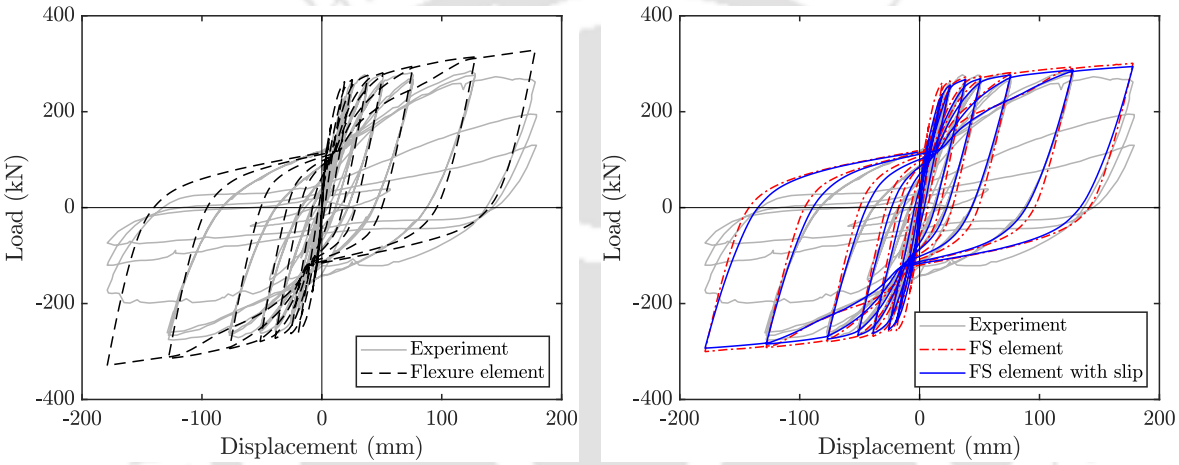

Figure 5.11: Comparison of load-displacement response for Lehman and Moehle (2000) column: (a) Flexure element, (b) Coupled flexure-shear element with slip element

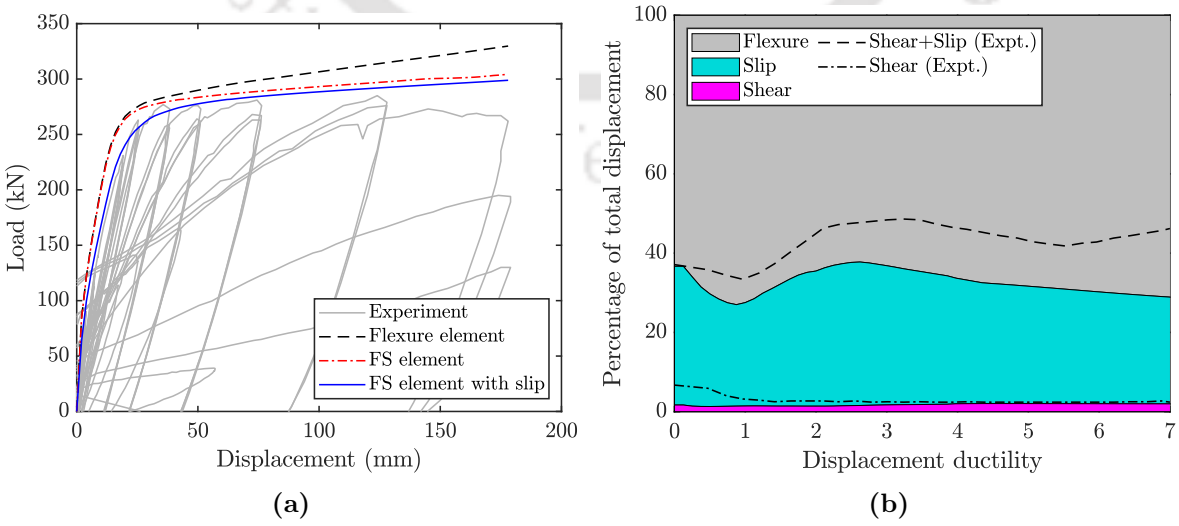

Figure 5.12: (a) Comparison of monotonic envelope curves, (b) Comparison of predicted displacement contribution with the reported data (Lehman and Moehle, 2000)

Figure 5.13 shows the effect of the anchorage slip on the moment-curvature response at the end section of the beam-column element which is indicative of damage in the plastic hinge region. The analysis with anchorage slip results in a lower curvature demand compared to the analysis that excludes it. This observation is similar to Zhao and Sritharan (2007) and highlights the importance of accounting for anchorage slip in the analysis of reinforced concrete members.

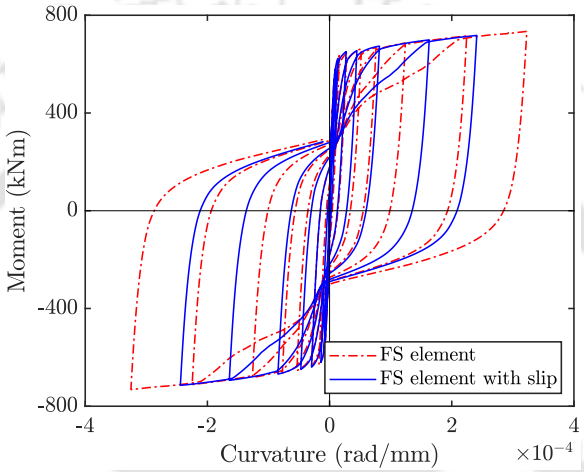

Figure 5.13: Effect of anchorage slip on the moment-curvature behaviour for Lehman column

5.6.3 Analysis of RC columns

After validating the anchorage slip element, it is used to reanalyse the column specimen considered in Chapter 3 and Chapter 4 to check the improvement. The six experimental studies considered are specimen A1 (Wehbe et al., 1999), specimen BG-8 (Saatcioglu and Grira, 1999), specimen 1 (Imai and Yamamoto, 1986), specimen SC3 (Aboutaha et al., 1999), specimen 4D13RS (Ohue et al., 1985), and specimen 17 (Ang et al., 1989). The first two columns were reported to fail in flexure mode, while the following columns failed in shear and flexure-shear modes, respectively. In this study, they are referred to as FC-1, FC-2, SC-1, SC-2, FS-1, and FS-2.

The geometric and material details of the columns and their experimental response are obtained from the PEER Structural Performance Database (PEER SPD) and the reference literature. The columns are modelled using a single force-based fibre beam element. Fibre section along the element length defined according to the 4-point Gauss-

Lobatto integration. The slip rotation due to anchorage bar slip is considered using a zero-length fibre element at the column-footing interface. Due to lack of data, sufficient development length is considered for all the columns. All fibre sections are uniformly discretized into 20 concrete layers and 'n' reinforcing fibres which are located as per the section detailing. The concrete and steel fibre material properties are selected according to the type of the element. For the shear-flexible element the concrete material behaviour is obtained from rotating smeared crack model, with equivalent uniaxial stress-strain relation in the principal directions Section 3.4. The concrete compression stress-strain relation is calculated according to Mander model (Mander et al., 1988). The concrete tensile strength is assumed as 10% of the concrete peak compressive strength. The concrete tensile stress-strain relation is calculated using tensile stiffening relation given in reference Vecchio and Collins (1986). The steel material behaviour is obtained using uniaxial bilinear stress-strain model. For zero-length fibre element the Mander stress-strain model along with an influence length of 0.5H is used to obtain the concrete material stress-displacement relation. The steel material stress-slip relations is obtained from the modified bilinear envelope calibrated to the analytically derived rebar stress-slip response.

The column is analysed using a load-controlled incremental-iterative procedure to analyse the constant axial load, followed by a displacement-controlled incremental-iterative procedure to analyse the cyclic lateral load. The predicted load-displacement responses are shown in Figures 5.14 and 5.15 for the coupled element with anchorage slip and semi-uncoupled element with anchorage slip. It is observed that with the consideration of the anchorage bond slip, the predicted global deformation responses are closer to the experimental response. The initial stiffness and the unloading are slightly in better agreement.

.

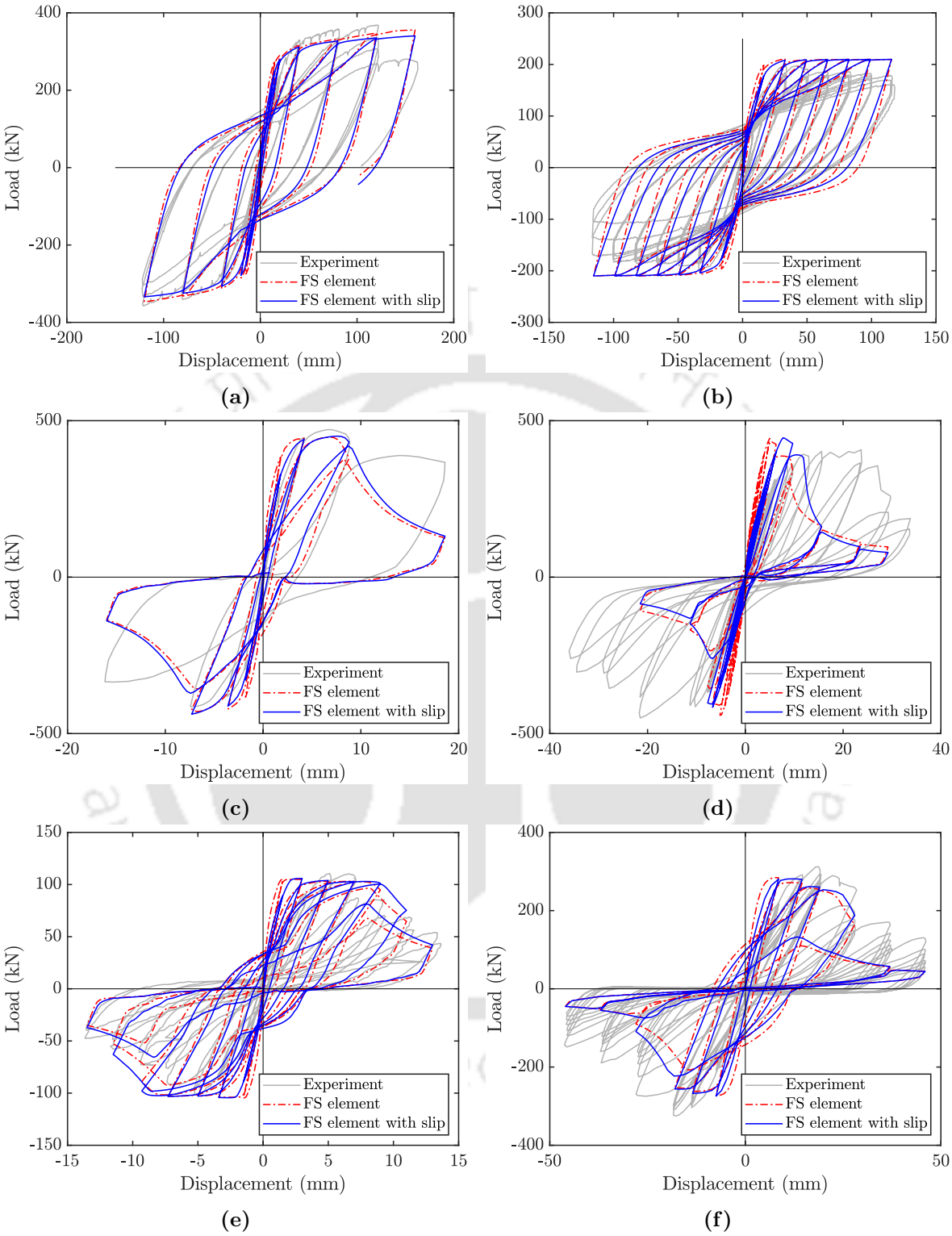

Figure 5.14: Load-displacement response using coupled flexure-shear element with anchorage slip: (a) Column FC-1, (b) Column FC-2, (c) Column SC-1, (d) Column SC-2, (e) Column FS-1, (f) Column FS-2

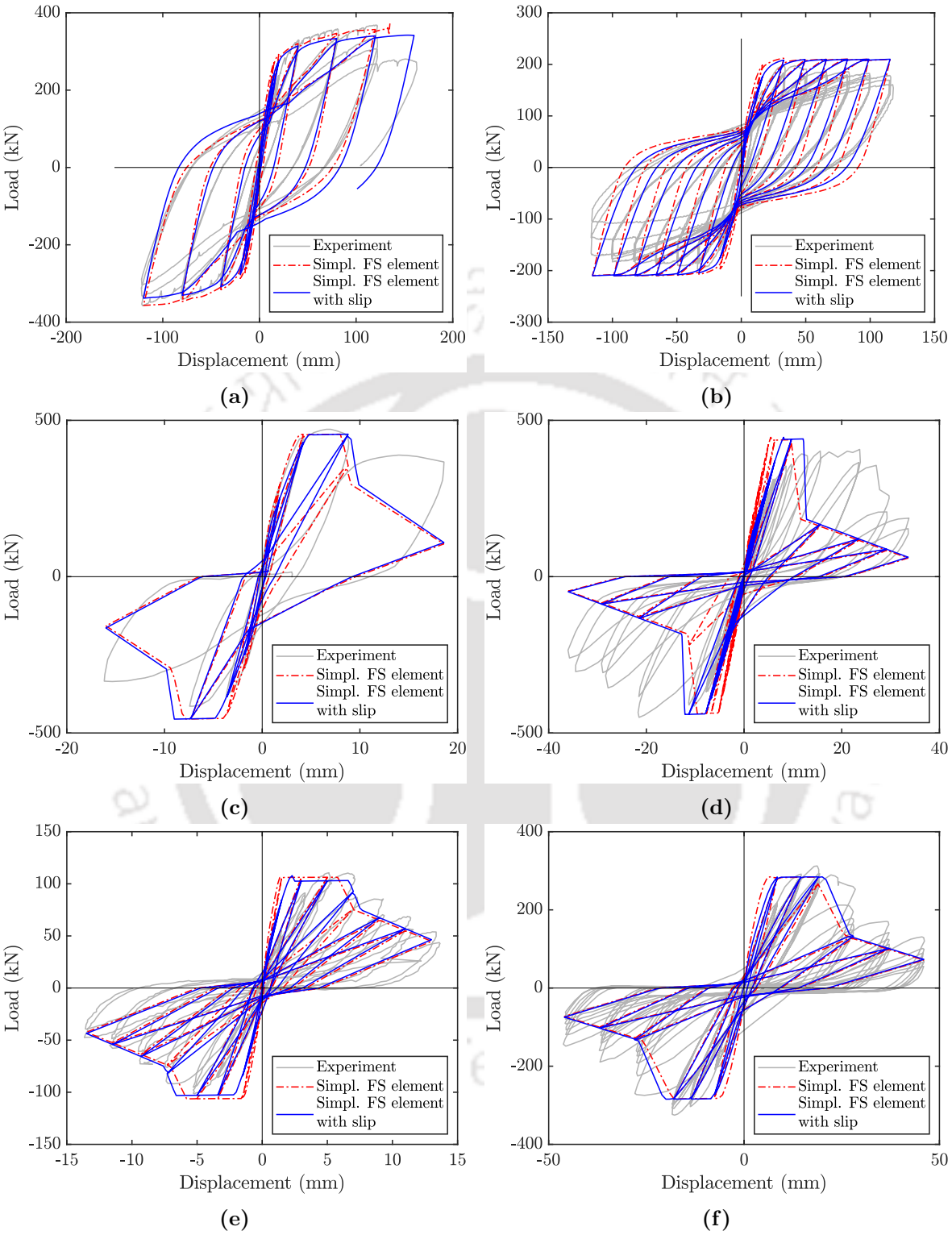

Figure 5.15: Load-displacement response using semi-uncoupled flexure-shear element with anchorage slip: (a) Column FC-1, (b) Column FC-2, (c) Column SC-1, (d) Column SC-2, (e) Column FS-1, (f) Column FS-2

5.7 Conclusion

In this chapter, a zero-length element is presented to model the column base rotation due to slippage of rebar in the anchorage region. The element can be used in series with the beam-column elements to account for the deformation due to the anchorage slip. The element performance is dependent on the adopted stress-displacement properties of the material. A parametric study is presented to determine the suitable stress-displacement relations for the materials. Numerical validation is presented for two experimental column tests from the literature. The result indicates that the use of the slip element along with the beam-column element leads to better prediction of global and local response.

Chapter 6

The Combined Framework under Transient Dynamic Excitation

6.1 Introduction

Behaviour of member or frame under combined axial-flexure-shear loading is vital for the study of reinforced concrete frame under seismic loading. We have developed fibre based element to account for axial-flexure-shear interaction and anchorage bond slip under static monotonic as well as cyclic loading. In this chapter these elements have been extended to consider transient dynamic loading. The reinforced concrete frames have been considered under seismic excitation. Typical experimental results are considered to evaluate the performance. The first example considered is a full-scale bridge pier tested on the shake table, while the other is a column specimen designed with large spacing between transverse reinforcement to make it critical in shear.

In the next section, an implementation of nonlinear dynamic procedure used in the present work is presented. It is followed by two numerical examples to study the accuracy of the models and the importance of considering the shear and bond slip deformations in the modelling of RC structures.

6.2 Transient Dynamic Analysis

The equation of motion for multi-degree freedom system at time $t + \Delta t$ is written as (Bathe, 1996)

$$\mathbf{M}\,{}^{t+\Delta t}\ddot{\mathbf{p}} + \mathbf{C}\,{}^{t+\Delta t}\dot{\mathbf{p}} + \mathbf{F}({}^{t+\Delta t}\mathbf{p}) = {}^{t+\Delta t}\mathbf{P} \tag{6.1}$$

where $\mathbf{M}$ and $\mathbf{C}$ are the structural mass matrix and structural damping matrix. $\mathbf{F}$ is the internal resisting force as a function of displacement. $\mathbf{p}$, $\dot{\mathbf{p}}$, $\ddot{\mathbf{p}}$ denotes the nodal displacement vector, velocity vector and acceleration vector, respectively. $\mathbf{P}$ denotes any time-varying external load. For structure under seismic ground excitation, the equation of motion is given by,

$$\mathbf{M}\,{}^{t+\Delta t}\ddot{\mathbf{p}} + \mathbf{C}\,{}^{t+\Delta t}\dot{\mathbf{p}} + \mathbf{F}({}^{t+\Delta t}\mathbf{p}) = -\mathbf{M}\mathbf{I}^{t+\Delta t}a_g \tag{6.2}$$

where $\mathbf{I}$ is the influence vector and a_g is the ground acceleration.

The above equation of motion (Equation (6.2)) is solved using a direct integration algorithm. In the present study, Equation (6.2) is integrated using Newmark methods (Newmark, 1959) and HHT-α method (Hilber et al., 1977). The solution procedure involves defining acceleration and velocity in terms of displacement to obtain a nonlinear equation in terms of nodal displacement vector. Then, displacement at time $t + \Delta t$ is obtained using Newton Raphson method. The resulting equation can be written in the incremental form as

$${}^{t+\Delta t}\widetilde{\mathbf{K}}_{st}^{(i-1)}\Delta\mathbf{p} = {}^{t+\Delta t}\Delta\widetilde{\mathbf{R}}^{(i-1)} \tag{6.3}$$

where $\widetilde{\mathbf{K}}_{st}$ denotes the effective stiffness matrix and $\Delta\widetilde{\mathbf{R}}$ denotes the effective force vector. The detailed derivation of the equation for the Newmark method and HHT-α method is given in the Appendix D for ready reference.

The global mass matrix, damping matrix and stiffness matrix are obtained by assembling element mass matrix, element damping matrix and element stiffness matrix, respectively. In the present implementation, the mass matrix $\mathbf{M}$ is modelled using lumped mass idealization. Since the lateral forces and displacements are assumed to

constitute the dominant effect, mass is assigned to translational horizontal degrees of freedom only and no rotational inertia is included in the model. As no significant spalling of concrete occurs during the analysis process, the mass matrix is assumption to remain constant during excitation.

The damping matrix consideration may affect the response of the structure, however, it is assumed that the majority of damping occurs due to hysteretic damping and thus a constant damping for a small damping ratio is considered. A brief procedure to calculate damping matrix is discussed in the next section. The stiffness matrix is obtained following the procedure discussed in Chapters 3 and 5.

6.2.1 Damping matrix

Rayleigh damping is considered in this study

$$\mathbf{C} = a_0\mathbf{M} + a_1\mathbf{K} \tag{6.4}$$

in which a_0 and a_1 are constants derived by assuming suitable damping ratios for two modes of vibration (Clough and Penzien, 1975). In present study, the damping matrix is expressed in proportion to current tangent stiffness of the structure as given by

$$\mathbf{C} = a_0\mathbf{M} + a_1\mathbf{K}_{st} \tag{6.5}$$

where $\mathbf{K}_{st}$ is the tangent stiffness matrix of the structure.

Using a normal coordinate transformation of the equation of motion, the damping ratio for the n-th mode of vibration is given by:

$$\xi_n = \frac{a_0}{2\omega_n} + \frac{a_1\omega_n}{2} \tag{6.6}$$

where ω_n is the natural frequency of the n-th mode. For mass-dependent damping ξ_n is inversely proportional to the frequency such that higher modes have little damping. Conversely, stiffness-proportional damping is proportional to the frequency of the structure and results in higher damping for higher modes thus decreasing the contribution

of higher modes to the response of the structure (Clough and Penzien, 1975).

With this type of damping, if two damping ratios are known for two modes of vibration, the constant a_0 and a_1 can be obtained as follows (Clough and Penzien, 1975)

$$\begin{bmatrix} \xi_m \\ \xi_n \end{bmatrix} = \frac{1}{2} \begin{bmatrix} \frac{1}{\omega_m} & \omega_m \\ \frac{1}{\omega_n} & \omega_n \end{bmatrix} \begin{Bmatrix} a_0 \\ a_1 \end{Bmatrix} \tag{6.7}$$

In the particular case wherein both modes are assumed to have the same damping ratio $\xi_m = \xi_n = \xi$, a_0 and a_1 are obtained as

$$a_0 = \xi \frac{2\omega_m \omega_n}{\omega_m + \omega_n} \tag{6.8}$$

$$a_1 = \xi \frac{2}{\omega_m + \omega_n} \tag{6.9}$$

6.3 Implementation

The dynamic analysis requires the element mass and element stiffness matrices to be established and assembled at the start of the solution procedure. The damping matrix is obtained by the linear combination of mass and stiffness matrix as in Equation (6.5). The coefficient of the damping matrix (a_0,a_1) are estimated using either Equation (6.7) or Equations (6.8) and (6.9). In the current implementation the mass matrix and the damping coefficients are assumed to remain constant during the analysis. The solution procedure starts with a gravity analysis. It is then followed by the direct time integration. The details steps of the implementation is enumerated below.

1. At the initializing step, lumped mass of each element is computed and is assembled to obtain structural mass matrix. Similarly tangent stiffness matrix of each element is computed and assembled to obtain the initial stiffness matrix of the structure.

2. Eigen analysis is perfomed and the first two natural frequencies are selected to compute the coefficients of Rayleigh damping. In the current study, a small

damping ratio is considered as the majority of damping is assumed to occur due to hysteresis damping.

3. Gravity analysis is performed for the dead load and imposed load (if any) on the structure. This is usually performed using standard load-controlled algorithm.

4. Time is incremented to obtain the time step $t+\Delta t$ for the direct time integration algorithm. The external load vector ${}^{t+\Delta t}\mathbf{P}$ is calculated due to the gravity load $\mathbf{P}_0$ and inertial load at the time step.

$$ {}^{t+\Delta t}\mathbf{P} = \mathbf{P}_0 - \mathbf{M}\mathbf{I}^{t+\Delta t}a_g $$

5. Iteration number $i = 1$ is inizialized.

6. The effective stiffness matrix of the structure, $\widetilde{\mathbf{K}}_{st}^{(i-1)}$, and effective residual vector, $\Delta\widetilde{\mathbf{R}}^{(i-1)}$ are computed. The expressions for the effective stiffness matrix and effective residual force vector are given as in Equations (D.10) and (D.11) for Newmarks methods and Equations (D.16) and (D.17) for HHT-α method, respectively.

7. The nodal displacement vector $\Delta\mathbf{p}^{(i)}$ is evaluated as

$$ \Delta\mathbf{p}^{(i)} = \Delta\widetilde{\mathbf{R}}^{(i-1)}/\widetilde{\mathbf{K}}_{st}^{(i-1)} $$

8. The displacement vector $\mathbf{p}^{(i)}$ is updated and the convergence criteria is checked . If convergence criteria is satisfied, the acceleration vector $\ddot{\mathbf{p}}^{(i)}$ and velocity vector $\dot{\mathbf{p}}^{(i)}$ are evaluated using Equations (D.3) and (D.4)) respectively. Then the procedure is repeated for next time step from Step 4. If convergence criteria is not satisfied, the following steps are performed.

9. The element state determination is performed, as described in Chapters 3 and 5 to compute the element internal force vector and element stiffness matrix.

10. The element internal force vector and element stiffness matrix are assembled to obtain the structural force vector $\mathbf{R}^{(i)}$ and tangent stiffness matrix $\mathbf{K}_{st}^{(i)}$.

11. Iteration number is incremented and Step 6 onward is repeated

6.4 Numerical Study

Two experimental results are considered to evaluate the transient dynamic performance of proposed elements. The first example considered is a full-size bridge pier tested on the shake table. The second case is a column specimen designed to fail in shear mode.

6.4.1 UCSD column

A full-scale reinforced-concrete bridge column tested under consecutive unidirectional ground motions of different intensities on the NEES shake table at the University of California, San Diego (Schoettler et al. 2015) was simulated to check the performance of the developed elements. This column is referred to as UCSD column in the present work. The test data are available in the public domain such as DEEDS dataset (`https://datacenterhub.org`) and DesignSafe Date Depot (`https://www.designsafe-ci.org/data/`) (Rathje et al., 2017) under the project name NEES-2010-0987. The schematic diagram of the column is shown in Figure 6.1. The column had a diameter of 1.22 m (4 ft) and a span of 7.31 m (24 ft) above the footing. A large concrete block weighing 2.32 MN (521.9 kip) was cast on the top of the column to simulate the superstructure mass. The longitudinal reinforcement consisted of eighteen 35.8 mm diameter (#11) bars in a single concentric layer. Butt-welded, double 15.9 mm diameter (#5) hoops, spaced at 152 mm (6 in.) on-centre, were used as transverse reinforcement. The clear cover to the hoops was 51 mm (2 in.). The concrete had a compressive strength of 40.9 MPa (5.9 ksi) and a corresponding strain of 0.0026. The longitudinal reinforcement had a yield strength of 519 MPa and an ultimate strength of 707 MPa. The transverse reinforcement had a yield strength of 454 MPa (65.8 ksi) and the ultimate tensile strength of 600 MPa. Four historical earthquake recordings were used for the test input motion, including three motions from the 1989 Loma Prieta earthquake and a fourth record from the 1995 Kobe earthquake. A total of ten earthquake simulations were conducted; however, only the first six were simulated

here. These records are identified in the Table 6.1 along with recorded peak ground acceleration (PGA).

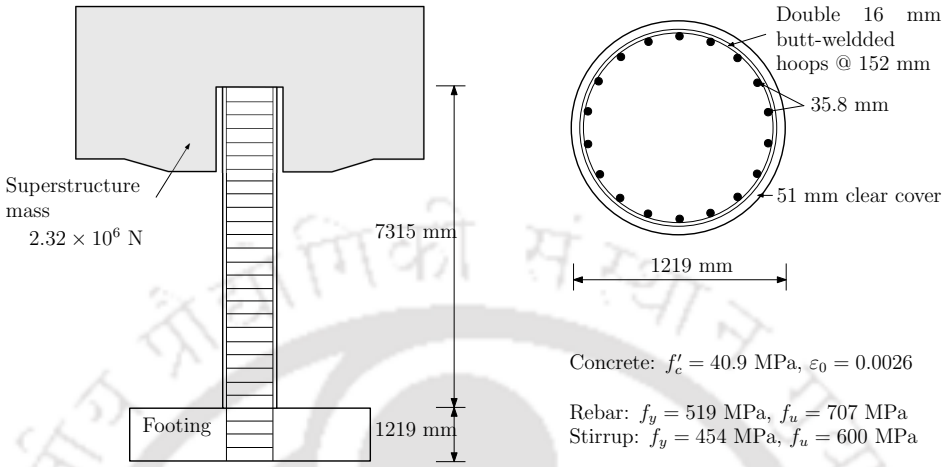

Figure 6.1: Column geometry and cross-section of UCSD column (Schoettler et al., 2015)

Table 6.1: Ground motion scale factor and table PGA for UCSD column

Test	Earthquake	Date	Station	Component	Scale factor	Table PGA (g)
EQ1	Loma Prieta	10/18/1989	Agnew State Hospital	90	1	-0.196
EQ2	Loma Prieta	10/18/1989	Corralitos	90	1	0.407
EQ3	Loma Prieta	10/18/1989	LGPC	00	1	0.522
EQ4	Loma Prieta	10/18/1989	Corralitos	90	1	0.442
EQ5	Kobe	01/16/1995	Takatori	00	-0.8	-0.531
EQ6	Loma Prieta	10/18/1989	LGPC	00	1	-0.501

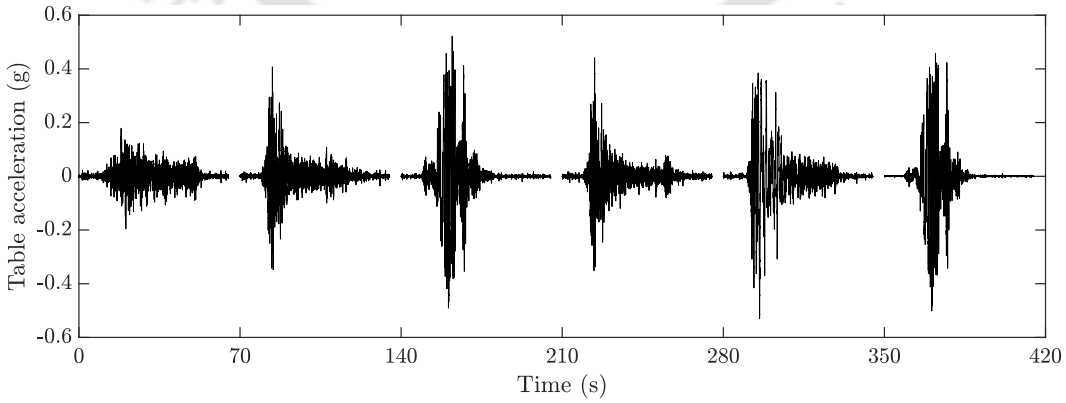

Figure 6.2: Input acceleration time histories EQ1 to EQ6

The column is modelled using a single force-based fibre element. The fibre section along the element length is defined according to the 4-point Gauss-Lobatto integration.

For the case where the end rotation due to anchorage bar slip is considered, a zero-length fibre element is used at the column-footing interface. All fibre sections are discretized into 11 circumferential divisions and 5 radial divisions. The reinforcement fibres are located as per the section detailing. The concrete and steel material properties are selected according to the type of element. For the developed coupled flexure-shear element, the concrete material is modelled using Modified Compression Field Theory (Vecchio and Collins, 1986). For the conventional flexure element, the concrete material is modelled using the Mander model (Mander et al., 1988). In both models the steel material is modelled using G-M-P model (Menegotto and Pinto, 1973).

The column mass is modelled using a lumped mass approach. The half of mass due to the self-weight of the column is lumped at the column top and the total mass at the column top is obtained by adding the dead weight with the superstructure mass. Mass and tangent stiffness proportional Rayleigh damping is used in the model with a damping ratio of 0.01 for the first two modes of vibration. For the shake table simulation, the gravity analysis for the constant axial load is performed first, and then ground motion analysis is performed by sequentially applying the table motions. Between the successive motions sufficient large period is considered to damp out all the free vibrations. The dynamic analysis is performed using HHT-α method with α value -0.2. The other parameters β and γ are obtained following the recommendation of Hilber et al. (1977) for stability condition. The HHT-α method is used as it offers numerical damping for the higher frequency modes.

Figure 6.3 compares the measured column top displacement history with that obtained using the conventional flexural model and the shear flexible model with slip element (Chapters 3 and 5). To reduce the accumulated error from previous earthquake simulation tests, the numerical column displacement results are adjusted so that the initial numerical column displacement result is the same as the experimental result for each test. The results indicate that good accuracy is obtained with the developed flexure-shear model with slip in simulating the column displacement time history. The conventional element underestimates the column response. This is particularly evident in the cases EQ2 and EQ4. The predicted peak displacement using both the numerical model is given in Table 6.2. The developed element predicts the peak displacement

closer to the measured value compared to the conventional element especially for EQ2, EQ3 and EQ4. There are some discrepancy in the predicted peak displacements and vibration characteristics of the numerical model, this may be due to the lack of consideration of important factors such as error accumulation and the variation of damping throughout the tests (Schoettler et al., 2015).

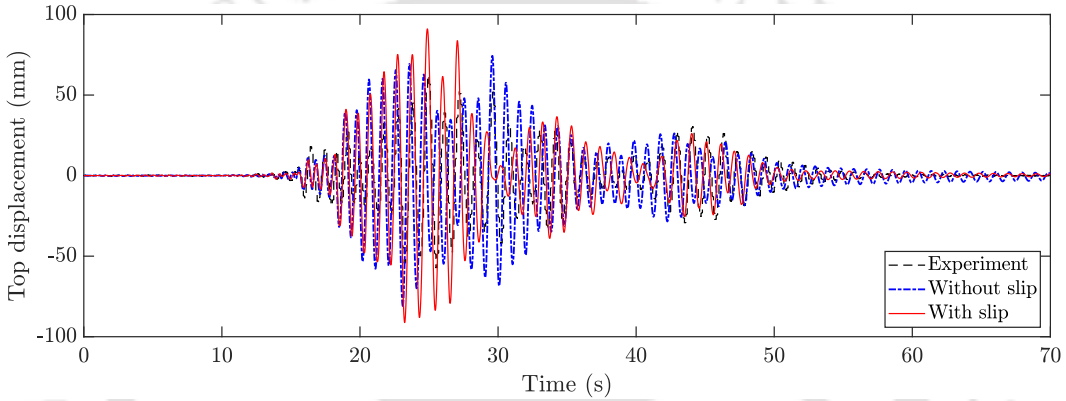

(a) EQ1

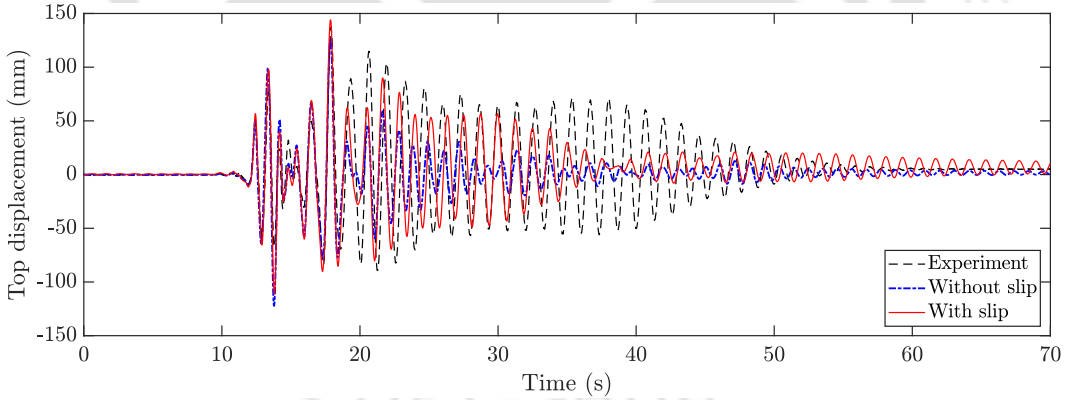

(b) EQ2

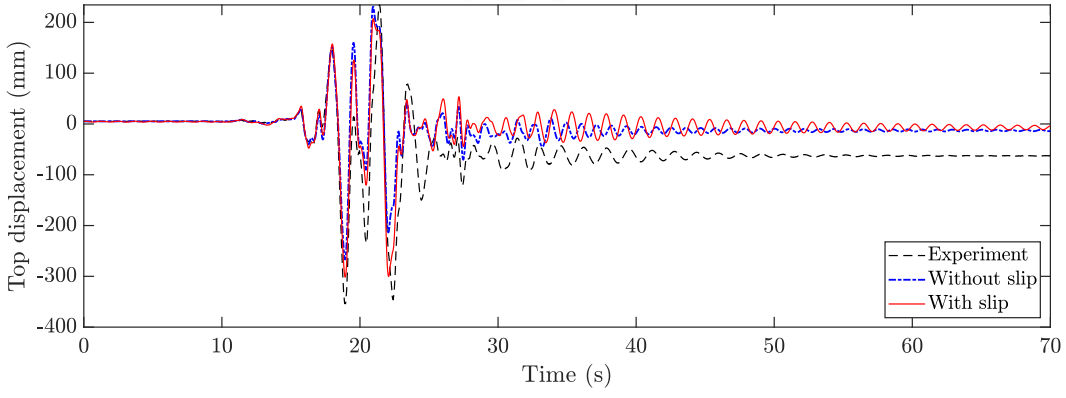

(c) EQ3

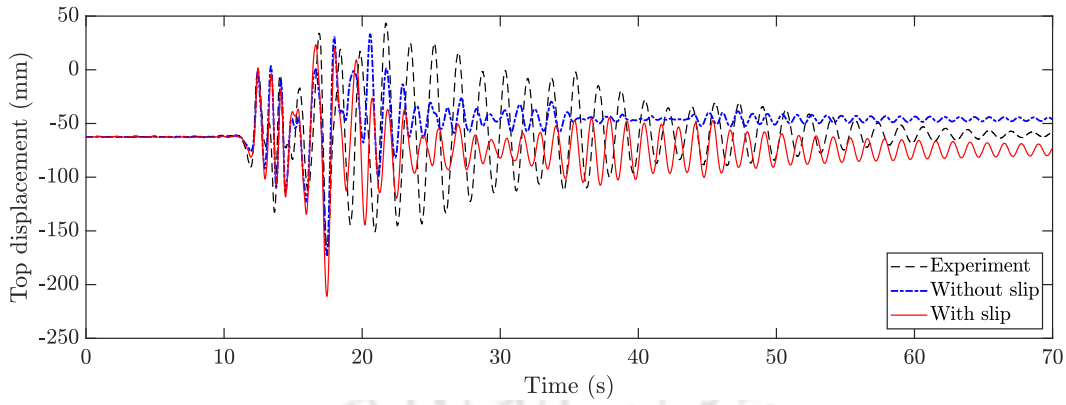

(d) EQ4

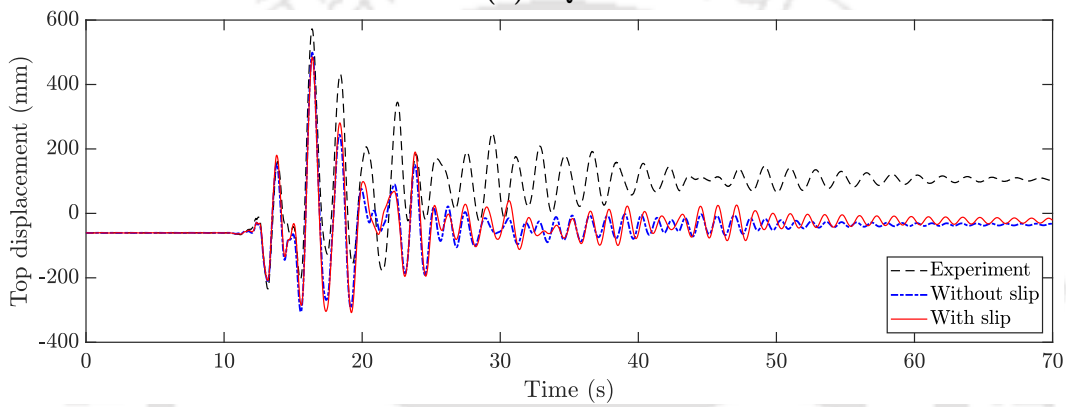

(e) EQ5

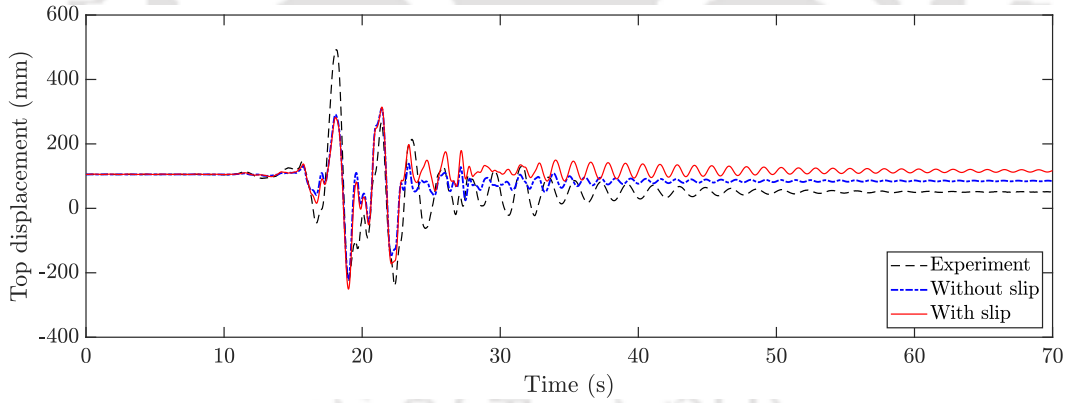

(f) EQ6

Figure 6.3: Column top displacement time history for EQ1 to EQ6

Figure 6.4 shows the predicted shear force-top displacement response and compared with the measured response. The figure indicate that the inclusion of shear and bond induce flexibility and good accuracy is obtained in the structure level. The conventional model predicts a stiffer response, denoted by the higher slope of the shear force-displacement curves, in all the simulations. whereas the developed element with slip predicted force-displacement slope is closer to that of the experimental observation.

Table 6.2: Comparison of predicted peak displacement

		Experiment	Conventional element	Developed element with slip
EQ1	Max	61.978	74.391	91.054
	Min	-57.402	-80.976	-91.198
EQ2	Max	137.36	126.14	144.02
	Min	-89.266	-122.29	-111.35
EQ3	Max	234.4	230.91	207.22
	Min	-354.06	-266.83	-301.56
EQ4	Max	43.69	33.199	23.342
	Min	-173.14	-172.03	-210.96
EQ5	Max	573.12	498.83	485.26
	Min	-234.75	-306.01	-307.84
EQ6	Max	492.56	310.96	314.12
	Min	-240.35	-221.68	-250.54

There is some variation in the peak shear force, this is again reasoned due the variation of the damping characteristics.

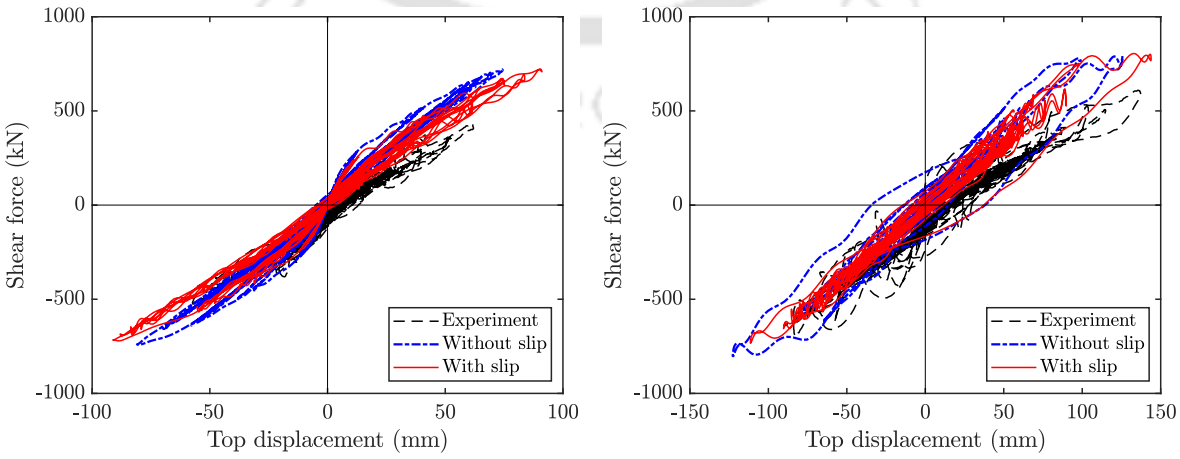

Figure 6.4: Shear force-displacement response for EQ1 to EQ6

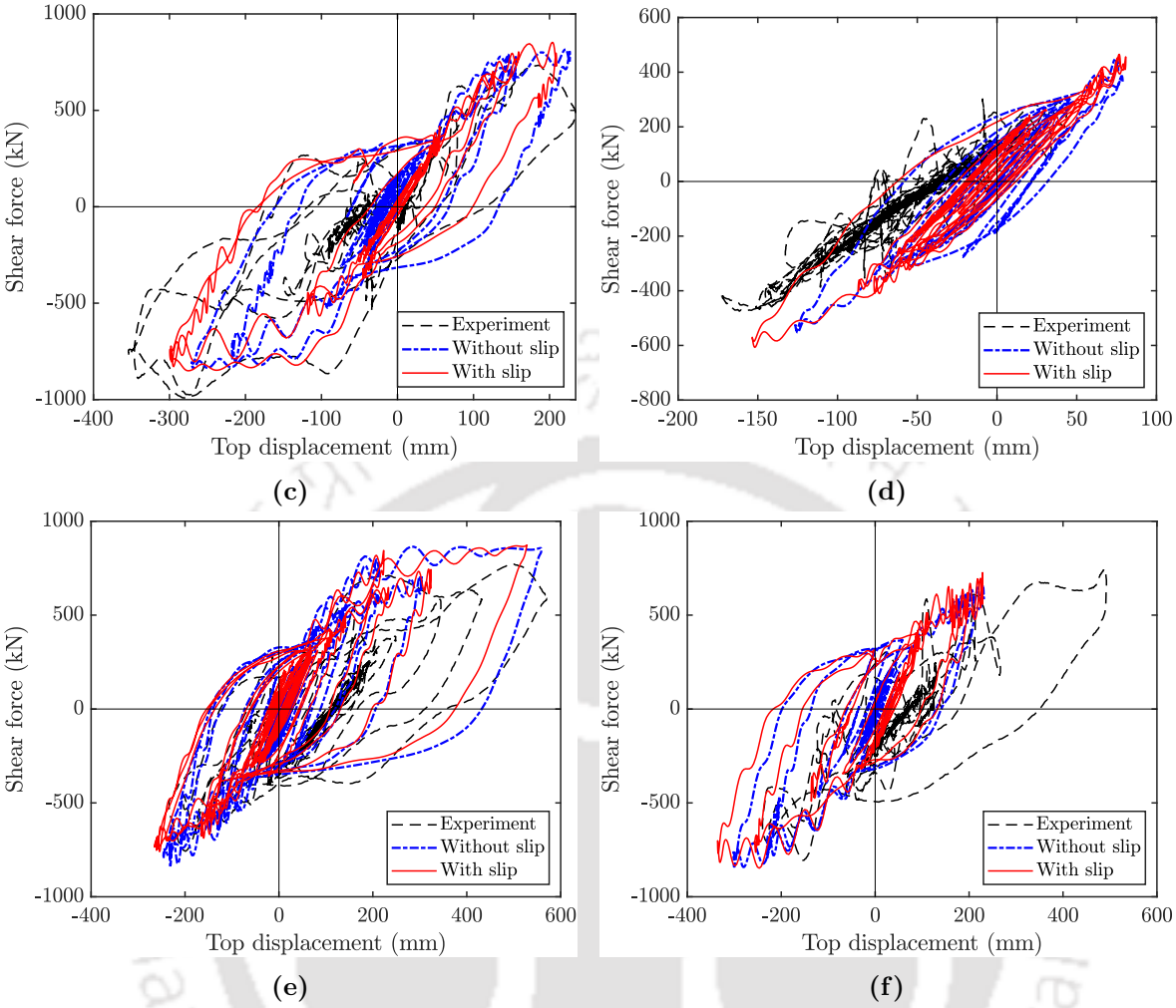

Figure 6.4: Shear force-displacement response for EQ1 to EQ6

Figure 6.5 compares the predicted base moment-curvature response with the experimental measurements. The figures indicate that the consideration of slip rotation in the model yields significant variation in the local response. The developed model considering slip rotation predicts less curvature demand compared to the conventional flexural model. It underestimated the curvature at the initial simulations, however, at the latter stage of the simulation for EQ5 and EQ6 the predictions are close to the experiment.

The advantage of the developed element with slip over the conventional element is further evident from the Table 6.3 and Figure 6.6. The development model is able to predict the ratio of slip displacement to the total displacement in most of the simulations. Thus, slip should be considered in the numerical modelling.

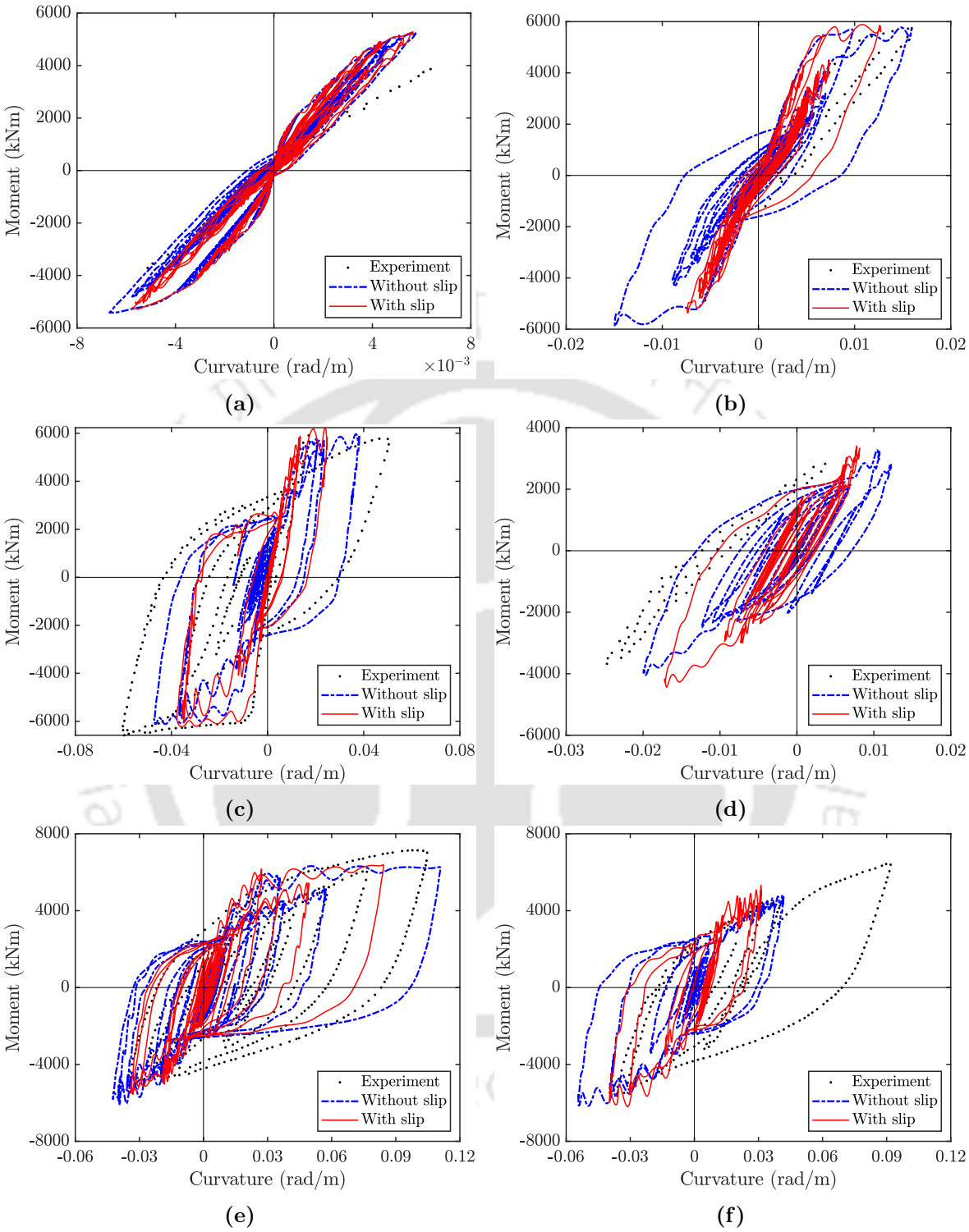

Figure 6.5: Base moment-curvature response for EQ1 to EQ6

Table 6.3: Comparison of displacement component ratios at peak displacement

EQ	Experiment				Developed element with slip			
	Max flex.+ shear disp. (%)	Max slip disp. (%)	Min flex.+ shear disp. (%)	Min slip disp. (%)	Max flex.+ shear disp. (%)	Max slip disp. (%)	Min flex.+ shear disp. (%)	Min slip disp. (%)
EQ1	80.33	16.58	71.42	16.03	81.82	18.17	81.80	18.19
EQ2	76.99	16.36	70.98	19.37	78.32	21.67	76.69	23.30
EQ3	78.66	20.48	75.99	19.48	78.61	21.38	75.01	24.98
EQ4	73.54	18.70	62.41	23.26	80.75	19.24	77.63	22.37
EQ5	75.43	18.36	78.77	14.25	82.81	17.18	75.99	24.00
EQ6	78.66	19.81	75.77	14.91	80.48	19.52	69.48	30.51

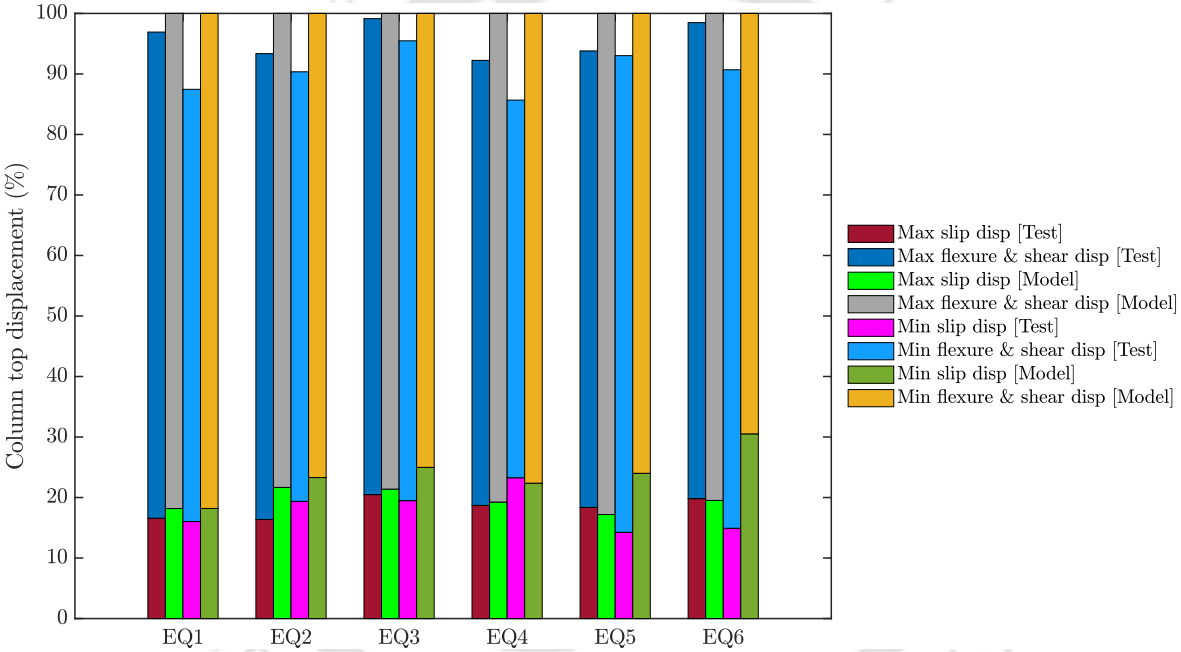

Figure 6.6: Displacement components at peak displacements

6.4.2 UNR column

To further evaluate the performance of the developed elements, a circular RC bridge column 9S1 tested by Laplace (2001) at the University of Nevada, Reno is considered. The column is referred as UNR column in the present study. The column was designed to be shear critical. The column was designed with a high ratio of longitudinal steel ratio to increase the flexural capacity ensuring a shear dominated failure. The schematic diagram of the column is shown in Figure 6.1. The column was subject to an axial load of 356 kN. The column specimen has a diameter of 406.44 mm and clear length of

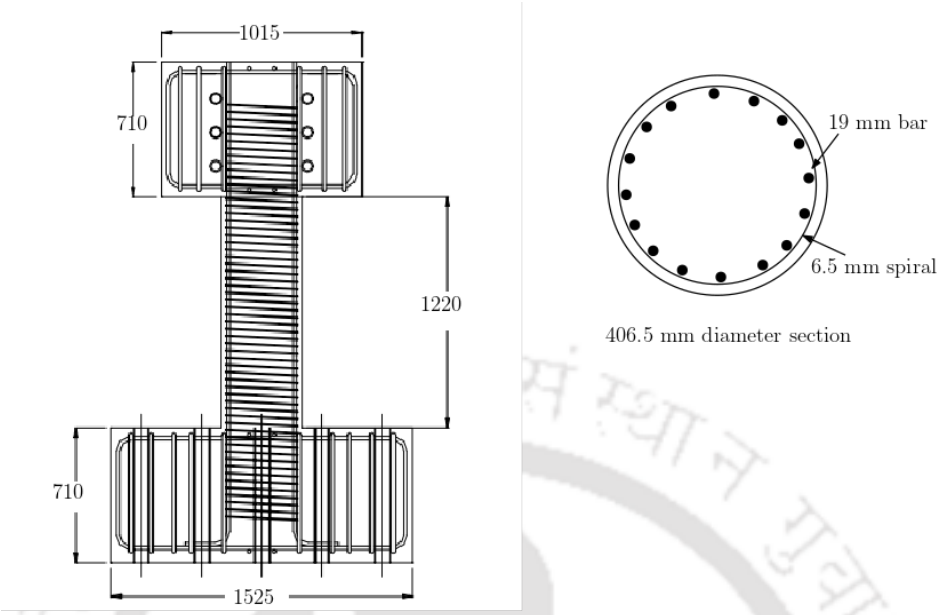

Figure 6.7: Column details and cross-section of UNR column

1220 mm. The column reinforcement consists of sixteen 19 mm longitudinal bars, and 6.5 mm spiral as transverse reinforcement. The spacing of transverse reinforcement is 38.1 mm. The concrete has compressive strength 36.7 MPa. The yield stresses of longitudinal and transverse reinforcement were 458.2 MPa and 397.4 MPa respectively.

The column was analyzed with the 1940 Imperial Valley (El Centro) earthquake excitation having a PGA of 0.32g. The column is modelled as a cantilever using a single force-based fibre element. The column was modelled using the conventional flexure element and the developed coupled flexure-shear element. In both model, the fibre section along the element length is defined according to the 4-point Gauss-Lobatto integration. All fibre sections are discretized into 11 circumferential divisions and 5 radial divisions. The reinforcement fibres are located as per the section detailing. The concrete and steel material properties are selected according to the type of element. For the developed coupled flexure-shear element, the concrete material is modelled using Modified Compression Field Theory (Vecchio and Collins, 1986). For the conventional flexure element, the concrete material is modelled using the Mander model (Mander et al., 1988). In both models the steel material is modelled using G-M-P model (Menegotto and Pinto, 1973).

The column mass is modelled using a lumped mass approach. Mass and tangent

stiffness proportional Rayleigh damping is used in the model with a damping ratio of 0.01 for the first two modes of vibration. For the transient dynamic analysis, the gravity analysis for the constant axial load is performed prior to the ground motion is application. The dynamic analysis is performed using HHT-α method with α value -0.2. The other parameters β and γ are obtained following the recommendation of Hilber et al. (1977) for stability condition. The HHT-α method is used as it offers numerical damping for the higher frequency modes.

Before simulating the shake table experiment, pushover analysis is performed following a displacement-controlled procedure on the column with an imposed axial load at the top of the column. The response of the column is shown in the Figure 6.8. It is observed that the monotonic response of the column is affected by shear deformation, which is evident from the degradation of the load-displacement curve obtained from the developed flexure-shear element. Whereas, the conventional model predicted a hardening-type of response. The effect of shear in the transient dynamic excitation is studied in the following.

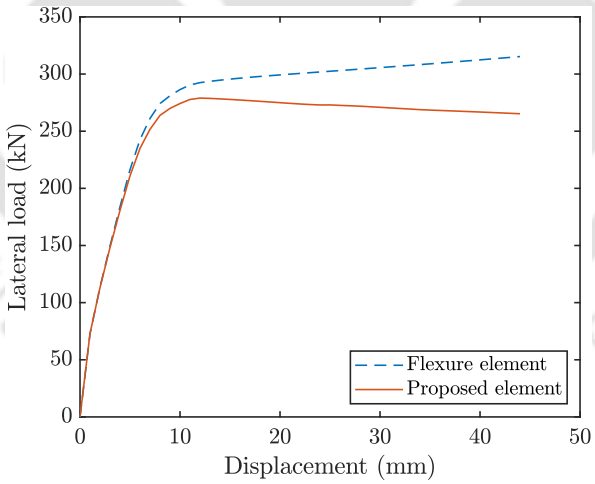

Figure 6.8: Pushover response of UNR column

Figure 6.9 shows the column top displacement history obtained from the conventional element and developed coupled flexure-shear element. The result indicates the conventional flexure model underestimation of the top displacement history. The flexure-shear model predicted a residual displacement at the end of the element, where as the conventional model did not.

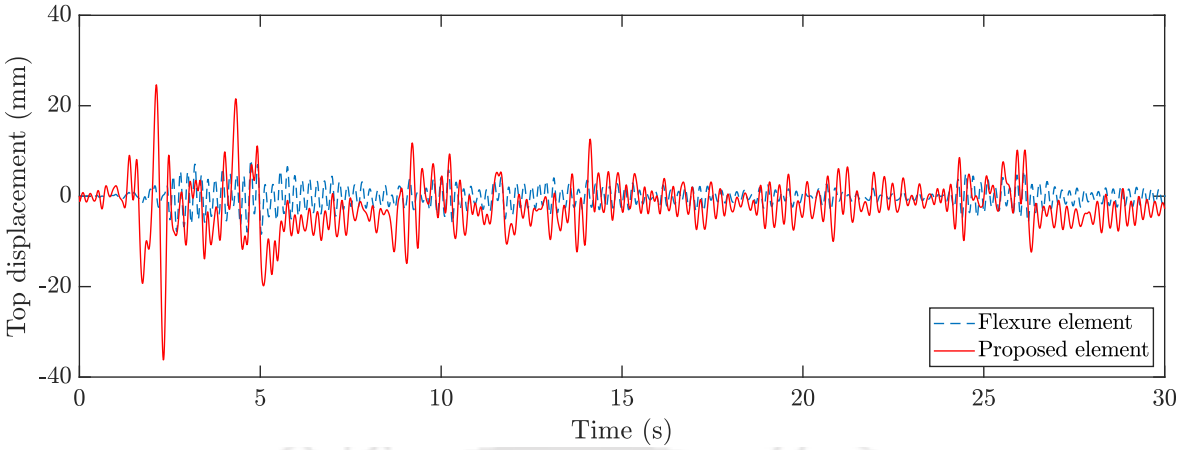

Figure 6.9: Comparison of top displacement history of UNR column

6.5 Conclusion

In this chapter, the performance of the developed element is assessed for the transient dynamic analysis. Two numerical examples are presented to study the performance of the developed element under earthquake excitation. The numerical result clearly demonstrates the importance of shear deformation and anchorage-slip deformation in the modelling of RC members. Neglecting shear and/or anchorage bond-slip deformation leads to underestimation of the top displacement history, prediction of high initial stiffness of load-displacement response and high curvature at the end section of the element. The developed elements considering coupled flexure-shear interaction and anchorage bond-slip are able to predict the response closer to the experimental observed result.

Chapter 7

Conclusions and Recommendations

Fibre frame elements are getting more and more popular for seismic assessment of reinforced concrete structures. Incorporation of shear, anchorage bond-slip, transient dynamic behaviour is essential for reliable model of the fibre frame element. This thesis has investigated the conventional fibre element and developed fibre-based element to effectively consider the axial, flexure, shear deformation in an reinforced concrete members and slip in the anchorage region. This chapter summarizes the overall work in the thesis, highlights the contributions, and presents the possible future directions in the related domain.

7.1 Conclusions and Contributions

7.1.1 Development of axial-flexure-shear coupled force-based fibre frame element

An axial-flexure-shear coupled fibre section is developed which uses multiaxial stress-strain relation based on the Modified Compression Field Theory (Vecchio and Collins, 1986) for concrete material. Tangent formulation of the method is adopted. The model also incorporates the confining effect of the stirrup in the concrete compression stress-strain relation in the principal plane by the relation proposed by Mander et al. (1988). The shear modulus in the principal plane is modelled by Zhu et al. (2001) which ensures the coaxiality of principal direction for strain and stress. The coupled

section is implemented in a force-based fibre element framework. The element uses an additional parabolic shear strain kinematic. The advantage of the developed element is the ease of implementation due to the parabolic assumption and consideration of the axial-flexure-shear force interaction effect from the stress-strain relation. Several numerical examples are presented to study the performance of the proposed element. By consideration of the shear deformation and flexure-shear interaction effect, the fibre element is able to capture the shear critical response. The model is able to identify the initiation of the shear degradation as observed in the experimental specimens.

7.1.2 Localization problem in axial-flexure-shear coupled force-based fibre frame element

The inherent localization issue of the force-based element in the presence of softening material is also observed in the developed element. For the softening type of response, the strain localizes at the end extremes. The end section strain continues to grow in the softening region while the remaining regions unload. The suitability of the available regularization techniques based on the scaling of the integration weight approach is accessed for the developed element. It is found that the available approaches can be suitably used with a proper definition of characteristic length to obtain an objective post-peak response.

7.1.3 Development of force-based fibre frame element with semi-uncoupled flexure-shear interaction

The use of multiaxial constitutive relations for the concrete fibre requires an iterative procedure to determine the strain and stress state of the fibre. A semi-uncoupled fibre section is developed to overcome the iterative calculation. The developed model uses a variable nonlinear shear relation between shear force and shear strain at the section level. The shear force is considered in an uncoupled manner. However, the effect of flexure on the shear force is accounted for by varying the nonlinear shear relation as a function of the moment level on the section. The implementation of the element requires an extra preprocessing step where the variable shear relation is obtained from

the several analyses of the axial-flexure-shear coupled fibre section. The numerical examples presented imply the response of the element is similar to that of the coupled element.

7.1.4 Development of fibre hinge element for anchorage-slip effect

Experimental studies by several researchers have revealed that anchorage-slip has a significant effect on the response of the element together with shear. A fibre hinge element is developed to consider the anchorage-slip effect. It consists of a single fibre section where the fibre properties are defined in terms of stress-displacement relation instead of stress-strain relation. The reinforcement fibre stress-displacement relation is obtained using an analytical model with average stepped bond stress distribution. The concrete fibre stress-displacement relation is obtained using an influence length factor to denote the relationship between the strain and displacement term. A parametric study is presented to show the effect of adopted fibre properties on the response of the slip element. It is observed that although the fibre properties have a negligible effect on the global response these are found to affect the local response of the element. The numerical examples are presented to study the performance of the proposed element. The consideration of anchorage bond-slip leads to flexible response and has an effect on the initial stiffness and unloading stiffness. The overall response is close to the experimental response. The consideration of these responses is also found to have an effect on the local-moment curvature response. These predicted curvature profiles are close to the experimental result.

7.1.5 Study of reinforced concrete member under transient dynamic excitation

Newmarks method (Newmark, 1959) and HHT-α (Hilber et al., 1977) methods were implemented to study the performance of the structures under transient dynamic loading. Two numerical examples are presented to study the performance of the developed element under earthquake excitation. The numerical result clearly demonstrates the

importance of shear deformation and anchorage-slip deformation in the modelling of RC members. Neglecting these deformation overestimates the initial stiffness, ductility, and energy dissipation capacity of the member, especially for the member with inadequate transverse reinforcement detailing and anchorage condition.

7.2 Limitations of the Study

The presented results as outcomes of the current research work are subjected to the following limitations, though the conclusions extracted from those results remain unaffected.

- Only degradation (softening) in the concrete material is considered. Other degradations such as the buckling of the rebar etc are not considered.
- The geometric nonlinearity is not considered in the analysis.
- The developed uncoupled shear model the variation of axial force is not considered. The variable shear envelope can be made a function of moment and axial force to better represent the force interaction effect.
- The incorporated anchorage bond-slip model assumes two boundary conditions typical in the footing (straight and anchored).
- effect of localization for the bond-slip element is not studied.

7.3 Recommendation for Future Works

The research work in this thesis has investigated and proposed an efficient method to include shear deformation along the element and anchorage bond-slip deformation. Although the numerical validations provided in this thesis are satisfactory, there are some scopes for further improvement apart from eliminating the limitations mentioned in the prior section.

➤ The developed fibre elements are formulated for two-dimensional RC frames. The scope of the work can be extended to three dimensions by considering the

bi-directional moment and bi-directional shear effect. The torsional effect may be included to further improve the scope of the beam-column element.

- The developed elements were used in the current thesis to analyze bare frame structures. The model can be used to analyze the interaction of additional structural elements, such as a frame with infill and soil-structure interaction.

- The implemented rotating smeared crack model of concrete can account for the normal stress-shear stress interaction effect for the plane stress problem. The effectiveness of the model for the three-dimensional case or some other advanced concrete constitutive model can be investigated.

- As there are limited software with fibre element that consider axial-flexure-shear interaction, developing open-source software can be beneficial. The developed element can be used in the design process to create efficient section designs as well as to analyse the existing structure to estimate capacity for deciding on appropriate retrofitting solutions.

Appendix A

Effect of Different Shear Kinematics

The shear deformable beam element, developed in Chapter 3, is based on a fixed pattern approach due to its ease of implementation. A comparative study is performed to evaluate the fixed pattern shear kinematic. The basis for the use of fixed pattern assumptions in this study has been discussed. In the present work, two common fixed-pattern shear kinematics (uniform, and parabolic) are considered and the responses are compared with the result of an inner-fibre equilibrium method. The fibre discretization and constitutive model are kept uniform for all the cases.

Some of the inner-fibre equilibrium fibre models have been proposed by Vecchio and Collins (1988); Bentz (2000); Bairan and Mari (2007); Mohr et al. (2010); Kagermanov and Ceresa (2017) among others. In the present study, the procedure proposed by Kagermanov and Ceresa (2017) to calculate the exact shear strain profile is adopted for comparison purposes. The derivation of the shear strain profile is described below for convenience.

A.1 Inner-fibre equilibrium method

In this approach, the shear strain over the section is evaluated at each load step, satisfying the stress equilibrium condition.

$$\frac{\partial \sigma_{xx}}{\partial x} + \frac{\partial \tau_{xy}}{\partial y} = 0 \tag{A.1}$$

The shear strain profile is obtained by solving the weak form of the stress equilibrium equation over the cross-section. The shear strains are approximated using the nodal shear strain values at the surface of the concrete layers, as shown in Figure A.1.

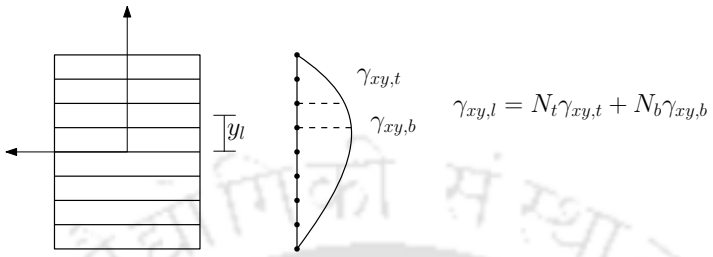

Figure A.1: Interpolation of shear strain profile

Let's say the reduced material stiffness of a fibre after imposing $\sigma_{yy} = 0$ is

$$\begin{Bmatrix} \sigma_{xx} \\ \tau_{xy} \end{Bmatrix} \begin{bmatrix} \overline{D}_{11} & \overline{D}_{12} \\ \overline{D}_{21} & \overline{D}_{22} \end{bmatrix} \begin{Bmatrix} \varepsilon_{xx} \\ \gamma_{xy} \end{Bmatrix} \tag{A.2}$$

Substituting Equation (A.2) in Equation (A.1), we have

$$\overline{D}_{11}\frac{\partial \varepsilon_{xx}}{\partial x} + \overline{D}_{12}\frac{\partial \gamma_{xy}}{\partial x} + \overline{D}_{21}\frac{\partial \varepsilon_{xx}}{\partial y} + \overline{D}_{22}\frac{\partial \gamma_{xy}}{\partial y} = 0 \tag{A.3}$$

The first two strain derivatives in Equation (A.3) can be approximately calculated from the compatibility and the section constitutive relation

$$\boldsymbol{\epsilon} = \begin{Bmatrix} \varepsilon_{xx} \\ \gamma_{xy} \end{Bmatrix} = \begin{bmatrix} 1 & -y & 0 \\ 0 & 0 & 1 \end{bmatrix} \begin{Bmatrix} \varepsilon_0 \\ \chi \\ \gamma_0 \end{Bmatrix} = \mathbf{Bd} \tag{A.4}$$

$$\mathbf{S} = \begin{Bmatrix} N \\ M \\ V \end{Bmatrix} = \mathbf{Kd} \tag{A.5}$$

That is,

$$\frac{\partial \boldsymbol{\epsilon}}{\partial x} = \begin{bmatrix} \frac{\partial \varepsilon_{xx}}{\partial x} \\ \frac{\partial \gamma_{xy}}{\partial x} \end{bmatrix} = \mathbf{B}(\mathbf{K})^{-1}\frac{\partial \mathbf{S}}{\partial x} \tag{A.6}$$

The third derivative term in Equation (A.3) is

$$\frac{\partial \varepsilon_{xx}}{\partial y} = -y \tag{A.7}$$

With the linear interpolation of the nodal shear strain values, the shear strain at the mid-surface of the layer can be expressed as

$$\gamma_{xy} = N_t \gamma_{xy,t} + N_b \gamma_{xy,b} \tag{A.8}$$

Thus, the fourth derivate is

$$\frac{\partial \gamma_{xy}}{\partial y} = {\gamma_{xy}}' = \begin{bmatrix} {N_t}' & {N_b}' \end{bmatrix} \begin{Bmatrix} \gamma_{xy,t} \\ \gamma_{xy,b} \end{Bmatrix} = \mathbf{N}'\boldsymbol{\gamma} \tag{A.9}$$

Now, expressing the stress equilibrium equation over the cross-section, in the weak form, with $\frac{\partial \gamma_{xy}}{\partial y}$as the weighting function.

$$\sum_{l=1}^{nl} \int_A ({\delta\gamma_{xy}}')^T \left(\frac{\partial \sigma_{xx}}{\partial x} + \frac{\partial \tau_{xy}}{\partial y} \right) dA = 0 \tag{A.10}$$

On simplifying, we get

$$\delta\boldsymbol{\gamma}^T \sum_{l=1}^{nl} (\mathbf{N}')^T \left(\overline{D}_{11} \frac{\partial \varepsilon_{xx}}{\partial x} + \overline{D}_{12} \frac{\partial \gamma_{xy}}{\partial x} + \overline{D}_{21} \frac{\partial \varepsilon_{xx}}{\partial y} + \overline{D}_{22} \mathbf{N}'\boldsymbol{\gamma} \right) A_l = 0 \tag{A.11}$$

or

$$\sum_{l=1}^{nl} (\mathbf{N}')^T \left(\overline{D}_{11} \frac{\partial \varepsilon_{xx}}{\partial x} + \overline{D}_{12} \frac{\partial \gamma_{xy}}{\partial x} + \overline{D}_{21} \frac{\partial \varepsilon_{xx}}{\partial y} \right) A_l + \sum_{l=1}^{nl} (\mathbf{N}')^T \overline{D}_{22} \mathbf{N}' A_l \boldsymbol{\gamma} = 0 \tag{A.12}$$

This can be written as

$$\boldsymbol{\gamma} = (\mathbf{k})^{-1} \mathbf{f} \tag{A.13}$$

where

$$\mathbf{k} = \sum_{l=1}^{nl} (\mathbf{N}')^T \overline{D}_{22} \mathbf{N}' A_l \tag{A.14}$$

$$\mathbf{f} = -\sum_{l=1}^{nl} (\mathbf{N}')^T \left(\overline{D}_{11} \frac{\partial \varepsilon_{xx}}{\partial x} + \overline{D}_{12} \frac{\partial \gamma_{xy}}{\partial x} + \overline{D}_{21} \frac{\partial \varepsilon_{xx}}{\partial y} \right) A_l \tag{A.15}$$

The solution of Equation (A.13) with proper boundary conditions (i.e. shear strain at the extreme top and bottom fibre is zero) gives the required nodal shear strain values of the layers.

A.2 Comparative study

The effect of fixed pattern shear kinematic on the sectional response is numerically studied in this section. The considered section belongs to the reinforced concrete column tested by Imai and Yamamoto (1986). It has a cross-section dimension of 400 mm × 500 mm. The longitudinal reinforcement is made of 14-22 mm diameter bars. The transverse reinforcement consists of a 9 mm stirrup at 100 mm spacing. The reinforcement arrangement along with the material properties are shown in Figure A.2.

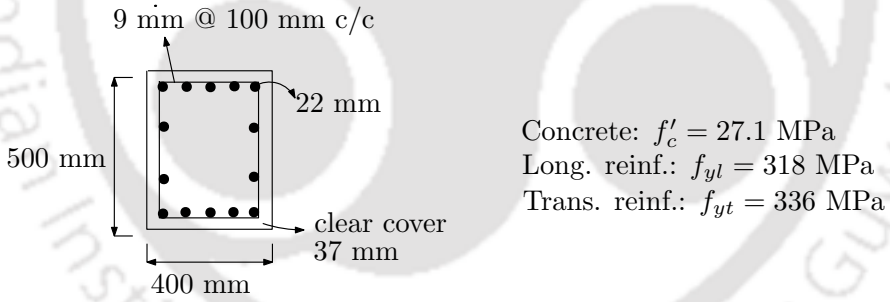

Figure A.2: Example column section geometry and material properties

The example section is analyzed for shear force-shear strain response for a constant axial load of 392 kN and bending-shear ratio of 825. The shear strain is incrementally applied following the displacement control algorithm, where shear strain is incrementally applied and the corresponding shear force is iteratively corrected. The predictions using different shear kinematic assumptions are compared in Figure A.3. It is observed that the parabolic shear strain assumption gives a reasonably close result to that obtained with the inner-fibre equilibrium method. The uniform shear strain distribution largely overestimates the strength and stiffness.

The strain and stress distributions over the section using different shear kinematic

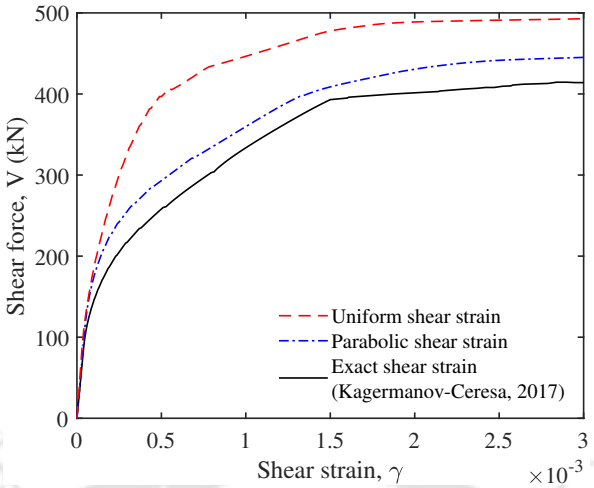

Figure A.3: Shear response of example column section

assumptions are compared in Figures A.4 to A.6. It is seen that all three assumptions yield approximately similar axial strain and stress distribution. However, there is a difference in the shear strain and stress distribution. The parabolic shear strain assumption yields a comparatively similar distribution to that of the inner-fibre equilibrium technique, whereas significant deviation is found with uniform shear strain assumption.

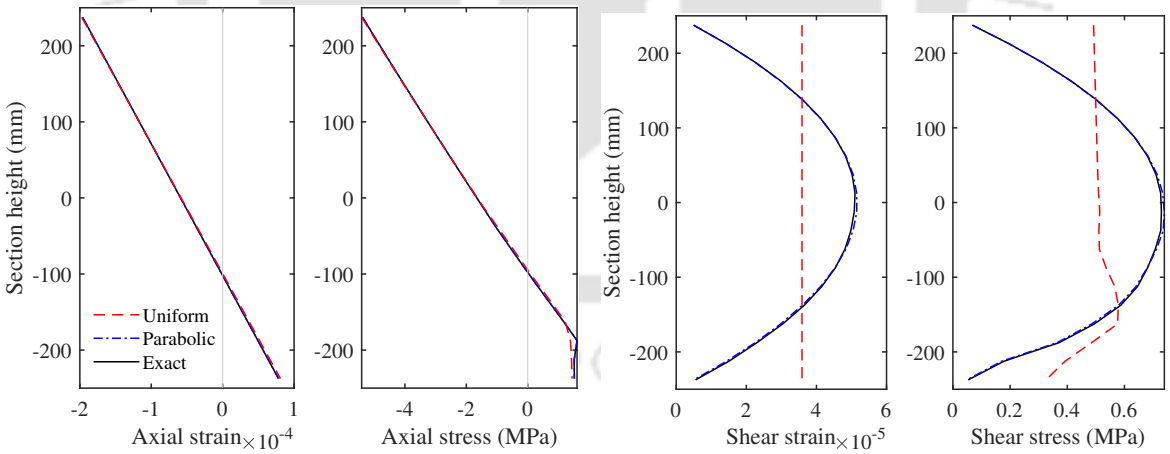

Figure A.4: (a) Axial strain and axial stress distribution, (b) shear strain and shear stress distribution corresponding to load level 100 kN in Figure A.3

.

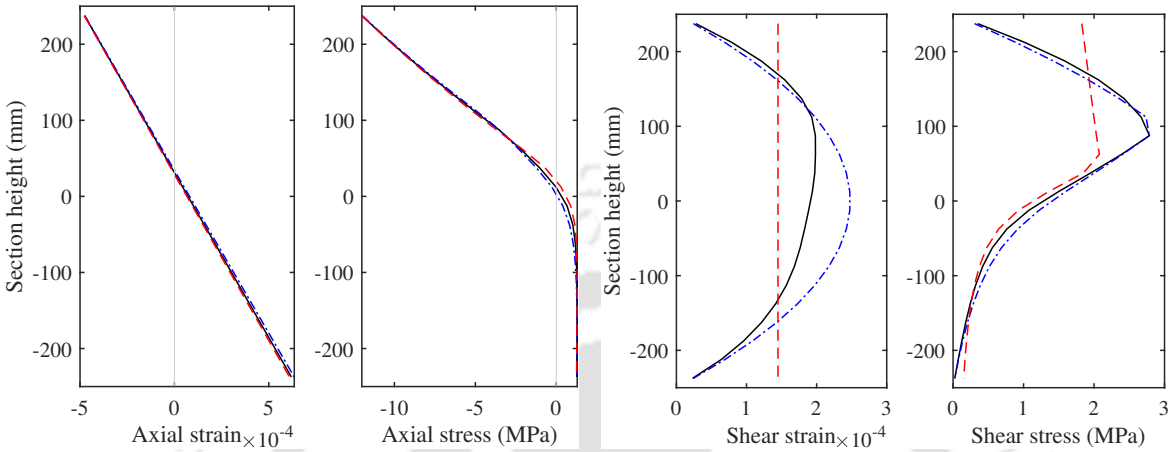

Figure A.5: (a) Axial strain and axial stress distribution, (b) shear strain and shear stress distribution corresponding to load level 225 kN in Figure A.3

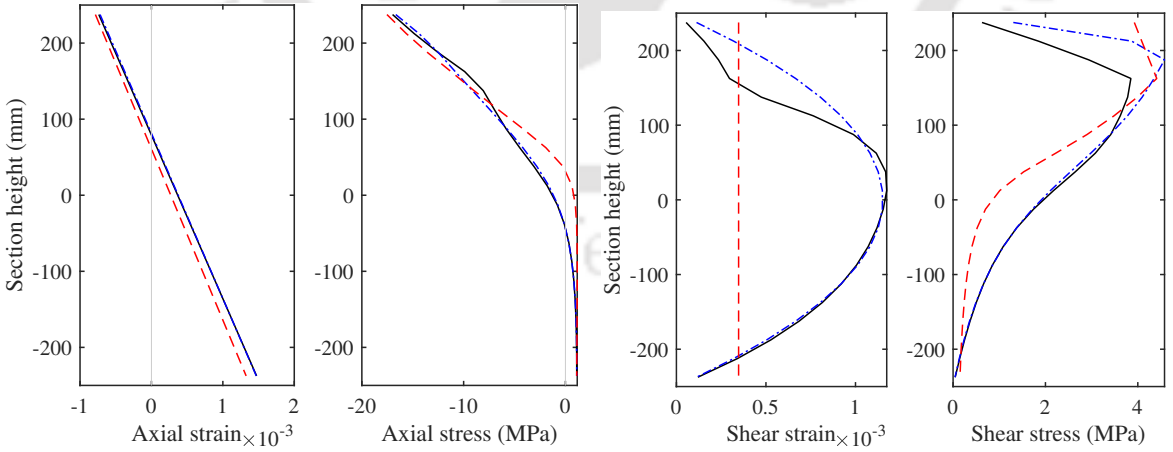

Figure A.6: (a) Axial strain and axial stress distribution, (b) shear strain and shear stress distribution corresponding to load level 300 kN in Figure A.3

Appendix B

Euler-Bernoulli Section Model

A brief discussion of Euler-Bernoulli model is presented which is based on the assumption: *a plane section perpendicular to the neutral axis remains plane and perpendicular to the neutral axis during deformation.* In other words, the section has an infinite shear stiffness and it does not affect the axial stress. Normal stress in the transverse direction is neglected. The state of strain is predominately uniaxial. Thus material relationship is expressed using uniaxial stress-strain relation for normal strain and linear elastic relation with very high stiffness for shear strain. It should be noted that these simplified assumptions simulate only the flexural response of the member.

The section compatibility matrix for the assumed section kinematic relation.

$$\mathbf{a}_s(y) = \begin{bmatrix} -y & 0 & 1 \\ 0 & 1 & 0 \end{bmatrix} \tag{B.1}$$

The stresses and material modulus are determined from the uniaxial relationship between normal stress and strain and shear stress and strain as

$$\mathbf{s} = \begin{Bmatrix} \sigma_{xx} \\ \tau_{xy} \end{Bmatrix}, \qquad \mathbf{k} = \frac{\partial \mathbf{s}}{\partial \mathbf{e}} = \begin{bmatrix} E & 0 \\ 0 & G \end{bmatrix} \tag{B.2}$$

where $\sigma_x = f(\epsilon_x)$ and $\tau_{xy} = G\gamma_{xy}$ and G = very large number, to simulate the high rigidity in shear.

The corresponding expression of section resisting forces and the tangent section

stiffness matrix of the Euler-Bernouli fibre section are calculated by midpoint integration rule as

$$\hat{\mathbf{S}}(x) = \sum_i \mathbf{a}_s^T(y_i)\mathbf{s}(\mathbf{e}(x, y_i))A_i = \begin{Bmatrix} -\sum_i \sigma_i A_i y_i \\ \tau_{xy} \sum_i A_i \\ \sum_i \sigma_i A_i \end{Bmatrix} \tag{B.3}$$

$$\mathbf{K}_s(x) = \sum_i \mathbf{a}_s^T(y_i)\mathbf{k}(\mathbf{e}(x, y_i))\mathbf{a}_s(y_i)A_i = \begin{bmatrix} \sum_i E_i^{tan} A_i y_i^2 & 0 & -\sum_i E_i^{tan} A_i y_i \\ 0 & G\sum_i A_i & 0 \\ -\sum_i E_i^{tan} A_i y_i & 0 & \sum_i E_i^{tan} A_i \end{bmatrix}. \tag{B.4}$$

where, the subscript i refers to the respective quantity of the ith fiber.

Appendix C

Standard solution procedures for nonlinear static analysis

The basic problem in a general nonlinear analysis is to find the state of equilibrium of a body corresponding to the applied loads. The response calculation is effectively carried out using a step-by-step incremental iterative solution. It is to assume that the solution for the discrete time $k-1$ is known and that the solution for the discrete time k is required. The problem is solved by linearizing the residual expression till the satisfaction of applied load P and the internal force F. The expression is obtained from Taylor expansion of the residual function $f(u^{(i)}) = P(u^{(i)}) - F(u^{(i)})$ about $u^{(i)} = u^{(i-1)} + \delta u^{(i)}$ as

$$K^{(i-1)}\delta u^{(i)} = P^{(i)} - F^{(i-1)} = P_u \tag{C.1}$$

The above equation can be written for both static and dynamic equilibrium equations. For static case $P(u^{(i)})$ is constant equal to the applied load but it contains other terms for dynamic case (Bathe, 1996). This equation is cast in a slightly different form to facilitate the definition of other incremental iterative solution methods in the following.

$$K^{(i-1)}\delta u^{(i)} = (P^{(i-1)} + \delta\lambda^{(i)}P_{ref}) - F^{(i-1)} \tag{C.2}$$

or

$$K^{(i-1)}\delta u^{(i)} = R^{(i-1)} + \delta\lambda^{(i)}P_{ref} \tag{C.3}$$

where $R = P - F$.

In the above equations subscript 'i' corresponding to the iteration number for an increment step k. With a known state u^{k-1} and P^{k-1} the incremental state u^k and P^k is expressed as

$$u^k = u^{k-1} + \Delta u \tag{C.4}$$

$$P^k = P^{k-1} + \Delta P \tag{C.5}$$

where

$$\Delta u = \Sigma \delta u^{(i)} \tag{C.6}$$

$$\Delta P = \Delta \lambda P_{ref} = \Sigma \delta \lambda^{(i)} P_{ref} \tag{C.7}$$

Note Equation (C.3) requires determination of one extra unknown. For a structure with N degrees of freedom, there are a total of N equations. However, involves N+1 unknowns (N incremental displacement vector δu and 1 incremental load parameter $\delta\lambda$). There are several different versions of incremental-iterative solution methods based on how one wishes to control the load increment parameter $\delta\lambda$ and the way iterations are carried out within an incremental step.

C.1 Load-control method

The load control method sets the load increment parameter $\delta\lambda^{(1)} = 1$ for first iteration ($i = 1$) and $\delta\lambda^{(i)} = 0$ for the subsequent iterations ($i > 1$). In other terms, the external load is applied at the first load step and in the subsequent iteration the unbalanced load vector is used to iterate until a predefined convergence criteria is satisfied. The load control method has a limitation that it cannot trace the nonlinear region of the load-displacement curve beyond the limit load point. When an applied external load exceeds the load capacity of the structure, the convergence fails. A pseudo-code of the procedure is given below.

Algorithm 1 LCM

for $k = 1 : kmax$ **do**
  Increment $\Delta\lambda$
  Update P
  $\Delta u \leftarrow 0$
  $R \leftarrow \Delta\lambda P_{ref}$
  while $norm(R) > tol$ **do**
    $\delta u \leftarrow K^{-1}R$
    $\Delta u \leftarrow \Delta u + \delta u$
    Calculate $F(u^{k-1} + \Delta u)$ and $K(u^{k-1} + \Delta u)$
    $R \leftarrow P - F$
  end while
  Update u
end for

C.2 Displacement-control method

The displacement control method treats load factor $\delta\lambda$ as a variable and is modified at each iteration. The method uses a prescribed displacement at a selected degree of freedom (control displacement) in each incremental step and iterations are carried out until a convergence criteria is achieved. The method proposed by Batoz and Dhatt (1979) is described here. The displacement $\delta u^{(i)}$ is decomposed into two parts

$$\delta u^{(i)} = \delta u_a^{(i)} + \delta\lambda^{(i)}\delta u_b^{(i)} \tag{C.8}$$

where $\delta u_a^{(i)}$ and $\delta u_b^{(i)}$ corresponds to the solution of

$$K^{(i-1)}\delta u_a^{(i)} = R^{(i-1)} \tag{C.9}$$

$$K^{(i-1)}\delta u_b^{(i)} = P_{ref} \tag{C.10}$$

The load parameter $\delta\lambda^{(i)}$ is determined using the prescribed control displacement as the constraint equation. Consider the control degree of freedom is 'q'. Then for the first iteration $\delta u^{(1)}(q) = \Delta\overline{u}$.

$$\delta\lambda^{(1)} = \frac{\Delta\overline{u}}{\delta u_b^{(1)}(q)} \tag{C.11}$$

For the subsequent iterations, $\delta u^{(i)}(q)$ is set to zero and

$$\delta\lambda^{(i)} = \frac{-\delta u_a^{(i)}(q)}{\delta u_b^{(i)}(q)} \tag{C.12}$$

A pseudo-code for the displacement-controlled procedure is given below.

Algorithm 2 DCM

for $k = 1 : kmax$ **do**
  $\Delta u \leftarrow 0$
  $\Delta\lambda \leftarrow 0$
  Increment $\delta u^{(1)}(q) = \Delta\overline{u}$
  $R \leftarrow 1$
  while $norm(R) > tol$ **do**
    if i=1 **then**
      $\delta u_a^{(1)} \leftarrow 0$
      $\delta u_b^{(1)} \leftarrow K^{-1}P_{ref}$
      $\delta\lambda^{(1)} = \dfrac{\Delta\overline{u}}{\delta u_b^{(1)}(q)}$
    else
      $\delta u_a^{(i)} = [K^{(i-1)}]^{-1}R^{(i-1)}$
      $\delta u_b^{(i)} = [K^{(i-1)}]^{-1}P_{ref}$
      $\delta\lambda^{(i)} = \dfrac{-\delta u_a^{(i)}(q)}{\delta u_b^{(i)}(q)}$
    end if
    $\delta u^{(i)} = \delta u_a^{(i)} + \delta\lambda^{(i)}\delta u_b^{(i)}$
    $\Delta u \leftarrow \Delta u + \delta u$
    $\Delta\lambda \leftarrow \Delta\lambda + \delta\lambda$
    Calculate $F(u^{k-1} + \Delta u)$ and $K(u^{k-1} + \Delta u)$
    $R \leftarrow (P^{k-1} + \Delta\lambda P_{ref}) - F$
  end while
  Update u
  Update P
end for

C.3 Arc-length method

The arc-length method also treats load factor $\delta\lambda$ as a variable, it is modified at each iteration so that the solution follows some specified path until convergence is achieved. In this method, an initial arc-length is determined, the subsequent iterations lie on the constraint surface created by the arc. There are several versions of the arc-length

method, the cylindrical method by Crisfield (1981) is described in the following. The constraint equation is given by

$$\Delta u_i.\Delta u_i = (\Delta s_i)^2 \tag{C.13}$$

where Δs is the arc-length. Simplification of the constraint equation leads to a quadratic equation, whose roots are used for determining the load-factor. Substituting $\Delta u = \Delta u + \delta u$ and $\delta u = \delta u^a + \delta\lambda\delta u^b$ into the constraint equation yields

$$c_1\delta\lambda^2 + c_2\delta\lambda + c_3 = 0 \tag{C.14}$$

where

$$c_1 = \delta u^b.\delta u^b \tag{C.15}$$

$$c_2 = 2\delta u^b(\Delta u + \delta u^a) \tag{C.16}$$

$$c_3 = (\Delta u + \delta u^a).(\Delta u + \delta u^a) - (\Delta s)^2 \tag{C.17}$$

Proper selection of root is one of the key issues of the method. Crisfield suggested that the angle between the incremental displacement vector before the current iteration and the incremental load vector after the current iteration must be minimal. In present study, the appropriate root is selected by ensuring an acute angle 'θ' between Δu_i and Δu_{i+1}, for which $\cos\theta$ will be positive.

For the first load increment $k = 1$, the value of $\delta\lambda_1$ is suitably assumed. The corresponding arc length Δs is calculated as

$$\Delta s_1 = \delta\lambda_1\sqrt{\delta u^b.\delta u^b} \tag{C.18}$$

For all iterations within an increment, Δs is kept constant. For the subsequent load increment $k > 1$, the first estimate of $\delta\lambda$ is obtained from

$$\delta\lambda = \sqrt{\frac{\Delta s^2}{\delta u^b.\delta u^b}} = \frac{\pm\Delta s}{\sqrt{\delta u^b.\delta u^b}} = \frac{a(\Delta s)}{\sqrt{\delta u^b.\delta u^b}} \tag{C.19}$$

where indicate the sign of the $\delta\lambda^{(1)}$. A pseudo-code for the constant arc-length method

is given below.

Algorithm 3 ALM

for $k = 1 : kmax$ **do**
  $\Delta u \leftarrow 0$
  $\Delta\lambda \leftarrow 0$
  $R \leftarrow 1$
  while $norm(R) > tol$ **do**
    if i=1 **then**
      $\delta u_a^{(1)} \leftarrow 0$
      $\delta u_b^{(1)} \leftarrow K^{-1} P_{ref}$
      if k=1 **then**
        Assume suitable $\delta\lambda^{(1)}$
        $\Delta s = \delta\lambda^{(1)} \sqrt{\delta u^b . \delta u^b}$
      else
        $\delta\lambda^{(1)} = \dfrac{a(\Delta s)}{\sqrt{\delta u^b . \delta u^b}}$
        where a indicate the sign of the $\delta\lambda^{(1)}$
      end if
    else
      $\delta u_a^{(i)} = [K^{(i-1)}]^{-1} R^{(i-1)}$
      $\delta u_b^{(i)} = [K^{(i-1)}]^{-1} P_{ref}$
      $c_1 = \delta u^b . \delta u^b$
      $c_2 = 2\delta u^b (\Delta u + \delta u^a)$
      $c_3 = (\Delta u + \delta u^a).(\Delta u + \delta u^a) - (\Delta s)^2$
      Choose appropriate $\delta\lambda^{(i)}$ from the roots of equation

$$c_1 \delta\lambda^2 + c_2 \delta\lambda + c_3 = 0$$

    end if
    $\delta u^{(i)} = \delta u_a^{(i)} + \delta\lambda^{(i)} \delta u_b^{(i)}$
    $\Delta u \leftarrow \Delta u + \delta u$
    $\Delta\lambda \leftarrow \Delta\lambda + \delta\lambda$
    Calculate $F(u^{k-1} + \Delta u)$ and $K(u^{k-1} + \Delta u)$
    $R \leftarrow (P^{k-1} + \Delta\lambda P_{ref}) - F$
  end while
  Update u
  Update P
end for

Appendix D

Standard solution procedures for transient dynamic analysis

D.1 Newmark method

In the Newmark method the velocity and displacement vector at time $t + \Delta t$ are approximated as

$$^{t+\Delta t}\dot{\mathbf{p}} = {}^{t}\dot{\mathbf{p}} + \left[(1-\gamma)^{t}\ddot{\mathbf{p}} + \gamma^{t+\Delta t}\ddot{\mathbf{p}}\right]\Delta t \tag{D.1}$$

$$^{t+\Delta t}\mathbf{p} = {}^{t}\mathbf{p} + {}^{t}\dot{\mathbf{p}}\Delta t + \left[(1-2\beta)^{t}\ddot{\mathbf{p}} + 2\beta^{t+\Delta t}\ddot{\mathbf{p}}\right]\frac{\Delta t^2}{2} \tag{D.2}$$

where γ and β are the parameters that determine the stability and other numerical characteristic of the method (Bathe, 1996).

Solving Equation (D.2)

$$^{t+\Delta t}\ddot{\mathbf{p}} = \frac{1}{\beta\Delta t^2}\left({}^{t+\Delta t}\mathbf{p} - {}^{t}\mathbf{p}\right) - \frac{1}{\beta\Delta t}{}^{t}\dot{\mathbf{p}} - \left(\frac{1}{2\beta} - 1\right){}^{t}\ddot{\mathbf{p}} \tag{D.3}$$

Substituting Equation (D.3) into (D.1)

$$^{t+\Delta t}\dot{\mathbf{p}} = \frac{\gamma}{\beta\Delta t}\left({}^{t+\Delta t}\mathbf{p} - {}^{t}\mathbf{p}\right) - \left(\frac{\gamma}{\beta} - 1\right){}^{t}\dot{\mathbf{p}} - \left(\frac{\gamma}{2\beta} - 1\right){}^{t}\ddot{\mathbf{p}}\Delta t \tag{D.4}$$

Equation D.3 and D.4 defines acceleration and velocity in terms of displacement. Substituting the expression of acceleration and velocity in Equation 6.2 and rearranging

leads to a nonlinear function in the single variable $\mathbf{p}$. The residual of the nonlinear equation $\mathbf{r}({}^{t+\Delta t}\mathbf{p})$ is defined as

$$\mathbf{r}({}^{t+\Delta t}\mathbf{p}) = \frac{1}{\beta\Delta t^2}\mathbf{M}\,{}^{t+\Delta t}\mathbf{p} + \frac{\gamma}{\beta\Delta t}\mathbf{C}\,{}^{t+\Delta t}\mathbf{p} + \mathbf{R}({}^{t+\Delta t}\mathbf{p}) - {}^{t+\Delta t}\mathbf{Q} = 0 \tag{D.5}$$

where

$$\begin{aligned} {}^{t+\Delta t}\mathbf{Q} = {}^{t+\Delta t}\mathbf{P} + \mathbf{M}\left[\frac{1}{\beta\Delta t^2}{}^{t}\mathbf{p} + \frac{1}{\beta\Delta t}{}^{t}\dot{\mathbf{p}} + \left(\frac{1}{2\beta} - 1\right){}^{t}\ddot{\mathbf{p}}\right] + \\ \mathbf{C}\left[\frac{\gamma}{\beta\Delta t}{}^{t}\mathbf{p} + \left(\frac{\gamma}{\beta} - 1\right){}^{t}\dot{\mathbf{p}} + \left(\frac{\gamma}{2\beta} - 1\right){}^{t}\ddot{\mathbf{p}}\Delta t\right] \end{aligned} \tag{D.6}$$

The above equation is solved by the Newton-Raphson method. The Taylor expansion of the residual $\mathbf{r}$ for the ith iteration gives

$$\mathbf{r}\left({}^{t+\Delta t}\mathbf{p}^{(i)}\right) = \mathbf{r}\left({}^{t+\Delta t}\mathbf{p}^{(i-1)}\right) + \frac{\partial \mathbf{r}\left({}^{t+\Delta t}\mathbf{p}^{(i-1)}\right)}{\partial \mathbf{p}}\Delta\mathbf{p} + \ldots \tag{D.7}$$

where

$$\Delta\mathbf{p} = {}^{t+\Delta t}\mathbf{p}^{(i)} - {}^{t+\Delta t}\mathbf{p}^{(i-1)} \tag{D.8}$$

Neglecting higher order terms and equating Equation (D.7) to zero yields

$${}^{t+\Delta t}\widetilde{\mathbf{K}}_{st}^{(i-1)}\Delta\mathbf{p} = {}^{t+\Delta t}\Delta\widetilde{\mathbf{R}}^{(i-1)} \tag{D.9}$$

where

$${}^{t+\Delta t}\widetilde{\mathbf{K}}_{st}^{(i-1)} = \frac{\partial \mathbf{r}\left({}^{t+\Delta t}\mathbf{p}^{(i-1)}\right)}{\partial \mathbf{p}} = {}^{t+\Delta t}\mathbf{K}_{st}^{(i-1)} + \frac{1}{\beta\Delta t^2}\mathbf{M} + \frac{\gamma}{\beta\Delta t}\mathbf{C} \tag{D.10}$$

$$\begin{aligned} {}^{t+\Delta t}\Delta\widetilde{\mathbf{R}}^{(i-1)} = & -\mathbf{r}\left({}^{t+\Delta t}\mathbf{p}^{(i-1)}\right) = {}^{t+\Delta t}\mathbf{P} - {}^{t+\Delta t}\mathbf{R}^{(i-1)} - \\ & \mathbf{M}\left[\frac{1}{\beta\Delta t^2}\left({}^{t+\Delta t}\mathbf{p}^{(i-1)} - {}^{t}\mathbf{p}\right) - \frac{1}{\beta\Delta t}{}^{t}\dot{\mathbf{p}} - \left(\frac{1}{2\beta} - 1\right){}^{t}\ddot{\mathbf{p}}\right] - \\ & \mathbf{C}\left[\frac{\gamma}{\beta\Delta t}\left({}^{t+\Delta t}\mathbf{p}^{(i-1)} - {}^{t}\mathbf{p}\right) - \left(\frac{\gamma}{\beta} - 1\right){}^{t}\dot{\mathbf{p}} - \left(\frac{\gamma}{2\beta} - 1\right){}^{t}\ddot{\mathbf{p}}\Delta t\right] \end{aligned} \tag{D.11}$$

$${}^{t+\Delta t}\mathbf{p}^{(i)} = {}^{t+\Delta t}\mathbf{p}^{(i-1)} + \Delta\mathbf{p}^{(i)} \tag{D.12}$$

Parameters γ and β determine the stability and other numerical characteristic of the method. $\gamma = 1/2$ and $\beta = 1/6$, corresponds to linear acceleration variation and $\gamma = 1/2$ and $\beta = 1/4$, corresponds to constant average acceleration and is unconditionally stable. The Newmark linear acceleration method is more precise than the Newmark constant acceleration method for the same time step Δt. But it is conditionally stable requiring $\Delta t \leq 0.551 T_{n_{eq}}$ where $T_{n_{eq}}$ is the smallest period of the system with n_{eq} DOF (Bathe, 1996).

D.2 HHT method

In addition to being unconditionally stable, when only low mode response is of interest it is often advantageous for an algorithm to possess some form of numerical dissipation to damp out any spurious participation of the higher modes. The Newmark method with parameter $\gamma > 1$, $\beta \geq (\gamma + \frac{1}{2})^2/4$. The numerical dissipation in the N-γ method is too dissipative for the important low-frequency modes and the method is only first-order accurate. To improve upon this, Hilber et al. (1977) developed a family of second-order unconditionally stable implicit algorithms for application to structural dynamics problems. The difference equation for velocity and displacement of the Newmark method (Equation (D.1) and (D.2)) are adopted in this method whereas the time-discrete equation of motion is written in a modified form as (Hughes, 2000):

$$\mathbf{M}^{t+\Delta t}\ddot{\mathbf{p}} + (1+\alpha)\mathbf{C}^{t+\Delta t}\dot{\mathbf{p}} - \alpha\mathbf{C}^{t}\dot{\mathbf{p}} + (1+\alpha)\mathbf{K}^{t+\Delta t}\mathbf{p} - \alpha\mathbf{K}^{t}\mathbf{p} = (1+\alpha)^{t+\Delta t}\mathbf{P} - \alpha^{t}\mathbf{P} \tag{D.13a}$$

$$\mathbf{M}\ddot{\mathbf{p}}(t_0) + \mathbf{C}\dot{\mathbf{p}}(t_0) + \mathbf{K}\mathbf{p}(t_0) = \mathbf{P}(t_0) \tag{D.13b}$$

The range of the parameters, for the family of stable algorithms, proposed in Hilber et al. (1977) is $\beta = (1-\alpha)^2/4$, $\gamma = \dfrac{1}{2} - \alpha$ and $-\dfrac{1}{3} \leq \alpha \leq 0$

For nonlinear analysis Equation (D.13) can be written as

$$\mathbf{M}^{t+\Delta t}\ddot{\mathbf{p}} + (1+\alpha)\mathbf{C}^{t+\Delta t}\dot{\mathbf{p}} - \alpha\mathbf{C}^{t}\dot{\mathbf{p}} + (1+\alpha)^{t+\Delta t}\mathbf{F} - \alpha^{t}\mathbf{F} = (1+\alpha)^{t+\Delta t}\mathbf{P} - \alpha^{t}\mathbf{P} \tag{D.14}$$

where $\mathbf{F}$ is nonlinear restoring force

Substituting the expressions for the velocity and the acceleration at the time $t+\Delta t$ from Equations (D.4) and (D.3) and upon rearranging and linearizing yields

$$ {}^{t+\Delta t}\widetilde{\mathbf{K}}_{st}^{(i-1)} \Delta\mathbf{p}^{(i)} = {}^{t+\Delta t}\Delta\widetilde{\mathbf{R}}^{(i-1)} \tag{D.15} $$

where

$$ {}^{t+\Delta t}\widetilde{\mathbf{K}}_{st}^{(i-1)} = \frac{1}{\beta\Delta t^2}\mathbf{M} + (1+\alpha)\left(\frac{\gamma}{\beta\Delta t}\mathbf{C} + {}^{t+\Delta t}\mathbf{K}_{st}^{(i-1)}\right) \tag{D.16} $$

$$ \begin{aligned} {}^{t+\Delta t}\Delta\widetilde{\mathbf{R}}^{(i-1)} = {} & (1+\alpha)\left({}^{t+\Delta t}\mathbf{P} - {}^{t+\Delta t}\mathbf{R}^{(i-1)}\right) - \alpha\left({}^{t}\mathbf{P} - {}^{t}\mathbf{R}\right) - \\ & \mathbf{M}\left[\frac{1}{\beta\Delta t^2}\left({}^{t+\Delta t}\mathbf{p}^{(i-1)} - {}^{t}\mathbf{p}\right) - \frac{1}{\beta\Delta t}{}^{t}\dot{\mathbf{p}} - \frac{1-2\beta}{2\beta}{}^{t}\ddot{\mathbf{p}}\right] - \\ & \mathbf{C}\left[\frac{(1+\alpha)\gamma}{\beta\Delta t}\left({}^{t+\Delta t}\mathbf{p}^{(i-1)} - {}^{t}\mathbf{p}\right) - \left(-1 + \frac{(1+\alpha)\gamma}{\beta}\right){}^{t}\dot{\mathbf{p}} - \frac{(1+\alpha)(\gamma-2\beta)}{2\beta}{}^{t}\ddot{\mathbf{p}}\Delta t\right] \end{aligned} \tag{D.17} $$

$$ {}^{t+\Delta t}\mathbf{p}^{(i)} = {}^{t+\Delta t}\mathbf{p}^{(i-1)} + \Delta\mathbf{p}^{(i)} \tag{D.18} $$

Bibliography

Aboutaha, R. S., Engelhardt, M. D., Jirsa, J. O., and Kreger, M. E. (1999). Rehabilitation of shear critical concrete columns by use of rectangular steel jackets. *Structural Journal*, 96(1):68–78. 17, 73, 98, 125

Addessi, D. and Ciampi, V. (2007). A regularized force-based beam element with a damage–plastic section constitutive law. *International Journal for Numerical Methods in Engineering*, 70(5):610–629. 12, 63

Almeida, J., Das, S., and Pinho, R. (2012). Adaptive force-based frame element for regularized softening response. *Computers & Structures*, 102:1–13. 12

Alsiwat, J. M. and Saatcioglu, M. (1992). Reinforcement anchorage slip under monotonic loading. *Journal of Structural Engineering*, 118(9):2421–2438. 28, 33, 112

Ang, B. G., Priestley, M. N., and Paulay, T. (1989). Seismic shear strength of circular reinforced concrete columns. *Structural Journal*, 86(1):45–59. 14, 75, 78, 100, 101, 125

Ascheim, M. and Moehle, J. (1992). Shear strength and deformability of RC bridge columns subjected to inelastic cyclic displacements. Technical Report UCB/EERC-92/04, University of California, Berkeley. 15

Ayoub, A. (2006). Nonlinear analysis of reinforced concrete beam–columns with bond-slip. *Journal of engineering mechanics*, 132(11):1177–1186. 25, 32

Bairan, J. and Mari, A. (2004). Non-linear interaction of normal and tangential internal forces on 3d RC beam-column structural systems. In *World Conference on Earthquake Engineering*. 87

Bairan, J. M. and Mari, A. R. (2007). Multiaxial-coupled analysis of RC cross-sections subjected to combined forces. *Engineering structures*, 29(8):1722–1738. 19, 22, 23, 155

Bathe, K.-J. (1996). *Finite Element Procedures*. Prentice-Hall Upper Saddle River, NJ. 132, 163, 169, 171

Batoz, J.-L. and Dhatt, G. (1979). Incremental displacement algorithms for nonlinear problems. *International Journal for Numerical Methods in Engineering*, 14(8):1262–1267. 165

Bazant, Z. and Bhat, P. (1977). Prediction of hysteresis of reinforced concrete members. *ASCE J STRUCT DIV*, 103(1):153–167. 21

Bažant, Z. P. and Oh, B. H. (1983). Crack band theory for fracture of concrete. *Matériaux et construction*, 16:155–177. 11

Belarbi, A. and Hsu, T. T. (1994). Constitutive laws of concrete in tension and reinforcing bars stiffened by concrete. *Structural Journal*, 91(4):465–474. xvii, 26, 27

Belarbi, A. and Hsu, T. T. (1995). Constitutive laws of softened concrete in biaxial tension compression. *Structural Journal*, 92(5):562–573. 14, 44

Bentz, E. C. (2000). *Sectional analysis of reinforced concrete members*. University of Toronto Toronto. 19, 22, 155

Berry, M., Parrish, M., and Eberhard, M. (2004). Peer structural performance database, user's manual (version 1.0). *University of California, Berkeley*. 65

Berry, M. P. (2006). *Performance Modeling Strategies for Modern Reinforced Concrete Bridge*. Department of Civil and Environmental Engineering, University of Washington, Seattle. 25, 29, 116

Bett, B. J., Klingner, R. E., and Jirsa, J. O. (1985). Behavior of strengthened and repaired reinforced concrete columns under cyclic deformations. Technical report, University of Texas at Austin. 87

Bhide, S. B. and Collins, M. P. (1989). Influence of axial tension on the shear capacity of reinforced concrete members. *Structural Journal*, 86(5):570–581. 45

Biskinis, D. E., Roupakias, G. K., and Fardis, M. N. (2004). Degradation of shear strength of reinforced concrete members with inelastic cyclic displacements. *Structural Journal*, 101(6):773–783. 15

Braga, F., Caprili, S., Gigliotti, R., Salvatore, W., et al. (2015). Hardening slip model for reinforcing steel bars. *Earthquakes and Structures*, 9(3):503–539. 28

Braga, F., Gigliotti, R., Laterza, M., D'Amato, M., and Kunnath, S. (2012). Modified steel bar model incorporating bond-slip for seismic assessment of concrete structures. *Journal of Structural Engineering*, 138(11):1342–1350. 25, 27

Calabrese, A., Almeida, J. P., and Pinho, R. (2010). Numerical issues in distributed inelasticity modeling of RC frame elements for seismic analysis. *Journal of Earthquake Engineering*, 14(S1):38–68. 9, 10, 63, 67

CEB (1996). *RC elements under cyclic loading: State of the art report*. CEB Bulletin No. 230, Thomas Telford. 44

Ceresa, P., Petrini, L., Pinho, R., and Sousa, R. (2009). A fibre flexure–shear model for seismic analysis of RC-framed structures. *Earthquake Engineering & Structural Dynamics*, 38(5):565–586. 19, 21

Chen, P. F. S. and Powell, G. H. (1982). *Generalized Plastic Hinge Concepts for 3D Beam-Column Elements*. UCB/EERC-82/20, Earthquake Engineering Research Center, University of California, Berkeley, CA. 2

Ciampi, V. and Carlesimo, L. (1986). A nonlinear beam element for seismic analysis of structures. In *8th European Conference on Earthquake Engineering*, volume 3, pages 6–3. 10

Clough, R. and Penzien, J. (1975). *Dynamics Of structures*. McGraw-Hill. 133, 134

Coleman, J. and Spacone, E. (2001). Localization issues in force-based frame elements. *Journal of Structural Engineering*, 127(11):1257–1265. 10, 11, 67

Collins, M. P. (1978). Towards a rational theory for RC members in shear. *Journal of the Structural Division*, 104(4):649–666. 14, 44

Crisfield, M. A. (1981). A fast incremental/iterative solution procedure that handles "snap-through". In *Computational methods in nonlinear structural and solid mechanics*, pages 55–62. Elsevier. 167

D'Ambrisi, A. and Filippou, F. C. (1999). Modeling of cyclic shear behavior in RC members. *Journal of Structural Engineering*, 125(10):1143–1150. 14

Deierlein, G. G., Reinhorn, A. M., and Willford, M. R. (2010). Nonlinear structural analysis for seismic design. *NEHRP seismic design technical brief*, 4:1–36. xvii, 1, 2

Di Re, P., Addessi, D., and Filippou, F. C. (2018). Mixed 3d beam element with damage plasticity for the analysis of RC members under warping torsion. *Journal of Structural Engineering*, 144(6):04018064. 19, 24

Ding, R., Tao, M.-X., Nie, J.-G., and Mo, Y. (2016). Shear deformation and sliding-based fiber beam-column model for seismic analysis of reinforced concrete coupling beams. *J. Struct. Eng*, 142(7):04016032. 92

Duong, K. V., Sheikh, S. A., and Vecchio, F. J. (2007). Seismic behavior of shear-critical reinforced concrete frame: Experimental investigation. *ACI Structural Journal*, 104(3):304. xix, xxiii, 78, 79, 80

El-Tawil, S. and Deierlein, G. G. (1998). Stress-resultant plasticity for frame structures. *Journal of engineering mechanics*, 124(12):1360–1370. 3

Elwood, K. J. (2004). Modelling failures in existing reinforced concrete columns. *Canadian Journal of Civil Engineering*, 31(5):846–859. 15

Elwood, K. J. and Moehle, J. P. (2003). *Shake table tests and analytical studies on the gravity load collapse of reinforced concrete frames*. Pacific Earthquake Engineering Research Center, University of California, Berkeley, PEER Report 2003/01. 15

Fardis, M. N. (2009). *Seismic design, assessment and retrofitting of concrete buildings: based on EN-Eurocode 8*, volume 8. Springer. 25

Feng, D., Ren, X., and Li, J. (2016). Implicit gradient delocalization method for force-based frame element. *Journal of Structural Engineering*, 142(2):04015122. 11

Feng, D.-C. and Ren, X.-D. (2017). Enriched force-based frame element with evolutionary plastic hinge. *Journal of Structural Engineering*, 143(10):06017005. 12

Feng, D.-C., Wu, G., and Ning, C.-L. (2019). A regularized force-based timoshenko fiber element including flexure-shear interaction for cyclic analysis of RC structures. *International Journal of Mechanical Sciences*, 160:59–74. 19, 21, 22

Feng, D.-C., Wu, G., Sun, Z.-Y., and Xu, J.-G. (2017). A flexure-shear timoshenko fiber beam element based on softened damage-plasticity model. *Engineering Structures*, 140:483–497. 19, 21, 22

Feng, D.-C. and Xu, J. (2018). An efficient fiber beam-column element considering flexure–shear interaction and anchorage bond-slip effect for cyclic analysis of RC structures. *Bulletin of Earthquake Engineering*, 16(11):5425–5452. 25, 27

Filippou, F. C. and Fenves, G. L. (2004). *Methods of analysis for earthquake-resistant structures*. In Y. Bozorgnia and VV Bertero, eds, Earthquake Engineering: From engineering seismology to performance-based engineering, CRC Press LLC. 39

Filippou, F. C., Popov, E. P., and Bertero, V. V. (1983). Effects of bond deterioration on hysteretic behavior of reinforced concrete joints. Technical Report EERC-83, Earthquake Engineering Research Center, University of California Berkeley. 112

Filippou, F. C. and Saritas, A. (2006). A beam finite element for shear-critical RC beams. *ACI Special Publications*, 237:295. 19, 21

Galal, K. E. and Ghobarah, A. (2003). Flexural and shear hysteretic behaviour of reinforced concrete columns with variable axial load. *Engineering Structures*, 25(11):1353–1367. 17

Ghannoum, W. M. (2007). *Experimental and analytical dynamic collapse study of a reinforced concrete frame with light transverse reinforcement*. University of California, Berkeley. 25, 29, 30, 115

Ghannoum, W. M. and Moehle, J. P. (2012). Rotation-based shear failure model for lightly confined RC columns. *Journal of Structural Engineering*, 138(10):1267–1278. 15

Giuffre, A. (1970). Il comportamento del cemento armato per sollecitazioni cicliche di forte intensita. *Giornale del Genio Civile*. 54

Goodnight, J., Kowalsky, M., and Nau, J. (2014). A new look at strain limits and plastic hinge lengths for reinforced concrete bridge columns. In *10th US Natl. Conf. Earthq. Eng., Anchorage*. 26

Guedes, J. and Pinto, A. (1997). A numerical model for shear dominated bridge piers. In *Proc. of the second Italian-Japan Workshop on seismic design and retrofit of bridges*. 18

Guner, S. and Vecchio, F. J. (2011). Analysis of shear-critical reinforced concrete plane frame elements under cyclic loading. *Journal of Structural Engineering*, 137(8):834–843. 19, 21, 35

Hashemi, S. S. and Vaghefi, M. (2011). Cyclic analysis of RC frames with respect to employing different methods in the fiber model for consideration of bond-slip effect. *Turkish Journal of Engineering and Environmental Sciences*, 36(1):1–18. 32

Hilber, H. M., Hughes, T. J., and Taylor, R. L. (1977). Improved numerical dissipation for time integration algorithms in structural dynamics. *Earthquake Engineering & Structural Dynamics*, 5(3):283–292. 132, 138, 146, 151, 171

Hsu, T. T. and Zhu, R. R. (2002). Softened membrane model for reinforced concrete elements in shear. *Structural Journal*, 99(4):460–469. 14

Ichinose, T. (1992). A shear design equation for ductile R/C members. *Earthquake engineering & structural dynamics*, 21(3):197–214. 15

Imai, H. and Yamamoto, Y. (1986). A study on causes of earthquake damage of izumi high school due to miyagi-ken-oki earthquake in 1978. *Transactions of the Japan Concrete Institute*, 8(1):405–418. 65, 73, 77, 98, 125

Kaba, S. A. and Mahin, S. A. (1984). Refined modelling of reinforced concrete columns for seismic analysis. Report EERC 84-3. *University of California Berkeley*. 10

Kagermanov, A. and Ceresa, P. (2016). Physically based cyclic tensile model for RC membrane elements. *Journal of Structural Engineering*, 142(12):04016118. 44

Kagermanov, A. and Ceresa, P. (2017). Fiber-section model with an exact shear strain profile for two-dimensional RC frame structures. *Journal of Structural Engineering*, 143(10):04017132. 19, 22, 155

Kaufmann, W. and Marti, P. (1998). Structural concrete: cracked membrane model. *Journal of Structural Engineering*, 124(12):1467–1475. 44

Kaul, R. (2004). *Object oriented development of strength and stiffness degrading models for reinforced concrete structures*. Stanford University. 17

Kwak, H.-G. and Kim, J.-K. (2006). Implementation of bond-slip effect in analyses of RC frames under cyclic loads using layered section method. *Engineering structures*, 28(12):1715–1727. 25, 26

Lai, S.-S., Will, G. T., and Otani, S. (1984). Model for inelastic biaxial bending of concrete members. *Journal of structural engineering*, 110(11):2563–2584. 3

Laplace, P. N. (2001). *Experimental study and analysis of retrofitted flexure and shear dominated circular reinforced concrete bridge columns subjected to shake table excitation*. Report No. CCEER 01-6, University of Nevada, Reno. 144

Le Corvec, V. (2012). *Nonlinear 3d frame element with multi-axial coupling under consideration of local effects*. PhD thesis, UC Berkeley. 24

Lee, C.-L. and Filippou, F. (2010). Mixed formulation for composite and RC frame element with bond-slip. In *Structures Congress 2010: 19th Analysis and Computation Specialty Conference*, pages 516–526. 25, 32

Lee, C.-L. and Filippou, F. C. (2015). Frame element with mixed formulations for composite and RC members with bond slip. i: Theory and fixed-end rotation. *Journal of Structural Engineering*, 141(11):04015039. 33

Lee, D. H. and Elnashai, A. S. (2002). Inelastic seismic analysis of RC bridge piers including flexure-shear-axial interaction. *Structural Engineering and Mechanics*, 13(3):241–260. 16

Lehman, D. E. and Moehle, J. P. (2000). *Seismic performance of well-confined concrete bridge columns*. PEER 1988/01, Pacific Earthquake Engineering Research Center, University of California, Berkeley. xxi, xxiii, 29, 123, 124

Limkatanyu, S. and Spacone, E. (2002). Reinforced concrete frame element with bond interfaces. i: Displacement-based, force-based, and mixed formulations. *Journal of Structural Engineering*, 128(3):346–355. 25, 31, 32

Lobo, P. S. and Almeida, J. (2015). RC fiber beam–column model with bond-slip in the vicinity of interior joints. *Engineering Structures*, 96:78–87. 25, 32

Lodhi, M. and Sezen, H. (2012). Estimation of monotonic behavior of reinforced concrete columns considering shear-flexure-axial load interaction. *Earthquake engineering & structural dynamics*, 41(15):2159–2175. 16

Mander, J. B., Priestley, M. J., and Park, R. (1988). Theoretical stress-strain model for confined concrete. *Journal of structural engineering*, 114(8):1804–1826. 49, 50, 82, 94, 96, 119, 126, 138, 145, 149

Mansour, M. and Hsu, T. T. (2005). Behavior of reinforced concrete elements under cyclic shear. ii: Theoretical model. *Journal of Structural Engineering*, 131(1):54–65. 14

Mari, A. R. and Scordelis, A. (1984). *Nonlinear geometric, material and time dependent analysis of three dimensional reinforced and prestressed concrete frames*. SESM Report 82-12, Department of Civil Engineering, University of California, Berkeley. 3

Marini, A. and Spacone, E. (2006). Analysis of reinforced concrete elements including shear effects. *ACI Structural Journal*, 103(5):645. 18, 19, 84, 85, 89

Martinelli, L. (2000). The behavior of reinforced concrete piers under strong seismic

actions. In *Proceedings of the Twelfth Word Conference on Earthquake Engineering Auckland, New Zealand*. 18

Martino, R., Spacone, E., and Kingsley, G. (2000). Nonlinear pushover analysis of RC structures. In *Advanced technology in structural engineering*, pages 1–8. 19, 84

Mazars, J., Kotronis, P., Ragueneau, F., and Casaux, G. (2006). Using multifiber beams to account for shear and torsion: Applications to concrete structural elements. *Computer Methods in Applied Mechanics and Engineering*, 195(52):7264–7281. 21, 22

Menegotto, M. and Pinto, P. E. (1973). Method of analysis for cyclically loaded RC plane frames including changes in geometry and non-elastic behavior of elements under combined normal force and bending. In *Proc. of IABSE symposium on resistance and ultimate deformability of structures acted on by well defined repeated loads*, pages 15–22. 54, 94, 96, 138, 145

Mergos, P. and Kappos, A. (2008). A distributed shear and flexural flexibility model with shear–flexure interaction for R/C members subjected to seismic loading. *Earthquake Engineering & Structural Dynamics*, 37(12):1349–1370. 92

Mergos, P. E. and Kappos, A. J. (2012). A gradual spread inelasticity model for R/C beam–columns, accounting for flexure, shear and anchorage slip. *Engineering Structures*, 44:94–106. 17

Mohr, S., Bairán, J. M., and Marí, A. R. (2010). A frame element model for the analysis of reinforced concrete structures under shear and bending. *Engineering structures*, 32(12):3936–3954. 19, 22, 23, 155

Monti, G., Filippou, F. C., and Spacone, E. (1997). Finite element for anchored bars under cyclic load reversals. *Journal of structural engineering*, 123:614–623. 31

Monti, G. and Spacone, E. (2000). Reinforced concrete fiber beam element with bond-slip. *Journal of structural engineering*, 126(6):654–661. xvii, 25, 30, 31, 32

Mostafaei, H. and Kabeyasawa, T. (2007). Axial-shear-flexure interaction approach for reinforced concrete columns. *ACI Materials Journal*, 104(2):218. 16

Mostafaei, H. and Vecchio, F. (2008). Uniaxial shear-flexure model for reinforced concrete elements. *J. Eng. Struct.* 16

Mostafaei, H., Vecchio, F. J., and Kabeyasawa, T. (2009). Deformation capacity of reinforced concrete columns. *ACI structural journal*, 106(2). 15

Mullapudi, T. R. and Ayoub, A. (2010). Modeling of the seismic behavior of shear-critical reinforced concrete columns. *Engineering Structures*, 32(11):3601–3615. 19, 21

Navarro-Gregori, J., Miguel, P., Fernández, M., and Martí-Vargas, J. R. (2013). A theoretical model for including the effect of monotonic shear loading in the analysis of reinforced concrete beams. *Engineering structures*, 52:257–272. 19, 21

Neuenhofer, A. and Filippou, F. C. (1997). Evaluation of nonlinear frame finite-element models. *Journal of Structural Engineering*, 123(7):958–966. 10

Newmark, N. M. (1959). A method of computation for structural dynamics. *Journal of the engineering mechanics division*, 85(3):67–94. 132, 151

Ohue, M., Morimoto, H., Fujii, S., and Morita, S. (1985). The behavior of RC short columns failing in splitting bond-shear under dynamic lateral loading. *Transactions of the Japan Concrete Institute*, 7(1):293–300. 75, 100, 125

Oñate, E. (2013). *Thick/Slender Plane Beams. Timoshenko Theory*, pages 37–97. Springer Netherlands, Dordrecht. 9

Orakcal, K., Massone, L. M., and Ulugtekin, D. (2019). A hysteretic constitutive model for reinforced concrete panel elements. *International Journal of Concrete Structures and Materials*, 13:1–23. 44

Otani, S. (1973). *Behavior of multistory reinforced concrete frames during earthquakes*. University of Illinois at Urbana-Champaign. 28

Ozcebe, G. and Saatcioglu, M. (1989). Hysteretic shear model for reinforced concrete members. *Journal of Structural Engineering*, 115(1):132–148. 15, 90, 91, 92

Pan, W.-H., Tao, M.-X., and Nie, J.-G. (2017). Fiber beam–column element model considering reinforcement anchorage slip in the footing. *Bulletin of Earthquake Engineering*, 15(3):991–1018. 25, 27

Pan, W.-H., Tao, M.-X., Nie, X., and Fan, J.-S. (2018). Rebar anchorage slip macro model considering bond stress distribution: Monotonic loading and model application. *J. Struct. Eng*, 144(8):04018097. 25, 27, 28

Pang, X.-B. D. and Hsu, T. T. (1995). Behavior of reinforced concrete membrane elements in shear. *Structural Journal*, 92(6):665–679. 14, 44

Pang, X.-B. D. and Hsu, T. T. (1996). Fixed angle softened truss model for reinforced concrete. *Structural Journal*, 93(2):196–208. 14, 44

Pantò, B., Rapicavoli, D., Caddemi, S., and Caliò, I. (2019). A fibre smart displacement based (fsdb) beam element for the nonlinear analysis of reinforced concrete members. *International Journal of Non-Linear Mechanics*, 117:103222. 9

Park, T., Ahmed, B., and Voyiadjis, G. Z. (2022). A review of continuum damage and plasticity in concrete: Part i–theoretical framework. *International Journal of Damage Mechanics*, 31(6):901–954. 44

Petrangeli, M., Pinto, P. E., and Ciampi, V. (1995). Towards a formulation of a fiber model for elements under cyclic bending and shear. In *European Seismic Design Practice*, pages 411–419. Routledge. 35

Petrangeli, M., Pinto, P. E., and Ciampi, V. (1999). Fiber element for cyclic bending and shear of RC structures. I: Theory. *Journal of Engineering Mechanics*, 125(9):994–1001. 19, 21, 59

Pimanmas, A. and Maekawa, K. (2001). Finite element analysis and behaviour of pre-cracked reinforced concrete members in shear. *Magazine of Concrete Research*, 53(4):263–282. 44

Pincheira, J., Dotiwala, F. S., and D'Souza, J. T. (1999). Seismic analysis of older reinforced concrete columns. *Earthquake Spectra*, 15(2):245–272. 14

Popovics, S. (1973). A numerical approach to the complete stress-strain curve of concrete. *Cement and concrete research*, 3(5):583–599. 49

Priestley, M. N., Verma, R., and Xiao, Y. (1994). Seismic shear strength of reinforced concrete columns. *Journal of structural engineering*, 120(8):2310–2329. 14, 15

Priestley, N., Calvi, G. M., and Kowalsky, M. J. (2007). *Displacement-Based Seismic Design of Structures*. IUSS Press, Pavia, Italy. 25

Pujol, S., Ramfrez, J., and Sozen, M. (1999). Drift capacity of reinforced concrete columns subjected to cyclic shear reversals. *Special Publication*, 187:255–274. 15

Rajapakse, R., Wijesundara, K., Nascimbene, R., Bandara, C., and Dissanayake, R. (2019). Accounting axial-moment-shear interaction for force-based fiber modeling of RC frames. *Engineering Structures*, 184:15–36. 19, 21, 22

Ranzo, G. and Petrangeli, M. (1998). A fibre finite beam element with section shear modelling for seismic analysis of RC structures. *Journal of earthquake engineering*, 2(03):443–473. 18, 19, 84, 85, 89

Rathje, E. M., Dawson, C., Padgett, J. E., Pinelli, J.-P., Stanzione, D., Adair, A., Arduino, P., Brandenberg, S. J., Cockerill, T., Dey, C., et al. (2017). Designsafe: New cyberinfrastructure for natural hazards engineering. *Natural Hazards Review*, 18(3):06017001. 136

Rericha, P. (1991). Layer model of bending-shear failure in RC plates and beams. *Journal of Structural Engineering*, 117(10):2865–2883. 19, 21, 59

Reshotkina, S. S. (2015). *3D Stiffness and Strength Degradation Models for Seismic Progressive Collapse Analysis of Reinforced Concrete Structures–Formulations and Implementations Framework*. PhD thesis, Carleton University, Ottawa, Ontario. 17

Ricles, J. M., Yang, Y.-S., and Priestley, M. N. (1998). Modeling nonductile R/C columns for seismic analysis of bridges. *Journal of Structural Engineering*, 124(4):415–425. 17

Roufaiel, M. S. and Meyer, C. (1987). Analytical modeling of hysteretic behavior of R/C frames. *Journal of Structural Engineering*, 113(3):429–444. 17

Saatcioglu, M., Alsiwat, J. M., and Ozcebe, G. (1992). Hysteretic behavior of anchorage slip in R/C members. *Journal of Structural Engineering*, 118(9):2439–2458. xxi, xxiii, 4, 120, 121, 122

Saatcioglu, M. and Grira, M. (1999). Confinement of reinforced concrete columns with welded reinforced grids. *Structural Journal*, 96(1):29–39. 71, 77, 96, 125

Sae-Long, W. and Limkatanyu, S. (2018). Shear model with shear-flexure interaction for non-linear analysis of reinforced concrete frame element. In *MATEC Web of Conferences*, volume 192, page 02003. EDP Sciences. 18, 19

Sae-Long, W., Limkatanyu, S., Hansapinyo, C., Imjai, T., and Kwon, M. (2020). Forced-based shear-flexure-interaction frame element for nonlinear analysis of non-ductile reinforced concrete columns. *Journal of Applied and Computational Mechanics*. 19, 84, 85, 89

Sae-Long, W., Limkatanyu, S., Prachasaree, W., Horpibulsuk, S., and Panedpojaman, P. (2019). Nonlinear frame element with shear–flexure interaction for seismic analysis of non-ductile reinforced concrete columns. *International Journal of Concrete Structures and Materials*, 13(1):1–19. 19, 84, 85, 89

Sasani, M. (2007). Life-safety and near-collapse capacity models for seismic shear behavior of reinforced concrete columns. *ACI Structural Journal*, 104(1):30. 15

Schoettler, M., Restrepo, J., Guerrini, G., Duck, D., and Carrea, F. (2015). A full-scale, single-column bridge bent tested by shake-table excitation. peer report 2015/02. pacific earthquake engineering research center (peer). *University of California, Berkeley, CA*. xxii, 137, 139

Scott, M. and Hamutçuoğlu, O. (2008). Numerically consistent regularization of force-based frame elements. *International journal for numerical methods in engineering*, 76(10):1612–1631. 12, 64, 68

Scott, M. H. and Fenves, G. L. (2006). Plastic hinge integration methods for force-based beam–column elements. *Journal of Structural Engineering*, 132(2):244–252. 12, 63, 69

Setzler, E. J. and Sezen, H. (2008). Model for the lateral behavior of reinforced concrete columns including shear deformations. *Earthquake Spectra*, 24(2):493–511. 15

Sezen, H. and Chowdhury, T. (2009). Hysteretic model for reinforced concrete columns including the effect of shear and axial load failure. *Journal of Structural Engineering*, 135(2):139–146. 15, 29

Sezen, H. and Moehle, J. P. (2004). Shear strength model for lightly reinforced concrete columns. *Journal of structural engineering*, 130(11):1692–1703. 4, 15

Sezen, H. and Setzler, E. J. (2008). Reinforcement slip in reinforced concrete columns. *ACI Structural Journal*, 105(3):280. xvii, 28, 29, 111, 112

Shirai, N., Moriizumi, K., and Terasawa, K. (2001). Cyclic analysis of RC columns: Macro-element approach. *Modeling of Inelastic Behavior of RC Structures Under Seismic Loads*, page 435. 14

Shoraka, M. B. and Elwood, K. (2013). Mechanical model for non ductile reinforced concrete columns. *Journal of Earthquake Engineering*, 17(7):937–957. 16

Sideris, P. and Salehi, M. (2016). A gradient inelastic flexibility-based frame element formulation. *Journal of Engineering Mechanics*, 142(7):04016039. 11

So, M.-G. (2008). *Total strain based bond/slip and shear/friction membrane model for finite element analysis of reinforced concrete*. Washington University in St. Louis. 44

Sousa, R., Correia, A. A., Almeida, J. P., and Pinho, R. (2017). A fibre-based frame element with explicit consideration of bond-slip effects. In *World Conference on Earthquake Engineering*. 25, 29, 30

Spacone, E., Filippou, F. C., and Taucer, F. F. (1996). Fibre beam–column model for non-linear analysis of R/C frames: Part i. formulation. *Earthquake Engineering & Structural Dynamics*, 25(7):711–725. 3, 8, 10, 31, 36, 41, 56

Takizawa, H. and Aoyama, H. (1976). Biaxial effects in modelling earthquake response of R/C structures. *Earthquake Engineering & Structural Dynamics*, 4(6):523–552. 2

Tarquini, D., Almeida, J. P., and Beyer, K. (2017). Axially equilibrated displacement-based beam element for simulating the cyclic inelastic behaviour of RC members. *Earthquake Engineering & Structural Dynamics*, 46(9):1471–1492. 9

Tortolini, P., Spacone, E., and Petrangeli, M. (2012). A RC fibre beam element for full modelling of the bending-shear response by dual section approach. *Proceedings of SSCS Numerical Modeling Strategies for Sustainable Concrete Structures*. 22

Ueda, T., Lin, I., and Hawkins, N. (1986). Beam bar anchorage in exterior column-beam connections. *ACI Journal Proceedings*, 83(3):412–422. xxi, 114

Valipour, H. R. and Foster, D. S. J. (2007). *A novel flexibility based beam-column element for nonlinear analysis of reinforced concrete frames*. University of New South Wales, School of Civil and Environmental Engineering. 11

Vecchio, F. J. (1989). Nonlinear finite element analysis of reinforced concrete membranes. *ACI Structural Journal*, 86(1):26–35. 46

Vecchio, F. J. (1999). Towards cyclic load modeling of reinforced concrete. *ACI Structural Journal*, 96:193–202. 52

Vecchio, F. J. (2000). Disturbed stress field model for reinforced concrete: formulation. *Journal of structural engineering*, 126(9):1070–1077. 14, 44

Vecchio, F. J. and Collins, M. P. (1986). The modified compression-field theory for reinforced concrete elements subjected to shear. *ACI J.*, 83(2):219–231. 14, 44, 45, 50, 51, 71, 82, 94, 96, 119, 126, 138, 145, 149

Vecchio, F. J. and Collins, M. P. (1988). Predicting the response of reinforced concrete beams subjected to shear using modified compression field theory. *ACI Structural Journal*, 85(3):258–268. 20, 22, 41, 45, 86, 155

Vecchio, F. J. and Emara, M. B. (1992). Shear deformations in reinforced concrete frames. *ACI Structural journal*, 89(1):46–56. 45

Watanabe, F. and Ichinose, T. (1991). Strength and ductility design of RC members subjected to combined bending and shear. In *Proceeding of workshop on concrete shear in earthquake*, pages 429–438. 14

Wehbe, N. I., Saiidi, M. S., and Sanders, D. H. (1999). Seismic performance of rectangular bridge columns with moderate confinement. *ACI Structural Journal*, 96(2):248–258. 71, 96, 125

Xu, S.-Y. and Zhang, J. (2011). Hysteretic shear–flexure interaction model of reinforced concrete columns for seismic response assessment of bridges. *Earthquake Engineering & Structural Dynamics*, 40(3):315–337. 16, 92

Xu, S.-Y. and Zhang, J. (2012). Axial–shear–flexure interaction hysteretic model for RC columns under combined actions. *Engineering Structures*, 34:548–563. 16

Zeris, C. A. and Mahin, S. A. (1988). Analysis of reinforced concrete beam-columns under uniaxial excitation. *Journal of Structural Engineering*, 114(4):804–820. 3, 10

Zhao, J. and Sritharan, S. (2007). Modeling of strain penetration effects in fiber-based analysis of reinforced concrete structures. *ACI Materials Journal*, 104(2):133. xvii, 25, 28, 29, 30, 115, 116, 122, 125

Zhu, R. (2000). *Softened-membrane model of cracked reinforced concrete considering poisson effect*. PhD thesis, University of Houston. 44

Zhu, R. R., Hsu, T. T., and Lee, J.-Y. (2001). Rational shear modulus for smeared-crack analysis of reinforced concrete. *Structural Journal*, 98(4):443–450. 51, 82, 149

Zienkiewicz, O. C. and Taylor, R. L. (2005). *The finite element method for solid and structural mechanics*. Elsevier. 9

Zimos, D. K., Mergos, P. E., and Kappos, A. J. (2018). Modelling of R/C members accounting for shear failure localisation: Hysteretic shear model. *Earthquake Engineering & Structural Dynamics*, 47(8):1722–1741. 15, 17

List of Publications

Refereed Journals

1. **Saroj Kumar Sahu**, Arbind Kumar Singh. A simplified fibre beam element with shear-deformation for the analysis of reinforced concrete members. (Under communication)

2. **Saroj Kumar Sahu**, Arbind Kumar Singh. Modelling of RC structures considering shear and anchorage bond-slip using fibre-based elements. (Under communication)

Book Chapter

1. **Saroj Kumar Sahu**, Arbind Kumar Singh (2023). Comparative Study of Fibre-Based Frame Elements to Analyse Shear-Critical RC Frames. In: Shrikhande, M., Agarwal, P., Kumar, P.C.A. (eds) *Proceedings of 17th Symposium on Earthquake Engineering (Vol. 2)*. Lecture Notes in Civil Engineering, vol 330. pp. 353-365. Springer, Singapore. https://doi.org/10.1007/978-981-99-1604-7_27

International Conferences

1. **Saroj Kumar Sahu**, Arbind Kumar Singh (2024). Study of different shear kinematic assumptions on coupled axial-flexure-shear sectional analysis in shear deformable beam element. In *3rd Advances in Concrete, Structural & Geotechnical Engineering, ACSGE 2024*. 26-28 February 2024, BITS Pilani, India.

2. **Saroj Kumar Sahu**, Arbind Kumar Singh (2023). On softening behaviour of

force-based shear-flexible concrete frame element. In *13th Structural Engineering Convention, SEC 2023*. 7-9 December 2023, VNIT Nagpur, India.

3. **Saroj Kumar Sahu**, Arbind Kumar Singh (2022). On flexure-shear interaction in fibre model for the analysis of RC section. In *12th Structural Engineering Convention, SEC 2022*. 19-22 December 2022, MNIT Jaipur, India. https://doi.org/10.38208/acp.v1i2